UNIVERSITÀ
DI SIENA
1240

Dipartimento di
Scienze fisiche, della Terra e dell'ambiente

Dottorato in Scienze e tecnologie ambientali, geologiche e polari

38° Ciclo

Coordinatrice: Prof.ssa Letizia Marsili

Chondrite components: archives of protoplanetary disk processes.

From natural samples to experimental approaches

Settore scientifico disciplinare: *GEOS-01/B*

Candidato:
Andrea Vitrano
DSFTA, UNISI

Supervisor:
Prof. Francesco P. Vetere
DSFTA, UNISI

Anno accademico di conseguimento del titolo di Dottore di ricerca

2024-2025

This page intentionally left blank.

Università degli Studi di Siena

Dottorato in **Scienze e tecnologie ambientali, geologiche e polari**

38° Ciclo

Data dell'esame finale

20 marzo 2026

Commissione giudicatrice

Cecilia Viti

Dipartimento di Scienze Fisiche, della Terra e dell'Ambiente, Università di Siena

_____

Gianluca Iezzi

Dipartimento di Ingegneria e Geologia, Università "G. d'Annunzio" Chieti-Pescara

_____

Maurizio Petrelli

Dipartimento di Fisica e Geologia, Università di Perugia

_____

Supplenti

_____

_____

This page intentionally left blank.

Preface

This Ph.D. thesis investigates the formation and evolution of the Solar System's earliest building blocks. Chondrites are recognised as archives of protoplanetary disk processes, extending the geosciences' conventional disciplinary boundaries to link astrophysics and cosmochemistry. Despite decades of study, the formation of chondrites components—particularly chondrules and refractory inclusions—remains unresolved. This work addresses open questions regarding carbonaceous chondrites and the record of protoplanetary disk processes. The thesis is structured around distinct research efforts, which integrate analyses of natural samples with experimental petrology and laboratory activities. **Chapter 1** provides a comprehensive overview of chondrites and their components, establishing the fundamental petrological context for the research. In **Chapter 2**, I propose a review of the classical rock cycle, extending this concept to a cosmic scale. **Chapter 3** presents the analysis of natural meteorite samples. The principal investigations detailed in this chapter include the classification of a new carbonaceous chondrite (NWA 16768), the study of Wark-Lovering (WL) rims on two exceptionally well-preserved Calcium-Aluminum-rich Inclusions and the characterization of melt inclusions in chondrules. Finally, **Chapter 4** presents a diverse set of experimental investigations and their implications for planetary science. The principal studies detailed in this chapter include an evaluation of the prebiotic potential of carbonaceous chondrites, the design and preliminary testing of the VF-Smelt (Vacuum Furnace for Space Melts) experimental apparatus and a Brillouin spectroscopy study on natural and complex volcanic glasses to determine the role of divalent cations.

"Rocks are records of events that took place at the time they formed. They are books. They have a different vocabulary, a different alphabet, but you learn how to read them."

— John McPhee, *Annals of the Former World*, 2000

"The carbonaceous chondrites have been around for more than 4 billion years; I suspect they will remain enigmatic, at least in part, for a few more years."

— Edwin Roedder, *Fluid inclusions*, 1981

"Geology is the study of planets, asteroids, comets, stardust, giant molecular clouds, stars and supernovae. Geology is the study of anything with rocks in the Universe."

— Matthew Genge, *London Lecture - Geology in Space: Meteorites and Cosmic Dust*, 2014

Contents

This page intentionally left blank.

Chapter 1

Introduction

Chondrites represent the oldest known rocks and the most pristine evidence of the formation of the Solar System. They are sedimentary rocks, composed of a heterogeneous mixture of components that formed while free-floating in the solar nebula and accreted during the first million years of the protoplanetary disk's evolution [1]. Their bulk chemical composition closely matches that of the solar photosphere, indicating that they preserve the primitive composition of the solar nebula. Having escaped large-scale melting and differentiation, chondrites retain their primary mineralogical, chemical, and isotopic signatures, recording processes that occurred 4.56 billion years ago.

Petrology allows us to reconstruct the processes that led to the formation of rocks. However, to correctly interpret these processes, it is also essential to understand their broader geological context. Unfortunately, this is not possible for the components of chondrites, as their original environment is no longer accessible. Theoretical and numerical models, as well as simulations of protoplanetary disc evolution, have advanced significantly, thanks to increasing computational power. But only in the past decade, next-generation instruments have made it possible to obtain high-resolution observations of the gas and dust structures surrounding young stars.

Instruments such as the Very Large Telescope of the European Southern Observatory and the Atacama Large Millimeter/submillimeter Array, both located in the Atacama Desert of Chile, allow observations at visible, infrared, and millimeter wavelengths, revealing the thermal emission from dust grains in protoplanetary disks and, in some cases, even planets in formation (Fig. 1.1). These spectral observations have led to significant advances in numerical models and simulations; however, they still remain limited by their relatively coarse resolution.

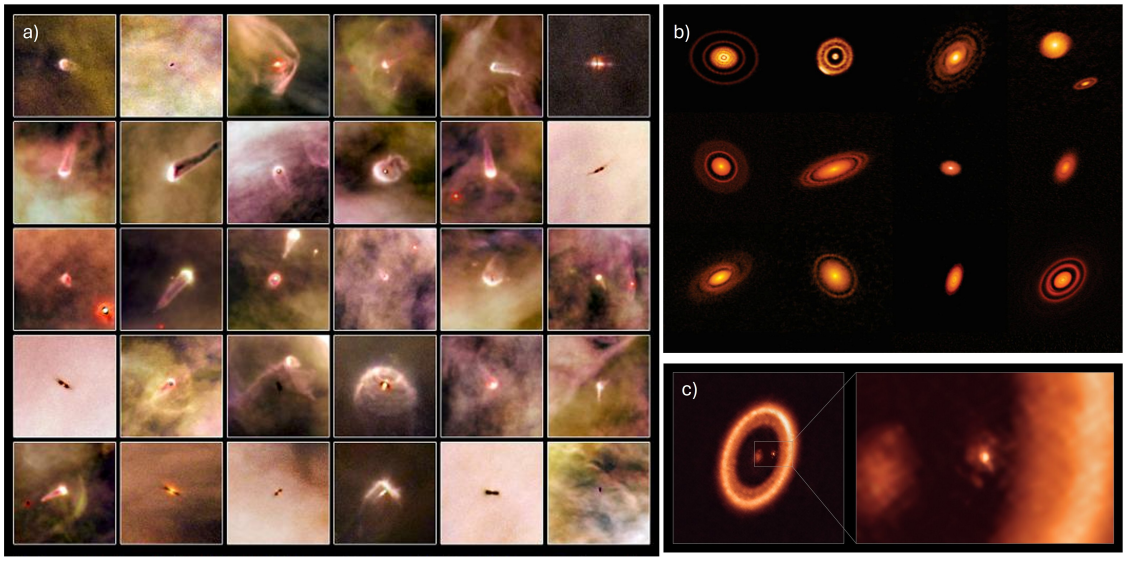

Figure 1.1: Telescope observations of protoplanetary disk formation and evolution. **(a)** Hubble Space Telescope survey of 30 protoplanetary disks in the Orion Nebula; credit: NASA/ESA and L. Ricci (ESO). **(b)** High-resolution ALMA observations from the Disk Substructures at High Angular Resolution Project revealing detailed annular gaps, dust rings, and spiral structures in protoplanetary disks, indicative of ongoing planet formation; credit: ALMA (ESO/NAOJ/NRAO), S. Andrews et al.; NRAO/AUI/NSF, S. Dagnello. **(c)** The PDS 70 system: left panel shows an overview of the disk, while on the right a detail panel reveals the in-situ formation of a Jupiter-mass protoplanet PDS 70c within the disk gap; credit: ALMA (ESO/NAOJ/NRAO)/Benisty et al.

By applying the *principle of actualism*, formulated by James Hutton and Charles Lyell, we can regard these systems as modern analogues of the protoplanetary disk from which the components of chondrites in our early Solar System formed. Astrophysics constrains meteoritics as much as meteoritics constrain astrophysics

[2]. In this context, chondrite components serve as *in situ* probes, providing direct access to the physicochemical conditions within protoplanetary disks at microscopic scales that will always remain beyond the reach of any telescope.

Among chondrite components, **refractory inclusions** are the first solids (excluding ices) to condense out of a gas of solar composition, as predicted by thermodynamic models [3, 4]. They are primarily divided into two main types: Calcium-Aluminum-rich Inclusions (CAIs) and Amoeboid Olivine Aggregates (AOAs). CAIs are composed of high-temperature Ca–Al–Ti minerals, stable above 1127 °C (1400 K), such as corundum (Al_2O_3), hibonite ($CaAl_{12}O_{19}$), grossite ($CaAl_4O_7$), perovskite ($CaTiO_3$), spinel ($MgAl_2O_4$), melilite (a solid solution of gehlenite, $Ca_2Al_2SiO_7$, and åkermanite, $Ca_2MgSi_2O_7$), Al-diopside ($Ca(Mg,Al)(Si,Al)_2O_6$), and anorthite ($CaAl_2Si_2O_8$). CAIs are considered the starting point of the Solar System's birth and have been dated to have formed around 4567.3 ± 0.2 Ma [5]. AOAs, in contrast, are aggregates dominated by forsteritic olivine with embedded refractory minerals similar to those found in CAIs, but they are generally less refractory and formed at slightly lower temperatures. The textures of CAIs are divided into two broad groups: fine-grained and coarse-grained inclusions [6]. Fluffy-shaped, fine-grained CAIs are widely considered to be direct condensates from the solar nebula. In contrast, CAIs that are coarse-grained with spheroidal shapes and igneous textures probably formed from fine-grained inclusions through melting and crystallization. As a consequence, CAIs provide direct evidence for high-temperature events, including evaporation, condensation, and melting that occurred in the early solar system. An exemplary structure of this are Wark-Lovering (WL) rims: thin, multi-layered mineral sequences that testify to a complex, multi-stage formation history involving repetitive flash-heating, evaporation, melting, and condensation events [7]. These structures provide a unique record of the high-temperature and dynamic conditions present in the early solar

nebula, offering clues about the formation and evolution of the first solids in the solar system. Multiple models have been proposed for WL rim formation, but several aspects have not yet been resolved. Among all chondrites, as shown in Table 1.1, pristine Vigarano-type carbonaceous chondrites (CV3) exhibit the highest abundance of CAIs (∼3 area% [8]) and contain some of the largest CAIs, reaching centimetre-scale diameters. Consequently, CAIs in CV3 chondrites are the most extensively studied [9, 10]. However, due to the scarcity of this group, which represents only ∼1% of all known meteorite finds, classifying new CV specimens is required.

Table 1.1: Calcium-aluminum-rich inclusion (CAI) abundances in various chondrites groups.

	Carbonaceous chondrites								
	CI	CM	CO	**CV**	CK	CR	CH	CB_a	CB_b
CAIs (area%)	<0.01	1.21	0.99	**2.98**	0.2	0.12	0.1	<0.1	0.1
	Ordinary chondrites			**Enstatite chondrites**		**Others**			
	H	L	LL	EH	EL	R	K		
CAIs (area%)	0.01–0.2	<0.1	<0.1	<0.1	<0.1	<0.1	<0.1		

Modal abundances of calcium-aluminium-rich inclusions (CAIs), determined by Hezel et al. 2008 and expressed as area percent. Reported values represent the observed range or upper limits, as indicated. CV chondrites are highlighted in bold, reflecting their characteristically high refractory inclusion content and status as the carbonaceous chondrite group with the highest CAI abundance.

Chondrules are signature objects of chondrites. They were first identified in 1802 by Edward Howard as "rounded globules", but they were not the subject of detailed scientific study. Only in 1863 did Henry Sorby provide detailed microscopic descriptions that led him to famously describe them as '*drops of fiery rain*' [11]. Today, chondrules are described as sub-millimetre mafic silicate (± metal and sulfide) spherules, formed from molten or partially molten free-floating droplets between 0 and 4 million years after CAIs. By the late 20th and early 21st centuries, consensus

shifted toward chondrule formation by transient brief high-temperature events such as shock waves, bow shocks, or impacts that melted fine-dust aggregates in the protoplanetary disk. The textural variety of chondrules arises from differences in their initial composition and thermal history, as illustrated in Fig. **??**. The main textural classifications are broadly subdivided into porphyritic and non-porphyritic textures. Among porphyritic textures, there are porphyritic olivine chondrules (PO), porphyritic pyroxene chondrules (PP), and the more common porphyritic olivine-pyroxene chondrules (POP). Non-porphyritic chondrules have textures in which olivine and pyroxene grains are elongate, a sign of rapid crystal growth. An iconic and common texture is the barred olivine chondrule (BO), which shows subparallel plates of olivine with a common optical crystal orientation. Among the less common textures are glassy chondrules (GC), cryptocrystalline chondrules (CC), and radial pyroxene chondrules (RP).

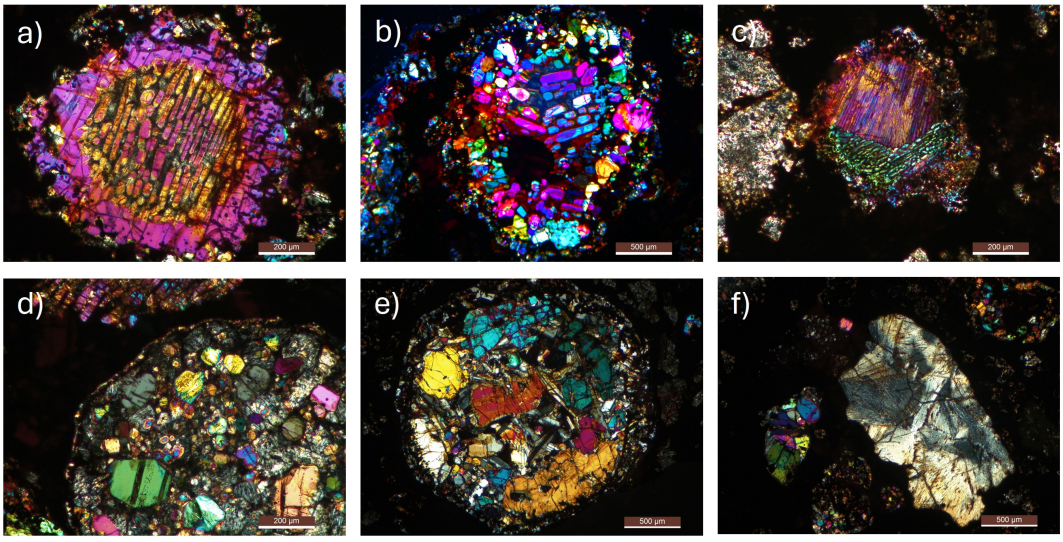

Figure 1.2: Optical micrographs in cross-polarized light showing characteristic chondrule textures from meteoritic samples. **(a-c)** Barred olivine (BO) chondrules displaying variations in bar morphology and crystallographic properties. **(d-e)** Porphyritic olivine-pyroxene (POP) chondrules exhibiting characteristic crystal frameworks. **(f)** Fragment of a radial pyroxene (RP) chondrule showing distinctive spherulitic texture.

The dating of chondrules and the presence of multiple generations of recycled chondrules suggest that chondrule formation was a more prolonged process rather than a single event. Among the various proposed mechanisms are: nebular lightning, X-wind, planetesimal collisions, and nebular shock waves. The debate is ongoing, but there is a consensus that the thermal histories of chondrules—such as the heating rate of the precursor material, the peak temperatures reached, the duration of heating, and the cooling rate—can constrain or test these models and must, therefore, be decoded from chondrule chemistry and textures.

Carbonaceous chondrites are also an important topic in astrobiology, as they contain **prebiotic organic compounds** and hydrated minerals. Thus, these meteorites represent a potential environment for the formation and evolution of the building blocks of life. Experiments that simulate the aqueous alteration of meteoritic minerals and organic matter can therefore shed light on the processes that govern the formation and evolution of prebiotic compound in the cosmos.

1.1 Aims of the Project

This thesis is built on the premise that the protoplanetary disk was a definable geological environment whose processes are recorded in the rocks we can hold in our hands. Here, petrology is the discipline capable of deciphering the history of rocks (as illustrated conceptually in Fig. **??**). Significant gaps remain in our understanding of meteoritic components, necessitating further investigation, data acquisition, and interpretation. This thesis aims to build a bridge between astrophysical observations of protoplanetary disks, by extending the classical rock cycle to a cosmic scale as a new conceptual framework, improve the record of CV3 chondrite classification and identification, analyze the microscopic petrological record preserved in chondritic

meteorites to constrain the physical and chemical conditions within the early Solar System's protoplanetary disk, focusing on Calcium-Aluminum-rich Inclusions (CAIs) and chondrules and develop experiments to investigate the origin of life processes that may have occurred within chondrite parent bodies, the origin of chondrules with a novel furnace and the application of a new Brillouin spectroscopy technique that could be useful for space mission. The work presented here is a compilation of the information I have gathered and the research questions I have posed, which I believe deserve future exploration concerning the puzzle of these fascinating rocks.

Figure 1.3: The chondrite meteorite is conceptualized as a physical recording medium (analogous to a vinyl disc) of protoplanetary disk processes. In this analogy, petrology acts as the analytical stylus required to resolve and interpret the microscopic record grooves.

References

[1] E. Jacquet, C. Dullemond, J. Drka.zkowska, and S. Desch (2024). The Early Solar System and Its Meteoritical Witnesses. *Space Science Reviews* vol. https://doi.org/10.1007/s11214-024-01112-y.

[2] E. Jacquet (2014). Transport of solids in protoplanetary disks: comparing meteorites and astrophysical models. *Comptes Rendus Geoscience* vol. **346**, 3–12. https://doi.org/10.1016/j.crte.2013.11.002.

[3] L. Grossman (1972). Condensation in the primitive solar nebula. *Geochimica et Cosmochimica Acta* vol. **36**, 597–619. https://doi.org/10.1016/0016-7037(72)90078-6.

[4] D. S. Ebel *Condensation Calculations in Planetary Science and Cosmochemistry*. 2021. https://doi.org/10.1093/acrefore/9780190647926.013.201. http://dx.doi.org/10.1093/acrefore/9780190647926.013.201.

[5] J. N. Connelly, M. Bizzarro, A. N. Krot, Å. Nordlund, D. Wielandt, and M. A. Ivanova (2012). The Absolute Chronology and Thermal Processing of Solids in the Solar Protoplanetary Disk. *Science* vol. **338**, 651–655. https://doi.org/10.1126/science.1226919.

[6] L. Grossman (1975). Petrography and mineral chemistry of Ca-rich inclusions in the Allende meteorite. *Geochimica et Cosmochimica Acta* vol. **39**, 433–454. https://doi.org/https://doi.org/10.1016/0016-7037(75)90099-X.

[7] D. Wark and W. V. Boynton (2001). The formation of rims on calcium-aluminum-rich inclusions: Step I—Flash heating. *Meteoritics & Planetary Science* vol. **36**, 1135–1166.

[8] D. C. Hezel, S. S. Russell, A. J. Ross, and A. T. Kearsley (2008). Modal abundances of CAIs: Implications for bulk chondrite element abundances and fractionations. *Meteoritics & Planetary Science* vol. **43**, 1879–1894. https://doi.org/10.1111/j.1945-5100.2008.tb00649.x.

[9] M. C. Michel-Lévy (1968). An exceptional chondrule in the Vigarano meteorite. *Bulletin de la Société Française de Minéralogie et de Cristallographie* vol. **91**, 212–213.

[10] E. Scott and A. Krot "1.2 - Chondrites and Their Components". In: *Treatise on Geochemistry (Second Edition)*. Ed. by H. D. Holland and K. K. Turekian. Second Edition. Oxford: Elsevier, 2014, 65–137. https://doi.org/https://doi.org/10.1016/B978-0-08-095975-7.00104-2. https://www.sciencedirect.com/science/article/pii/B9780080959757001042.

[11] G. J. H. McCall (2006). Chondrules and calcium-aluminium-rich inclusions (CAIs). *Geological Society, London, Special Publications* vol. **256**, 345–361. https://doi.org/10.1144/gsl.sp.2006.256.01.17.

Chapter 2

Extending the Rock Cycle to a Cosmic Scale

Published in 2025 in *Geosciences* by Andrea Vitrano, Nicola Mari, Daniele Musumeci, Luigi Ingaliso and Francesco Vetere.

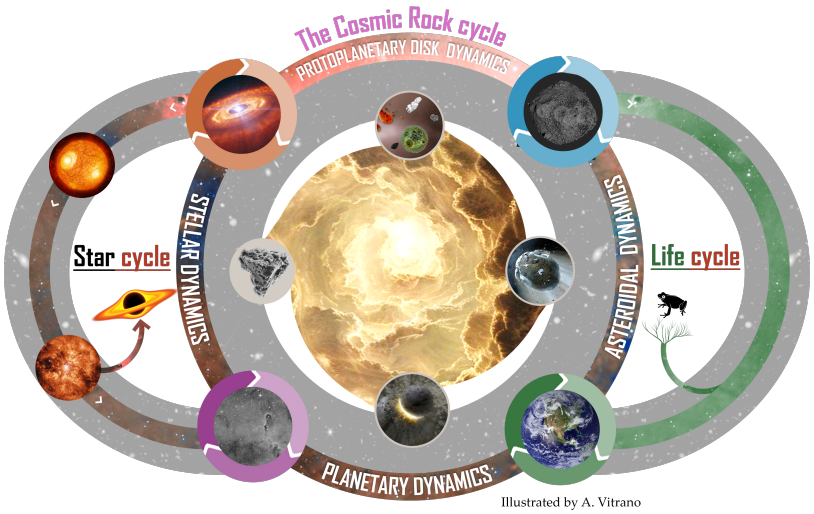

Figure 2.1: Visual abstract.

Abstract

The rock cycle, a cornerstone of geosciences, describes rock formation and transformation on Earth. However, this Earth-centric view overlooks the broader history of rock evolution across the cosmos, with two fundamental limitations: (i) Earth-centric paradigms that ignore extraterrestrial lithogenesis, excluding cosmically significant rocks and processes, and (ii) disciplinary fragmentation between geological and astrophysical sciences, from the micro- to the macroscale. This review proposes an extension of the rock cycle concept to a cosmic scale, exploring the origin of rocks and their evolution from interstellar space, through the aggregation of solid materials in protoplanetary disks, and their subsequent evolution on planetary bodies. Through systematic analysis of igneous, metamorphic, and sedimentary processes occurring beyond Earth, we identify four major domains in which distinct dynamics govern the rock cycle, each reworking rocks with domain specific characteristics: (1) stellar and nebular dynamics, (2) protoplanetary disk dynamics, (3) asteroidal dynamics, and (4) planetary dynamics. Here we propose the cosmic rock cycle as a new epistemic tool that could transform interdisciplinary research and geoscience education. This perspective reveals Earth's rock cycle as a rare and invaluable subset of rock genesis in the cosmos.

Keywords: *Rock cycle; planetary geology; teaching geosciences; philosophy of geology.*

2.1 Introduction

The rock cycle is a cornerstone of geological science; however, surprisingly, no formal definition has been established. Early ideas from Leonardo da Vinci (1452–1519) and Steno (1638–1686), later improved by Hutton (1726–1797) and Lyell (1797–1875), have described how the interactions between the atmosphere, hydrosphere, biosphere,

and geological processes shape and transform rocks on Earth [1–3]. This concept experienced a perspective shift with the formulation of plate tectonics, evolving from a fixist view to a mobilist model [4–6]. To introduce the concept of the rock cycle at a cosmic scale, one must first extend the definition of rocks. The widely accepted definition of "rocks" as *"solid, naturally occurring aggregates of minerals*" is pragmatically useful but suffers from both scientific and conceptual limitations. For example, referring to rock as only an aggregate of minerals fails to account for rocks composed substantially of glass or mineraloids. Providing a formal definition of rock is beyond the scope of this paper. We consider it more philosophically productive to engage with the concept of rock, rather than to pursue a universal, possibly unattainable, definition.

The informal idea of "rocks" often excludes other crystalline aggregates, such as water ice or even CO_2 and CH_4 ices, nitrogen ices, and even mixtures of different ices or mixed ices with rocky materials, despite their clear lithological significance in the outer Solar System and beyond. Another clear and illustrative example of a persistent misconception about the definition of rocks is the conventional distinction between "stony" and "iron" meteorites—as if iron meteorites were somehow not considered "rocks". In reality, iron meteorites are composed of minerals such as taenite and kamacite and should therefore be regarded as true rocks. Of course, geoscientists recognize that ices and metals meet petrological criteria, yet a terrestrial-centric perspective often implicitly excludes these lithologies from the concept of "rock". Planetary geoscientists need to think more broadly about their concept of rocks to include naturally occurring metals and ices, as they represent lithologies no less significant than commonly intended rocks and are widespread throughout the Solar System and beyond.

The rock cycle, as traditionally defined, describes Earth's system of interacting endogenic and exogenic processes that continuously reshape rocks. **Endogenic**

processes are driven by internal heat—primarily from radioactive decay—which leads to the melting of rocks into magma, later crystallizing into igneous rocks. Mantle convection and tectonics drive rocks through different temperature and pressure conditions, causing metamorphism, metasomatism, or re-melting. **Exogenic processes** modify rocks through complex interactions between the lithosphere and atmosphere, hydrosphere, cryosphere, and biosphere—mainly powered by solar radiation and gravity. Although they involve only the Earth's crust, which represents a smaller volume than planet Earth, these processes produce a wide variety of rocks and involve numerous interconnected processes depending on the climate, the duration of the action of the exogenous agents, and the chemical/petrological characteristics of the rock. These dynamics operate via two fundamental mechanisms: weathering and erosion.

Weathering is the in situ physical and chemical breakdown of rocks and minerals at or near Earth's surface, occurring without material transport. It includes physical weathering and chemical weathering. Physical weathering involves the fragmentation of rocks into smaller particles without altering their mineralogical composition. Common mechanisms include thermal expansion, where repeated heating and cooling induce stress fractures; frost wedging, in which water infiltrates rock fractures, freezes, and expands, exerting mechanical force; and root wedging, whereby plant roots penetrate and widen cracks. Chemical weathering alters the original minerals in rocks through water- and atmosphere-driven reactions influenced by factors such as pH and redox conditions. Water–rock interactions can promote processes like dissolution and hydrolysis, which break down minerals into ions and secondary products. Atmosphere–rock interactions can also cause changes in mineral oxidation states, as well as other reactions such as carbonation. Chemical weathering processes are most active in warm, humid climates.

Erosion refers to the suite of processes responsible for the removal of rock and

mineral fragments from exposed outcrops, as well as their transport toward depositional environments. Any dynamic flow interacting with the Earth's surface (e.g., air, water, ice, or gravity) can act as an erosive agent. These agents mobilize and displace surface materials through mechanisms such as aeolian abrasion (wind-driven sandblasting), fluvial entrainment and cavitation (in turbulent water), glacial plucking and scouring (by moving ice), and mass wasting (e.g., landslides). The erosive capacity of these flows depends on their velocity and density, and the physical properties of the materials involved. Collectively, these processes generate a continuous flux of sediment, redistributing particles from source areas to sedimentary basins. The activity of the different life forms on Earth, such as plants, fungi, lichens, and microorganisms, can significantly enhance both erosion and weathering. Over time, the buried sediments may undergo diagenesis, a combination of physical, chemical, and biological processes including compaction, cementation, and recrystallization, that lithifies them into sedimentary rocks. However, these newly formed rocks may later be re-eroded, metamorphosed, or even melted. The Earth's rock cycle is too complex to fully describe because it involves several physicochemical processes, and the above-mentioned are only the most well-known. In this paper, we aim to extend this complex network of Earth's processes beyond planet Earth.

Today, after 80 years, the rock cycle is considered established knowledge and is not often revisited in light of current knowledge. A new perspective is needed to solve two key problems in the traditional rock cycle. (i) First, the Earth-centered perspective of the rock cycle is now outdated. In the last century, studies in cosmochemistry and planetary geology have shown that geological processes extend beyond Earth's boundaries with analogue processes or very exotic ones. The proliferation of data and materials from distant worlds is exponentially increasing. (ii) Second, astronomy and planetary and Earth-based sciences are still considered distinct scientific fields due to differences in methodologies, terminologies, research approach, and dissemination

platforms [7]. This rift requires an integrated approach that reconciles microscopic analysis of rocks, the mesoscale processes of planetary geology, and the cosmic scale of astrophysical and astrochemical phenomena [8]. Scientists have underlined the importance of applying this vision together from perspectives such as the astrobiological [9] or geochemical [10]. This approach, based on a flexible view of disciplinary paradigms, makes the boundaries less rigidly dependent upon epistemological models, leading to continuous intersections between knowledge [11], as happens for example between geophysics and medicine [12].

The *rock cycle*, in its various simplified graphic representations [13], is composed of the three main rock types—sedimentary, igneous, and metamorphic—and the processes that drive their transformations. This picture can be viewed as a functional pedagogical tool. Over the last century, diagrams have been considerably implemented in scientific research to such an extent that they have increasingly taken on an epistemic function. It is no coincidence that today they are considered true **tools for thinking** because they are, for all intents and purposes, elements of research [14]. They serve to outline the phenomenon being examined; the relationships, constant and variable, that explain their genesis; and the mechanisms that determine them [15].

2.2 The Four Domains of the Rock Cycle

To explain the formation and transformation of rocky materials, we identify four main lithogenic domains characterized by different physical and chemical conditions, resulting in distinct rock-forming mechanisms. The following sections discuss the four key domains of the cosmic rock cycle: (1) stellar and nebular dynamics, (2) protoplanetary disk dynamics, (3) asteroidal dynamics, and (4) planetary dynamics.

2.2.1 Stellar and Nebular Dynamics

Stars do more than shine; they are the cosmic factories that create the building blocks for planets and rocks [16]. Obviously, the rock cycle requires the presence of "rock-forming elements" in specific abundances. When a star reaches the end of its life as a supernova, it scatters rock-forming elements into the surrounding space. This process enriches the interstellar medium, paving the way for the formation of possible new stars, planets, and other celestial bodies. In this way, the **star life cycle** determines the available elements for the creation of rocks. Looking back in time, one question arises: "What was the first mineral in the cosmos [17]?" In the early stages, stars were primarily made up of hydrogen and helium, so it is plausible that only after the formation of carbon and oxygen, graphite and ices—such as water, methane, and carbon monoxide—or their polymorphs may have been among the first minerals to form in space [18]. The element abundances and chemo-physical characteristics of a nebula are also shaped by external factors such as stellar winds, cosmic rays, and supernova explosions, which "sculpt" the chemistry of molecular clouds, clearing low-density gas and creating denser regions, influencing planetary system formation [19, 20]. Those dynamic interactions resemble geological processes on Earth, such as selective erosion, transport, and accumulation. The mineralogical evidence that interstellar minerals expelled from ancient stellar systems become the starting material for new stellar systems lies in what we call **presolar grains**—small bits of solid interstellar matter that formed in the outflows or explosions of ancient stars [21, 22]. These stardust particles made of silicon carbide (SiC), diamond, and graphite survived the voyage through space and time. Their age predates the Solar System by up to 7 billion years [23], proving that their origin does not derive from our much younger Solar System. In any cyclic system, the choice of a starting point is arbitrary. Within the framework of a cosmic-scale rock cycle, we choose interstellar

grains as a pragmatic reference, as they represent the mineralogical evidence that can be confidently identified and characterized. More broadly, the onset of the cosmic rock cycle lies in the transition from stellar processes to the formation of minerals in the interstellar medium.

Thus, stellar and nebular dynamics constitute the indispensable first stage of the rock cycle, seeding the interstellar medium with rock-forming elements and minerals, and governing subsequent rock-forming processes.

2.2.2 Protoplanetary Disk Dynamics

As gravity pulls nebular material inward, it forms a **protoplanetary disk** around a young star, where gas, dust, and ice will be mixed and processed to rocks. Protoplanetary disks host a wide range of physical and chemical processes, many of which remain only partially understood and continue to be the focus of active research. What we know about this environment has improved through the study of chondritic rocks and astrophysical modeling, and only recently directly imaged [24, 25]. The chemistry of protoplanetary disks is not merely a continuation of interstellar chemistry but is processed by the radial and vertical gradients in temperature and density, accretion, and turbulent mixing [26–28]. The main first protoplanetary disk process, consisting of formation of a chemical dichotomy marked by the **snow line** [29, 30], beyond which temperatures are low enough for volatile compounds like water, methane, and ammonia to freeze into ice while rocky materials still in the hot inner regions [31]. This process is recorded in rocks with distinct lithological characteristics: carbonaceous chondrites from the icy outer disk and non-carbonaceous chondrites from the dry inner disk [32, 33].

Chondrite components preserve a micrometric record of early Solar System processes. Intense heating from viscous dissipation and irradiation from the pro-

tosun vaporize pre-existing dust. As cooling progresses, condensation of minerals occurs. **Refractory inclusions** (e.g., calcium-aluminum-rich inclusions) are high-temperature mineral assemblages condensed from a gas of solar composition and represent the oldest known rocks in the Solar System [34, 35]. These tiny rocks consist mostly of refractory Ca, Al, Mg, and Ti minerals thermodynamically stable in a gas of solar composition above the condensation temperature of forsterite, at a total pressure of 10^{-4} bar [36, 37]. Refractory inclusions also underwent multistage processes, driven by transient heating events, including partial or complete melting, evaporation, and reactions with nebular gas [38]. Those igneous-like processes happened in restricted regions near the protosun; then, refractory inclusions were transported radially outward to the chondrite-accretion regions [39]. Micrometric dust in the early solar nebula coalesced into larger clumps through electrostatic attraction and adhesion between solid dust grains. These aggregates were subsequently heated, partially or fully melted, and shaped into spherical droplets by surface tension, forming **chondrules**—millimeter-sized igneous rocks. Although there is no complete consensus regarding the process that led to the melting of the precursors of chondrules, several hypotheses have been proposed [40, 41]. These hypotheses could all represent potential melting processes that occurred within our Solar System, or, possibly, in other stellar systems. Shock-wave heating, driven by eccentric planetesimals and protoplanets perturbed by Jovian and secular resonances, is a leading candidate for chondrule formation in the solar nebula [42]. **Compound chondrules** consist of two or more chondrules welded together formed through interactions between crystallized chondrules and melted chondrules [43]. **Fine-grained dust** rims are matrix-like materials surrounding chondrules [44]. These rims may have acted as a "velcro", facilitating the accretion of rimmed chondrules into centimeter-sized aggregates to asteroid formation [45]. Meanwhile, chondrules with dust accretionary rims floating free in space can undergo additional flash heating events that melt the

surrounding dust. The petrographic evidence of this early Solar System process is directly observable in the chondrule textures, known as igneous rims [46]. Refractory inclusions, chondrules, and fine-grained dust follow a complex rock-cycle path, as exemplified in 2.1. Those components undergo a wide spectrum of collisional processes, including sticking, bouncing, mass transfer, cratering, erosion, abrasion, and fragmentation. Such processes have been characterized, modeled, and experimentally constrained, and in many cases quantitatively parameterized in terms of velocity- and energy-dependent thresholds [47, 48], as well as through theoretical and numerical models [48, 49]. Additionally, thermal processes, like melting or flash heating and chemical reaction in the protoplanetary disk environment, further modify these materials. Finally, refractory inclusions, chondrules, presolar grains, and matrix materials accreted and were processed in planetesimals to form chondrites, the oldest known sedimentary rocks in the Solar System [40]. The accretion of chondrite components into chondrites marks the fading of processes dominated by the protoplanetary disk and the onset of asteroidal processes.

Ultimately, we offer an example that highlights how the early formation of planets influenced processes within the protoplanetary disk. Observations of diverse exoplanetary systems and numerical models indicate that planetary formation perturbs the evolution of the protoplanetary disk through **planet–disk interactions** [50–54]. Such interactions can modulate turbulence, as well as radial and vertical mixing, thereby significantly contributing to the redistribution of solid material. In the early Solar System, for instance, it has been proposed that proto-Jupiter created a gravitational barrier that restricted the inward drift of carbonaceous chondrite material, limiting mixing between the two reservoirs [33, 55]. However, this barrier was not entirely impermeable, as Jupiter's orbital migration scattered carbonaceous chondrite material into the inner disk [56, 57], highlighting that early planetary formation, alongside the establishment of the snow line, is an important process in

planetary evolution and must be considered in the rock cycle.

All the above-illustrated processes play a role in the formation of planetary materials. In the protoplanetary disk, rocks are cyclically reprocessed, representing a turbulent, chaotic, and highly energetic "factory" of rock formation in the early Solar System. As the rock cycle describes the environment in which rocks form, including the protoplanetary disk dynamics into the rock cycle is mandatory.

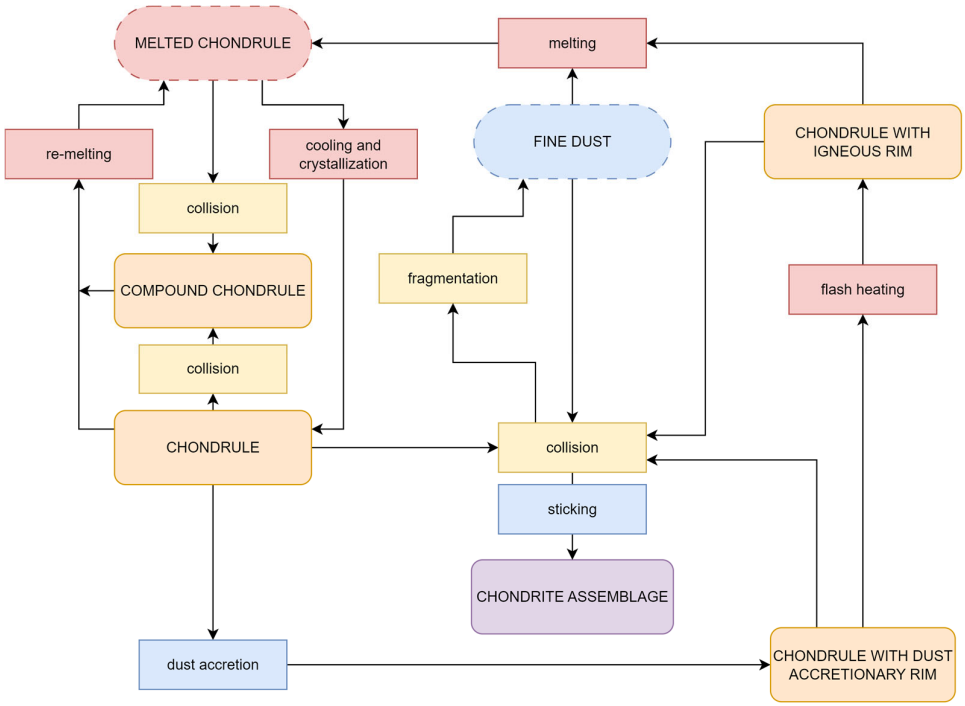

Scheme 2.1: This flowchart illustrates the complex chondrule rock cycle within the protoplanetary disk, showing how chondrules and fine-grained dust evolve through various thermal and collisional processes. Rounded rectangles represent products (e.g., chondrule, fine dust), and sharp-cornered rectangles represent processes (e.g., melting, fragmentation, dust accretion). Red = high-energy processes (melting, flash heating); Yellow = mid-energy processes (fragmentation, collisions); Blue = low-energy processes (sticking, accretion). Purple= the potential final stage of protoplanetary disk dynamics.

2.2.3 Asteroidal Dynamics

As chondritic pebbles accreted into asteroids, their increasing mass enabled the retention of internal heat. The main heat source in early asteroids was short-lived

radioactive isotopes, particularly ^{26}Al. Chondritic material underwent progressive **thermal metamorphism**, causing chemical equilibration of chondrules and matrix, matrix crystallization, and ultimately chondrule destruction with complete recrystallization [58]. This thermal gradient, observed as a continuum in chondritic meteorites, supports the **onion-shell** model structure, where the most metamorphosed chondrites originate from the asteroid's deeper layers, closer to the heat source [59]. **Shock metamorphism**, resulting from hypervelocity collisions on their parent bodies, is a known exotic metamorphic process that can occur on a progressive scale of intensity [60]. Shock impact can also act as a melting process, producing melt veins [61, 62].

Moreover, some asteroids underwent **aqueous alteration** [63, 64], as evidenced by the presence of phyllosilicate minerals in carbonaceous chondrites. The process consists of a chemical reaction between anhydrous silicates and co-accreted water ice, melted by heat from radioactive decay or impacts [65]. Variations in the degree of aqueous alteration among chondrite specimens reflect differences in the relative abundances of initially co-accreted water ice, chondrules, and matrix [66]. In addition to short-lived radioisotopes, models (e.g., [67]) also suggest that water–rock interactions can lead to serpentinization, an exothermic process that can significantly contribute to the heat budget of asteroids.

Collisional grinding among planetesimals was extensive during early Solar System evolution. Those impacts can cause **brecciation** [68]. Some clasts may have been transported over significant distances before their incorporation, as evidenced by carbonaceous xenoliths found within ordinary chondrite hosts [69], indicating mixing between hydrous (e.g., phyllosilicate-rich) and anhydrous rocks that were subsequently incorporated into other forming planetesimals. Moreover, the asteroids Ryugu, Bennu, and Itokawa exhibit a **rubble-pile** structure, testifying to the continuous impact fragmentation and re-accumulation of these rocks. Obviously, the asteroids' rubble-

pile structure is composed of different lithologies and thus consist of polygenetic materials [70] and also of different types occasionally. Thus, fragmentation and re-accretion into second-generation bodies can lead to further aqueous alteration [71] and metamorphism as illustrated in Fig. 2.2. Petrographic evidence from the global meteorite collection indicates that aqueous alteration, metamorphism, brecciation, and re-accretion cyclically characterise asteroidal dynamics. Aqueous alteration followed by thermal metamorphism and also retrograde aqueous alteration has been reported (e.g., [71–73]). In line with previous work, Elephant Moraine 96029 is a representative CM chondrite that exhibits evidence of unusually mild aqueous alteration followed by a later phase of heating in its parent body [74]. The authors identify it as a regolith breccia because it is characterised by distinct lithologies mixed through impacts and re-accreted. Similarly, the exceptional finding of the Winchcombe meteorite shows eight distinct lithological units plus a cataclastic matrix [75]. The authors report significant heterogeneity in aqueous alteration across the specimen, ranging from intensely to moderately altered domains. The authors state that grain size and texture analyses indicate disruption of the original parent asteroid, with subsequent re-accretion forming a poorly lithified body. Sample-return missions on Ryugu (Hayabusa2) and Bennu (OSIRIS-REx) reinforced with petrologic evidence that the asteroids experienced thermal metamorphism, aqueous alteration, brecciation, and gravitational re-accretion, showing a complex geologic evolution (e.g., [76–80]). The growing body of evidence on petrogenetic processes in asteroidal environments—derived from both the meteoritic record and direct sampling through space exploration—demands the development of a robust framework linking rock textures and compositions to their formative asteroidal processes. Establishing such a framework is essential for recognizing that asteroidal evolutionary pathways of meteorites involve complex geological cycles and that decoding the mineralogical and petrographic record of these rocks is key to understanding how these processes

operate within the broader rock cycle of the Solar System.

Asteroidal **differentiation** was widespread among planetesimals in the early Solar System. It occurred through a spectrum of metamorphic to igneous processes driven by the decay of short-lived ^{26}Al, impacts, formation time, accretion duration, chemical heat sources, and accretion models [81]. Asteroidal magmatism, well recorded in meteorite samples, ranges from limited partial melting to extensive magmatic activity, including the generation of basaltic and, in rare cases, more evolved lithologies. A well-documented example is provided by the HED meteorites, which are widely interpreted as products of magmatic differentiation on asteroid 4 Vesta [82]. Similarly, iron meteorites offer insights into the crystallisation of iron melts and point to an additional category of magmatism: ferromagmatism, that extends into planetary-scale evolution. Asteroid 16 Psyche is an excellent candidate for investigating geological processes involving iron melts, including the hypothesized phenomenon of ferrovolcanism recently proposed [83–86]. This emerging hypothesis shows how molten iron beneath an asteroid's crust rises and erupts onto the surface, like how silicate magma behaves on Earth. Ferrovolcanism may explain the anomalously low bulk density of asteroid 16 Psyche despite its metallic surface, by suggesting that iron lava flows cover an underlying rocky mantle. Intrusive ferromagmatism has been proposed as the formation mechanism for pallasites—meteorites comprising olivine crystals within an iron–nickel matrix. A new avenue of research has emerged to better understand ferrovolcanism, focusing on constraining the volatile gas content and temperature of the melts, as well as the stress state governing fracture mechanics in the asteroid's crust. NASA's Psyche spacecraft, scheduled to arrive at asteroid 16 Psyche in 2029, promises to deliver groundbreaking insights into these enigmatic metallic worlds.

Weathering, in the classical rock cycle on Earth, is commonly illustrated as a main agent of erosion that produces sediments. Similarly, in non-Earth environments,

space weathering is a process that alters the exposed surface of airless planetary bodies in open space, driven by cosmic ray exposure, solar wind irradiation, and micrometeoroid bombardment [87]. Space weathering can lead to significant surface modifications in different ways. Such effects include the formation of nanophase metallic iron, amorphization of silicate, and the darkening of asteroid surfaces, which masks the original rock composition and complicates spectral analysis [88, 89].

Figure 2.2: The cosmic rock cycle. This diagram shows the cosmic rock cycle across four interconnected domains: nebular, protoplanetary disk, asteroidal, and planetary. At its center, Earth's processes are driven by the atmosphere, hydrosphere, lithosphere, biosphere, and magnetosphere, which shield against space weathering. However, Earth is an open system, influenced by meteoritic flux. This implies that the rock cycle extends beyond Earth, and the triangle of igneous, sedimentary, and metamorphic rocks can be applied on a cosmic scale, incorporating processes not considered in the conventional rock cycle. The cycle begins with interstellar grains spread by stellar processes. Then, chondritic components form in the protoplanetary disk and accrete into chondritic rocks. These rocks undergo metamorphism, aqueous alteration, impacts, and re-accretion in the asteroid parent body. Asteroids merge to form planetesimals, protoplanets, and eventually planets, which experience volcanism, tectonics, surface weathering, and material transport. Impact events eject material back into space, where it can be recycled onto other bodies. At the end of a star's life, mineral material is scattered into the cosmos, providing the raw ingredients for a new rock cycle.

Petrologic evidence from meteorites, supported by experiments and models, reveals that asteroids have experienced complex and recurrent cycles of fragmentation, accretion, alteration, metamorphism, and melting, highlighting the unique characteristics of the rock cycle in the asteroidal dynamics.

2.2.4 Planets Dominance

In classical conceptualizations of the rock cycle, Earth is often conceptualized as a closed system. However, the mass of our planet, which is commonly perceived as stable, is subject to a continuous small variation. A recent study has estimated that approximately 5.2×10^7 kg of interplanetary particles reach Earth's surface annually [90]. Although this amount represents only a minimal contribution to Earth's mass today, it was significantly more substantial during the earliest formative period of the planet's evolution—when the influx of extraterrestrial material had significant influence [91, 92].

With this perspective, continuing the cosmic rock cycle, this section presents an overview of how rocks can be incorporated in planets, entering a new stage of the rock cycle: the planetary domain. The way planets form resembles a summary of the classical rock cycle, where pre-existing rocks—dust, meteoroids, and asteroids—gradually assemble together, undergoing melting, crystallization, metamorphism, and erosion over and over again until the planet becomes dynamically dominant in its orbital zone. Planet accretion is much studied and debated in the literature regarding the accretionary models of the Earth, for which we have more extensive information [93–96]. But the models can be applied broadly as universal models [97]. The two main proposed accretionary models are the homogeneous accretionary model and the heterogeneous accretionary model, involving different timescales and leading to diverse outcomes [98]. Indeed, the birth of a planet can be seen as partly analogous

to the formation of a rock, which is why planetary accretion belongs in a cosmic rock cycle.

Once the planetary formation phase is over (since no universal threshold separates formation from evolution) a planet can be conceptualized as having obtained a mainly closed rock cycle that occurs through its own endogenic and exogenic processes, or at least that internal planetary processes govern the evolution of a planet's rock cycle more than external influences. While this may hold true for Venus, Earth, and Mars, it does not necessarily apply to other worlds in Solar System and beyond, where both surface and internal processes are currently influenced by dynamics beyond their planetary boundaries—such as tidal forces, cosmic radiation, and other phenomena that will be discussed in this subsection. Thinking about the rock cycle at a cosmic scale allows us to question the idea of complete isolation of Venus, Earth, and Mars from geological processes triggered from beyond their planetary boundaries (e.g., [99–103]) and to explore these processes in the context of their evolution over time (e.g., [104–106]).

In this review, we choose to not discuss those processes on other planetary bodies that are essentially analogous to those on Earth (e.g., volcanic eruption, magma crystallization, contact or regional metamorphism, wind erosion, etc.). Instead, we focus on more exotic processes that have never been considered in the classical cycle. In this way, we highlight how many processes are excluded from the canonical conceptualization of the Earth-centered rock cycle. Although Earth's rock cycle is well-known, it represents just one model among many lithogenetic processes operating throughout the Solar System. On Earth, the rock cycle is driven by both endogenic and exogenic forces, including interactions with the atmosphere, hydrosphere, and biosphere. However, not all planetary bodies in the cosmos share these features; some possess only a subset, while others lack them entirely. The vast majority of known planetary bodies, like Venus and Mercury, have long been considered to follow

a one-way rock cycle, in which primordial magma oceans crystallize to form igneous rocks without significant rock recycling processes [107–109].

The efficiency of rock-processing mechanisms varies from planet to planet, depending on intrinsic factors such as gravity, composition, internal energy sources, and proximity to other celestial bodies. These mechanisms are also subject to change over time. For instance, Earth's rock cycle is highly dynamic due to its still-active plate tectonics, in stark contrast to Mars, where today tectonic activity is limited and the rock cycle correspondingly subdued [108, 110]. During the Noachian and early Hesperian periods, however, the Martian rock cycle was more complex due to the widespread presence of liquid water and a more active hydrological system [111]. Magmatic activity generated igneous rocks which, under the influence of water, could undergo weathering, erosion, transport, and deposition, leading to the formation of sedimentary rocks. Additionally, localized thermal or shock metamorphism could modify both igneous and sedimentary precursors, with the possibility—unlike today—of reinitiating the sedimentary cycle through renewed surface processes. In contrast, the Amazonian period is characterized by colder, drier conditions and limited surface water activity, restricting the rock cycle to mainly unidirectional paths: either magma $\rightarrow$ igneous rocks $\rightarrow$ thermal or shock metamorphism, or direct alteration and cementation into sedimentary rocks without the possibility of recycling through aqueous processes. This results in a fragmented and incomplete rock cycle in the Amazonian terrains. Furthermore, Mars exhibits a partially decoupled geochemical cycle compared to Earth, with limited exchange between surface and subsurface reservoirs and sparse active recycling. Recent work highlights outstanding questions regarding element mobilization, preservation of redox gradients, and the long-term fate of volatiles and organics on Mars [112]. These unresolved issues are central to understanding both the geological evolution and the planet's past habitability. Reconstructing the Martian sedimentary cycle attracted

attention (e.g., [113]), with orbital spectroscopy providing critical regional context for aqueous mineral distributions [114]. Recent in situ rover analyses document past rock cycle processes on Mars. For example, fracture-associated alteration halos in mudstones and sandstones—identified in Gale Crater—underwent multiple aqueous stages, including acidic leaching followed by mineral precipitation (e.g., [115]). Similarly, the Perseverance rover investigated Jezero crater's floor, revealing mafic igneous rocks modified by fluid-mediated reactions (e.g., [116]). Despite orbital and in situ data, reconstructing rock cycling and its temporal evolution remain challenging. A comparative planetary perspective is essential to correctly interpret planetary geological processes.

Contrary to the view that many planetary bodies across the Solar System are considered "geologically dead" [117] when compared to Earth, evidence of tectonic structures and other resurfacing processes reveals ongoing dynamism in their rock cycles. This subsection will explore some of the mechanisms that drive rock cycles in the planetary domain. Planetary surface age dating—by crater chronology, stratigraphy, and investigations of resurfacing processes—has long been an attractive area of research. The extensive literature produced in this field proves that the rock cycle is not exclusive to Earth's plate tectonics, but rather operates across the Solar System through a variety of mechanisms [118, 119]. For example, lobate scarps and wrinkle ridges on Mercury and the Moon are surface expressions of endogenic forces, reflecting global shrinking due to interior cooling [120–123] or tidal despinning. On the airless planetary surface, as mentioned for the asteroid domain, space weathering occurs as an exogenic force. A striking example of its impact is the formation of hollows on Mercury, which illustrates how intense and transformative these processes can be [124].

Tidal heating is a significant energy source in some planetary systems, capable of inducing rock melting and sustained volcanic activity. Jupiter's moon Io serves

as a prime example, where intense tidal forces from Jupiter and neighboring moons generate substantial internal heat, leading to widespread volcanism [125–127]. This tidal heating mechanism is not exclusive to Io; it affects various objects in the Solar System and may represent a widespread phenomenon across the cosmos [128, 129].

Tidal forces and tidal heating can have significant consequences on icy worlds. The observed complex surface morphology of icy moons like Europa and Dione suggests that the surfaces of these worlds may have undergone tectonic cycles similar to Earth's Wilson cycles [130, 131]. This Earth-like tectonic process is referred to as **cryotectonics** and has opened a new chapter in planetary geology. The way the icy crust, the possible underlying liquid ocean, and a possible rocky core interact with one another, and their respective thicknesses and characteristics raise a wide spectrum of geologic possibilities. Surface structures even strongly suggest subduction processes, indicating that the icy crust can be recycled into the interior. Additionally, **cryovolcanism**, observed on or suspected for numerous icy bodies across the Solar System—such as Europa, Enceladus, and Titan—plays a significant role in shaping the surfaces of icy worlds [132]. Cryovolcanism involves the eruption of ammonia-water or other volatile-rich fluids from a deep cryomagma reservoir onto the surface, mimicking terrestrial volcanism. Cryoeruptions contribute to the resurfacing of icy bodies by transporting fresh material from the interior to the surface, facilitating material recycling and crustal renewal. Erupted cryolava subsequently undergoes "weathering" through sublimation or radiation-driven breakdown, exemplifying a possible "icy rock cycle." On Titan, for example, the presence of cryovolcanoes such as Sotra Facula suggests active geological processes involving the eruption of slushy ice or other materials from the interior to the surface [133]. These cryovolcanic activities contribute to the geological evolution of these icy bodies. Similarly, Europa's surface and subsurface are chemically linked through dynamic processes including cryovolcanism, tectonics, and melting. Cryovolcanic activity can transport reduced

compounds (e.g., H_2, CH_4) from the interior to the surface, while oxidized species—generated by sulfur implantation from Io and radiolytic processing of the ice shell—are transported downward via tectonic subduction, melting, and brine migration [134–136].

On small bodies, both volcanic and cryovolcanic plumes can escape due to low gravity and tenuous or absent atmospheres, dispersing material into space [137]. In some cases, this material may even be deposited onto neighboring planets or moons [138, 139] mixing allogenic planetary material with local geology. Such interplanetary material exchanges represent geological processes operating on a truly cosmic scale.

The water cycle on Earth is a primary driver of the rock cycle, but other different types of **hydrospheres and atmospheres** exist in planetary environments across the cosmos. On Titan, Saturn's largest moon, a methane-based hydrosphere actively sculpts the landscape through rainfall, rivers, and lakes involved in complex photochemical–meteorological–hydrogeochemical processes [140]. Recent radar studies have revealed detailed information about the chemical composition and physical characteristics of Titan's hydrocarbon seas, indicating active tidal currents and ripples near estuaries [141]. The presence of rivers, lakes, and dunes formed by methane and ethane suggests a complex hydrological cycle analogous to Earth's, albeit with different substances [142].

Gas giant planets, both within our Solar System and among known exoplanets, present a different kind of challenge. Though lacking solid surfaces, their gravitational dominance influenced the formation of the protoplanetary disk and continues to regulate material flow between the inner and outer Solar System [143]. As previously mentioned, they also influence nearby moons through tidal forces. While traditionally seen as irrelevant to lithogenesis, gas giants exhibit extreme atmospheric conditions that can induce mineral formation, including the precipitation of diamonds [144].

Some exoplanets may undergo even more processes, such as the precipitation of molten metals [145]. As Earth's atmosphere actively shapes surface geology and drives the rock cycle, extreme planetary atmospheres should also be recognized as key agents in lithogenetic processes in the cosmos. Micrometeorites are a record of atmospheric entry melting, showing that ablation constitutes an additional igneous process capable of producing silicate melts on planets with substantial atmospheres [146].

Collisions are among the most widespread transformative processes in the cosmic rock cycle, capable of initiating a broad spectrum of geological effects. These include mechanical erosion, high-energy transport of materials, impact metamorphism, and the generation of melt through impact shock [147, 148]. On solid planetary surfaces, collisions with asteroids or comets can breach the crust and excavate deep lithological layers, ejecting rock fragments into interplanetary space [149]. The blanketing effect of ejecta, which deposits vast amounts of impact-derived material over large areas, contributes substantially to the surface lithological evolution of rocky planets in their early ages by redistributing and mixing crustal compositions. The energy released during impacts can generate localized vaporization or melting, producing impact melt rocks, breccias, and high-pressure polymorphs such as coesite or stishovite. In some cases, impacts may form large basins or initiate long-lasting tectonic or volcanic activity by redistributing stress in the lithosphere [147, 149]. The excavation of massive canyons or rift-like features can also result from the directional force of high-velocity impact streams [150]. On a larger scale, collisions have even shaped planetary systems themselves, as hypothesized for the Moon's formation through a giant impact [151]. Observations of other star systems, such as HD 23514 in the Pleiades cluster, reveal hot dust likely resulting from catastrophic collisions between rocky bodies, suggesting that such processes are common in planetary formation [152].

Therefore, collision-related processes are not only key to shaping individual planets, but also central to material redistribution and transformation on a system-wide

or even interstellar level. These ejected materials may travel as meteoroids, eventually falling onto other planetary bodies, contributing to cross-planetary lithological exchange. This is exemplified by the records of lunar and Martian meteorite samples found on Earth. Conversely, it is also plausible that meteorites originating from Earth may be present on the surfaces of other planetary bodies [153, 154]. Rocks formed on their parent planet may be ejected and travel through space for extended periods before arriving on a new planetary surface (potentially experiencing atmospheric ablation). Once deposited, the meteorite becomes part of the host planet's rock cycle, undergoing subsequent chemical alteration and physical modification. **Interstellar objects** are rocky bodies that have left their original stellar systems and travel through interstellar space [155–157]. In a theoretical scenario, they could potentially collide with planets in other stellar systems, re-entering a new rock cycle. Similarly, rogue planets ejected from their original systems may experience comparable fates.

The planetary dynamics outlined here demonstrate diverse efficiencies of rock processing, including mechanisms absent from Earth's rock cycle—such as interior shrinking, space weathering, tidal volcanism, cryotectonics and cryovolcanism, extensive collisional metamorphism, and intense impact-driven surface reshaping. The Solar System reveals an extraordinary variety of pathways through which rocks are transformed, inviting speculation on the yet-unknown processes that may operate on unexplored worlds across the universe.

2.3 Life and Death

The biosphere plays a fundamental role in the rock cycle, modulating global biogeochemical cycles and mediating atmosphere–hydrosphere interactions. Living organisms contribute to chemical alteration, transport, and sedimentation processes and, in some cases, are directly responsible for rock formation. For example, cyanobacteria

contributions dramatically altered Earth's geochemistry during the Great Oxidation Event (˜2.4 Ga), generating the deposition of banded iron formations (BIFs) and fundamentally reshaping planetary mineral evolution [158], and corals and foraminifera are extensive constituents of sedimentary rocks [159]. Furthermore, Homo sapiens has introduced "artificial rocks"—cements, ceramics, alloys, and polymers [160]. We do not aim to assess Homo sapiens' role in the rock cycle but simply note its ability as a life-form, moving away from an anthropocentric perspective. The DART mission demonstrated that human activity—as a biological process—can actively alter planetary surfaces through impact cratering and orbital deviation [161], and also transport rocks between previously isolated planetary environments [162]. Active research on asteroid mining suggests that microbial processes could facilitate extraterrestrial resource extraction, spreading, in this way, biosphere processes out from earth [163]. If similar biogeological processes occur elsewhere, the role of the biosphere in the rock cycle could be a universal phenomenon, influencing unexplored worlds. Moreover, the biosphere of one world might have the potential to spread to others.

As life dies, it returns into a biogeochemical cycle, including the rock cycle. As stars die, such as in a supernova, dust, rocks, and minerals are scattered across the universe, serving as raw material for new planetary systems [164]. Impact or gravity interaction may produce interstellar asteroids or launch into the cosmos rogue planets, transferring geological matter across stellar boundaries.

2.4 Conclusions

A comprehensive summary of all cosmic processes involving rocks is beyond the scope of this study. We focus on a particularly relevant subset to challenge the Earth-centric view of the rock cycle, emphasizing effects recorded in the petrologic record. Exotic igneous processes can arise from stellar and protoplanetary disk

processes (e.g., chondrules and CAIs) to asteroidal and planetary processes (e.g., iron magmatism or tidal heating, impact and ablation melting). Sedimentary processes like alteration, erosion, transport, and sedimentation are not only linked to hydrosphere and atmosphere interactions but also include space weathering, a type of weathering not previously considered in the classic rock cycle. Metamorphic processes on Earth are attributed mainly to plate tectonics; however, in a cosmic context, shock metamorphism occurs due to hypervelocity impacts, a process that could be more frequent during the early epoch of planet formation.

The progress of geoscience depends on its integration with other sciences such as physics, chemistry, astronomy, and biology. The interdisciplinary approach allows us a multilayer view of the problem: it is a methodology already in use that is being resemantized using current knowledge. The goal is to create wider approaches of understanding reality that include increasingly broader classes of phenomena. Contrary to "hard sciences", geological explanations are never univocal, but composite: multiple causes, agents, and energies simultaneously contribute to generating phenomena. For this reason, the role of geoscientists is to develop a broad, integrative perspective on natural systems and to critically reassess and refine models in light of new knowledge, continuously reshaping it to reflect advancing understanding. Indeed, the rock cycle, from both a scientific and a science popularization and teaching perspective, can be considered as a case of Big Ideas: a tool of thinking that can function as general models to explain complex aspects of reality and, at the same time, can be used for the solution of other problems that gravitate around their theoretical core, offering very original solutions [165].

Extending the rock cycle to a cosmic scale may appear conceptually straightforward, no more extraordinary than adding newly discovered geological aspects. However, it poses a true challenge in planetary science. Only by reconstructing the complex pathways of rocks across time and through diverse environments, deciphering

their continuous physical and chemical transformations, can we begin to address some of the field's most fundamental questions. An illustrative example of the power of this interdisciplinary framework is provided by Lugaro et al. ([16]), who reviewed the meteoritic short-lived radionuclide evidence, combined with their production in stars, applied to a galactic chemical evolution model. Their approach shows how the evolution of radionuclide abundances in the Milky Way Galaxy has important consequences for the thermo-mechanical and chemical evolution from a stellar nursery to thermal and chemical evolution of planetesimals, influencing early differentiation and potential habitability.

More open questions feed an active scientific debate and underscore the imperative for collaborative, interdisciplinary approaches that integrate diverse expertise. Indeed, despite increasing sophistication in analytical techniques, from remote sensing to petrography, mineralogy, elemental and isotopic geochemistry, experimental petrology, and modeling, results are often fragmented or contradictory. These inconsistencies highlight the absence of an integrative framework.

In addition to encouraging critical thinking, the cosmic rock cycle idea aims also to resolve the problem of fragmentation between micro- and macro-scale research. The increasing frequency of sample return missions provides microscopic insights into asteroidal and planetary processes, while remote sensing in the Solar System and observational studies of exo-solar systems contribute to a macroscopic understanding of planetary evolution and exoplanetary system formation. These processes are deeply interconnected, necessitating interdisciplinary collaboration and cross-domain knowledge transfer among scientists in planetary science, meteoritics, and astrophysics. Expanding the rock cycle to a cosmic scale is now essential for establishing a unified theoretical framework that integrates microscale processes with planetary and astrophysical phenomena and bridges isolated fields like geology, astrophysics, and planetary science.

The rock cycle has historically been developed through the study of the Earth, but these crystallized ideas are now limiting its scope, making it obsolete today and representing a missed opportunity for students and early career researchers to think about rocks in a broader context. This review reframes the rock cycle by moving beyond an Earth-centric perspective, situating Earth's geologic processes within a cosmic scale as ones among myriad environments where rocks are continuously shaped and transformed.

Therefore, we propose that this conceptual cosmic framework be formally recognized in the rock cycle. The rock cycle describes the petrogenetic processes that drive the continuous transformation of rocks—anywhere in the universe.

It conceptualizes the dynamic interaction between endogenic and exogenic forces, connects igneous, metamorphic, and sedimentary processes, encompasses microscopic and macroscopic scales, begins with the death of stars, participates in the formation and evolution of planetary systems, and coexists and evolves with possible biospheres.

Going beyond the meaning attributed so far, the significance of the rock cycle is now portrayed as a connecting ring, bridging the "stellar cycle" and the "life cycle"; it unifies fundamental processes across time, space, and disciplines, overcoming fragmented knowledge and affirming its epistemic dignity as a tool for interdisciplinary understanding.

References

[1] B. Gregor (1992). Some ideas on the rock cycle: 1788–1988. *Geochimica et Cosmochimica Acta* vol. **56**, 2993–3000. https://doi.org/10.1016/0016-7037(92)90285-Q.

[2] G. B. Vai (2021). Leonardo Da Vinci's and Nicolaus Steno's Geology. *Earth Sciences History* vol. **40**, 293–331. https://doi.org/10.17704/1944-6187-40.2.293.

[3] A. H. Cutler (2021). Steno and the rock cycle. *Substantia* vol. **5**, 89–97. https://doi.org/10.36253/Substantia-1280.

[4] L. S. Fichter (1996). Tectonic Rock Cycles. *Journal of Geoscience Education* vol. **44**, 134–148. https://doi.org/10.5408/1089-9995-44.2.134.

[5] L. S. Fichter *Tectonic Rock Cycles*. James Madison University Geology Department. Available online: https://csmgeo.csm.jmu.edu/geollab/fichter/wilson/ptrc.html (accessed on 1 August 2025). 1999.

[6] S. J. Whitmeyer, L. S. Fichter, and E. J. Pyle (2007). New directions in Wilson Cycle concepts: Supercontinent and Tectonic Rock Cycles. *Geosphere* vol. **3**, 511–526. https://doi.org/10.1130/GES00091.1.

[7] T. Gehrels and M. S. Matthews, eds. *Protostars and Planets: Studies of Star Formation and of the Origin of the Solar System*. IAU Colloquium 52. Tucson, AZ, USA, 1978.

[8] D. Apai and D. S. Lauretta, eds. *Protoplanetary Dust: Astrophysical and Cosmochemical Perspectives*. Vol. 12. Cambridge, UK: Cambridge University Press, 2010.

[9] L. L. S. D'hEndecourt (2011). Molecular complexity in astrophysical environments: From astrochemistry to "astrobiology"? *EPJ Web of Conferences* vol. **18**, 06001. https://doi.org/10.1051/epjconf/20111806001.

[10] I. Tolstikhin and J. Kramers *The Evolution of Matter: From the Big Bang to the Present Day*. Cambridge, UK: Cambridge University Press, 2008. https://doi.org/10.1017/CBO9780511535604.

[11] P. W. Langley, H. A. Simon, G. Bradshaw, and J. M. Zytkow *Scientific Discovery: Computational Explorations of the Creative Processes*. Cambridge, MA, USA: MIT Press, 1987. https://doi.org/10.7551/mitpress/6090.001.0001.

[12] R. K. Singh, N. P. Nayak, T. Behl, R. Arora, K. Anwer, M. Gulati, S. G. Bungau, and M. C. Brisc (2024). Exploring the Intersection of Geophysics and Diagnostic Imaging in the Health Sciences. *Diagnostics* vol. **14**, 139. https://doi.org/10.3390/diagnostics14020139.

[13] R. L. Eves and L. E. Davis (1988). Is the Rock Cycle an Outdated Idea, or a Unifying Concept? *Journal of Geological Education* vol. **36**, 108–110. https://doi.org/10.5408/0022-1368-36.2.108.

[14] C. Bigg "Diagrams". In: *A Companion to the History of Science*. Hoboken, NJ, USA: Wiley, 2016, 557–571. https://doi.org/10.1002/9781118620762.ch39.

[15] A. Abrahamsen and W. Bechtel (2014). Diagrams as Tools for Scientific Reasoning. *Review of Philosophy and Psychology* vol. **6**, 117–131. https://doi.org/10.1007/s13164-014-0215-2.

[16] M. Lugaro, U. Ott, and Á. Kereszturi (2018). Radioactive nuclei from cosmochronology to habitability. *Progress in Particle and Nuclear Physics* vol. **102**, 1–47. https://doi.org/10.1016/j.ppnp.2018.05.002.

[17] R. M. Hazen, D. Papineau, W. Bleeker, R. T. Downs, J. M. Ferry, T. J. McCoy, D. A. Sverjensky, and H. Yang (2008). Mineral evolution. *American Mineralogist* vol. **93**, 1693–1720. https://doi.org/10.2138/am.2008.2955.

[18] D. Fulvio, S. Góbi, C. Jäger, Á. Kereszturi, and T. Henning (2017). Laboratory Experiments on the Low-temperature Formation of Carbonaceous Grains in the ISM. *The Astrophysical Journal Supplement Series* vol. **233**, 14. https://doi.org/10.3847/1538-4365/aa9224.

[19] A. Burrows (2000). Supernova explosions in the Universe. *Nature* vol. **403**, 727–733. https://doi.org/10.1038/35001501.

[20] M. W. Blanco, M. A. Guerrero, L. F. Miranda, J. F. Gómez, H. U. Käufl, E. Lagadec, and O. Súarez "Unveiling the sculpting process of planetary nebulae with the Very Large Telescope". In: *Highlights of Spanish Astrophysics VII*. Ed. by J. C. Guirado, L. M. Lara, V. Quilis, and J. Gorgas. Madrid, Spain: Spanish Astronomical Society, 2013, 522–527.

[21] S. Amari and K. Lodders (2006). Pre-solar grains from supernovae and novae. *Proceedings of the International Astronomical Union* vol. **2**, 349–352. https://doi.org/10.1017/S1743921307010952.

[22] E. K. Zinner "Presolar grains". In: *Treatise on Geochemistry*. Vol. 1. 2003, 711. https://doi.org/10.1016/B0-08-043751-6/01144-0.

[23] P. R. Heck, J. Greer, L. Kööp, R. Trappitsch, F. Gyngard, H. Busemann, C. Maden, J. N. Ávila, A. M. Davis, and R. Wieler (2020). Lifetimes of interstellar dust from cosmic ray exposure ages of presolar silicon carbide. *Proceedings of the National Academy of Sciences* vol. **117**, 1884–1889. https://doi.org/10.1073/pnas.1904573117.

[24] M. Keppler, M. Benisty, A. Müller, T. Henning, R. van Boekel, F. Cantalloube, C. Ginski, R. van Holstein, A.-L. Maire, A. Pohl, et al. (2018). Discovery of a planetary-mass companion within the gap of the transition disk around PDS 70. *Astronomy & Astrophysics* vol. **617**, A44. https://doi.org/10.1051/0004-6361/201832957.

[25] L. Matrà, S. Marino, D. J. Wilner, G. M. Kennedy, M. Booth, A. V. Krivov, J. P. Williams, A. M. Hughes, C. del Burgo, J. Carpenter, et al. (2025). REsolved ALMA and SMA Observations of Nearby Stars (REASONS). *Astronomy & Astrophysics* vol. **693**, A151. https://doi.org/10.1051/0004-6361/202451397.

[26] D. Heinzeller, H. Nomura, C. Walsh, and T. J. Millar (2011). Chemical Evolution of Protoplanetary Disks—The Effects of Viscous Accretion, Turbulent Mixing, and Disk Winds. *The Astrophysical Journal* vol. **731**, 115. https://doi.org/10.1088/0004-637X/731/2/115.

[27] N. A. Starkey and I. A. Franchi (2013). Insight into the silicate and organic reservoirs of the comet forming region. *Geochimica et Cosmochimica Acta* vol. **105**, 73–91. https://doi.org/10.1016/j.gca.2012.11.040.

[28] K. Zhang (2024). Chemistry in Protoplanetary Disks. *Reviews in Mineralogy and Geochemistry* vol. **90**, 27–53. https://doi.org/10.2138/rmg.2024.90.02.

[29] L. A. Cieza, S. Casassus, J. Tobin, S. P. Bos, J. P. Williams, S. Perez, Z. Zhu, C. Caceres, H. Canovas, M. M. Dunham, et al. (2016). Imaging the water snow-line

during a protostellar outburst. *Nature* vol. **535**, 258–261. https://doi.org/10.1038/nature18612.

[30] R. G. Martin and M. Livio (2012). On the evolution of the snow line in protoplanetary discs. *Monthly Notices of the Royal Astronomical Society: Letters* vol. **425**, L6–L9. https://doi.org/10.1111/j.1745-3933.2012.01290.x.

[31] K. Kondo, S. Okuzumi, and S. Mori (2023). The Roles of Dust Growth in the Temperature Evolution and Snow Line Migration in Magnetically Accreting Protoplanetary Disks. *The Astrophysical Journal* vol. **949**, 119. https://doi.org/10.3847/1538-4357/acc840.

[32] J. A. Nanne, F. Nimmo, J. N. Cuzzi, and T. Kleine (2019). Origin of the non-carbonaceous–carbonaceous meteorite dichotomy. *Earth and Planetary Science Letters* vol. **511**, 44–54. https://doi.org/10.1016/j.epsl.2019.01.027.

[33] T. Kleine, G. Budde, C. Burkhardt, T. S. Kruijer, E. A. Worsham, A. Morbidelli, and F. Nimmo (2020). The Non-carbonaceous–Carbonaceous Meteorite Dichotomy. *Space Science Reviews* vol. **216**, 55. https://doi.org/10.1007/s11214-020-00675-w.

[34] J. N. Connelly, M. Bizzarro, A. N. Krot, Å. Nordlund, D. Wielandt, and M. A. Ivanova (2012). The Absolute Chronology and Thermal Processing of Solids in the Solar Protoplanetary Disk. *Science* vol. **338**, 651–655. https://doi.org/10.1126/science.1226919.

[35] G. J. MacPherson "Calcium-aluminum-rich inclusions in chondritic meteorites". In: *Meteorites and Cosmochemical Processes*. Ed. by A. M. Davis. Vol. 1. Amsterdam, The Netherlands: Elsevier, 2014, 139–179. https://doi.org/10.1016/B978-0-08-095975-7.00104-2.

[36] L. Grossman (1972). Condensation in the primitive solar nebula. *Geochimica et Cosmochimica Acta* vol. **36**, 597–619. https://doi.org/10.1016/0016-7037(72)90078-6.

[37] D. S. Ebel, D. S. Lauretta, and H. Y. McSween (2006). Condensation of rocky material in astrophysical environments. *Meteoritics & Planetary Science* vol. **1**, 253–277. https://doi.org/10.48550/arXiv.2306.15043.

[38] D. Wark and W. V. Boynton (2001). The formation of rims on calcium-aluminum-rich inclusions: Step I—Flash heating. *Meteoritics & Planetary Science* vol. **36**, 1135–1166. https://doi.org/10.1111/j.1945-5100.2001.tb01949.x.

[39] G. J. MacPherson, S. B. Simon, A. M. Davis, L. Grossman, and A. N. Krot "Calcium-aluminum-rich inclusions: Major unanswered questions". In: *Chondrules and the Protoplanetary Disk*. Vol. 341. San Francisco, NC, USA: Astronomical Society of the Pacific, 2005, 225.

[40] E. R. D. Scott (2007). Chondrites and the Protoplanetary Disk. *Annual Review of Earth and Planetary Sciences* vol. **35**, 577–620. https://doi.org/10.1146/annurev.earth.35.031306.140100.

[41] Y. Marrocchi, R. H. Jones, S. S. Russell, D. C. Hezel, J. Barosch, and A. Kuznetsova (2024). Chondrule Properties and Formation Conditions. *Space Science Reviews* vol. **220**, 69. https://doi.org/10.1007/s11214-024-01102-0.

[42] M. Nagasawa, K. K. Tanaka, H. Tanaka, H. Nomura, T. Nakamoto, and H. Miura (2019). Shock-generating Planetesimals Perturbed by a Giant Planet in a Gas

Disk. *The Astrophysical Journal* vol. **871**, 110. https://doi.org/10.3847/1538-4357/aaf795.

[43] S. Arakawa and T. Nakamoto (2019). Compound Chondrule Formation in Optically Thin Shock Waves. *The Astrophysical Journal* vol. **877**, 84. https://doi.org/10.3847/1538-4357/ab1b3e.

[44] A. Carballido, L. Matthews, T. Hyde, and C. Xiang "Early Accretion of Chondrule Dust Rims". In: *42nd COSPAR Scientific Assembly*. Pasadena, CA, USA, 2018.

[45] C. W. Ormel, J. N. Cuzzi, and A. G. G. M. Tielens (2008). Co-Accretion of Chondrules and Dust in the Solar Nebula. *The Astrophysical Journal* vol. **679**, 1588–1610. https://doi.org/10.1086/587836.

[46] Y. Matsumoto and S. Arakawa (2023). Igneous Rim Accretion on Chondrules in Low-velocity Shock Waves. *The Astrophysical Journal* vol. **948**, 73. https://doi.org/10.3847/1538-4357/acc57c.

[47] T. Birnstiel, M. Fang, and A. Johansen (2016). Dust Evolution and the Formation of Planetesimals. *Space Science Reviews* vol. **205**, 41–75. https://doi.org/10.1007/s11214-016-0256-1.

[48] J. Blum, D. Bischoff, and B. Gundlach (2022). Formation of Comets. *Universe* vol. **8**, 381. https://doi.org/10.3390/universe8070381.

[49] J. Brisset, D. Heißelmann, S. Kothe, R. Weidling, and J. Blum (2013). The suborbital particle aggregation and collision experiment (SPACE): Studying the collision behavior of submillimeter-sized dust aggregates on the suborbital rocket flight REXUS 12. *Review of Scientific Instruments* vol. **84**, 094501. https://doi.org/10.1063/1.4819443.

[50] F. Masset (2008). Planet–Disk Interactions. *EAS Publications Series* vol. **29**, 165–244. https://doi.org/10.1051/eas:0829006.

[51] W. Kley and R. Nelson (2012). Planet-Disk Interaction and Orbital Evolution. *Annual Review of Astronomy and Astrophysics* vol. **50**, 211–249. https://doi.org/10.1146/annurev-astro-081811-125523.

[52] C. Baruteau, X. Bai, C. Mordasini, and P. Mollière (2016). Formation, Orbital and Internal Evolutions of Young Planetary Systems. *Space Science Reviews* vol. **205**, 77–124. https://doi.org/10.1007/s11214-016-0258-z.

[53] S. N. Raymond and A. Morbidelli "Planet Formation: Key Mechanisms and Global Models". In: *Demographics of Exoplanetary Systems*. Cham, Switzerland: Springer, 2020.

[54] S. J. Paardekooper, R. Dong, P. Duffell, J. Fung, F. S. Masset, G. Ogilvie, and H. Tanaka (2020). Planet-disk interactions. *arXiv* vol.

[55] T. S. Kruijer, T. Kleine, and L. E. Borg (2019). The great isotopic dichotomy of the early Solar System. *Nature Astronomy* vol. **4**, 32–40. https://doi.org/10.1038/s41550-019-0959-9.

[56] S. N. Raymond and A. Izidoro (2017). Origin of water in the inner Solar System: Planetesimals scattered inward during Jupiter and Saturn's rapid gas accretion. *Icarus* vol. **297**, 134–148. https://doi.org/10.1016/j.icarus.2017.06.030.

[57] S. N. Raymond and A. Morbidelli (2014). The Grand Tack model: A critical review. *Proceedings of the International Astronomical Union* vol. **9**, 194–203. https://doi.org/10.1017/S1743921314008254.

[58] J. McSween H. Y., D. W. G. Sears, and R. T. Dodd "Thermal metamorphism". In: *Meteorites and the Early Solar System*. Ed. by J. F. Kerridge and M. S. Matthews. Tucson, AZ, USA: University of Arizona Press, 1988, 102–113.

[59] R. Dodd (1969). Metamorphism of the ordinary chondrites: A review. *Geochimica et Cosmochimica Acta* vol. **33**, 161–203. https://doi.org/10.1016/0016-7037(69)90138-0.

[60] D. Stöffler and K. Keil (1991). Shock metamorphism of ordinary chondrites. *Geochimica et Cosmochimica Acta* vol. **55**, 3845–3867. https://doi.org/10.1016/0016-7037(91)90078-J.

[61] M. Chen, T. G. Sharp, A. El Goresy, B. Wopenka, and X. Xie (1996). The Majorite-Pyrope + Magnesiowüstite Assemblage: Constraints on the History of Shock Veins in Chondrites. *Science* vol. **271**, 1570–1573. https://doi.org/10.1126/science.271.5255.1570.

[62] A. Bischoff, M. Schleiting, R. Wieler, and M. Patzek (2018). Brecciation among 2280 ordinary chondrites–Constraints on the evolution of their parent bodies. *Geochimica et Cosmochimica Acta* vol. **238**, 516–541. https://doi.org/10.1016/j.gca.2018.07.020.

[63] H. Y. McSween (1979). Alteration in CM carbonaceous chondrites inferred from modal and chemical variations in matrix. *Geochimica et Cosmochimica Acta* vol. **43**, 1761–1770. https://doi.org/10.1016/0016-7037(79)90024-3.

[64] M. R. Lee, C. M. O. Alexander, A. Bischoff, A. J. Brearley, E. Dobrić, W. Fujiya, C. Le Guillou, A. J. King, E. van Kooten, A. N. Krot, et al. (2025). Low-Temperature Aqueous Alteration of Chondrites. *Space Science Reviews* vol. **221**, 11. https://doi.org/10.1007/s11214-024-01132-8.

[65] M. McAdam, J. Sunshine, K. Howard, and T. McCoy (2015). Aqueous alteration on asteroids: Linking the mineralogy and spectroscopy of CM and CI chondrites. *Icarus* vol. **245**, 320–332. https://doi.org/10.1016/j.icarus.2014.09.041.

[66] A. Rubin, J. Trigo-Rodríguez, H. Huber, and J. Wasson (2007). Progressive alteration of CM carbonaceous chondrites. *Geochimica et Cosmochimica Acta* vol. **71**, 2361–2382. https://doi.org/10.1016/j.gca.2007.02.008.

[67] A. Farkas-Takács, C. Kiss, S. Góbi, and Á. Kereszturi (2022). Serpentinization in the Thermal Evolution of Icy Kuiper Belt Objects in the Early Solar System. *The Planetary Science Journal* vol. **3**, 54. https://doi.org/10.3847/PSJ/ac5175.

[68] A. Bischof, M. Schleiting, and M. Patzek (2019). Shock stage distribution of 2280 ordinary chondrites—Can bulk chondrites with a shock stage of S6 exist as individual rocks? *Meteoritics & Planetary Science* vol. **54**, 2189–2202. https://doi.org/10.1111/maps.13208.

[69] V. Semenenko, E. Jessberger, M. Chaussidon, I. Weber, T. Stephan, and C. Wies (2005). Carbonaceous xenoliths in the Krymka LL3.1 chondrite: Mysteries and established facts. *Geochimica et Cosmochimica Acta* vol. **69**, 2165–2182. https://doi.org/10.1016/j.gca.2004.10.027.

[70] F. Jourdan, N. E. Timms, T. Nakamura, W. D. A. Rickard, C. Mayers, S. M. Reddy, D. Saxey, L. Daly, P. A. Bland, E. Eroglu, et al. (2023). Rubble pile asteroids are forever. *Proceedings of the National Academy of Sciences* vol. **120**, e2214353120. https://doi.org/10.1073/pnas.2214353120.

[71] L. Wilson, K. Keil, L. B. Browning, A. N. Krot, and W. Bourcier (1999). Early aqueous alteration, explosive disruption, and reprocessing of asteroids. *Meteoritics & Planetary Science* vol. **34**, 541–557. https://doi.org/10.1111/j.1945-5100.1999.tb01362.x.

[72] E. Quirico, L. Bonal, P. Beck, C. Alexander, H. Yabuta, T. Nakamura, A. Nakato, L. Flandinet, G. Montagnac, P. Schmitt-Kopplin, et al. (2018). Prevalence and nature of heating processes in CM and C2-ungrouped chondrites as revealed by insoluble organic matter. *Geochimica et Cosmochimica Acta* vol. **241**, 17–37. https://doi.org/10.1016/j.gca.2018.08.029.

[73] A. King, P. Schofield, and S. Russell (2021). Thermal alteration of CM carbonaceous chondrites: Mineralogical changes and metamorphic temperatures. *Geochimica et Cosmochimica Acta* vol. **298**, 167–190. https://doi.org/10.1016/j.gca.2021.02.011.

[74] M. Lee, P. Lindgren, A. King, R. Greenwood, I. Franchi, and R. Sparkes (2016). Elephant Moraine 96029, a very mildly aqueously altered and heated CM carbonaceous chondrite: Implications for the drivers of parent body processing. *Geochimica et Cosmochimica Acta* vol. **187**, 237–259. https://doi.org/10.1016/j.gca.2016.05.008.

[75] M. Suttle, L. Daly, R. Jones, L. Jenkins, M. van Ginneken, J. Mitchell, J. Bridges, L. Hicks, D. Johnson, G. Rollinson, et al. (2022). The Winchcombe meteorite—A regolith breccia from a rubble pile CM chondrite asteroid. *Meteoritics & Planetary Science* vol. **59**, 1043–1067. https://doi.org/10.1111/maps.13938.

[76] T. Nakamura, M. Matsumoto, K. Amano, Y. Enokido, M. Zolensky, T. Mikouchi, H. Genda, S. Tanaka, M. Zolotov, K. Kurosawa, et al. (2023). Formation and evolution of carbonaceous asteroid Ryugu: Direct evidence from returned samples. *Science* vol. **379**, eabn8671. https://doi.org/10.1126/science.abn8671.

[77] E. Nakamura, K. Kobayashi, R. Tanaka, T. Kunihiro, H. Kitagawa, C. Potiszil, T. Ota, C. Sakaguchi, M. Yamanaka, D. Ratnayake, et al. (2022). On the origin and evolution of the asteroid Ryugu: A comprehensive geochemical perspective. *Proceedings of the Japan Academy, Series B* vol. **98**, 227–282. https://doi.org/10.2183/pjab.98.015.

[78] E. Tatsumi, C. Sugimoto, L. Riu, S. Sugita, T. Nakamura, T. Hiroi, T. Morota, M. Popescu, T. Michikami, K. Kitazato, et al. (2020). Collisional history of Ryugu's parent body from bright surface boulders. *Nature Astronomy* vol. **5**, 39–45. https://doi.org/10.1038/s41550-020-1179-z.

[79] H. Connolly, D. Lauretta, T. McCoy, S. Russell, P. Haenecour, A. Polit, J. Barnes, T. Zega, H. Yurimoto, N. Kawasaki, et al. (2025). An overview of the petrography and petrology of particles from aggregate sample from asteroid Bennu. *Meteoritics & Planetary Science* vol. **60**, 979–996. https://doi.org/10.1111/maps.14335.

[80] D. Lauretta, H. Connolly, J. Aebersold, C. Alexander, R. Ballouz, J. Barnes, H. Bates, C. Bennett, L. Blanche, E. Blumenfeld, et al. (2024). Asteroid (101955) Bennu in the laboratory: Properties of the sample collected by OSIRIS-REx. *Meteoritics & Planetary Science* vol. **59**, 2453–2486. https://doi.org/10.1111/maps.14227.

[81] W. Neumann, D. Breuer, and T. Spohn (2012). Differentiation and core formation in accreting planetesimals. *Astronomy & Astrophysics* vol. **543**, A141. https://doi.org/10.1051/0004-6361/201219157.

[82] K. Keil "Geological history of asteroid 4 Vesta: The "smallest terrestrial planet"". In: *Asteroids III*. Tucson, AZ, USA: The University of Arizona Press, 2002, 573.

[83] B. Johnson, M. Sori, and A. Evans "Ferrovolcanism, pallasites, and Psyche". In: *Proceedings of the 50th Lunar and Planetary Science Conference*. Woodlands, TX, USA, 2019, 18–22.

[84] B. Johnson, M. Sori, and A. Evans (2019). Ferrovolcanism on metal worlds and the origin of pallasites. *Nature Astronomy* vol. **4**, 41–44. https://doi.org/10.1038/s41550-019-0885-x.

[85] J. Abrahams and F. Nimmo (2019). Ferrovolcanism: Iron Volcanism on Metallic Asteroids. *Geophysical Research Letters* vol. **46**, 5055–5064. https://doi.org/10.1029/2019GL082542.

[86] S. Courville, H. Sanderson, C. Bierson, L. Elkins-Tanton, R. Oran, J. O'Rourke, C. Rusell, B. Weiss, and D. Williams (2025). Ferromagmatic intrusions on asteroid (16) Psyche may be magnetized. *Journal of Geophysical Research: Planets* vol. **130**, e2025JE009031. https://doi.org/10.1029/2025JE009031.

[87] K. Chrbolková, R. Brunetto, J. Ďurech, T. Kohout, K. Mizohata, P. Malý, V. Dědič, C. Lantz, A. Penttilä, F. Trojánek, et al. (2021). Comparison of space weathering spectral changes induced by solar wind and micrometeoroid impacts using ion- and femtosecond-laser-irradiated olivine and pyroxene. *Astronomy & Astrophysics* vol. **654**, A143. https://doi.org/10.1051/0004-6361/202140372.

[88] T. Matsumoto, S. Hasegawa, S. Nakao, M. Sakai, and H. Yurimoto (2018). Population characteristics of submicrometer-sized craters on regolith particles from asteroid Itokawa. *Icarus* vol. **303**, 22–33. https://doi.org/10.1016/j.icarus.2017.12.017.

[89] I. Gyollai, S. Biri, Z. Juhász, C. Király, R. Rácz, D. Rezes, B. Sulik, M. Szabó, Z. Szalai, P. Szávai, et al. (2024). Raman–Infrared Spectral Correlation of an Artificially Space-Weathered Carbonaceous Chondrite Meteorite. *Minerals* vol. **14**, 288. https://doi.org/10.3390/min14030288.

[90] J. Rojas, J. Duprat, C. Engrand, E. Dartois, L. Delauche, M. Godard, M. Gounelle, J. Carrillo-Sánchez, P. Pokorný, and J. Plane (2021). The micrometeorite flux at Dome C (Antarctica), monitoring the accretion of extraterrestrial dust on Earth. *Earth and Planetary Science Letters* vol. **560**, 116794. https://doi.org/10.1016/j.epsl.2021.116794.

[91] S. Pfalzner, M. Davies, M. Gounelle, A. Johansen, C. Münker, P. Lacerda, S. Zwart, L. Testi, M. Trieloff, and D. Veras (2015). The formation of the solar system. *Physica Scripta* vol. **90**, 068001. https://doi.org/10.1088/0031-8949/90/6/068001.

[92] A. Halliday and R. Canup (2022). The accretion of planet Earth. *Nature Reviews Earth & Environment* vol. **4**, 19–35. https://doi.org/10.1038/s43017-022-00370-0.

[93] H. Wanke and T. Gold (1981). Constitution of terrestrial planets. *Philosophical Transactions of the Royal Society of London. Series A, Mathematical and Physical Sciences* vol. **303**, 287–302. https://doi.org/10.1098/rsta.1981.0203.

[94] M. Drake and K. Righter (2002). Determining the composition of the Earth. *Nature* vol. **416**, 39–44. https://doi.org/10.1038/416039a.

[95] J. Badro and M. Walter, eds. *The Early Earth: Accretion and Differentiation*. Washington, DC, USA: American Geophysical Union, 2015. https://doi.org/10.1002/9781118860359.

[96] A. Morbidelli, T. Kleine, and F. Nimmo (2024). Did the terrestrial planets of the solar system form by pebble accretion? *Earth and Planetary Science Letters* vol. **650**, 119120. https://doi.org/10.1016/j.epsl.2024.119120.

[97] J. Venturini, M. Ronco, and O. Guilera (2020). Setting the Stage: Planet Formation and Volatile Delivery. *Space Science Reviews* vol. **216**, 86. https://doi.org/10.1007/s11214-020-00700-y.

[98] H. Palme and H. O'Neill "Cosmochemical estimates of mantle composition". In: *Treatise on Geochemistry*. Vol. 2. 2003, 568.

[99] D. Dzurisin (1978). The tectonic and volcanic history of mercury as inferred from studies of scarps, ridges, troughs, and other lineaments. *Journal of Geophysical Research* vol. **83**, 4883–4906. https://doi.org/10.1029/JB083iB10p04883.

[100] M. Contadakis, D. Arabelos, and S. Spatalas (2012). Evidence for tidal triggering for the earthquakes of the Ionian geological zone, Greece. *Annals of Geophysics* vol. **55**, 73–81. https://doi.org/10.4401/ag-5314.

[101] T. Watters, M. Robinson, G. Collins, M. Banks, K. Daud, N. Williams, and M. Selvans (2015). Global thrust faulting on the Moon and the influence of tidal stresses. *Geology* vol. **43**, 851–854. https://doi.org/10.1130/G37120.1.

[102] Y. Wang, Z. Xiao, Y. Chang, and J. Cui (2020). Lost Volatiles During the Formation of Hollows on Mercury. *Journal of Geophysical Research: Planets* vol. **125**, e2020JE006559. https://doi.org/10.1029/2020JE006559.

[103] J. Green and J. Duarte, eds. *A Journey Through Tides*. Amsterdam, The Netherlands: Elsevier, 2022.

[104] G. Williams (2000). Geological constraints on the Precambrian history of Earth's rotation and the Moon's orbit. *Reviews of Geophysics* vol. **38**, 37–59. https://doi.org/10.1029/1999RG900016.

[105] S. Meyers and A. Malinverno (2018). Proterozoic Milankovitch cycles and the history of the solar system. *Proceedings of the National Academy of Sciences* vol. **115**, 6363–6368. https://doi.org/10.1073/pnas.1717689115.

[106] H. Davies, J. Green, and J. Duarte (2020). Back to the future II: Tidal evolution of four supercontinent scenarios. *Earth System Dynamics* vol. **11**, 291–299. https://doi.org/10.5194/esd-11-291-2020.

[107] G. Schubert, D. Turcotte, and P. Olson *Mantle Convection in the Earth and Planets*. Cambridge, UK: Cambridge University Press, 2001.

[108] D. Breuer and T. Spohn (2003). Early plate tectonics versus single-plate tectonics on Mars: Evidence from magnetic field history and crust evolution. *Journal of Geophysical Research: Planets* vol. **108**, 5072. https://doi.org/10.1029/2002JE001999.

[109] L. Elkins-Tanton (2012). Magma Oceans in the Inner Solar System. *Annual Review of Earth and Planetary Sciences* vol. **40**, 113–139. https://doi.org/10.1146/annurev-earth-042711-105503.

[110] H. McSween (2015). Petrology on Mars. *American Mineralogist* vol. **100**, 2380–2395. https://doi.org/10.2138/am-2015-5257.

[111] M. Carr and J. Head (2010). Geologic history of Mars. *Earth and Planetary Science Letters* vol. **294**, 185–203. https://doi.org/10.1016/j.epsl.2009.06.042.

[112] H. Changela, E. Chatzitheodoridis, A. Antunes, D. Beaty, K. Bouw, J. Bridges, K. Capova, C. Cockell, C. Conley, E. Dadachova, et al. (2021). Mars: New insights and unresolved questions. *International Journal of Astrobiology* vol. **20**, 394–426. https://doi.org/10.1017/S1473550421000276.

[113] S. McLennan, J. Grotzinger, J. Hurowitz, and N. Tosca (2019). The Sedimentary Cycle on Early Mars. *Annual Review of Earth and Planetary Sciences* vol. **47**, 91–118. https://doi.org/10.1146/annurev-earth-053018-060332.

[114] J. Carter, L. Riu, F. Poulet, J.-P. Bibring, Y. Langevin, and B. Gondet (2022). A Mars orbital catalog of aqueous alteration signatures (MOCAAS). *Icarus* vol. **389**, 115164. https://doi.org/10.1016/j.icarus.2022.115164.

[115] A. Yen, D. Ming, D. Vaniman, R. Gellert, D. Blake, R. Morris, S. Morrison, T. Bristow, S. Chipera, K. Edgett, et al. (2017). Multiple stages of aqueous alteration along fractures in mudstone and sandstone strata in Gale Crater, Mars. *Earth and Planetary Science Letters* vol. **471**, 186–198. https://doi.org/10.1016/j.epsl.2017.04.033.

[116] E. Scheller, J. Hollis, E. Cardarelli, A. Steele, L. Beegle, R. Bhartia, P. Conrad, K. Uckert, S. Sharma, B. Ehlmann, et al. (2022). Aqueous alteration processes in Jezero crater, Mars—Implications for organic geochemistry. *Science* vol. **378**, 1105–1110. https://doi.org/10.1126/science.abo5204.

[117] M. Grott (2008). Is Mars Geodynamically Dead? *Science* vol. **320**, 1171–1172. https://doi.org/10.1126/science.1159365.

[118] J. Williams, C. van der Bogert, A. Pathare, G. Michael, M. Kirchoff, and H. Hiesinger (2017). Dating very young planetary surfaces from crater statistics: A review of issues and challenges. *Meteoritics & Planetary Science* vol. **53**, 554–582. https://doi.org/10.1111/maps.12924.

[119] T. Gregg and P. Byrne "Ages of planetary surfaces". In: *Planetary Volcanism Across the Solar System*. Amsterdam, The Netherlands: Elsevier, 2022, 271–286. https://doi.org/10.1016/B978-0-12-813987-5.00007-9.

[120] B. Cordell and R. Strom (1977). Global tectonics of Mercury and the moon. *Physics of the Earth and Planetary Interiors* vol. **15**, 146–155. https://doi.org/10.1016/0031-9201(77)90027-9.

[121] M. Zuber, L. Montési, G. Farmer, S. Hauck, J. Ritzer, R. Phillips, S. Solomon, D. Smith, M. Talpe, J. Head, et al. (2010). Accommodation of lithospheric shortening on Mercury from altimetric profiles of ridges and lobate scarps measured during MESSENGER flybys 1 and 2. *Icarus* vol. **209**, 247–255. https://doi.org/10.1016/j.icarus.2010.02.026.

[122] P. Byrne, C. Klimczak, A. Şengör, S. Solomon, T. Watters, and I. Hauck (2014). Mercury's global contraction much greater than earlier estimates. *Nature Geoscience* vol. **7**, 301–307. https://doi.org/10.1038/ngeo2097.

[123] B. Man, D. Rothery, M. Balme, S. Conway, and J. Wright (2023). Widespread small grabens consistent with recent tectonism on Mercury. *Nature Geoscience* vol. **16**, 856–862. https://doi.org/10.1038/s41561-023-01281-5.

[124] D. Blewett, N. Chabot, B. Denevi, and C. Ernst "The nature of Mercury's hollows, and space weathering close to the Sun". In: *Mercury: The View after MESSENGER*. Vol. 2047. Cambridge University Press, 2018, 6051.

[125] S. Peale, P. Cassen, and R. Reynolds (1979). Melting of Io by Tidal Dissipation. *Science* vol. **203**, 892–894. https://doi.org/10.1126/science.203.4383.892.

[126] A. McEwen, L. Keszthelyi, P. Geissler, D. Simonelli, M. Carr, T. Johnson, K. Klaasen, H. Breneman, T. Jones, J. Kaufman, et al. (1998). Active Volcanism on Io as Seen by Galileo SSI. *Icarus* vol. **135**, 181–219. https://doi.org/10.1006/icar.1998.5972.

[127] M. Kervazo, G. Tobie, G. Choblet, C. Dumoulin, and M. Běhounková (2021). Solid tides in Io's partially molten interior. *Astronomy & Astrophysics* vol. **650**, A72. https://doi.org/10.1051/0004-6361/202039433.

[128] P. Driscoll and R. Barnes (2015). Tidal Heating of Earth-like Exoplanets around M Stars: Thermal, Magnetic, and Orbital Evolutions. *Astrobiology* vol. **15**, 739–760. https://doi.org/10.1089/ast.2015.1325.

[129] J. Becker, D. Seligman, F. Adams, and M. Styczinski (2023). The Influence of Tidal Heating on the Habitability of Planets Orbiting White Dwarfs. *The Astrophysical Journal* vol. **945**, L24. https://doi.org/10.3847/2041-8213/acbe44.

[130] S. Howell and R. Pappalardo (2018). Band Formation and Ocean-Surface Interaction on Europa and Ganymede. *Geophysical Research Letters* vol. **45**, 4701–4709. https://doi.org/10.1029/2018GL077594.

[131] B. Bradák, J. Kimura, D. Asahina, M. El Yazidi, and C. Orgel (2023). Introduction to Dione's Wispy Terrain as a Putative Model Region for "Micro" Wilson Cycles on Icy Satellites. *Remote Sensing* vol. **15**, 5177. https://doi.org/10.3390/rs15215177.

[132] T. Gregg, R. Lopes, and A. Sarah "Cryovolcanism". In: *Planetary Volcanism across the Solar System*. Amsterdam, The Netherlands: Elsevier, 2022. https://doi.org/10.1016/B978-0-12-813987-5.00005-5.

[133] R. Lopes, R. Kirk, K. Mitchell, A. LeGall, J. Barnes, A. Hayes, J. Kargel, L. Wye, J. Radebaugh, E. Stofan, et al. (2013). Cryovolcanism on Titan: New results from Cassini RADAR and VIMS. *Journal of Geophysical Research: Planets* vol. **118**, 416–435. https://doi.org/10.1002/jgre.20062.

[134] K. Hand, C. Chyba, R. Carlson, and J. Cooper (2006). Clathrate Hydrates of Oxidants in the Ice Shell of Europa. *Astrobiology* vol. **6**, 463–482. https://doi.org/10.1089/ast.2006.6.463.

[135] S. Kattenhorn and L. Prockter (2014). Evidence for subduction in the ice shell of Europa. *Nature Geoscience* vol. **7**, 762–767. https://doi.org/10.1038/ngeo2245.

[136] M. Hesse, J. Jordan, S. Vance, and A. Oza (2022). Downward Oxidant Transport Through Europa's Ice Shell by Density-Driven Brine Percolation. *Geophysical Research Letters* vol. **49**, e2021GL095416. https://doi.org/10.1029/2021GL095416.

[137] J. Sauer, F. Neubauer, J. Connerney, P. Zarka, and M. Kivelson "Plasma interaction of Io with its plasma torus". In: *Jupiter. The Planet, Satellites and Magnetosphere*. London, UK: Cambridge University Press, 2004.

[138] N. Hirata, H. Miyamoto, and A. Showman (2014). Particle deposition on the saturnian satellites from ephemeral cryovolcanism on Enceladus. *Geophysical Research Letters* vol. **41**, 4135–4141. https://doi.org/10.1002/2014GL060470.

[139] A. Pommier and A. McEwen (2022). Io: A Unique World in our Solar System. *Elements* vol. **18**, 368–373. https://doi.org/10.2138/gselements.18.6.368.

[140] S. Atreya, E. Adams, H. Niemann, J. Demick-Montelara, T. Owen, M. Fulchignoni, F. Ferri, and E. Wilson (2006). Titan's methane cycle. *Planetary and Space Science* vol. **54**, 1177–1187. https://doi.org/10.1016/j.pss.2006.05.028.

[141] A. G. Hayes (2016). The Lakes and Seas of Titan. *Annual Review of Earth and Planetary Sciences* vol. **44**, 57–83. https://doi.org/10.1146/annurev-earth-060115-012247.

[142] J. I. Lunine and R. D. Lorenz (2009). Rivers, Lakes, Dunes, and Rain: Crustal Processes in Titan's Methane Cycle. *Annual Review of Earth and Planetary Sciences* vol. **37**, 299–320. https://doi.org/10.1146/annurev.earth.031208.100142.

[143] Y.-P. Li, Y.-X. Chen, D. N. C. Lin, and X. Zhang (2021). Accretion of Gas Giants Constrained by the Tidal Barrier. *The Astrophysical Journal* vol. **906**, 52. https://doi.org/10.3847/1538-4357/abc883.

[144] D. Kraus, J. Vorberger, A. Pak, N. J. Hartley, L. B. Fletcher, S. Frydrych, E. Galtier, E. J. Gamboa, D. O. Gericke, S. H. Glenzer, et al. (2017). Formation of diamonds in laser-compressed hydrocarbons at planetary interior conditions. *Nature Astronomy* vol. **1**, 606–611. https://doi.org/10.1038/s41550-017-0219-9.

[145] D. Ehrenreich, C. Lovis, R. Allart, M. R. Z. Osorio, F. Pepe, S. Cristiani, R. Rebolo, N. C. Santos, F. Borsa, O. Demangeon, et al. (2020). Nightside condensation of iron in an ultrahot giant exoplanet. *Nature* vol. **580**, 597–601. https://doi.org/10.1038/s41586-020-2107-1.

[146] T. Sönmez and N. Aysal (2025). Crystal Morphology of Antarctic Micrometeorites Based on Melting–Cooling Processes During Atmospheric Entry. *Crystals* vol. **15**, 179. https://doi.org/10.3390/cryst15020179.

[147] R. A. F. Grieve, G. R. Osinski, and L. L. Tornabene "Planetary impacts". In: *Encyclopedia of the Solar System*. Ed. by T. Spohn, D. Breuer, and T. V. Johnson. 3rd ed. Amsterdam, The Netherlands: Elsevier, 2014, 83–99. https://doi.org/10.1016/B978-0-12-415845-0.00004-9.

[148] A. Boujibar, D. Andrault, N. Bolfan-Casanova, M. A. Bouhifd, and J. Monteux (2015). Cosmochemical fractionation by collisional erosion during the Earth's accretion. *Nature Communications* vol. **6**, 8295. https://doi.org/10.1038/ncomms9295.

[149] A. Y. Glikson and F. Pirajno "Asteroids Impacts". In: *Asteroids Impacts, Crustal Evolution and Related Mineral Systems with Special Reference to Australia*. Vol. 14. Modern Approaches in Solid Earth Sciences. Berlin/Heidelberg, Germany: Springer, 2018. https://doi.org/10.1007/978-3-319-74545-9_1.

[150] D. A. Kring, D. P. Kallenborn, and G. S. Collins (2025). Grand canyons on the Moon. *Nature Communications* vol. **16**, 1146. https://doi.org/10.1038/s41467-024-55675-z.

[151] Y. Zhou, R. Bi, and Y. Liu (2024). Research Advances in the Giant Impact Hypothesis of Moon Formation. *Space Science and Technology* vol. **4**, 0153. https://doi.org/10.34133/space.0153.

[152] J. H. Rhee, I. Song, and B. Zuckerman (2008). Warm Dust in the Terrestrial Planet Zone of a Sun-like Pleiades Star: Collisions between Planetary Embryos? *The Astrophysical Journal* vol. **675**, 777–783. https://doi.org/10.1086/524935.

[153] I. A. Crawford, E. C. Baldwin, E. A. Taylor, J. A. Bailey, and K. Tsembelis (2008). On the Survivability and Detectability of Terrestrial Meteorites on the Moon. *Astrobiology* vol. **8**, 242–252. https://doi.org/10.1089/ast.2007.0215.

[154] J. C. Armstrong, L. E. Wells, and G. Gonzales (2002). Rummaging through Earth's attic for remains of ancient life. *Nature* vol. **160**, 183–196. https://doi.org/10.1006/icar.2002.6957.

[155] K. J. Meech, R. Weryk, M. Micheli, J. T. Kleyna, O. R. Hainaut, R. Jedicke, R. J. Wainscoat, K. C. Chambers, J. V. Keane, A. Petric, et al. (2017). A Brief Visit from a Red and Extremely Elongated Interstellar Asteroid. *Nature* vol. **552**, 378–381. https://doi.org/10.1038/nature25020.

[156] D. Z. Seligman and A. Moro-Martín (2022). Interstellar objects. *Contemporary Physics* vol. **63**, 200–232. https://doi.org/10.1080/00107514.2023.2203976.

[157] M. J. Hopkins, C. Lintott, M. T. Bannister, J. T. Mackereth, and J. C. Forbes (2023). The Galactic Interstellar Object Population: A Framework for Prediction and Inference. *The Astronomical Journal* vol. **166**, 241. https://doi.org/10.3847/1538-3881/ad03e6.

[158] J. Olejarz, Y. Iwasa, A. H. Knoll, and M. A. Nowak (2021). The Great Oxygenation Event as a consequence of ecological dynamics modulated by planetary change. *Nature Communications* vol. **12**, 3985. https://doi.org/10.1038/s41467-021-23286-7.

[159] H. A. Lowenstam (1981). Minerals Formed by Organisms. *Science* vol. **211**, 1126–1131. https://doi.org/10.1126/science.7008198.

[160] P. J. Capelotti *The Human Archaeology of Space: Lunar, Planetary and Interstellar Relics of Exploration.* Jefferson, NC, USA: McFarland Publisher, 2010.

[161] S. P. Naidu, S. R. Chesley, N. Moskovitz, C. Thomas, A. J. Meyer, P. Pravec, P. Scheirich, D. Farnocchia, D. J. Scheeres, M. Brozovic, et al. (2024). Orbital and Physical Characterization of Asteroid Dimorphos Following the DART Impact. *Planetary Science Journal* vol. **5**, 74. https://doi.org/10.3847/PSJ/ad26e7.

[162] M. Anand, S. Russell, Y. Lin, M. Wadhwa, K. K. Marhas, and S. Tachibana (2020). Editorial to the Topical Collection: Role of Sample Return in Addressing Major Questions in Planetary Sciences. *Space Science Reviews* vol. **216**, 101. https://doi.org/10.1007/s11214-020-00724-4.

[163] L. Tonietti, B. Barosa, E. Pioltelli, D. Giovannelli, G. Covone, P. Di Donato, A. Cordone, L. Inno, C. Magliano, S. Fiscale, et al. (2023). Exploring the Development of Astrobiology Scientific Research through Bibliometric Network Analysis: A Focus on Biomining and Bioleaching. *Minerals* vol. **13**, 797. https://doi.org/10.3390/min13060797.

[164] A. F. Ertel and B. D. Fields (2024). Distances to Recent Near-Earth Supernovae from Geological and Lunar ^{60}Fe. *The Astrophysical Journal* vol. **972**, 179. https://doi.org/10.3847/1538-4357/ad5a93.

[165] C. Chalmers, M. Carter, T. Cooper, and R. Nason (2017). Implementing "Big Ideas" to Advance the Teaching and Learning of Science, Technology, Engineering, and Mathematics (STEM). *International Journal of Science and Mathematics Education* vol. **15**, 25–43. https://doi.org/10.1007/s10763-017-9799-1.

Chapter 3

Analysis of natural meteorite samples

3.1 Classification of Northwest Africa 16768

Abstract. We classified a meteorite from North West Africa. A comprehensive investigation—including petrographic analysis, scanning electron microscopy (SEM), and electron probe micro-analysis (EPMA)—suggested characteristics typical of the Vigarano-type chondrites group. We classified this meteorite as a CV3 carbonaceous chondrite. CV3 chondrites are rare finds within the meteorite record; thus, the finding and classification of such a specimen provide a significant contribution to the scientific community. The classification has been approved by the Nomenclature Committee with the official name of NWA 16768 on 26 Jun 2025. A specimen fragment was donated to the Museo Nazionale dell'Antartide in Siena (MNA-SI), ensuring its availability for future scientific study.

3.1.1 Introduction

The meteorite **Northwest Africa 16768** (NWA 16768) has been formally classified as a CV3 carbonaceous chondrite. This classification was approved by the Nomenclature Committee (NomCom) of the Meteoritical Society on 26 June 2025, with formal publication scheduled for the *Meteoritical Bulletin*, no. 114 (in preparation, 2025). CV3 chondrites are relatively rare (less than 1% of all meteorites belong to the CV group), with only 510 approved specimens worldwide, placing NWA 16768 among a select group of 10,373 officially approved meteorites from Northwest Africa, out of a total of 78,159 valid meteorite names.

3.1.2 Specimen details and curation

The specimen was find in 2022 and purchased from dealer Saïd Yousfi in February 2023. The material studied for classification is a 22.3 g endcut exhibiting a glossy black fusion crust (Figure 3.1a) and a cut surface rich in chondrules and refractory inclusions (Figure 3.1b). A 7.7 g chip was removed from the main mass for analytical purposes. A polished thin section was prepared from this sample by Domenico Mannetta at the Laboratorio Macinazione e Sezioni Sottili Petrografiche, Dipartimento di Scienze della Terra, Sapienza Università di Roma. A 5.12 g fragment has been donated and is now curated at the Museo Nazionale dell'Antartide in Siena (MNA-SI), in accordance with the requirements of the Meteoritical Society.

3.1.3 Classification procedure

The classification of NWA 16768 as a CV3 carbonaceous chondrite is supported by petrographic and mineralogical analyses. As emphasized by Weisberg et al. [1], "the vast majority of meteorites are characterized based on their petrology alone", and accordingly, petrographic features were central to this classification. The meteorite

(a) Fusion crust view of NWA 16768 endcut.

(b) Cut surface view of NWA 16768 endcut, showing chondrules and CAIs.

Figure 3.1: Two views of the 22.3 g endcut of the CV3 carbonaceous chondrite Northwest Africa 16768. The cut surface reveals the interior components.

sample was first analyzed through preliminary visual inspection, followed by stereomicroscopic observation of the entire sample to assess its general texture and structure. A petrographic analysis was then conducted using a transmitted light polarized petrographic microscope, focusing on features such as undulose extinction in silicate minerals and the clarity and isotropy of the mesostasis to determine petrologic type, shock stage, and weathering grade. For the assessment of shock stage, I adopted the criteria established by Stöffler et al. [2] and Scott et al. [3]. The evaluation of terrestrial alteration followed the weathering scale proposed by Wlotzka [4].

A preliminary SEM (Scanning Electron Microscope) investigation was carried out at the Department of Life Sciences, San Miniato (Via Aldo Moro, 2), in collaboration with Prof.ssa Giovanna Giorgetti. A more detailed SEM analysis and quantitative mineral analyses were conducted using EPMA (Electron Probe Micro-Analysis) at the University of Hannover in collaboration with Dr. Renat Almeev. Based on the results of this investigation, a detailed classification report—including mineralogical descriptions, petrographic observations, chemical data, and supporting images—was compiled and submitted to the NomCom. Following review, the proposed CV3 classification was formally accepted, leading to the assignment of the official name, NWA 16768 [5].

3.1.4 Petrography

The meteorite is dominated by an abundant slightly porous, dark, fine-grained **matrix** (~ 72 vol%), homogeneous in color with a grain size of approximately 1-4 µm. Well-defined, unequilibrated **chondrules** range in size from 40 μm to 2 mm in diameter, with a mean chondrule diameter of 722 ± 404 μm ($\pm 1\sigma$, $n = 18$ chondrules). A variety of textures are present, including barred olivine (BO), porphyritic olivine-pyroxene (POP), radial pyroxene (RP) and also armoured, and compound chondrules (Figure 3.3). Greyish **CAIs** are observed, up to approximately 0.5 mm in diameter, exhibiting both compact and fluffy textures.

In many chondrules, the mesostasis is no longer entirely clear or glassy; instead, it is partially devitrified. Troilite and Fe-Ni metal are present and show minor oxidation. Matrix shows evidence of Fe-rich alteration fronts (Figure 3.5) and in CAIs are foundend pervasive alteration products, although still recognizable. These observations are interpreted as products of fluid-assisted alteration, recording low-temperature aqueous processes on the parent body.

A notable observed petrofabric feature of this meteorite is the preferential long axis orientation of chondrule (see Figure 3.1b). Petrographic observations, including transmitted light photomicrographs and Back-Scattered Electron (BSE) images, are shown in Figures 3.2 and 3.4.

Mineral chemistry and geochemistry

The mean composition of olivine grains in chondrules and chondrule fragments is $\mathrm{Fa}_{\mathbf{1.7\pm1.4}}$ ($\mathrm{Fa}_{0.2-6.6}$, $n = 12$). The mean composition of low-Ca pyroxene in chondrules and chondrule fragments is $\mathrm{Fs}_{\mathbf{5.4\pm6.0}}$ ($\mathrm{Fs}_{0.6-18.3}$, $n = 5$), $\mathrm{Wo}_{\mathbf{0.8\pm0.3}}$ ($\mathrm{Wo}_{0.6-2.0}$, $n = 5$).Results of electron microprobe analyses of olivines, low-Ca pyroxenes, and metal grains are presented in Table 3.1 and Table 3.2.

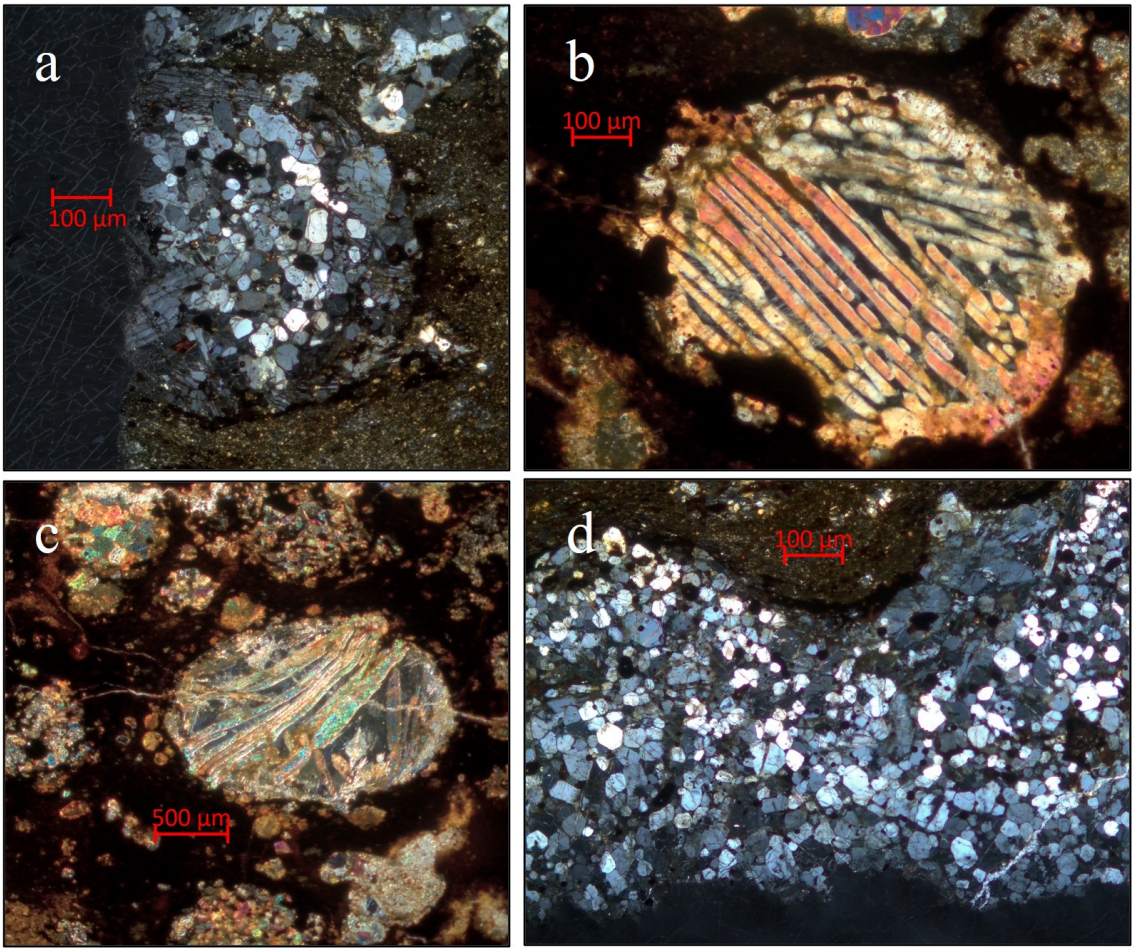

Figure 3.2: Cross-polarized light (XPL) petrography of chondrules in NWA 16768 CV3 carbonaceous chondrite. **(a)** Porphyritic olivine-pyroxene (POP) chondrule exhibiting abundant euhedral to subhedral olivine and pyroxene microcrysts set in a feldspathic mesostasis, poikilitically enclosed crystals are presents probably formed by epitaxial growth during chondrule crystallization. The distinct interference colors reveal crystallographic orientations. **(b)** Barred olivine (BO) chondrule showing characteristic parallel growth of olivine bars with uniform extinction positions, **(c)** BO with skeletal olivine morphology and abundant interstitial glassy mesostasis. **(d)** Composite chondrule texture showing porphyritic texture, suggesting complex formation history. The fine-grained carbonaceous matrix exhibits typical dark under cross-polarized conditions.

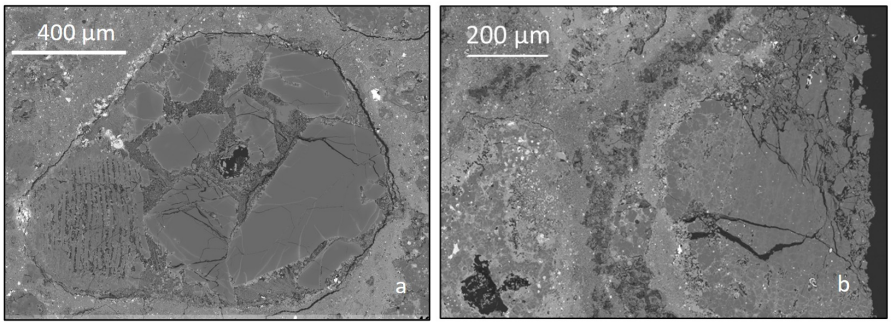

Figure 3.3: Back-scattered electron (BSE) images showing detailed petrographic features in NWA 16768. **(a)** Compound chondrule show fusion of two chondrule during formation. **(b)** Well-developed dust accretionary rim surrounding a chondrule, indicating gentle accretion of fine-grained material onto the chondrule surface in the solar nebula.

Table 3.1: Electron microprobe analyses (wt.%) and forsterite (Fo) contents (mol.%) of olivine from NWA 16768.

	Olivine analysis											
Oxide composition (wt.%)												
	1	2	3	4	5	6	7	8	9	10	11	12
SiO_2	42.45	42.44	41.40	42.17	58.22	42.21	42.29	41.65	41.82	41.78	42.14	42.40
TiO_2	0.08	0.05	0.08	0.08	0.14	0.18	0.12	0.07	0.04	0.02	0.11	0.05
Al_2O_3	0.17	0.15	0.52	0.08	0.65	0.13	0.08	0.07	0.01	0.09	0.24	0.11
Cr_2O_3	0.18	0.17	0.19	0.29	0.71	0.11	0.08	0.26	0.32	0.15	0.27	0.16
FeO	0.37	0.58	2.37	1.14	0.98	1.78	1.02	3.15	4.44	3.37	0.35	0.35
MnO	0.01	0.04	0.00	0.10	0.08	0.07	0.05	0.15	0.20	0.04	0.00	0.06
MgO	56.23	56.11	54.89	55.78	37.65	55.25	56.10	54.31	52.89	54.08	56.41	56.46
CaO	0.49	0.45	0.55	0.35	1.54	0.27	0.26	0.34	0.25	0.46	0.48	0.39
Total	99.98	99.99	100.00	99.99	99.97	100.00	100.00	100.00	99.97	99.99	100.00	99.98
End-member composition (mol.%)												
Fo	99.63	99.42	97.63	98.87	98.56	98.22	98.99	96.85	95.51	96.62	99.66	99.65
Fa	0.37	0.58	2.37	1.13	1.44	1.78	1.01	3.15	4.49	3.38	0.34	0.35

Fo = forsterite (Mg_2SiO_4); Fa = fayalite (Fe_2SiO_4). Analysis n.5 is a pyroxene and is excluded from compositional statistics. Mean composition: $Fa_{1.7\pm1.4}$ ($Fa_{0.2-6.6}$, $n = 12$).

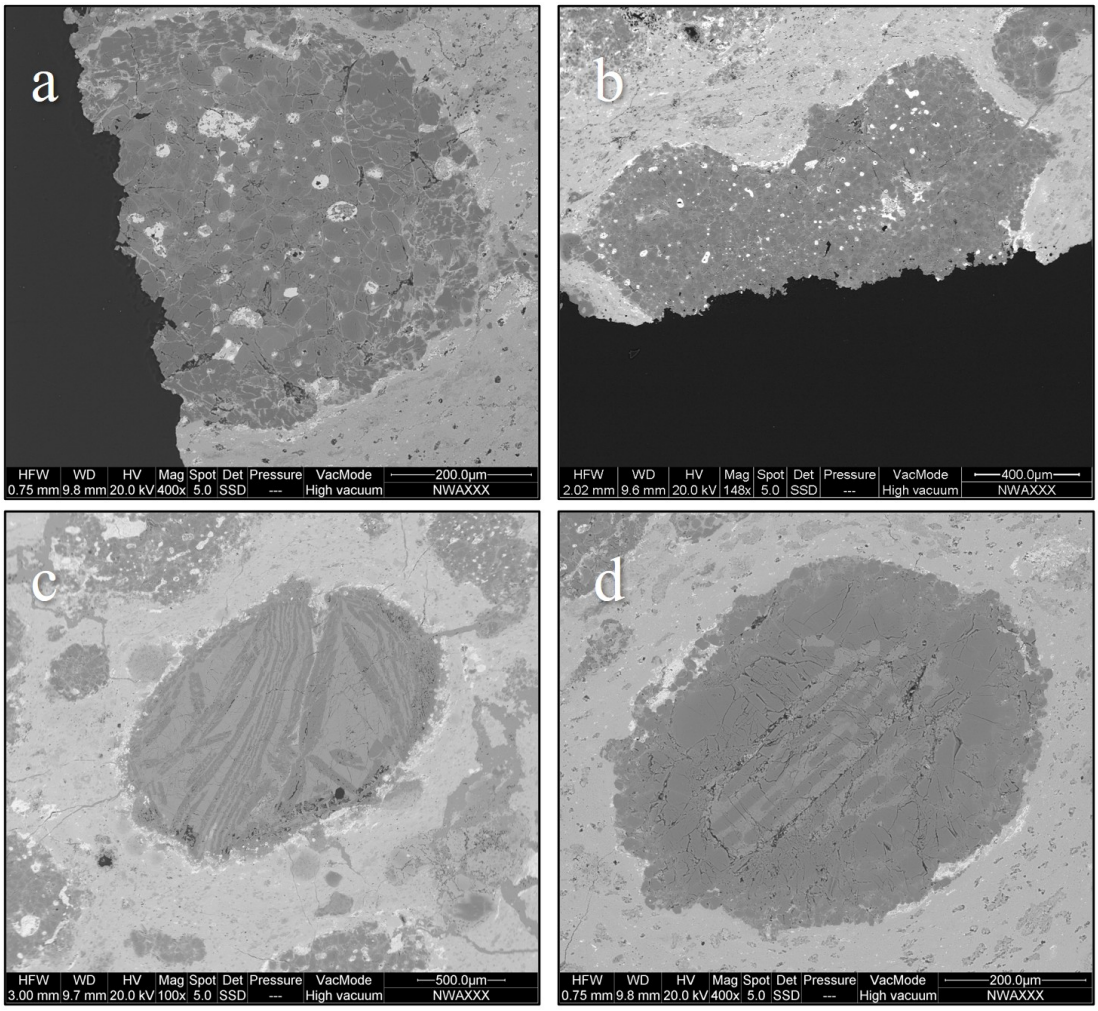

Figure 3.4: Back-scattered electron (BSE) images of chondrules in NWA 16768 CV3 carbonaceous chondrite showing atomic number contrast, where brighter phases indicate higher average atomic number. The bright spots within chondrules are Fe-Ni metal and troilite (FeS), frequently concentrated at chondrule edges. These metal blebs represent immiscible sulfide-metal liquid separation during cooling. The matrix appears light gray due to its Fe-rich composition compared to the Mg-rich chondrules. **(a)** Porphyritic olivine-pyroxene (POP) chondrule exhibiting a distinct enstatite-rich igneous rim (dark gray), formed by flash heating events and melt-gas exchange. **(b)** Two fused chondrules, likely resulting from a low-velocity impact under supersolidus conditions. A terminal iron-rich rim is emblematic of formation under subsolidus conditions following gentle collision of the two chondrules and subsequent crystallization.**(c) (d)** Two barred olivine chondrules exhibiting clear orientation of olivine bars (dark gray) and mesostasis (light gray).

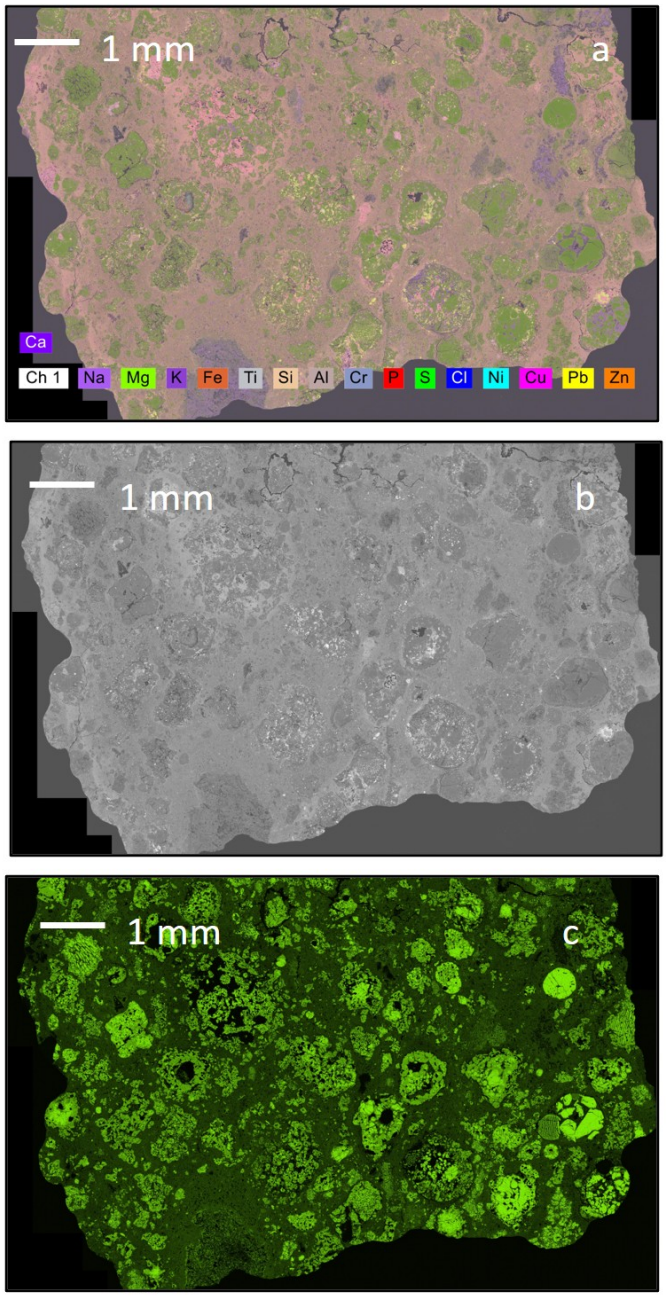

Figure 3.5: Elemental distribution maps of NWA 16768 obtained by EPMA. The large overview shows the heterogeneous distribution of major elements including Ca, Mg, Fe, and Si, highlighting chondrules, CAIs, and matrix components. Mesostasis alteration and CAI modification are evident from the elemental redistribution patterns, consistent with moderate aqueous alteration on the parent body.

Table 3.2: Electron microprobe analyses (wt.%) and end-member compositions (mol.%) of pyroxene from NWA 16768.

	Pyroxene analysis				
Oxide composition (wt.%)					
	1	2	3	4	5
SiO_2	54.90	57.72	57.67	55.65	54.91
TiO_2	0.71	0.29	0.38	0.12	0.16
Al_2O_3	2.65	2.38	1.75	1.84	2.80
Cr_2O_3	0.78	0.60	0.66	1.25	1.53
FeO	0.52	0.47	0.76	7.68	7.65
MnO	0.16	0.06	0.08	0.20	0.19
MgO	23.89	36.62	37.18	31.93	31.19
CaO	16.37	1.85	1.52	1.33	1.55
Na_2O	0.00	0.00	0.00	0.01	0.01
K_2O	0.01	0.01	0.00	0.00	0.00
Total	100.00	100.00	100.00	100.00	100.00
End-member composition (mol.%)					
Wo	32.65	3.48	2.82	2.56	3.03
En	66.29	95.74	95.96	85.57	84.94
Fs	1.06	0.77	1.22	11.85	12.00

Note: Wo = wollastonite ($CaSiO_3$); En = enstatite ($MgSiO_3$); Fs = ferrosilite ($FeSiO_3$). Mean composition of low-Ca pyroxenes: $Fs_{5.4\pm6.0}$ ($Fs_{0.6-18.3}$, $n = 5$), $Wo_{0.8\pm0.3}$ ($Wo_{0.6-2.0}$, $n = 5$).

3.1.5 Conclusion

Collectively, these petrographic and mineral chemical features confirm the meteorite's classification as a carbonaceous chondrite (CV3), S2, W low. The classification has been formally approved by the Meteoritical Society Nomenclature Committee under the name NWA 16768 on 26 June 2025, as published in the online Meteoritical Bulletin database `https://www.lpi.usra.edu/meteor/metbull.cfm?code=85214` and to be published in *Meteoritical Bulletin*, no. 114 (in preparation, 2025).

References for 3.1

[1] M. K. Weisberg, T. J. McCoy, and A. N. Krot "Systematics and Evaluation of Meteorite Classification". In: *Meteorites and the Early Solar System II*. Ed. by D. S. Lauretta and H. Y. McSween. 2006, 19.

[2] D. Stöffler, K. Keil, and S. Edward R.D (1991). Shock metamorphism of ordinary chondrites. *Geochimica et Cosmochimica Acta* vol. **55**, 3845–3867. `https://doi.org/https://doi.org/10.1016/0016-7037(91)90078-J`.

[3] E. R. D. Scott, K. Keil, and D. St"offler (1992). Shock metamorphism of carbonaceous chondrites. *Geochimica et Cosmochimica Acta* vol. **56**, 4281–4293. `https://doi.org/10.1016/0016-7037(92)90268-O`.

[4] F. Wlotzka "A weathering scale for the ordinary chondrites". In: *29th Lunar and Planetary Science Conference*. Houston: Lunar and Planetary Institute, 1993, 145–146.

[5] The Meteoritical Society *Northwest Africa 16768 Entry (Code 85214)*. `https://www.lpi.usra.edu/meteor/metbull.cfm?code=85214`. The Meteoritical Bulletin Database. Lunar and Planetary Institute (LPI). Accessed: 30 September 2025. n.d.

3.2 CAIs high-temperature rims as traces of nebular processes: evidence from the NWA 12800 meteorite.

Submitted to ***Meteoritics & Planetary Science***, on January 10, 2025

Authors: A. Vitrano, R. Almeev, A. Pisello, C. Viti, F. Holtz, F. Vetere.

Abstract. Calcium-aluminum-rich inclusions (CAIs) recorded the most primordial processes inside the protoplanetary disk, but aqueous alteration often poses challenges in their study. We describe the mineralogy and petrography of two very pristine CAIs from the NWA 12800 CV3 carbonaceous chondrite using a scanning electron microprobe. Both CAIs have a diopside ± spinel core with high-temperature rims composed of melilite ± anorthite replacing, spinel + perovskite, ± olivine, and diopside. Although CAIs displays rims consistent with the classic Wark-Lovering rims (WL rims), the other exhibits a sequence of those rims that deviates from the *sensu strictu* WL definition but still reflects condensation, melting, evaporation, and re-crystallization processes analogous to those involved in WL rim formation. As the diversity of these rims in CAIs is essential to understanding the protoplanetary disk processes, the description of CAIs with differing rim characteristics is needed.

Key words: Ca,Al-rich inclusions, Wark-Lovering rims, High-temperature rims, CV chondrites.

3.2.1 Introduction

Understanding protoplanetary disks processes has become critical area of focus in planetary science over the past few decades, offering key insights into the mechanisms underlying the formation of other solar systems (e.g., [1]). However, the question

remains: how can we reconstruct the early evolutionary history of our own solar system with greater precision? What methodologies or technological advancements could enhance the spatial and temporal resolution required to probe the processes of the solar system's formative epochs? Petrological type 3 chondrites provide a valuable window into this primordial era. Among their components, calcium-aluminum-rich inclusions (CAIs) stand out as the earliest solids formed in the solar nebula, dating to approximately 4.567 billion years ago. These inclusions are critical markers, preserving essential information about the initial stages of the protoplanetary disk and offering a baseline for understanding the conditions and dynamics during the solar system's nascent phase [2].

CAIs exhibit morphological diversity that reflects their formation history. "Fluffy" CAIs, with irregular, nodular structures, likely formed through gas-solid condensation in the early solar nebula. In contrast, "Compact" CAIs are spherical, indicating they underwent complete melting in a microgravity environment, followed by cooling and solidification [3, 4]. However, the formation and evolution of CAIs extend beyond this simplified dichotomy. [5] were the first to identify and analyze concentric, monomineralic rims encircling CAIs. These rims provide a detailed record of subsequent thermal and chemical reprocessing events prior to the inclusions' incorporation into their parent bodies. These processes include episodic heating, evaporation, interactions with nebular gas, melting, and recrystallization [6]. Variations in the intensity and conditions of these events result in diverse mineral parageneses, reflecting the thermodynamic environments encountered during their history and underscoring the complexity of CAI genesis.

Later, Wark and Boynton refined the characterization of these structures, defining the "classic" Wark-Lovering (WL) rims as a sequence of spinel, melilite, and diopside layers, consistently arranged from the CAI core outward [7]. This precise stratigraphy offers further insight into the physicochemical processes within the protoplanetary

disk during CAI evolution. Variations in mineralogical sequences within CAIs reflect a diversity of nebular conditions, many of which remain poorly constrained [8].

Investigating CAIs and their associated rims poses significant challenges due to their fine-grained textures and susceptibility to alteration processes. Consequently, it is imperative to focus on chondrites that have escaped substantial metamorphic events, as such alterations can obscure the original records of CAI formation and evolution.

Specific meteorite groups demonstrate varying degrees of alteration:

1. CM and CI chondrites exhibit extensive histories of aqueous alteration [9–11]

2. CB and CH chondrites were affected by impact-generated plumes, complicating the interpretation of their primary components [12, 13]

3. Non-carbonaceous chondrites often experienced extensive secondary mineralization, including pervasive fluid-assisted thermal metamorphism on their asteroidal parent bodies [14]

In contrast, CV chondrites stand out for their relative abundance and large size of CAIs, making them the most extensively studied group. However, even CV chondrites are not immune to metasomatic alteration, as evidenced by multiple studies [15–17]. Nevertheless, some CV chondrites have largely escaped these processes, preserving mineralogically pristine CAIs that are of exceptional scientific value.

This study focuses on two pristine CAIs from the NWA 12800 CV3 meteorite, which feature distinctive reheating rims. These well-preserved inclusions provide a unique opportunity to investigate high-temperature events and processes that occurred in the early solar nebula. Through detailed mineralogical, textural, and chemical analyses, these CAIs offer critical insights into the thermal and chemical dynamics of the protoplanetary disk.

3.2.2 Starting material and analytical methods

NWA 12800 belongs to the CV3s group, with low shock stage (S = 2) and low weathering grade (W = 1). The original mass was 250 g. By using a high precision diamond saw, 5.73g slice was cut and mounted on a thin section for further analytical studies. The thin section preparation procedure followed as closely as possible the procedures recommended by NASA [18].

Electron probe microanalysis was performed using a JEOL JXA-iHP200F Hyper Probe equipped with a field emission gun. A focused beam of a few units of µm was set for all mineral phase analyses with 15 kV and 15 nA. Standardization was done at the beginning of each measuring day on well-known minerals and certified standards, with an acceptable deviation of less than 1%. Results are reported in Table 3.3 and Table 3.4 and in supplementary materials (Table S1 and S2). Two CAIs were identified and analyzed. Image analysis was performed by the software Mountains Lab Premium 10 (Digital Surf, Besancon, France) to quantify the solid phases (details are provided in the Results section). Even if very much care was used during the samples preparation processes, unfortunately, both CAIs exhibit holes, likely attributed to the loss of materials.

3.2.3 Results

CAI_1 Description

CAI_1 (Fig. 3.6) is an irregular, nodular object approximately 400 × 170 μm in size, primarily composed of diopside, spinel, melilite, and olivine. The chemical composition of the minerals is summarized in Table 3.3. The core is composed largely of anhedral pure diopside $CaMgSi_2O_6$ hosting numerous poikilitic anhedral spinel grains (please refer to Tab. S1 for details). Diopside shows chemical zoning (Tab. S1) with core showing Al_2O_3 increasing from 1.65 to 4.81 wt%. TiO_2 follows the Al

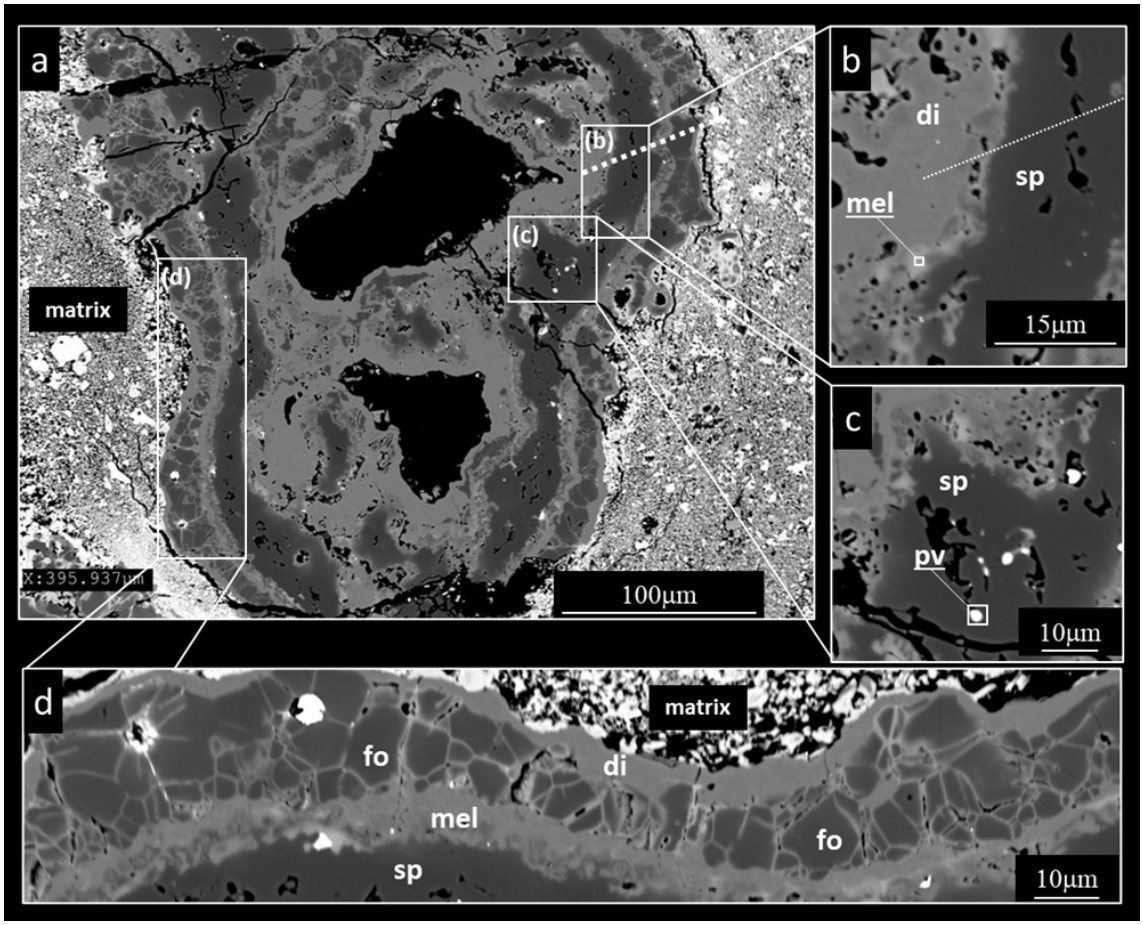

Figure 3.6: Backscattered electron (BSE) images of CAI_1 from NWA 12800. (a) Overview showing the irregular, nodular shape and complete rim sequence. (b) Detail of the spinel rim with perovskite inclusions. (c) Interstitial melilite between diopside core and spinel rim. (d) Outer rim sequence showing forsterite with 120° triple junctions and diopside rim. Mineral abbreviations: Di - diopside, Sp - spinel, Mel - melilite, Fo - forsterite, Pv - perovskite.

trend although with a slight increase from 0.22 to 0.58 wt% while Cr_2O_3 (0.04 wt%) and MnO (0.02 wt%) are negligible (Table 3.3). Interstitial anhedral melilite ($Åk_{>60}$; Table 3.3 and S1) are found between the diopside and spinel (Fig. 3.6c). Melilite show slight evidence for anorthite replacement.

Table 3.3: Electron microprobe analyses (wt.%) of mineral phases in CAI_1 from NWA 12800.

	Diopside core		1° Melilite rim		Spinel rim		2° Melilite rim		Olivine rim		Diopside rim
	Inner	Outer	Inner	Outer	Inner	Outer	Inner	Outer	Inner	Outer	
SiO_2	54.02	52.22	34.46	16.32	0.17	0.35	24.88	24.90	42.01	42.32	50.69
TiO_2	0.27	0.61	1.38	1.58	0.15	0.14	1.27	0.74	0.01	0.01	0.21
Al_2O_3	1.99	4.75	27.56	49.36	70.68	70.60	39.12	37.78	0.07	0.08	1.43
FeO	0.33	0.27	1.78	3.78	1.58	0.88	0.54	0.54	0.50	0.74	1.23
MnO	0.00	0.01	0.02	0.03	0.01	0.02	0.02	0.02	0.01	0.02	0.00
MgO	18.46	17.43	15.99	18.82	27.14	27.54	20.04	24.62	56.93	56.22	26.69
CaO	24.86	24.66	18.63	9.80	0.11	0.27	13.66	10.62	0.36	0.59	19.66
Na_2O	0.02	0.01	0.01	0.04	0.00	0.00	0.01	0.00	0.01	0.00	0.01
K_2O	0.00	0.01	0.00	0.01	0.00	0.00	0.00	0.00	0.00	0.00	0.00
Cr_2O_3	0.05	0.03	0.17	0.26	0.15	0.22	0.46	0.77	0.10	0.02	0.08
Total	100.00	100.00	100.00	100.00	100.00	100.00	100.00	100.00	100.00	100.00	100.00

Minerals compositions (oxides wt.%) for CAI_1. Here we show the average values of the representative compositions of the various minerals present in CAI_1. Complete set of data are reported in Tab. S1.

Surrounding the CAI's core is a continuous, monomineralic rim of anhedral spinel $MgAl_2O_4$, approximately 15 µm thick (Fig. 3.6a). The spinel chemical composition is homogeneous showing very low Cr_2O_3 (<0.1 wt%) content as well as low TiO_2 (0.11–0.16 wt%) and FeO (0.76–2.0 wt%). The Fe/(Fe + Mg) ratio decreases outward from 0.6 to 0.2. Rare micrometric inclusions of nearly pure perovskite $CaTiO_3$ are occasionally observed within the spinel (Fig. 3.6c). Although their size is too small (<2 µm) for quantitative electron microprobe analysis, they were identified via

energy-dispersive spectroscopy (EDS).

Covering the spinel rim is a layer of melilite ($Åk_{>50}$; Fig. 3.6d and Table 3.3 and S1). Then, nearly pure forsteritic olivine (FeO <1 wt.%; Table 3.3) rim exhibits well-developed 120° triple junctions (Fig. 3.6d). The olivine FeO increase outward (0.42 to 0.93 wt%) while the MgO content is slightly higher on the core of the crystals (please refer to Table S1 data olivine rim spots 48 and 49). CaO is <0.41 wt%, MnO negligible (<0.06 wt%) and Cr_2O_3 vary from 0.18 to 0.24 wt%.

As it is possible to see from the BSE image presented in Figure 3.6d, soon after the forsterite rim a thin layer of a continuous (<10 µm) diopside rim is present. It shows compositions with CaO ranging from 15.39 to 24.28 wt%, Al_2O_3 from 0.97 to 1.92 wt%, TiO_2 from 0.15 to 0.27 wt% and, finally the FeO from 0.89 <1.59 wt%.

CAI_2 Description

CAI_2 is nodular, irregular shape (Fig. 3.7) with size ∼500 × 230 µm composed by diopside, spinel and melilite. Olivine is absent. The core is predominantly composed of anhedral pure diopside $CaMgSi_2O_6$ (Table 3.4). It shows a chemical variation from inward to outward with Al_2O_3 ranging from 1.07 to 3.61 wt% that positively correlate with the FeO (0.01–0.14 wt%) and CaO (25.84–26.04 wt.%) and TiO_2 (0.15–0.55 wt%). Cr_2O_3 (<0.05 wt%) and MnO (<0.03 wt%) are negligible (Table 3.4 and S2).

Anhedral melilite is localized between the Ca-px and spinel. Composition are åkermanitic (Ak_{31}) near Ca-px and more gehlenitic (Ak_9 to Ak_2) close to spinel. Anhedral anorthite, $CaAl_2Si_2O_8$ (Table 3.4 and S2), occurs between pyroxene core and melilite rim (Fig. 3.7b).

Approximately 30 µm anhedral spinel $MgAl_2O_4$ (Table 3.4), hosting rare inclusions of micrometric perovskite (Fig. 3.7b). Increase from inward to outward, the spinel composition shows slight variation: Cr_2O_3 (0.1–0.3 wt%), TiO_2 (0.29–0.42 wt%) and

FeO (0.67–1.24 wt%). The Fe/(Fe + Mg) ratio does not show appreciable variation.

Covered spinel rim is a layer consists of intergrowths of melilite with anorthite replacing pointing to a slight to moderate alteration. This cope with the enrichment in FeO (1.62 wt%), and the MnO absence. Following the melilite, a rim of homogeneous diopside is present (Table 3.4).

The outer diopside rim of both studied CAIs has an irregular thickness and covers more the concave side then the convex side of bowl-shaped CAIs (as you can see on Fig. 3.6a and Fig. 3.7b).

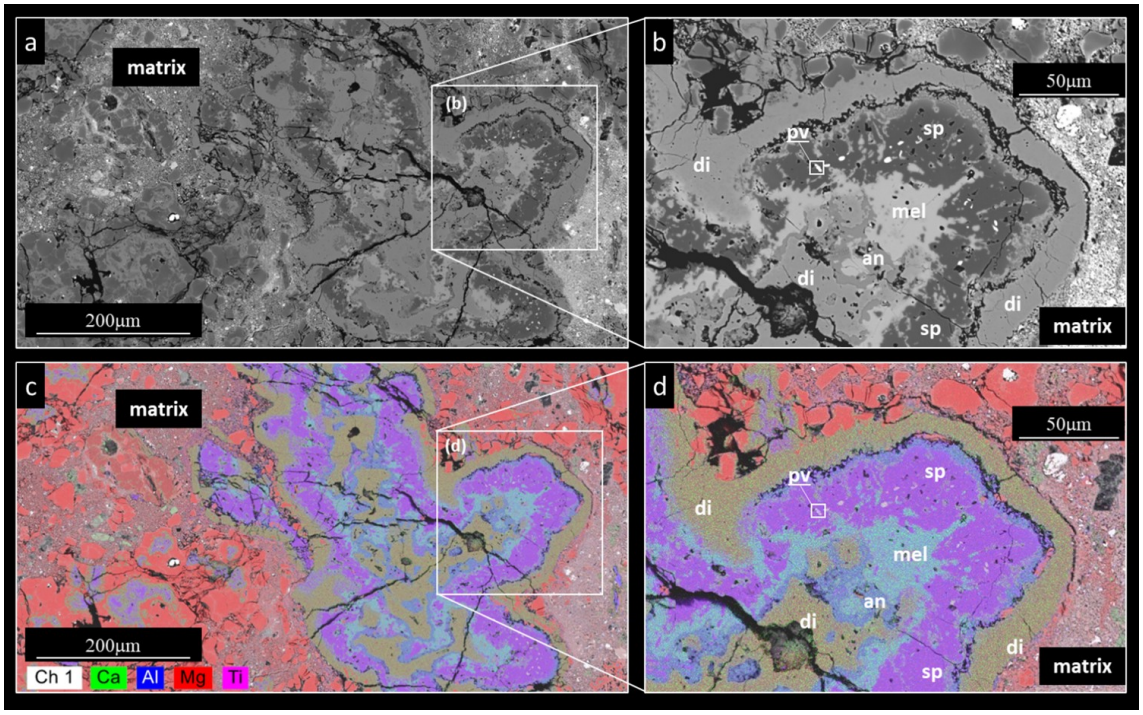

Figure 3.7: Backscattered electron (BSE) images of CAI_2 from NWA 12800. (a) Overview showing the irregular shape and rim sequence, note the absence of olivine. (b) Detailed view showing melilite localization between diopside core and spinel rim, with anorthite occurrence. (c) Spinel rim with perovskite inclusions and melilite-anorthite intergrowths. Mineral abbreviations: Di - diopside, Sp - spinel, Mel - melilite, An - anorthite, Pv - perovskite.

Table 3.4: Electron microprobe analyses (wt.%) of mineral phases in CAI_2 from NWA 12800.

	Diopside core		Melilite rim		Spinel rim		Melilite rim	Diopside rim	
	Inner	Outer	Inner	Outer	Inner	Outer	Anorthite	Inner	Outer
SiO_2	54.27	52.30	25.61	27.30	0.10	0.12	38.29	53.86	52.97
TiO_2	0.15	0.55	0.01	0.06	0.29	0.42	0.08	0.28	0.67
Al_2O_3	1.07	3.61	34.00	26.81	70.98	70.64	39.74	1.41	2.52
FeO	0.01	0.14	0.18	0.14	0.66	1.22	1.63	0.52	0.77
MnO	0.02	0.03	0.00	0.02	0.01	0.00	0.00	0.02	0.00
MgO	18.56	17.25	1.41	4.01	27.72	27.19	1.93	18.45	17.85
CaO	25.91	26.07	38.73	41.58	0.13	0.12	18.16	25.41	25.17
Na_2O	0.01	0.00	0.05	0.07	0.00	0.00	0.05	0.00	0.00
K_2O	0.00	0.00	0.01	0.00	0.00	0.00	0.00	0.01	0.00
Cr_2O_3	0.01	0.04	0.00	0.01	0.10	0.29	0.11	0.05	0.05
Total	100.00	100.00	100.00	100.00	100.00	100.00	100.00	100.00	100.00

Minerals compositions (oxides wt.%) in CAI_2. Values of the innermost and outermost phases compositions in CAI_2 are shown. Detailed data are reported in Tab. S2.

3.2.4 Discussions

The two studied CAIs have not been significantly altered by Earth or parent body processes. The lack of MnO, low FeO content in the CAI's outermost rim, the absence of secondary minerals (e.g., nepheline and sodalite), and the composition of melilite and pyroxene are indicative of significantly almost pristine conditions compared, for instance, with the similar Allende CAIs [19]. The irregular shapes of CAIs, as those presented in this study, are often interpreted as a result of condensation, suggesting an unlikely igneous origin. However, it has been experimentally demonstrated that crystal-bearing melts are more viscous than crystal-free melts [20, 21] and, as a result, the shapes of CAIs studied here may be the results due to the partially crystallised melts deformation. These irregular shapes may also be generated (or in concomitance with the above-mentioned process) by aerodynamic gas drag [22, 23].

Furthermore, the inclusions studied here show high temperature rims surrounding CAIs as first reported by [5]. Three layers, from interior to exterior are described by [5]: (1) spinel with perovskite inclusions, (2) melilite (± anorthite), and (3) diopsidic pyroxene (often zoned Ti-Al-rich on the interior, becoming diopside towards the exterior) [5, 7]. Following the previously described WL rims we also have tried to collect new information by deeply studying the rim sequence in our samples.

The minerals that make up CAIs 1 and 2 rims, along with their sequence and chemical composition, indicate a complex, high-temperature, multi-stage history. This process, as suggested by Wark and Lovering [5], likely involved evaporation, melting, and gas-solid reactions. We will now examine in detail how these minerals could have been formed and we propose a possible formation/petrologic history for the two CAIs.

Spinel nodules within the core of the CAI suggest that spinel formed prior to the pyroxene core. This is consistent with equilibrium condensation calculations as

proposed by Ebel and Grossman [24]. However, as shown by the equilibrium diagram proposed by Scott [25], the spinel likely did not condense directly from the solar gas but instead formed through reactions involving earlier phases, such as hibonite or melilite. The absence of these phases in the core indicates that they were consumed during the formation of spinel and later diopside as these reactions progressed.

Melilite and diopside have highly irregular and curved grain boundaries, suggesting disequilibrium conditions for their formation [26]. Condensation calculations predicted that melilite should condense at temperature and pressure ranging from 10^{-5} to 10^{-3} [24]. In such a scenario, the decrease in åkermanitic contents of melilite, in the mantle edge towards the WL rim, would have resulted from a gradual drop down of the total gas pressure during its condensation [27].

In CAI_1, the first melilite rim forms a thin, discontinuous layer beneath the spinel (Fig. 3.6b), whereas in CAI_2, it is continuous and much wider. Melilite is clearly enclosed within the spinel rim (Fig. 3.7b) resembling an intergrowth between these two phases. This implies a successive condensation event or, more probably, flash heating that produced melilite from diopside core with a vapor-melt interaction in the solar nebula [28]. Gehlenitic melilites in both CAIs also require that the onset of melilite crystallization occurred at temperatures higher than 1400 K.

Melilite mantles are produced not only during cooling of a melt but can also be produced by isothermal heat treatment given sufficient evaporation. Thus, in this scenario the formation of melilite, or their absence, might be due to different evaporation rates of Mg and Si from the surface of the partially molten droplets relative to their diffusion rates in the melt [29].

Gehlenitic to åkermanitic compositional zoning forms when melilite crystallizes from a high-Al melt and is conventionally referred to as 'normal zoning' [30]. CAI_2 shows normal zoning. These features are typically observed in Type B CAIs and are evidence for inward growth of molten droplets that cooled by radiation of heat from

their surfaces (e.g., [27, 31]).

Anorthite, only present in CAI_2, is minor and discontinuous (Fig. 3.7b), but its highly embayed and scalloped interfaces with underlying melilite suggest that melilite was replaced by anorthite after pyroxene formation.

Due to the textural contact between melilite and the coarse spinel rim (Fig. 3.7), we suggest a very intense and prolonged heating triggering Ca loss by evaporation and producing the thick rim of spinel from a melt, likely formed by rapid crystallization from a melt enriched in Ca and Al.

Forsterite condensed directly from the nebular gas at 1375 K [26, 32]:

$$2\mathrm{Mg(g)} + \mathrm{SiO(g)} + 3\mathrm{H_2O(g)} = \mathrm{Mg_2SiO_4(s)} + 3\mathrm{H_2(g)} \tag{3.1}$$

Grain boundaries in CAI_1 display 120° triple junctions (Fig. 3.6d), a characteristic also observed in amoeboid olivine aggregates (AOAs) from CV3 chondrites, as noted by [19]. This feature suggests high-temperature nebular (1375 K) annealing with minimal melting [26]. The compact texture of olivine grains with triple junctions can form through sub-solidus heating lasting only a few hours, without requiring partial melting [33–37].

The lower concentrations of CaO and Cr_2O_3 in forsterite have been attributed by some authors to forsterite condensation from a residual gas that was depleted in refractory elements after the condensation of refractory-rich minerals, with a subsequent isolation from the gas before Cr could condense [38, 39]. The increase in FeO content toward the outer regions is minimal and may result from overlap with the surrounding CAI matrix or minor Mg-Fe exchange occurring within the parent body.

The diopside rim possibly formed as a result of gas condensation at ∼1435 K and 10^{-3} bar on the surface of already-solid coarse-grained igneous CAIs [22, 26, 40].

Two textural occurrences of low-Ca pyroxene rims around forsterite may indicate its formation by two mechanisms as noted [32]. In details, they suggest an interaction between forsterite and gaseous SiO as shown in the following reactions (eq. 3.2 and 3.3):

$$Mg_2SiO_4(s) + SiO(g) + H_2O(g) = 2MgSiO_3(s) + H_2(g) \tag{3.2}$$

and by direct gas–solid condensation,

$$Mg(g) + SiO(g) + H_2O(g) = MgSiO_3(s) + H_2(g) \tag{3.3}$$

Different thicknesses in the convex and concave sides of CAIs could have resulted from the temperature and pressure gradients due to the ablation of the frontal part of the CAIs [22, 41]. This is further supported by the observation that the CAI_1 and 2 rims are thicker in the concave regions than in the convex areas due to aerodynamic gas drag [22].

The proposed formation sequences for both CAIs are illustrated in Figures 3.8 and 3.9, showing the stepwise development of rim layers through different nebular events. These schematic representations synthesize our interpretation of the complex petrogenetic history, highlighting the key differences in rim formation between the two inclusions while maintaining consistency with established condensation sequences and experimental constraints on high-temperature nebular processes.

3.2.5 Conclusions

The pristine condition of the NWA12800 CAIs analyzed in this study offers valuable insights into their origins, often concealed by secondary metasomatic and metamorphic processes typical in CV3 CAIs [42]. Our results suggest that the textures of

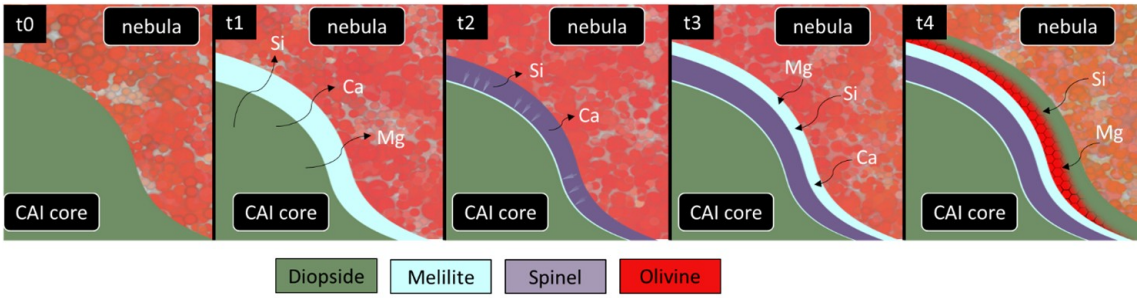

Figure 3.8: Schematic illustration of the stepwise formation of rims on CAI_1, explaining the process across different nebular events. The core of the inclusion consists of diopside (Di). During the first event (t1), flash heating causes the formation of a rim of melilite (Mel) and spinel (Sp) through the evaporative loss of silicon (Si), magnesium (Mg), and calcium (Ca) from the diopside. In the second event (t2), nebular conditions drive the condensation of melilite onto the spinel rim. A third event (t3) results in the condensation of forsterite (olivine, Ol), forming triple junctions indicative of thermal annealing, alongside additional diopside. Mineral abbreviations: Mel = melilite; Sp = spinel; Di = diopside; Ol = olivine.

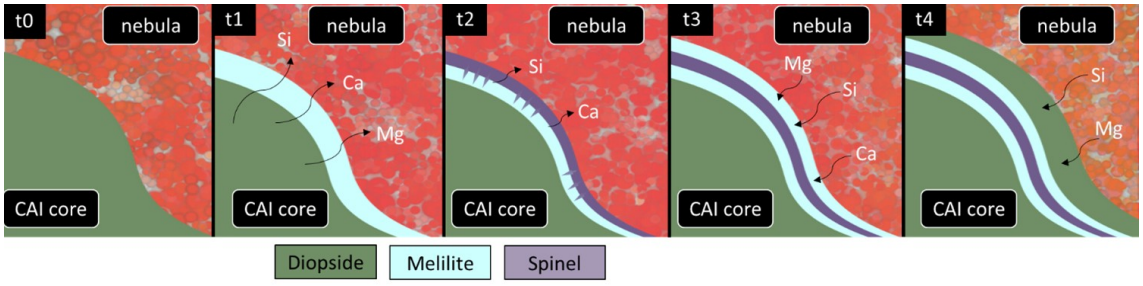

Figure 3.9: Schematic illustration of the stepwise formation of rims on CAI_2, explaining the process across different nebular events. The core of the inclusion consists of diopside (Di). During the first event (t1), flash heating causes the formation of a rim of melilite (Mel) and spinel (Sp) through the evaporative loss of silicon (Si), magnesium (Mg), and calcium (Ca) from the diopside. In the second event (t2), nebular conditions drive the condensation of melilite onto the spinel rim. Unlike CAI_1, CAI_2 does not exhibit a rim of olivine (Ol). However, the final rim of diopside (t3) is present and is notably thicker in concave regions than in convex ones, indicating a state of viscosity and gas drag during its formation. Mineral abbreviations: Mel = melilite; Sp = spinel; Di = diopside; Ol = olivine.

these CAIs cannot be explained solely by simple condensation mechanisms. Based on these observations, we conclude that the WL rim formation was initiated by flash melting and extensive evaporation of the original inclusion edge, followed by subsequent gas-solid reactions under highly dynamic conditions. Mineralogical observations reveal that CAIs 1 and 2 underwent a complex thermal history involving high-temperature episodes. The reconstructed sequence of their formation includes:

1. flash heating of the inclusion edges, resulting in the initial formation of melilite;
2. evaporative Ca-loss during crystallization, leading to the development of the spinel rim;
3. subsequent condensation of melilite from the nebular gas;
4. formation of the olivine rim via gas-solid condensation followed by thermal annealing;
5. condensation of the final diopside layer from the solar nebula;
6. final accretion of the CAIs onto the parent body.

This sequence illustrates a complex history of gas-solid condensation, evaporation, and re-condensation within the early solar nebula. Variations in temperature, pressure, and gas composition contributed to the formation of distinct mineral layers encasing the CAI core. Each rim layer likely formed in response to changing nebular conditions, marking separate episodes of mineral condensation during the evolution of these ancient inclusions. Based on mineralogical and textural evidence, these rims appear to result from flash heating events exceeding 2500 K for durations under 2 seconds [7]. The formation of these rims necessitated a multi-stage, high-temperature history involving transient heating processes, including evaporation, melting, and gas-solid reactions. Each rim layer developed sequentially, around 2 million years

after their host CAI [8]. The well-preserved, rimmed CAIs offer critical insights into early solar nebula conditions, providing a rare glimpse into the processes that shaped the formation and evolution of the first solid bodies in the solar system.

References for Section 2

[1] D. E. Anderson, S. Facchini, and K. I. Öberg (2023). Protoplanetary Disk Chemistry. *Annual Review of Astronomy and Astrophysics* vol. **61**, 287–328. https://doi.org/10.1146/annurev-astro-022823-040820.

[2] J. N. Connelly, M. Bizzarro, A. N. Krot, Å. Nordlund, D. Wielandt, and M. A. Ivanova (2012). The absolute chronology and thermal processing of solids in the solar protoplanetary disk. *Science* vol. **338**, 651–655. https://doi.org/10.1126/science.1226919.

[3] G. J. MacPherson and L. Grossman (1979). Melted and non-melted coarse-grained Ca-, Al-rich inclusions in Allende. *Meteoritics* vol. **14**, 479–480.

[4] L. Grossman (1980). Refractory Inclusions in the Allende Meteorite. *Annual Review of Earth and Planetary Sciences* vol. **8**, 559–608. https://doi.org/10.1146/annurev.ea.08.050180.003015.

[5] D. A. Wark and J. F. Lovering "Marker events in the early evolution of the solar system - Evidence from rims on Ca-Al-rich inclusions in carbonaceous chondrites". In: *Proceedings of the 8th Lunar Science Conference*. Vol. 1. Pergamon Press, 1977, 95–112.

[6] J. I. Simon, E. D. Young, S. S. Russell, E. K. Tonui, K. A. Dyl, and C. E. Manning (2005). A short timescale for changing oxygen fugacity in the solar nebula revealed by high-resolution 26Al-26Mg dating of CAI rims. *Earth and Planetary Science Letters* vol. **238**, 272–283. https://doi.org/10.1016/j.epsl.2005.08.005.

[7] D. Wark and W. V. Boynton (2001). The formation of rims on calcium-aluminum-rich inclusions: Step I—Flash heating. *Meteoritics & Planetary Science* vol. **36**, 1135–1166.

[8] J. Han, L. P. Keller, M. C. Liu, A. W. Needham, A. T. Hertwig, S. Messenger, and J. I. Simon (2020). A coordinated microstructural and isotopic study of a Wark-Lovering rim on a Vigarano CAI. *Geochimica et Cosmochimica Acta* vol. **269**, 639–660. https://doi.org/10.1016/j.gca.2019.10.040.

[9] A. E. Rubin, J. M. Trigo-Rodríguez, H. Huber, and J. T. Wasson (2007). Progressive aqueous alteration of CM carbonaceous chondrites. *Geochimica et Cosmochimica Acta* vol. **71**, 2361–2382. https://doi.org/10.1016/j.gca.2007.02.008.

[10] M. D. Suttle, A. J. King, P. F. Schofield, H. Bates, and S. S. Russell (2021). The aqueous alteration of CM chondrites, a review. *Geochimica et Cosmochimica Acta* vol. **299**, 219–256. https://doi.org/10.1016/j.gca.2021.02.001.

[11] H. C. Bates, A. J. King, K. L. Donaldson Hanna, N. E. Bowles, and S. S. Russell (2019). Linking mineralogy and spectroscopy of highly aqueously altered CM and CI carbonaceous chondrites in preparation for primitive asteroid sample return.

Meteoritics & Planetary Science vol. **54**, 2303–2319. https://doi.org/10.1111/maps.13380.

[12] A. N. Krot, K. Nagashima, and M. I. Petaev (2012). Isotopically uniform, 16O-depleted calcium, aluminum-rich inclusions in CH and CB carbonaceous chondrites. *Geochimica et Cosmochimica Acta* vol. **83**, 159–178. https://doi.org/10.1016/j.gca.2011.12.034.

[13] A. N. Krot, K. Nagashima, E. M. M. van Kooten, and M. Bizzarro (2017). Calcium-aluminum-rich inclusions recycled during formation of porphyritic chondrules from CH carbonaceous chondrites. *Geochimica et Cosmochimica Acta* vol. **201**, 185–223. https://doi.org/10.1016/j.gca.2016.09.035.

[14] E. T. Dunham, A. Sheikh, D. Opara, N. Matsuda, M.-C. Liu, and K. D. McKeegan (2023). Calcium-aluminum-rich inclusions in non-carbonaceous chondrites: Abundances, sizes, and mineralogy. *Meteoritics & Planetary Science* vol. **58**, 643–671. https://doi.org/10.1111/maps.13979.

[15] A. N. Krot, M. I. Petaev, E. R. D. Scott, B.-G. Choi, M. E. Zolensky, and K. Keil (1998). Progressive alteration in CV3 chondrites: More evidence for asteroidal alteration. *Meteoritics & Planetary Science* vol. **33**, 1065–1085. https://doi.org/10.1111/j.1945-5100.1998.tb01711.x.

[16] A. N. Krot, M. I. Petaev, and P. A. Bland (2004). Multiple formation mechanisms of ferrous olivine in CV carbonaceous chondrites during fluid-assisted metamorphism. *Antarctic Meteorite Research* vol. **17**, 153–171.

[17] K. Jogo, T. Nakamura, T. Noguchi, and M. Y. Zolotov (2009). Fayalite in the Vigarano CV3 carbonaceous chondrite: Occurrences, formation age and conditions. *Earth and Planetary Science Letters* vol. **287**, 320–328. https://doi.org/10.1016/j.epsl.2009.08.014.

[18] R. Harrington and K. Righter "Carbonaceous Chondrite Thin Section Preparation". In: *Annual Meeting of The Meteoritical Society*. JSC-CN-39781. 2017.

[19] M. Komatsu, A. N. Krot, M. I. Petaev, A. A. Ulyanov, K. Keil, and M. Miyamoto (2001). Mineralogy and petrography of amoeboid olivine aggregates from the reduced CV3 chondrites Efremovka, Leoville and Vigarano: Products of nebular condensation, accretion and annealing. *Meteoritics & Planetary Science* vol. **36**, 629–641. https://doi.org/10.1111/j.1945-5100.2001.tb01904.x.

[20] F. Vetere, H. Behrens, F. Holtz, G. Vilardo, and G. Ventura (2010). Viscosity of crystal-bearing hydrous andesites and its implication for magma ascent. *Journal of Mineralogical and Petrological Sciences* vol. **105**, 151–163. https://doi.org/10.2465/jmps.090128.

[21] F. Vetere, S. Merseburger, A. Pisello, D. Perugini, C. Viti, M. Petrelli, A. Musu, R. Almeev, L. Caricchi, G. Iezzi, M. Cassetta, and F. Holtz (2024). The role of deformation on the early crystallization and rheology of basaltic liquids. *Earth and Planetary Science Letters* vol. **644**, 118934. https://doi.org/10.1016/j.epsl.2024.118934.

[22] M. A. Ivanova (2023). Principal Studies of the First Solid Material Formed in the Early Solar System: A Review. *Geochemistry International* vol. **61**, 757–794. https://doi.org/10.1134/S0016702923080045.

[23] K. Liffman, N. Cuello, and D. A. Paterson (2016). A unified framework for producing CAI melting, Wark-Lovering rims and bowl-shaped CAIs. *Monthly Notices of the*

Royal Astronomical Society vol. **462**, 1137–1163. https://doi.org/10.1093/mnras/stw1525.

[24] D. S. Ebel and L. Grossman (2000). Condensation in dust-enriched systems. *Geochimica et Cosmochimica Acta* vol. **64**, 339–366. https://doi.org/10.1016/S0016-7037(99)00284-7.

[25] E. R. D. Scott (2007). Chondrites and the Protoplanetary Disk. *Annual Review of Earth and Planetary Sciences* vol. **35**, 577–620. https://doi.org/10.1146/annurev.earth.35.031306.140100.

[26] J. Han and A. J. Brearley (2015). Microstructural evidence for complex formation histories of amoeboid olivine aggregates from the ALHA77307 CO3.0 chondrite. *Meteoritics & Planetary Science* vol. **50**, 904–925. https://doi.org/10.1111/maps.12440.

[27] G. J. MacPherson and L. Grossman (1984). "Fluffy" Type A Ca-, Al-rich inclusions in the Allende meteorite. *Geochimica et Cosmochimica Acta* vol. **48**, 29–46. https://doi.org/10.1016/0016-7037(84)90351-9.

[28] R. A. Mendybaev, F. M. Richter, and A. M. Davis (2006). Crystallization of melilite from CMAS-liquids and the formation of the melilite mantle of Type B1 CAIs: Experimental simulations. *Geochimica et Cosmochimica Acta* vol. **70**, 2622–2642. https://doi.org/10.1016/j.gca.2006.02.013.

[29] F. M. Richter, A. M. Davis, D. S. Ebel, and A. Hashimoto (2002). Elemental and isotopic fractionation of Type B calcium-, aluminum-rich inclusions: experiments, theoretical considerations, and constraints on their thermal evolution. *Geochimica et Cosmochimica Acta* vol. **66**, 521–540. https://doi.org/10.1016/S0016-7037(01)00782-7.

[30] E. Stolper (1982). Crystallization sequences of Ca-Al-rich inclusions from Allende: An experimental study. *Geochimica et Cosmochimica Acta* vol. **46**, 2159–2180. https://doi.org/10.1016/0016-7037(82)90188-6.

[31] S. B. Simon and L. Grossman (2006). A comparative study of melilite and fassaite in Types B1 and B2 refractory inclusions. *Geochimica et Cosmochimica Acta* vol. **70**, 780–798. https://doi.org/10.1016/j.gca.2005.10.007.

[32] M. Komatsu, T. J. Fagan, A. N. Krot, K. Nagashima, M. I. Petaev, M. Kimura, and A. Yamaguchi (2018). First evidence for silica condensation within the solar protoplanetary disk. *Proceedings of the National Academy of Sciences* vol. **115**, 7497–7502. https://doi.org/10.1073/pnas.1722265115.

[33] S.-i. Karato (1989). Grain growth kinetics in olivine aggregates. *Tectonophysics* vol. **168**, 255–273. https://doi.org/10.1016/0040-1951(89)90221-7.

[34] S. J. Nichols and S. J. Mackwell (1991). Grain growth in porous olivine aggregates. *Physics and Chemistry of Minerals* vol. **18**, 269–278. https://doi.org/10.1007/BF00200184.

[35] U. H. Faul and D. Scott (2006). Grain growth in partially molten olivine aggregates. *Contributions to Mineralogy and Petrology* vol. **151**, 101–111. https://doi.org/10.1007/s00410-005-0046-3.

[36] S. A. Whattam, R. H. Hewins, B. A. Cohen, N. C. Seaton, and D. J. Prior (2008). Granoblastic olivine aggregates in magnesian chondrules: planetesimal fragments or thermally annealed solar nebula condensates? *Earth and Planetary Science Letters* vol. **269**, 200–211. https://doi.org/10.1016/j.epsl.2008.02.012.

[37] M. Komatsu, T. Mikouchi, and M. Miyamoto (2009). High temperature annealing of amoeboid olivine aggregates: Heating experiments on olivine-anorthite mixtures. *Polar Science* vol. **3**, 31–55. https://doi.org/10.1016/j.polar.2009.04.001.

[38] N. Sugiura, M. I. Petaev, M. Kimura, A. Miyazaki, and H. Hiyagon (2009). Nebular history of amoeboid olivine aggregates. *Meteoritics & Planetary Science* vol. **44**, 559–572. https://doi.org/10.1111/j.1945-5100.2009.tb00751.x.

[39] K. Fukuda, D. E. Brownlee, D. J. Joswiak, T. J. Tenner, M. Kimura, and N. T. Kita (2021). Correlated isotopic and chemical evidence for condensation origins of olivine in comet 81P/Wild 2 and in AOAs from CV and CO chondrites. *Geochimica et Cosmochimica Acta* vol. **293**, 544–574. https://doi.org/10.1016/j.gca.2020.10.019.

[40] S. Yoneda and L. Grossman (1995). Condensation of CaO-MgO-Al_2O_3-SiO_2 liquids from cosmic gases. *Geochimica et Cosmochimica Acta* vol. **59**, 3413–3444. https://doi.org/10.1016/0016-7037(95)00214-K.

[41] C. A. Lorenz, M. A. Ivanova, A. N. Krot, and V. V. Shuvalov (2019). Formation of disk- and bowl-shaped igneous Ca,Al-rich inclusions: Constraints from their morphology, textures, mineralogy and modelling. *Chemie der Erde* vol. **79**, 125523. https://doi.org/10.1016/j.chemer.2019.08.004.

[42] A. J. Brearley and A. N. Krot "Metasomatism in the early solar system: The record from chondritic meteorites". In: *Metasomatism and the Chemical Transformation of Rock*. Ed. by D. E. Harlov and H. Austrheim. Springer, 2013, 659–789. https://doi.org/10.1007/978-3-642-28394-9_17.

3.3 Melt Inclusions in Chondrules: A Window into Early Solar System Processes

Abstract. Melt inclusions, commonly studied in volcanic rocks, have long been a key tool for investigating magmatic processes. However, their role in understanding chondrules—small, spherical components of meteorites—remains poorly explored and presents significant challenges. Chondrules formed in a unique physicochemical environment compared to Earth's magmatic systems. They crystallized at temperatures above 1400 °C as free-floating droplets in microgravity, under a pressure of approximately 10^{-3} bar, cooling at rates of hundreds to thousands of $°C\,h^{-1}$, interacting with nebular vapor. This section highlights the importance of melt inclusions in chondrules as valuable insights into the conditions of the early solar system. Using an electron microprobe, olivine grains containing melt inclusions (with diverse shapes and compositions) were analytically examined. The analysis reveals that these melt inclusions exhibit diverse chemical compositions, including Al-rich, Na-poor and Al-rich, Na-rich glasses. The proposed scenario for the formation of this chondrule, is based on the chemistry of melt inclusions and the enstatite rim surrounding the isolated olivine grain. This possibly mirrors a splashing impact while the chondrule was still partially molten, followed by gas–melt interaction, during which the melt reacted with the surrounding nebular gas.

3.3.1 Introduction

Melt inclusions (MIs) are tiny glassy pockets hosted in minerals and formed by trapping melts during crystallisation. The composition of an MI is usually in equilibrium with its host at the temperature of the liquidus [1, 2]. Thus, MIs can preserve clues to the conditions and dynamics during melt crystallization. Isolated

olivine grains (IOGs) are euhedral to subhedral forsteritic crystals found embedded in the matrix of carbonaceous chondrites [1]. The origin of IOGs remains debated, with two principal formation mechanisms proposed: direct condensation from the solar nebula [1, 3–5] and fragmentation of pre-existing chondrules [6, 7].

According to the literature, MIs in type I chondrule olivines are classified into three compositional groups [2, 4, 5, 8]. *Primary* MIs form from the original melt during the crystallization of olivine and include two main compositional types: **(1) Al-rich** (SiO_2: 39–52 wt.%, Al_2O_3: 22.7–28.8 wt.%, high CaO: ∼21.7 wt.%) and **(2) Al-poor** (SiO_2 >55 wt.%, Al_2O_3 <21 wt.%), both characterized by low alkali contents. *Secondary* inclusions form when fluids heal pre-existing fractures in a crystal, after its crystallization; thus, they provide no information about the crystal's original growth conditions. In contrast, *pseudosecondary* inclusions form from residual melt trapped within healing micro-fractures during the growth of the host crystal. This results in a third compositional group, identified as the Ca-poor, **Na-rich subgroup** of the Al-rich glasses (Na_2O: 4.5–14.7 wt.%, low CaO: 0.9–8.5 wt.%). This classification of MIs compositional groups is summarized in Table 3.5.

A comprehensive dataset of MIs compositions in chondrules is currently lacking. For comparison, representative average compositions of chondrule glasses from the literature are shown in Table 3.7. A subset of MIs hosted in iron-rich olivine crystals exhibits highly evolved compositions with high SiO_2 contents (> 60 wt.%) that are incompatible with olivine equilibrium, leading to crystal dissolution at the melt-crystal interface [9]. These evolved melts show compositional ranges (SiO_2 = 58.1–74.5 wt.%, Al_2O_3 = 7.7–17.4 wt.%, FeO = 1.8–8.5 wt.%, Na_2O = 0.0–10.3 wt.%, MgO = 0.04–14.8 wt.%, CaO = 1.0–28.3 wt.%) that significantly exceed the majority of studied MIs. Those inclusions are excluded from further discussion in this chapter to focus on the more representative, less fractionated melt inclusion.

The study of MIs applied to IOGs has led to the formulation of several competing

Table 3.5: Resume of MIs compositional groups from Kurat et al. 1997 [4] and Varela et al. 2002 [5]

Group	**SiO_2**	**Al_2O_3**	**CaO**	**Na_2O**
Al-rich	39–52	22.7–28.8	15–26	$\leq$0.5
Na-rich *subgroup*	46–55	23.8–29.6	0.9–8.5	4.5–14.7
Al-poor	>55	<21	6.7–19	0.02–2.6

Data are presented in weight percent (wt.%).

hypotheses regarding their formation. Fuchs *et al.* [1] first identified glass blebs enclosed within isolated olivine grains in the Murchison meteorite. They observed that the chemical compositions of these glasses are not in equilibrium with olivine at liquidus temperatures and concluded that the glasses cannot represent melts trapped during magmatic crystallization. Following this study, subsequent early models proposed a nebular origin for such inclusions, suggesting that both the glass inclusions and their host olivine grains represent high-temperature condensates [1, 3]. The condensation-origin model for IOGs was later refined through the Vapor–Liquid–Solid (VLS) growth model [4, 5], which explains the euhedral shape of IOGs and interprets MIs as the trapped liquid layer formed during this growth process. In the VLS model, olivine grains grow in a melted droplet, which interfaces directly with the nebular gas. The growth is sustained by condensable elements from the vapor onto the liquid film. This continuous interaction enriches the liquid and allows olivine growth to continue.

In contrast to direct condensates, some authors have interpreted IOGs as fragments of pre-existing chondrules formed during subsolidus fragmentation (e.g.[6]). Others have proposed that IOGs originated from a melt, with MIs as droplets of the IOGs parental melt trapped during fractional crystallization [8]. This interpretation was further developed by the suggestion that IOGs are products of chondrule

Table 3.6: Evolution of genetic models for isolated olivine grains and MIs in carbonaceous chondrites.

Works	IOGs Origin Model	MIs Origin and Genetic Significance
Fuchs et al. *1973* [1]	First description of IOGs; suggested nebular condensation.	Glass inclusions interpreted as high-temperature condensates.
Olsen & Grossman *1978* [3]	IOG origin discussed as direct condensation.	Analyze MIs and favor an origin by direct condensation.
McSween *1977* [6]	**Fragmentation model**: IOGs as broken pieces of chondrules; based on chondrules compositional similarities.	Melt inclusions (MIs) represent trapped parental melts from fractional crystallization, just as the chondrule mesostasis, is considered the complementary residual melt.
Roedder 1981, 1984 [8] [2]	(non-planetary origin; non-condensate origin) **Two-Stage Formation**: Olivine crystals nucleated from a very "olivine-rich melt" (Stage 2) derived from the melting of refractory primitive materials condensed from the nebula (Stage 1).	MIs are trapped remnants of melts that evolve during fractional crystallization.
Jones 1992 [7]	**Recycling/Fragmentation**: IOGs derived from the recycling of chondrule fragments that underwent partial re-melting and crystallization, evidenced by the presence of pyroxene rims.	MIs are analyzed, and the literature is reviewed, but no original MIs genetic model is proposed.
Kurat et al. *1997* [4]	**VLS condensation**: Euhedral olivines grown by vapor-liquid-solid process from nebular gas.	MIs as trapped liquid layer from VLS growth; unfractionated trace elements support condensation.
Varela et al. *2002* [5]	Updated VLS Condensation model from Kurat et al. 1977 work; IOGs are nebular condensates.	**Refined MIs Chemical Classification**: Al-rich (primary high-T condensate), Al-poor (primary low-T), Na-rich (metasomatized). Updated VLS growth mechanism.
Libourel et al. 2006 [10]	**Gas-Melt Interaction**:IOG not discussed; focuses on chondrules, arguing they formed from pre-existing solids with extensive gas-melt interaction, a mechanism; extensible to IOGs.	MIs record open-system gas-melt interactions during chondrule formation.
Faure et al. *2012* [11]	**Planetesimal magmatism**: This study utilizes dynamic crystallization experiments to test the origin of chondrules and melt inclusions. The authors' experiments support an origin from a splash impact event on a molten planetesimal; extensible to IOGs.	Authors propose that silica-rich MIs are relicts of the primary, unfractionated magma of a planetesimal.
Florentin et al. *2018* [12]	Planetesimal magmatism: IOGs are not discussed, but Type I olivines are discussed as crystallized slowly within a molten planetesimal interior before being excavated by an impact; extensible to IOGs	**First ever 3D chemical images** of chondrule MIs; multi-stage MIs origin; *Primary* MIs were trapped during slow magmatic growth inside the planetesimal. After a splash impact, the olivine grain traps a *residual* melts, which re-equilibrated during an open-system interaction by gas-melt interactions in the nebula as a protochondrule.
Jacquet et al. *2020* [13]	**"Splash" model**: IOGs expelled from partially molten chondrules during collisions; explain the pyroxene rim.	MIs in IOGs show chemical mofidication from gas-melt interactions post-ejection.

recycling and fragmentation [7]. To explain the igneous origin of IOGs, as opposed to a condensation origin, recent experimental work [11] supports that Al-rich glass inclusion compositions can be reproduced by the slow crystallization of a magma ocean, implying a planetary magmatic setting. However, this model requires large-scale melting on planetesimals. Diverse MI compositions have also been explained through impact processes involving molten planetesimals [12], although the origin of IOGs was not explicitly addressed.

Table 3.7: Average compositions of chondrules glasses from various studies (wt.%).

	[1]	**[6]**	**[3]**	**[7]**	**[10]**	**[5]**
SiO_2	50.8	50.1	69.1	52.0	46.2	51.2
TiO_2	0.8	–	0.1	0.9	1.1	1.0
Al_2O_3	22.2	19.6	15.7	24.4	24.4	22.9
FeO	1.5	5.9	0.6	0.3	0.5	1.2
MnO	0.03	–	–	–	0.04	0.05
MgO	4.3	5.6	3.2	4.2	4.4	3.7
CaO	18.5	12.9	9.8	17.5	21.4	15.8
Na_2O	0.3	5.6	1.0	1.2	0.2	1.8
K_2O	0.05	0.1	0.03	0.02	–	0.1
Cr_2O_3	0.2	–	0.1	0.3	0.3	0.3
P_2O_5	–	–	–	–	–	0.2
Total	98.7	99.8	99.6	100.8	98.8	98.7
CaO/Al_2O_3	0.83	0.66	0.62	0.72	0.88	0.69

Data sources: [1] Fuchs et al. (1973) (Average n=14); [6] McSween et al. (1977) (Average n=7); [3] Olsen et al. (1978) (Average n=8); [7] Jones et al. (1992) (Average n=2); [10] Libourel et al. (2006) (Average n=4); [5] Varela et al. (2002) (Average n=33). All data verified in Appendix Table 3.13. – = not analyzed.

Condensation, sub-solidus recycling, fragmentation, and planetesimal melting have all been proposed as possible processes for IOG formation. Further constraints are needed to reconcile these scenarios with detailed MI studies. More recently, the planetary impact hypothesis has been re-scaled into a "chondrule collision–splash"

model [13], in which IOGs are interpreted as fragments expelled from partially molten chondrules during collisions. Their MIs show evidence of subsequent chemical modification resulting from gas–melt interactions after ejection. In this model, IOGs form through a supra-solidus "splash" collisional mechanism during chondrule formation [13]. In this scenario, a molten droplet begins crystallizing olivine, and while it remains mostly molten, a collision separates the early-formed crystals from the parent droplet. The isolated crystal then continues to crystallize with its adhered residual melt and may further interact with the surrounding gas, forming reaction rims. The enstatite rim develops when the isolated olivine grain reacts as an independent object with a SiO_2-enriched gas, promoting pyroxene crystallization at the expense of olivine through a gas–melt–solid interaction. A summary of all these competing genetic hypotheses is provided in Table 3.6.

In this work, we present preliminary analyses of MIs within chondrules from the NWA 12800 CV3 carbonaceous chondrite, with particular focus on a pristine isolated IOG that exhibits different type of MIs, an enstatite rim, and Fe-Ni metal blebs. This assemblage could provide useful insights into the formation of chondritic components in the early Solar System.

3.3.2 Materials and Methods

Petrographic and geochemical analyses were conducted on an isolated olivine grain from the NWA 12800 (CV3) carbonaceous chondrite. Initial petrographic characterization employed polarized light microscopy to identify IOG and chondrules (Fig. 3.10). High-resolution imaging and quantitative major-element analyses were performed at the *Institute of Mineralogy, Leibniz University of Hannover*. Imaging was carried out using a JEOL JSM-6700F field-emission scanning electron microscope (SEM) operating in back-scattered electron mode at 15 kV accelerating voltage, and

analyses were obtained using a JEOL JXA-iHP200F field emission electron microprobe. Operating conditions were 15 kV accelerating voltage, 15 nA beam current, and a focused beam diameter of approximately 2 μm. To minimize alkali migration, sodium and potassium were analyzed first in the measurement sequence. Calibration utilized well-characterized natural and synthetic standards, with analytical accuracy maintained below 1% deviation throughout each analytical session. ZAF corrections were applied to account for atomic number, absorption, and fluorescence effects. Metal blebs associated with the studied olivine grain were analyzed using identical EPMA conditions to characterize their Fe-Ni compositions.

3.3.3 Result and Discussion

Petrographic examination of NWA 12800 CV3 chondrite reveals that in most chondrules, particularly barred olivine types, MIs size are typically below the analytical resolution limit for quantitative electron microprobe analysis (Figure 3.10). An isolated olivine grain (IOG) was selected because it contains analyzable-size MIs (above $\approx 12\,\mu$m in diameter), to assess the relationship between the melt composition and the olivine host.

The chosen IOG represents a single, porphyritic equidimensional sub-euhedral olivine microphenocryst with a mean apparent diameter of 840 μm (Fig. 3.11). The grain exhibits no undulose extinction under cross-polarized light, indicating minimal shock deformation. Several irregular fractures cross-cut the grain, potentially related to post-formational stress events. Under polarized light microscopy, the IOG displays two distinct crystallographic orientations of olivine (see Fig. 3.10a). Microprobe analyses reveal that the IOG is predominantly forsteritic, exhibiting compositional zoning from core to rim (Table 3.9). The core region has a highly magnesium composition ($Fo_{99.3}$) with FeO content of 0.68 wt.%, while the outer region shows

slight iron enrichment ($Fo_{95.3}$) with 4.73 wt.% FeO. This zoning pattern suggests either growth from an evolving melt or subsequent diffusional exchange.

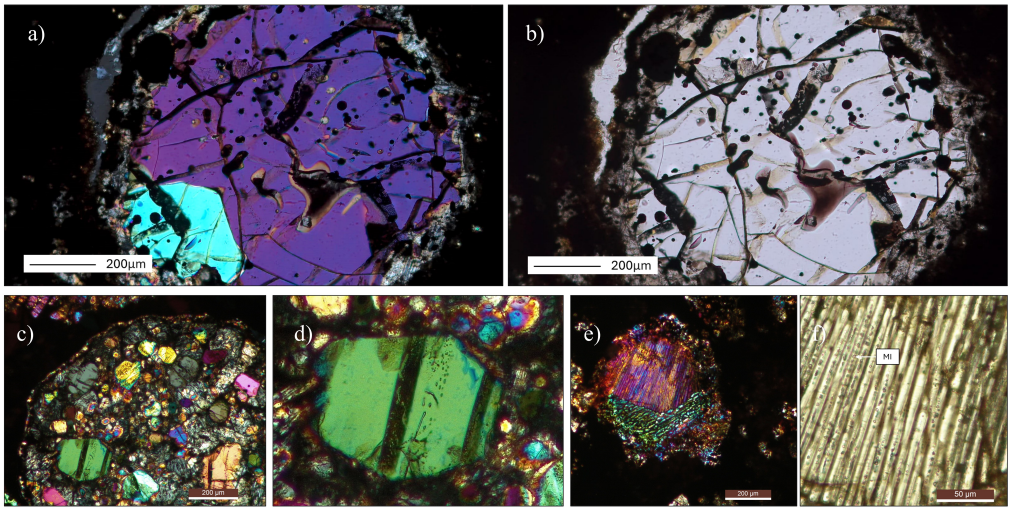

Figure 3.10: Petrographic overview of chondrules in the NWA 12800 meteorite, containing MIs. All images were acquired using transmitted light microscopy. (a) An isolated olivine grain (IOG) under crossed polarizers, exhibiting two distinct optical orientation domains. (b) The same IOG as in (a) under plane-polarized light, revealing numerous opaque inclusions. (c) A porphyritic olivine-pyroxene (POP) chondrule under crossed polarizers, showing a euhedral olivine crystal hosting numerous MIs. (d) A detailed view of a euhedral olivine grain within a POP chondrule, hosting MIs under crossed polarizers. (e) A barred olivine (BO) chondrule under crossed polarizers with MI, cross polarizers. (f) A detailed view of numerous MIs enclosed in olivine bars under plane-polarized light.

The IOG is rimmed by a continuous enstatite rim of uniform composition ($Fs_{1.1}Wo_{0.9}$), characterized by high MgO (38.82 wt.%) and low FeO (0.79 wt.%) contents (Table 3.9). This rim could suggest either overgrowth from the residual melt or reaction with the solar nebula during cooling. Experimental attempts to reproduce the enstatite rim by fractional crystallization failed (*e.g.*, [14, 15]). Petrographic and chemical characteristics of the enstatite rim around the olivine grain could be explained by gas-melt interaction under high $SiO_{(g)}$ partial pressures sourced from the solar nebula [16, 17]. In carbonaceous chondrites, isotopic studies suggested that olivines and their pyroxene rim are not co-magmatic and did not crystallise from the same melt [18], but 2/3 of the oxygen in the low-Ca pyroxene originated from

partially dissolved precursor olivine, while 1/3 was added by the reaction with SiO from the surrounding gas via the reaction sequence:

$$SiO_{(gas)} + \tfrac{1}{2}O_{2(gas)} \rightarrow SiO_{2(melt)} \quad (1)$$

$$Mg_2SiO_4 \text{ (olivine)} + SiO_{2(melt)} \rightarrow Mg_2Si_2O_6 \text{ (pyroxene)} \quad (2)$$

In high-temperature experiments, exposed partially molten, chondrule-like samples to high $SiO_{(g)}$ partial pressures reproduced the enstatite rim [17]. These high SiO partial pressures could result from evaporation in a dust-rich environment of the solar nebula [19, 20]. Gas-melt reaction might even occur in a regime of low $SiO_{(g)}$ partial pressures if the IOG formed during multiple melting and cooling events [21]. Because Si is a network-forming element in silicate melts, deep diffusion of silica into the chondrule melts is unfavored. Crystallization of enstatite stopped the interaction of melts with nebula gas, preventing further gas–melt interaction [19]. No glass or metal inclusions were observed within the pyroxene rim.

The measured composition of the metal blebs (Fe = 88.57 wt.%, Ni = 8.64 wt.%; Table 3.8) lies within the compositional field commonly attributed to high-Ni kamacite rather than taenite.

Table 3.8: Composition of a metal bleb enclosed in the isolated olivine grain (wt.%).

Element	**Mass %**	**Atom %**	**ZAF Corrected**
Fe	88.57	91.45	0.91
Ni	8.64	8.49	1.05
Other	0.08	0.06	-
Total	97.29	100.00	-

Moreover, the nearly spherical morphology and internal distribution of the blebs support a mechanism of liquid immiscibility, by which Fe–Ni metal droplets segregated from silicate melt during olivine crystallization under strongly reducing conditions.

Alternatively, direct condensation from a nebular gas at $\sim$ 1350–1450 K is a plausible source of metal, though this scenario requires sufficiently low oxygen fugacity and possibly local dust enrichment to stabilize metallic Fe–Ni [22]. Finally, given the relatively small scale of the metallic blebs, possible Ni diffusion at low temperatures and shock-induced re-equilibration remain non-negligible uncertainties that must be assessed.

Table 3.9: Compositional traverse across the isolated olivine grain and its enstatite rim (wt.%).

	Ol-core	**Ol-mid**	**Ol-outer**	**En-rim**
SiO_2	41.94	41.75	41.03	58.58
TiO_2	0.02	0.09	0.00	0.09
Al_2O_3	0.20	0.42	0.07	0.73
FeO	0.68	1.00	4.73	0.79
MnO	0.00	0.04	0.10	0.09
MgO	56.85	56.27	54.16	38.82
CaO	0.31	0.05	0.08	0.45
Na_2O	0.00	0.14	0.02	0.02
K_2O	0.00	0.01	0.01	0.00
P_2O_5	0.29	0.53	0.24	0.53
Total	100.30	100.31	100.43	100.09

Multiple MIs of varying morphology are distributed throughout the olivine host, including spherical, elongated, and irregular forms. Elemental mapping clearly distinguishes the MIs from the host olivine through pronounced color contrasts, with the inclusions exhibiting elevated Al and Ca signatures compared to the Mg-rich olivine host (Fig. 3.11). The locations of the spot analyses of MIs within the isolated olivine grain (IOG) are shown in Figure 3.12, and the corresponding analytical results are reported in Table 3.10.

No MIs observed in this study fit the criteria for the Al-poor group defined in Table 3.5. **MI-2** is classified as an Al-rich primary inclusion (Table 3.11). MI-2 is characterized by low SiO_2 (43.79 wt.%) and exceptionally high CaO (25.49 wt.%), which is at the upper end of the established range for this group (15–26 wt.%). Most

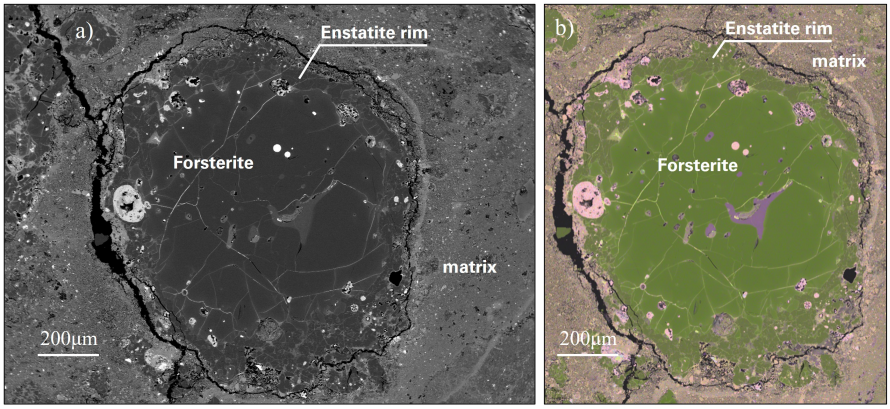

Figure 3.11: Elemental mapping of the isolated olivine grain (IOG). (a) Back-scattered electron image showing the IOG with enstatite rim and surrounding matrix. (b) False-color elemental map highlighting the distribution of major elements (see Chapter 3.1 Fig. 3.5a for color key). Dark green areas correspond to pyroxene, while violet regions indicate melt inclusion compositions.

notably, Na_2O content is below the detection limit (0.01 wt.%), consistent with the definition of primary Al-rich inclusions. The Al_2O_3 content is 19.17 wt.%, slightly lower than the reference range, but the overall chemical signature—high CaO and near-zero Na_2O—strongly aligns it with the primary Al-rich type.

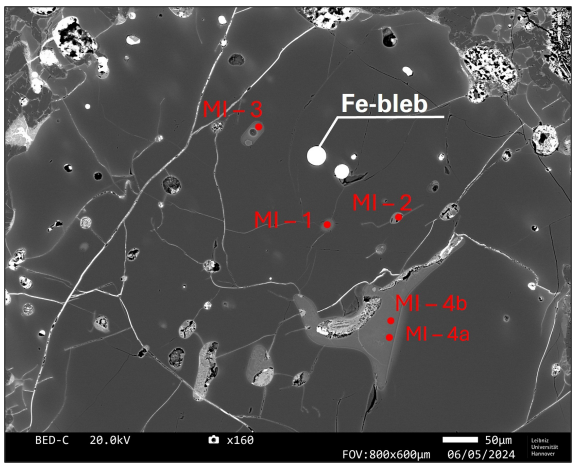

Figure 3.12: Close-up BSE image of the isolated olivine grain, highlighting the locations of analyzed melt inclusions (MI-1 to MI-4) and metal blebs. The Fe-Ni metal bleb and multiple melt inclusion analysis points are annotated, with their compositions reported in Tables 3.8 and 3.10.

MI-1, MI-3, and MI-4 are classified within the Al-rich, Ca-poor, Na-rich,

subgroup (Table 3.5), interpreted to be pseudosecondary [5]. These Na-rich inclusions exhibit a strong inverse correlation between Na_2O and CaO, alongside a positive correlation between Na_2O and SiO_2. All exhibit low (subchondritic) CaO/Al_2O_3 ratios (0.27–0.44) with respect to the chondrite ratio ($\sim$ 0.6–0.8), as shown in Table 3.10. In sharp contrast, the Al-rich primary MI-2 presents an elevated CaO/Al_2O_3 ratio of 1.33 (Table 3.11). The coexistence of these chemically distinct inclusions within the same olivine grain suggests distinct genetic histories for the two inclusion types.

Table 3.10: Representative compositions of MIs hosted in the IOG (wt.%).

	MI-1	**MI-2**	**MI-3**	**MI-4 (a)**	**MI-4 (b)**
SiO_2	48.13	43.79	47.45	46.78	47.15
TiO_2	1.22	0.85	0.95	1.01	0.99
Al_2O_3	24.39	19.17	23.48	23.64	24.02
FeO	0.30	0.27	2.33	5.46	4.63
MnO	0.04	0.00	0.00	0.02	0.02
MgO	3.50	10.90	5.01	2.44	3.07
CaO	10.84	25.49	8.38	6.44	6.62
Na_2O	12.28	0.00	11.91	13.31	13.07
K_2O	0.12	0.00	0.76	0.55	0.60
P_2O_5	0.05	0.04	0.10	0.20	0.20
Total	100.88	100.52	100.36	99.84	100.37
CaO/Al_2O_3	0.44	1.33	0.36	0.27	0.28

Notably, MI-4 is a large pocket of melts, texturally more similar to a chondrule mesostasis rather than a melt inclusion *sensu strictu*. Two distinct spots were analyzed within this feature: **MI-4 (a)** and **MI-4 (b)**, representing compositional variations within the same melt pocket. In stark contrast to the MI-1 and MI-3 Na-rich inclusions, MI-4 is a Na-rich inclusion characterized by high FeO content (4.63–5.46 wt.%), which is significantly higher than that of MI-1 (0.30 wt.%) and MI-3 (2.33 wt.%). The FeO content, combined with the lowest MgO values in the dataset (2.44–3.07 wt.%), suggests MI-4 represents a evolved residual melt.

The Fe-Mg partition coefficient value at equilibrium in magmatic systems is

Table 3.11: Classification of melt inclusions based on compositional groups [5].

MI name	SiO_2 (wt.%)	Al_2O_3 (wt.%)	CaO (wt.%)	Na_2O (wt.%)	CaO/Al_2O_3 ratio	Classification and origin
MI-1	48.13	24.39	10.84	12.28	0.44	Al-rich, Na-rich subgroup, pseudosecondary
MI-2	43.79	19.17	25.49	0.00	1.33	Al-rich primary: Low SiO_2, high CaO, very low Na_2O, contemporaneous with host crystallization
MI-3	47.45	23.48	8.38	11.91	0.36	Al-rich, Na-rich subgroup, pseudosecondary
MI-4 (a)	46.78	23.64	6.44	13.31	0.27	Al-rich, Na-rich subgroup, pseudosecondary
MI-4 (b)	47.15	24.02	6.62	13.07	0.28	Al-rich, Na-rich subgroup, pseudosecondary

$\mathbf{0.30 \pm 0.03}$. This value is applicable even under the highly reducing redox conditions characteristic of chondrules (e.g., buffered near IW) since crystalline olivine almost exclusively accepts Fe^{2+}, and under these reducing conditions, the melt contains virtually solely Fe^{2+}. Consequently, the standard K_D formula utilizing the total analyzed iron (FeO_{tot}) remains highly accurate, eliminating the need for complex oxidation state corrections for Fe^{3+}/Fe^{2+} partitioning.

The $K_D^{\text{Fe-Mg}}$ is formally defined as:

$$K_D^{\text{Fe-Mg}} = \frac{X_{\text{Fe}}^{\text{Ol}} \cdot X_{\text{Mg}}^{\text{Melt}}}{X_{\text{Mg}}^{\text{Ol}} \cdot X_{\text{Fe}}^{\text{Melt}}}$$

For practical application using the total measured weight percent (wt.%) of iron and magnesium oxides, the calculation is performed as:

$$\text{Calculated } K_D^{\text{Fe-Mg}} = \frac{(\text{FeO/MgO})_{\text{Ol-core}}}{(\text{FeO/MgO})_{\text{MI}}}$$

The calculated $K_D^{\text{Fe-Mg}}$ values (Table 3.12) indicate a significant disequilibrium state for all analyzed MIs relative to the Ol-core ($K_D \approx 0.005$ to 0.483). The majority of MIs (MI-3, MI-4a, MI-4b) yield extremely low K_D values, a strong indication of

extensive **post-entrapment crystallization** (PEC). Future work will require PEC correction to retrieve the true liquid composition at the time of entrapment.

Table 3.12: Calculated $K_D^{\text{Fe-Mg}}$ values between the Olivine Core and Melt Inclusions (MI).

Sample	**MI-1**	**MI-2**	**MI-3**	**MI-4 (a)**	**MI-4 (b)**	**Olivine Core**
FeO (wt%)	0.30	0.27	2.33	5.46	4.63	0.68
MgO (wt%)	3.50	10.90	5.01	2.44	3.07	56.86
(FeO/MgO)	0.086	0.025	0.465	2.238	1.508	0.0120
$\mathbf{K_D^{\text{Fe-Mg}}}$	0.140	0.480	0.0258	0.00536	0.00795	–

Note: The partition coefficient is calculated as $K_D^{\text{Fe-Mg}} = \frac{(\text{FeO/MgO})_{\text{Olivine}}}{(\text{FeO/MgO})_{\text{Melt}}}$. The expected equilibrium range for $K_D^{\text{Fe-Mg}}$ is 0.30 ± 0.03 [2]. Values significantly lower than this range suggest a lack of equilibrium.

The low SiO_2, high CaO, high CaO/Al_2O_3 ratio of 1.33 (well above the chondritic ratio $\approx$ 0.6–0.8) and near-zero alkali content of **MI-2** (Table 3.10) strongly indicate that the IOG initially crystallized from a highly refractory, Al-, Ca-, and Mg-rich melt that was severely depleted in volatile alkali concentrations. Probably the high temperatures prevented the condensation and incorporation of Na and K into the earliest melt. The very low FeO content of the IOG core (0.68 wt.%, Table 3.9), along with this Al-rich melt inclusion, suggest first step of formation in a highly reducing, high-temperature environment. Thus, **MI-2** records the early crystallization conditions of the IOG. Conversely, the pervasive occurrence of Al-rich *pseudosecondary* inclusions (MI-1, MI-3, MI-4a-b) reveals a significant gas reaction during successive crystallization events. The diverse chemistry of the MIs, coupled with the presence of the enstatite rim, strongly supports an open-system model involving gas–melt interaction during transient high-temperature events, where the partial pressures of elements such as Si and Na enabled rapid exchange and reaction with the residual melt.

According to Jaquet et al. model [13], we resume the sequence of events to explain this IOG history in Fig. 3.13:

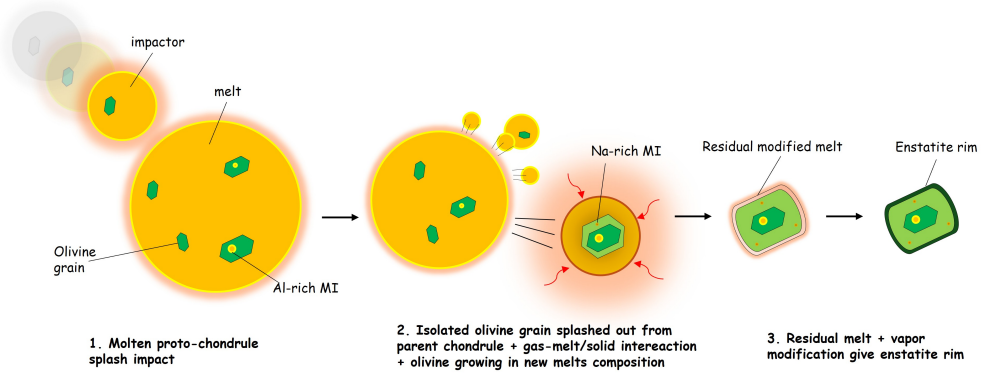

Figure 3.13: Sketch of the proposed formation scenario for Isolated Olivine Grains (IOGs). The process involves: (a) Initial crystallization of olivine phenocrysts within a molten chondrule. (b) A Collisional Splash Event expels olivine fragments with adhered residual melt. (c) The Ejected IOG interacts with the surrounding SiO_2-enriched nebular gas. (d) Enstatite Rim Formation results from gas-melt-solid interaction, completing the IOG structure.

1. **Initial Chondrule Crystallization:** Formation started when the chondrule-precursor aggregates melted during brief high-temperature events. Few forsteritic olivine crystallized inside a proto-chondrule melt, trapping primary Al-rich, Na-poor MIs (e.g., MI-2) that represent the primary magmatic compositions [5, 11].

2. **Micro-Scale Impact and Ejection:** While the chondrule was still partially molten, it experienced a kinetic event (e.g. collision). This event led to the fragmentation of the droplet and the ejection of a single or few olivine crystals with small amounts of adhering melt.

3. **Post-Ejection Crystallization and Melt Modification:** Isolated in the nebular environment, the expelled olivine continued to grow, and the residual melts evolved due to fractional crystallization and gas-melt interaction in the solar nebula. Olivine trapping new MI interstitially between the growing crystal from a chemically evolving system. This process is not at equilibrium because the impact may have altered the chemical equilibria, and the nebular

environment may also have modified the composition. In this case, trappings of Na-rich olivines such as MI-1 formed through interaction with the nebular vapour, likely involving Ca-Na exchange processes.

4. **Rim formation:** The outermost surface of the crystal, still coated with melt, interacted with SiO-rich nebular gas. Olivine reacted with the melt and SiO from the surrounding gas to form enstatite rim around the olivine grain [10]. The FeO zonation in the olivine likely could reflects re-equilibration during this late-stage processing.

3.3.4 Concluding remarks and future works

We report preliminary results from isolated olivine grain in NWA 12800 suggesting evidence for a multi-stage, open-system formation history in the nebular environment. These analyses should be considered preliminary, as the quality of the studied MIs was often compromised by analytical challenges, including small size, the presence of post-entrapment fractures, daughter crystals, and shrinkage bubbles. Consequently, a follow-up study with advanced micro-analytical techniques, such as NanoSIMS, is required. The presence of an early-trapped, refractory Al-rich, Na-poor inclusion with a high CaO/Al_2O_3 ratio and later Al-rich, Na-rich inclusions suggest that the IOG interacted with a volatile-rich nebular gas. Despite the compelling constraints provided by our petrographic and compositional data, the analysis of chondrule melt inclusions remains challenging due to their minute size and the extreme, non-terrestrial conditions of their formation. While state-of-the-art computational tools, such as MIMiC and Melts, are invaluable in terrestrial petrology, their application to these exceptional, high-temperature, open-system nebular conditions is currently limited, precluding the inclusion of quantitative modeling results in this study. The enigmatic nature of MIs in chondrules thus persists, representing a significant

challenge and a fruitful avenue for future investigations in modern petrology.

3.3.5 Appendix

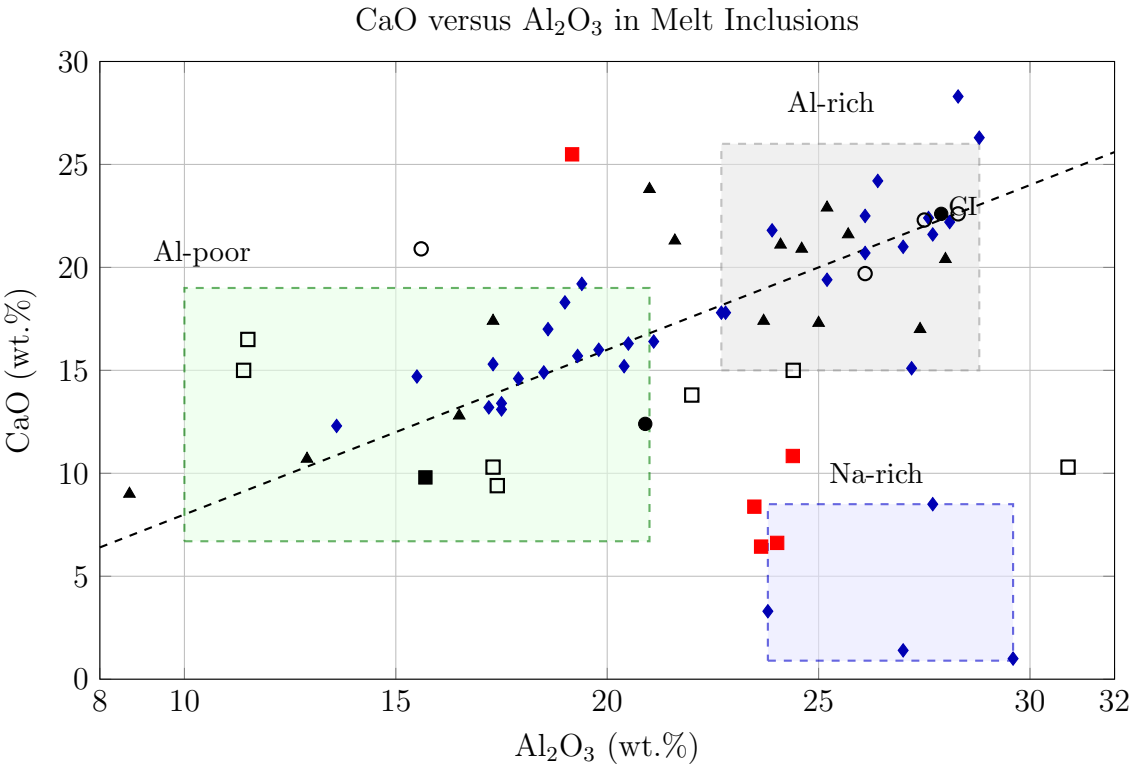

Figure 3.14: Compositional variation diagram of CaO versus Al_2O_3 (in wt.%) for melt inclusions (MIs) in carbonaceous chondrites. Shaded fields represent compositional groups. The dashed line marked CI indicates the bulk chondritic CaO/Al_2O_3 ratio (0.8). **Our data** are shown as solid red squares (■). Literature data: Fuchs et al. [1] (▲, n=14); McSween [6] (□, n=7); Olsen and Grossman [3] (■, n=1); Jones [7] (●, n=2); Varela et al. [5] (⧫, n=34); Libourel et al. [10] (○, n=4).

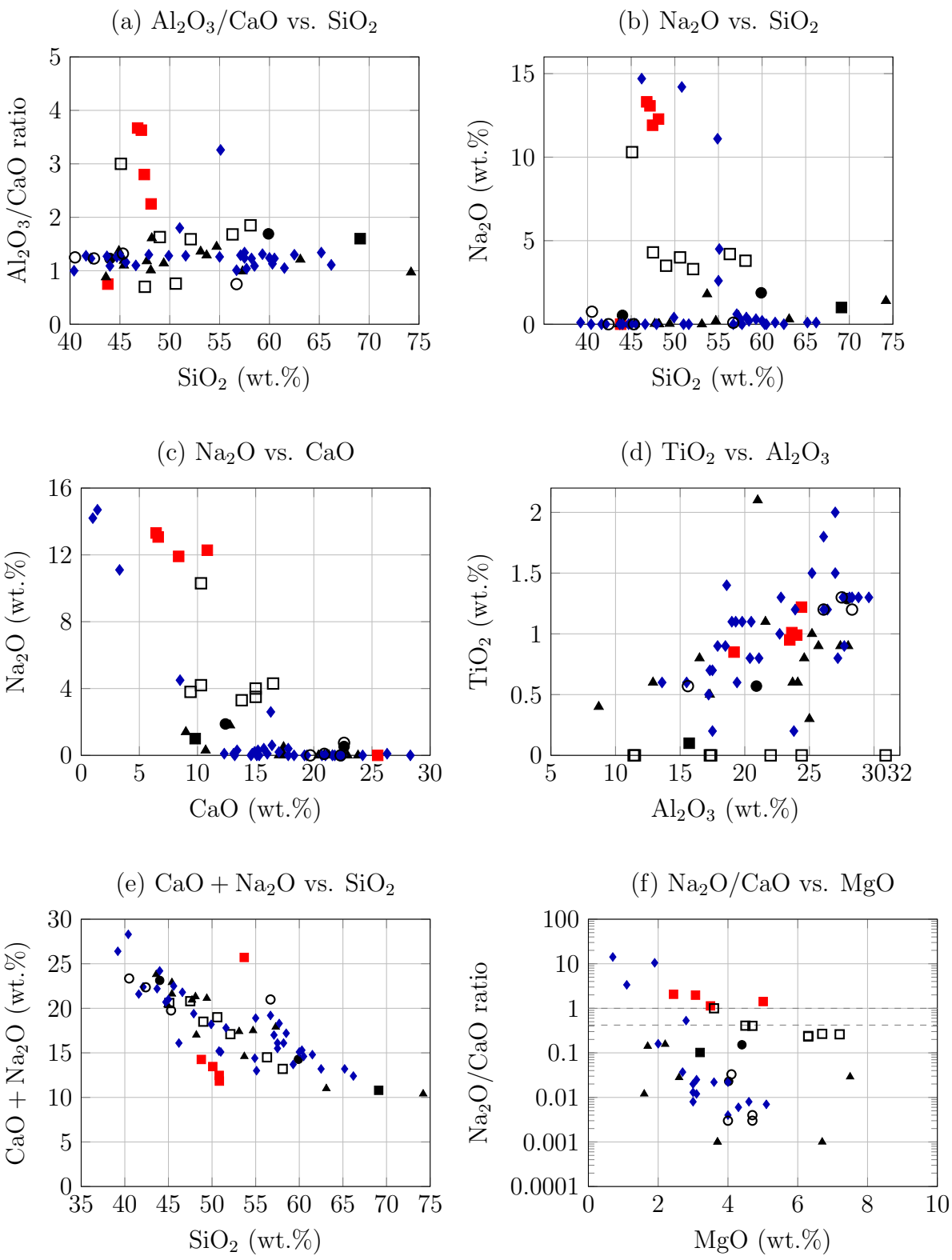

Figure 3.15: Compositional diagrams of MIs in carbonaceous chondrites. All oxides in wt%. Symbols: **Our data** (■); Fuchs et al. [1] (▲); McSween [6] (□); Olsen and Grossman [3] (■); Jones [7] (●); Varela et al. [5] (⧫); Libourel et al. [10] (○).

Table 3.13: Complete electron microprobe analyses (wt.%) of all samples from various studies. Blank cells indicate not analyzed or below detection limit.

Study	Sample	SiO_2	TiO_2	Al_2O_3	Cr_2O_3	FeO	MnO	MgO	CaO	Na_2O	K_2O	P_2O_5	Total
Fuchs et al. (1973) [1]													
	1a	48.20	0.90	27.40	0.20	0.20	0.00	6.70	17.00	0.01	0.00		100.60
	1b	48.10	1.10	21.60	0.10	0.30	0.00	3.60	21.30	0.01	0.00		96.10
	2	45.40	0.90	25.70	0.20	0.20	0.00	4.60	21.60	0.01	0.00		98.60
	3	63.10	0.60	12.90	0.20	7.10	0.10	2.60	10.70	0.30	0.00		97.60
	4a	45.40	1.00	25.20	0.20	0.10	0.00	3.30	22.90	0.00	0.00		98.10
	4b	43.60	2.10	21.00	0.10	0.20	0.03	9.40	23.80	0.00	0.00		100.20
	4c	54.70	0.30	25.00	0.00	0.10	0.00	1.60	17.30	0.20	0.00		99.20
	5	44.90	0.90	28.00	0.20	0.20	0.00	3.80	20.40	0.00	0.00		98.40
	6	53.10	0.60	23.70	0.30	0.20	0.00	4.00	17.40	0.00	0.00		99.30
	7	49.40	0.60	24.10	0.10	0.10	0.00	3.70	21.10	0.03	0.00		99.10
	8	74.20	0.40	8.70	0.20	2.00	0.10	2.20	9.00	1.40	0.20		98.40
	9	57.30	0.50	17.30	0.30	0.10	0.03	7.50	17.40	0.50	0.10		101.00
	10	47.70	0.80	24.60	0.30	0.20	0.03	3.70	20.90	0.03	0.00		98.30
	11	53.70	0.80	16.50	0.03	6.80	0.10	1.70	12.80	1.80	0.40		94.60
Varela et al. (2002) [5]													
	R1	51.0	0.8	27.2	nd	0.5	0.1	3.5	15.1	0.0	nd	0.3	98.5
	R2a	42.1	1.3	27.6	0.3	0.7	0.1	4.8	22.4	nf	nf	0.3	99.6
	R3a	41.6	1.3	27.7	0.3	0.6	nf	4.9	21.6	nf	nf	0.3	98.3
	R4	39.2	1.3	28.8	0.1	0.1	0.1	4.0	26.3	0.1	nd	0.3	100.2
	R5a	44.7	1.8	26.1	0.4	0.9	nd	3.5	20.7	nd	0.0	nd	98.2
	R6a	40.4	1.3	28.3	0.0	0.1	nd	3.9	28.3	0.0	nd	0.2	97.5
	R7a	45.6	1.2	26.1	0.1	0.2	nd	3.9	22.5	nd	nd	0.2	99.7
	R8	45.0	1.5	27.0	nd	0.9	0.0	4.6	21.0	nd	0.1	0.5	100.5
	R9	47.9	1.5	25.2	nd	0.7	0.2	3.4	19.4	nd	0.0	0.3	98.5
	R10	44.0	1.2	26.4	0.2	0.1	0.0	3.3	24.2	nd	nd	nd	99.4
	R11	49.9	1.0	22.7	0.5	1.7	0.2	4.0	17.8	0.4	0.0	nd	98.2
	Acfer1	46.6	1.2	23.9	nd	0.8	nf	4.1	21.8	nf	nd	0.0	98.5
	Acfer3	51.6	1.3	22.8	0.7	1.5	nf	4.2	17.8	nf	nf	0.1	99.9
	Acfer4	43.7	1.3	28.1	0.1	0.7	0.0	3.9	22.2	nf	nf	nf	99.9
	R12	46.2	2.0	27.0	0.1	3.9	nd	1.9	1.4	14.7	2.1	nd	99.2
	R13	50.8	1.3	29.6	0.2	1.6	0.0	0.7	1.0	14.2	0.5	0.0	100.0
	R14	55.1	0.9	27.7	0.6	0.6	nd	2.8	8.5	4.5	0.1	0.1	100.8
	R15a	54.9	0.2	23.8	0.3	2.2	0.1	1.1	3.3	11.1	1.3	0.2	98.5
	R16	55.0	1.1	20.5	0.4	0.5	nd	2.0	16.3	2.6	0.5	0.1	99.1
	R17a	58.5	1.4	18.6	0.5	0.5	0.0	3.1	17.0	0.2	nd	0.3	100.0
	R18	56.7	0.6	19.4	0.2	0.3	0.0	3.2	19.2	0.0	nf	0.2	99.9
	R19	60.5	0.9	17.9	nd	2.5	0.0	3.5	14.6	nf	0.0	0.2	100.1
	R20	60.3	0.7	17.3	0.5	0.7	0.2	3.7	15.3	0.0	0.0	nd	98.6
	R21	61.5	0.6	15.5	nd	1.5	0.2	5.1	14.7	0.1	nd	0.1	99.4
	R22	58.2	1.1	19.3	0.5	1.3	0.1	3.1	15.7	0.4	nd	0.1	99.9
	R23	57.1	0.8	21.1	0.4	0.6	nd	2.7	16.4	0.6	0.2	0.2	100.0
	R24	57.7	1.1	19.0	0.4	0.7	0.2	3.2	18.3	nd	nd	nd	100.5
	R25	59.3	0.7	17.5	0.5	4.1	0.3	3.6	13.4	0.3	0.2	nd	100.0
	R26	62.5	0.5	17.2	0.6	0.6	0.0	3.9	13.2	nd	0.0	nd	98.5
	R27a	57.5	0.8	20.4	0.3	1.1	0.1	3.0	15.2	0.3	nd	nd	98.8
	Acfer2	66.2	0.6	13.6	nd	1.0	0.0	4.6	12.3	0.1	nd	nd	98.3
	Acfer5	57.5	1.1	19.8	0.3	1.1	0.1	4.3	16.0	0.1	nf	nf	100.4
	ED1	60.0	0.9	18.5	0.7	1.3	0.1	3.0	14.9	0.2	0.0	0.2	99.8
	ED2	65.2	0.2	17.5	0.5	0.5	nf	3.0	13.1	0.1	nf	nf	100.1

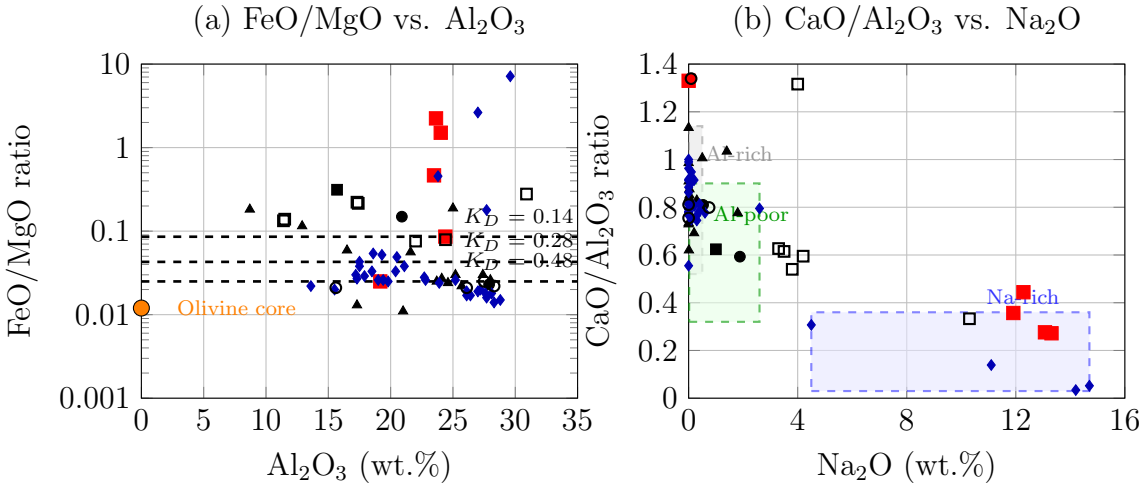

Figure 3.16: Compositional relationships in melt inclusions from chondrules. (a) FeO/MgO ratio versus Al_2O_3 content showing equilibrium relationships with host olivine (dashed lines represent different $K_D^{\text{Fe-Mg}}$ values). (b) CaO/Al_2O_3 ratio versus Na_2O content illustrating the three main compositional groups of melt inclusions. Symbols: **Our data** (■); Fuchs et al. [1] (▲); McSween [6] (□); Olsen and Grossman [3] (■); Jones [7] (●); Varela et al. [5] (⧫); Libourel et al. [10] (○).

Table 3.13: Complete electron microprobe analyses (wt.%) of all samples from various studies (continued).

Study	Sample	SiO_2	TiO_2	Al_2O_3	Cr_2O_3	FeO	MnO	MgO	CaO	Na_2O	K_2O	P_2O_5	Total
Olsen (1978) [3]	Average of n. 8 glasses												
	8gls.	69.10	0.10	15.70	0.10	0.60		3.20	9.80	1.00	0.03		99.60
Jones (1992) [7]													
	high-Si	59.90	0.57	20.90	0.33	0.34	<d.l.	4.40	12.40	1.88	0.04		100.76
	low-Si	44.00	1.29	27.90	0.24	0.30	<d.l.	4.02	22.60	0.53	<d.l.		100.88
McSween (1977) [6]													
	K-1 mes	49.00	<d.l.	24.40	<d.l.	1.00	<d.l.	6.30	15.00	3.50	0.10		99.30
	K-1 incl	52.10	<d.l.	22.00	<d.l.	1.10	<d.l.	6.30	13.80	3.30	0.10		98.70
	K-6 mes	47.50	<d.l.	11.50	<d.l.	11.70	<d.l.	7.20	16.50	4.30	0.10		98.80
	K-6 incl	50.60	<d.l.	11.40	<d.l.	10.70	<d.l.	6.70	15.00	4.00	0.10		98.50
	L-2 mes	56.30	<d.l.	17.30	<d.l.	6.30	<d.l.	4.50	10.30	4.20	0.10		98.90
	L-2 incl	58.10	<d.l.	17.40	<d.l.	5.70	<d.l.	4.70	9.40	3.80	0.10		99.20
	K-3 incl	45.10	<d.l.	30.90	<d.l.	0.20	<d.l.	3.60	10.30	10.30	0.10		100.50
Libourel (2006) [10]													
	ch5	45.30	1.20	26.10	0.46	0.76	<0.07	4.70	19.70	<0.06	<0.04		98.30
	ch5	42.40	1.30	27.50	0.27	0.62	<0.07	4.00	22.30	<0.06	<0.04		98.40
	ch7	56.70	0.57	15.60	0.18	0.15	<0.07	4.70	20.90	0.09	<0.04		98.90
	ch7	40.50	1.20	28.30	0.22	0.34	<0.07	4.10	22.60	0.75	<0.04		98.00

References for Section 3

[1] L. Fuchs, E. Olsen, and K. Jensen (1973). Mineralogy, mineral-chemistry and composition of the Murchison (C2) meteorite. *Smithson. Contrib. Earth Sci.* vol. **10**, 1–39.

[2] E. Roedder *Fluid inclusions*. Vol. 12. Mineralogical Society of America, 1984.

[3] E. Olsen and L. Grossman (1978). On the origin of isolated olivine grains in type 2 carbonaceous chondrites. *Earth and Planetary Science Letters* vol. **41**, 111–127. https://doi.org/https://doi.org/10.1016/0012-821X(78)90001-8.

[4] G. Kurat, M. Varela, P. Hoppe, and R. Clocchiatti (1997). Glass inclusions in Renazzo olivine: condensates from the solar nebula? *Meteoritics & Planetary Science* vol. **32**, A76.

[5] M. Varela, G. Kurat, P. Hoppe, and F. Brandstätter (2002). Chemistry of glass inclusions in olivines of the CR chondrites Renazzo, Acfer 182, and El Djouf 001. *Geochimica et Cosmochimica Acta* vol. **66**, 1663–1679.

[6] H. Y. McSween (1977). On the nature and origin of isolated olivine grains in carbonaceous chondrites. *Geochimica et Cosmochimica Acta* vol. **41**, 411–418. https://doi.org/https://doi.org/10.1016/0016-7037(77)90269-1.

[7] R. Jones (1992). On the relationship between isolated and chondrule olivine grains in the carbonaceous chondrite ALHA77307. *Geochimica et Cosmochimica Acta* vol. **56**, 467–482.

[8] E. Roedder "Significance of Ca-Al-rich silicate melt inclusions in olivine crystals from the Murchison Type II carbonaceous chondrite". In: *Bull. Mineral.* Vol. 104. 1981, 339–353.

[9] É. Tronche, P. Reinhardt, S. Mostefaoui, N. Guilhaumou, and F. Robert (2007). Melt inclusions in olivine crystals from chondrules: New insights from nanoscale concentration profiles in the Semarkona chondrite. *Comptes Rendus Geoscience* vol. **339**, 667–673. https://doi.org/https://doi.org/10.1016/j.crte.2007.08.009.

[10] G. Libourel, A. Krot, and L. Tissandier (2006). Role of gas-melt interaction during chondrule formation. *Earth and Planetary Science Letters* vol. **251**, 232–240.

[11] F. Faure, L. Tissandier, G. Libourel, R. Mathieu, and B. Welsch (2012). Origin of glass inclusions hosted in magnesium porphyritic olivines chondrules: Deciphering planetesimal compositions. *Earth and Planetary Science Letters* vol. **319**, 1–8.

[12] L. Florentin, E. Deloule, F. Faure, and D. Mangin (2018). Chemical 3D-imaging of glass inclusions from allende (CV3) olivine via SIMS: A new insight on chondrule formation conditions. *Geochimica et Cosmochimica Acta* vol. **230**, 83–93. https://doi.org/10.1016/j.gca.2018.03.021.

[13] E. Jacquet, M. Piralla, P. Kersaho, and Y. Marrocchi (2020). Origin of isolated olivine grains in carbonaceous chondrites. *Meteoritics & Planetary Science* vol. **55**, 1–21.

[14] H. C. Connolly Jr and R. H. Hewins (1996). Experimental studies of the formation of compound chondrules. *Meteoritics & Planetary Science* vol. **31**, 47–55.

[15] R. H. Hewins, B. Zanda, and H. C. Connolly (2005). Condensation and experimental petrology of chondrules. *Chondrites and the Protoplanetary Disk* vol. **341**, 619–634.

[16] J. Barosch, D. Hezel, D. Ebel, and P. Friend (2019). Mineralogically zoned chondrules in ordinary chondrites as evidence for open system chondrule behaviour. *Geochimica et Cosmochimica Acta* vol. **249**, 1–16.

[17] L. Tissandier, G. Libourel, and F. Robert (2002). Gas-melt interactions and their bearing on chondrule formation. *Meteoritics & Planetary Science* vol. **37**, 1377–1389.

[18] M. Chaussidon, G. Libourel, and A. N. Krot (2008). Oxygen isotopic constraints on the origin of magnesian chondrules and on the gaseous reservoirs in the early Solar System. *Geochimica et Cosmochimica Acta* vol. **72**, 1924–1938.

[19] G. Libourel, A. N. Krot, and L. Tissandier (2006). Role of gas–melt interaction during chondrule formation. *Earth and Planetary Science Letters* vol. **251**, 232–240.

[20] M. Javoy, E. Balan, M. Méheut, M. Blanchard, and M. Lazzeri (2012). First-principles investigation of equilibrium isotopic fractionation of O- and Si-isotopes between refractory solids and gases in the solar nebula. *Earth and Planetary Science Letters* vol. **319**, 118–127.

[21] A. E. Rubin (2017). Type-1AB chondrules in LL3.0 Semarkona: no need for high partial pressures of $SiO_{(g)}$ in the solar nebula. *48th Lunar Planet. Sci. Conf., #2700, (abstr.)* vol.

[22] L. Grossman (1972). Condensation in the primitive solar nebula. *Geochimica et Cosmochimica Acta* vol. **36**, 597–619. https://doi.org/10.1016/0016-7037(72)90078-6.

This page intentionally left blank.

Chapter 4

A laboratory approach to astrogeological questions.

4.1 Prebiotic potential of carbonaceous chondrites

Abstract. The polymerization of simple organic matter is a key factor in assembling the building blocks of life. However, in a water-rich environment, the condensation of amino acids into peptides is thermodynamically disfavored, a conflict known as the "water paradox". Carbonaceous chondrites, which contain significant amounts of organic compounds, phyllosilicates, and evidence of aqueous alteration processes, provide a compelling geochemical context for investigating this challenge. Here, the catalytic potential of carbonaceous chondrites was investigated in driving glycine oligomerization under two distinct scenarios: wet-dry cycling and impact-induced mechanochemistry. Our preliminary finding demonstrate that carbonaceous chondrites provide significantly better catalytic activity than montmorillonite in facilitating peptide bond formation. These findings suggest that the parent bodies of carbonaceous chondrites represent efficient environments for overcoming the water paradox and promoting the molecular assembly of early prebiotic compounds.

4.1.1 Introduction

The detection of organic matter in meteorites has given rise to a long-standing scientific debate about the origin of life's building blocks. Their history can be described as a continuum of chemical evolution across distinct formation environments, from interstellar space to protoplanetary disk formation, to asteroidal and finally planetary processes, as shown schematically in Figure 4.2. Since the pioneering abiotic-synthesis experiments by Miller and Urey in 1953 [1], decades of research have argued that water–rock interaction is a necessary condition for the formation of complex organic molecules (e.g., [2–4]). Water–rock interaction contributes in several ways: minerals release ions through dissolution, while components such as metallic iron, silicates, and sulfides can act as catalysts. Furthermore, textural characteristics, especially porosity, concentrate reactants and provide sheltered micro-environments [5–7]. Consequently, mineral surfaces, particularly phyllosilicates like montmorillonite, are central to prebiotic chemistry hypotheses.

However, while water is indispensable as a solvent and reagent, its abundance presents a well-known thermodynamic obstacle: the condensation of monomers into polymers (e.g., peptide bonds) is thermodynamically unfavorable in a water-rich environment. This conflict is known as the "water paradox". Overcoming this paradox likely required geochemical scenarios involving periodic wet–dry cycles [4, 8]. Following Bernal's proposal, minerals surfaces promote peptide formation by concentrating amino acids, protecting peptides from hydrolysis, acting as dehydrating agents, and lowering the energy barriers for condensation [5, 9, 10]. These scenarios often consider evolved planetary environments, such as pools, craters, lakes, oceans, and hydrothermal systems [11–13]. However, defining the precise geochemical conditions and the specific combinations of chemical processes that drove the transition from monomers to the building blocks of life remains a key challenge. Therefore,

the comprehensive characterization of these multiple, viable prebiotic systemse is a central theme in modern astrobiological research. Within carbonaceous chondrites, all the previously listed elements that may favour the polymerization of organic matter are observed.

This study investigates the catalytic potential of carbonaceous chondrites as a interesting geochemical environment for complex organic synthesis. Carbonaceous chondritic meteorites are fragments of undifferentiated bodies, characterized by a fine-grained porous matrix, mafic silicates (olivine and pyroxene), metallic alloys (including Fe–Ni), sulfides, and organic matter (e.g [14]). These minerals are highly thermodynamically unstable in aqueous solutions, creating a more favourable chemical environment for the condensation and polymerization of organic matter [6, 15]. Studies of meteoritic evidence report numerous examples of aqueous alteration in such bodies, such as aqueous weathering fronts, iron-enriched rims, transformation of primary anhydrous silicates (olivine, pyroxene) into phyllosilicates, oxidation of sulfides and metals (e.g.[16, 17]).

Phyllosilicate formation is linked to aqueous alteration from melting ice inside the parent body [17, 18]. Asteroids could trap ice that melts due to internal heating, orbital changes, or impacts [19], allowing water to interact with minerals and organic matter before potentially refreezing [20]. Phyllosilicates can retain and later release this water [21], and subsequent impacts can remix material, redistributing water/ice and initiating new hydration-dehydration cycles [22–24]. This sequence of processes in icy planetesimals is schematically represented in Figure 4.2. Therefore, carbonaceous chondrites are investigated as providing a realistic geochemical setting to test prebiotic peptide bond formation. Understanding organic synthesis through wet-dry cycling within this geochemical “cocktail” helps decipher prebiotic chemistry in the early Solar System.

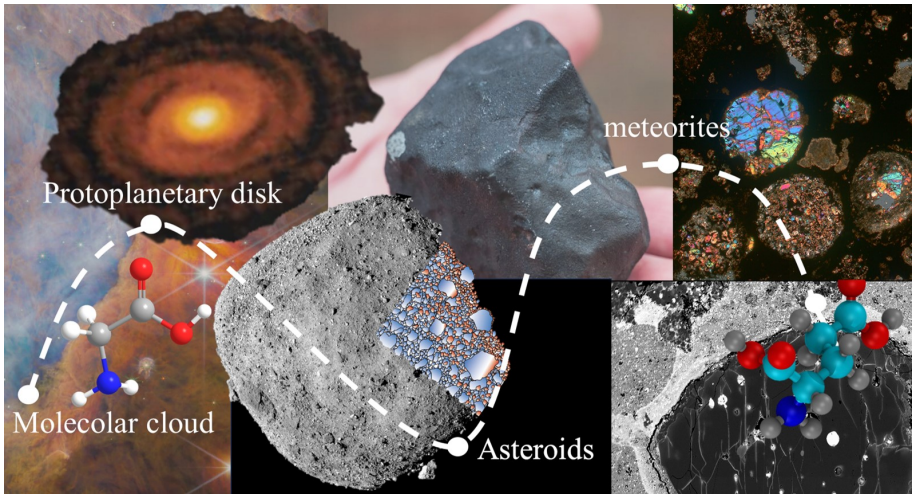

Figure 4.1: Pathway of organic matter: from astronomical to micrometric scales. This schematic illustrates the journey of organic matter, showcasing its formation mechanisms across various scales. The trajectory begins in astronomical contexts, such as interstellar clouds and protoplanetary disks, and progresses to asteroidal processes, specifically impacts and aqueous alteration. Traces of these events are observable at both the macroscale (e.g., via space missions) and the micrometric scale recorded within meteorites.

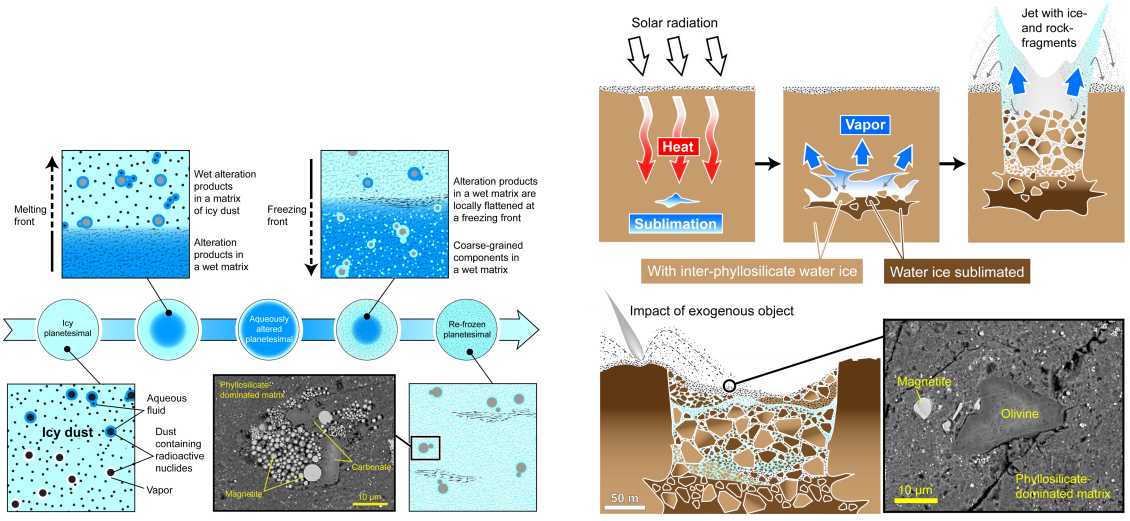

Figure 4.2: (Left) Micro-scale aqueous environment within a primitive icy planetesimal, where interstitial water ice undergoes melting and re-freezing cycles, leading to the formation of secondary phases. (Right) Macro-scale scheme illustrating how solar irradiation and impact processing drive ice sublimation and the mixing of hydrated and anhydrous materials within a planetesimal. Schematics from Ota et al. (2023) [20].

This research investigates the prebiotic synthesis of oligoglycine on carbonaceous chondrites, examining the role of wet-dry cycles and mechanochemistry. It directly compares their performance against montmorillonite. The oligomerization of glycine was tested using diverse carbonaceous chondrite samples under two distinct prebiotic scenarios: 1) wet-dry cycles and 2) mechanochemical activation due to impact events. Following this introduction, the methodology is detailed, the key results of the comparative experiments are presented, and the findings are discussed in terms of the implications for the role of carbonaceous chondrite materials in prebiotic chemistry.

4.1.2 Materials and methods

Meteorite samples

Meteorite samples investigated in this study were provided by the Museo Nazionale dell'Antartide (MNA), Siena, Italy. All procedures involving sample handling and preparation were conducted following strict contamination-control protocols, with complete documentation maintained throughout all experimental stages. Meteorites were manipulated exclusively using powder-free gloves and stainless-steel laboratory tools. All selected samples belong to the class of carbonaceous chondrites and are summarized in Table 4.1. The investigated set includes two CV chondrites (DAG 533, DAG 521), one CO chondrite (FRO 99040), and one CM chondrite (RKP 17075). In addition, three samples from a private collection were employed exclusively in preliminary experiments aimed at optimizing experimental conditions: NWA 16768 (CV3), NWA 11545 (CV3), and NWA 11085 (CO3).

Sample preparation

Meteorite samples were gently powdered using an agate mortar and pestle in order to minimize contamination (Fig. 4.3). For each sample, an aliquot of powdered

Table 4.1: Inventory of carbonaceous chondrites used in this study.

Sample	Classification	Source	Material Form	Mass (mg)
MNA Collection				
FRO 99040	CO3	MNA	Powder	90
RKP 17075	CM1	MNA	Powder	90
DAG 533	CV3	MNA	Powder	90
DAG 521	CV3	MNA	Powder	60
Private Collection				
NWA 16768	CV3	Private	Powder	90
NWA 11545	CV3	Private	Powder, chips, raw	Various
NWA 11085	CO3	Private	Powder	50

material was reserved for mineralogical characterization by X-ray powder diffraction (XRPD). The remaining material was weighed using an analytical balance and stored in aluminum foil until use. All preparation tools were thoroughly cleaned with acetone between samples to avoid cross-contamination.

Each powdered meteorite was subjected to wet–dry cycling experiments, mechanochemical treatments, or both. For each sample, two aliquots were selected: one untreated and one subjected to solvent processing and pyrolysis following the procedure described by Saladino et al. [25]. The resulting products were subsequently analyzed by chromatographic and spectrometric techniques.

To evaluate the influence of textural properties on experimental outcomes, chips, coarse powder, and fine powder from sample NWA 11545 were tested independently. This approach allowed direct comparison between experiments performed on intact material and homogenized powders.

Figure 4.3: Grinding process of meteorite samples.

Mineralogical and petrological characterization

XRPD analyses were performed at the X-ray Diffraction Laboratory of the Department of Physical Sciences, Earth and Environment (DSFTA), University of Siena with Dr. Andrea Scala. Diffraction patterns were collected using a Philips X'Pert PRO PW 3050 diffractometer operating in Bragg–Brentano geometry, with Cu Kα radiation (40 kV, 30 mA). Data were acquired over the 3°–80° 2θ range. Samples were mounted on silicon zero-background holders to maximize the signal-to-noise ratio, particularly for limited material quantities. The mineralogical phases identified by XRD analysis for the respective meteorite samples are summarized in Table 4.2. Representative thin sections, as shown in Figure 4.4, illustrate the typical petrographic context of these meteorites.

Scanning electron microscopy (SEM) analyses were conducted on polished petrographic thin sections at the Department of Life Sciences, University of Siena (San Miniato, Italy). Imaging and energy-dispersive X-ray spectroscopy (EDS) analyses were performed using a FEI Quanta 400 environmental scanning electron microscope operating at an accelerating voltage of 20 kV and equipped with an EDS detector. Samples were carbon-coated prior to analysis to ensure adequate surface conductivity. Back-scattered electron (BSE) images, exemplified in Figure 4.5, were acquired to

Table 4.2: Meteorite sample information and identified mineral phases

Sample Name	**Class**	**Identified Minerals**
FRO 9940	CO3	Forsterite; Olivine; Clinoenstatite; Clinopyroxene
RKP 17075	CM1	Fayalite; Lyzardite; Antigorite; Cronstedtite; Pyrrhotite
DAG 533	CV3	Forsterite; Olivine; Clinoenstatite; Magnetite
DAG 521	CV3	Not analyzed
NWA XXX	CV3	Forsterite; Clinoenstatite
NWA 11545	CV3	Forsterite; Olivine; Clinoenstatite; Hematite
Pyr.	CV3	Forsterite; Fayalite; Clinoenstatite
Pyr. + solv.	CV3	Forsterite; Fayalite; Clinoenstatite
NWA 11085	CO3	Forsterite; Olivine; Enstatite; Clinoenstatite; Magnetite; Chromite

*T*he table lists the official meteorite names and their petrological classifications. The abbreviation *Pyr.* indicates samples that underwent pyrolysis treatment to investigate whether the organic matter removal process also affects the mineralogical composition. *Pyr. + solv.* refers to samples subjected to combined pyrolysis and solvent extraction. The minerals listed in the right column were identified from diffraction peaks obtained by X-ray diffraction analysis.

highlight compositional contrasts between mineral phases, reflecting variations in average atomic number.

The heterogeneous texture, characterized by chondrules embedded within a fine-grained matrix (Fig. 4.4), constitutes an interesting interfacial region. This mineralogical heterogeneity offers a wide range of catalytic surfaces and redox couples capable of driving prebiotic chemistry in the presence of water. In contrast to the CV3 and CO3 samples, which are dominated by primary anhydrous silicates (forsterite, clinoenstatite) and oxides (magnetite, chromite) and represent less aqueously altered, more pristine materials, the detection of secondary serpentine-group minerals (lizardite, antigorite) and cronstedtite in the CM1 meteorite RKP 17075 (Table 4.2) confirms extensive low-temperature aqueous alteration on its parent body. This alteration process is visually suggested by the greenish phases in thin section (Fig. 4.4). Moreover, the presence of metallic Fe–Ni phases and sulphides, clearly visible and dispersed in the BSE image (Fig. 4.5), is particularly significant. These phases are potent reductants that could drive chemical reactions relevant to astrobiology when interacting with aqueous fluids.

These preliminary results describe the rationale underlying our astrobiological experiments, although further studies will be necessary to fully unravel the detailed mechanisms linking specific mineralogical assemblages to the observed catalytic activity.

Reagents and organic compounds

All reagents were of analytical grade and used without further purification. Glycine (GLY, 98.0%), 2,5-piperazinedione (DKP, 99%), glycylglycine (Gly_2, $\geq$ 99%), glycylglycylglycine (Gly_3, $\geq$ 99%), 1,8-dihydroxynaphthalene (DHN, 95.0%), horseradish peroxidase (HRP, 15 U mL^{-1}), hydrogen peroxide ($\geq$ 30%), montmorillonite K-10, and sodium 1-pentanesulfonate were purchased from Sigma-Aldrich. Potassium

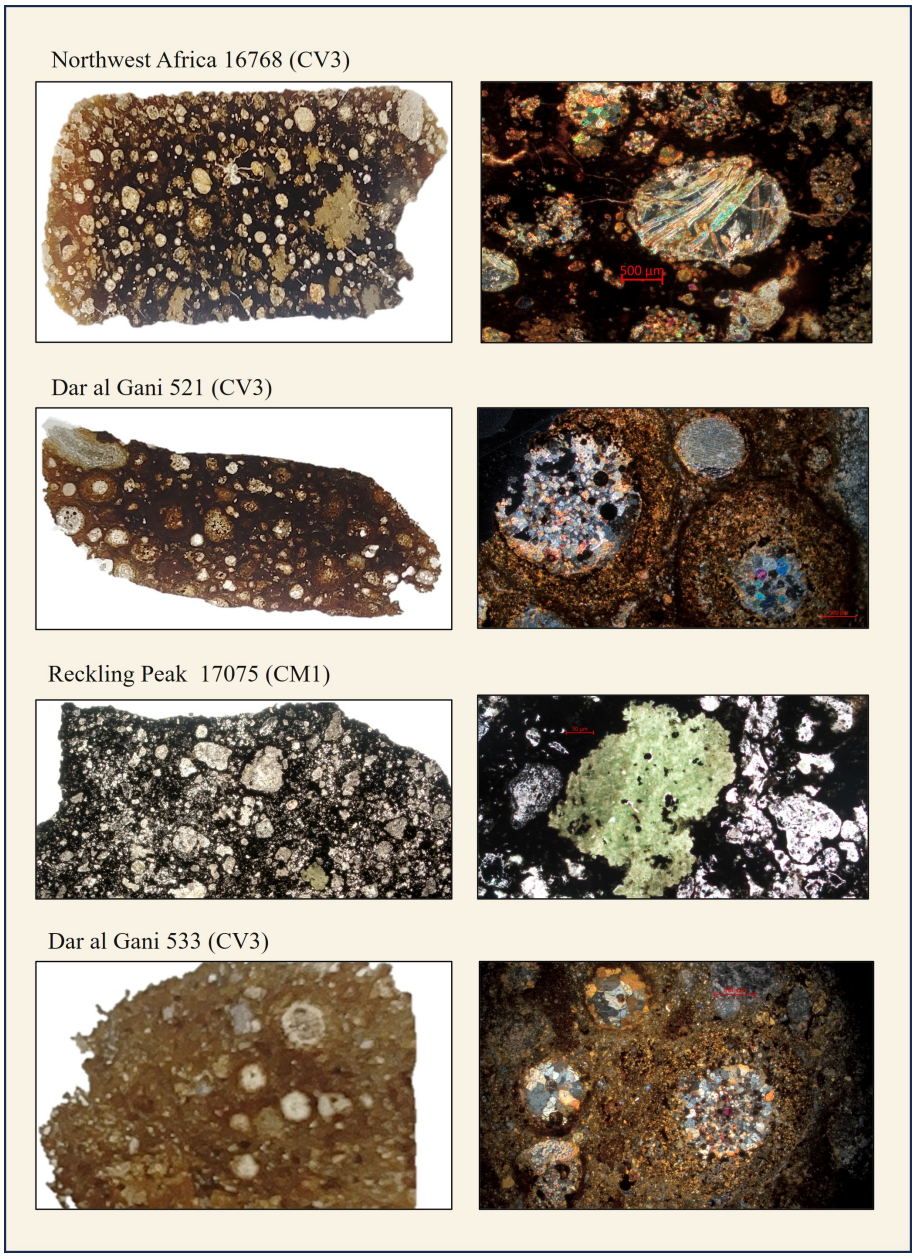

Figure 4.4: Exemplifying photomicrographs in transmitted light of thin sections from meteorites used in the experiments. The characteristic chondritic texture is heterogeneous, comprising chondrules and a fine-grained matrix, with distinct dust accretionary rims. The interface between the chondrules and the matrix fosters a significant mineralogical diversity, providing varied substrates for reactions involving water, minerals, and organic compounds. Of particular note is the green mineral in the RKP 17075 sample likely consisting of serpentine-group minerals.

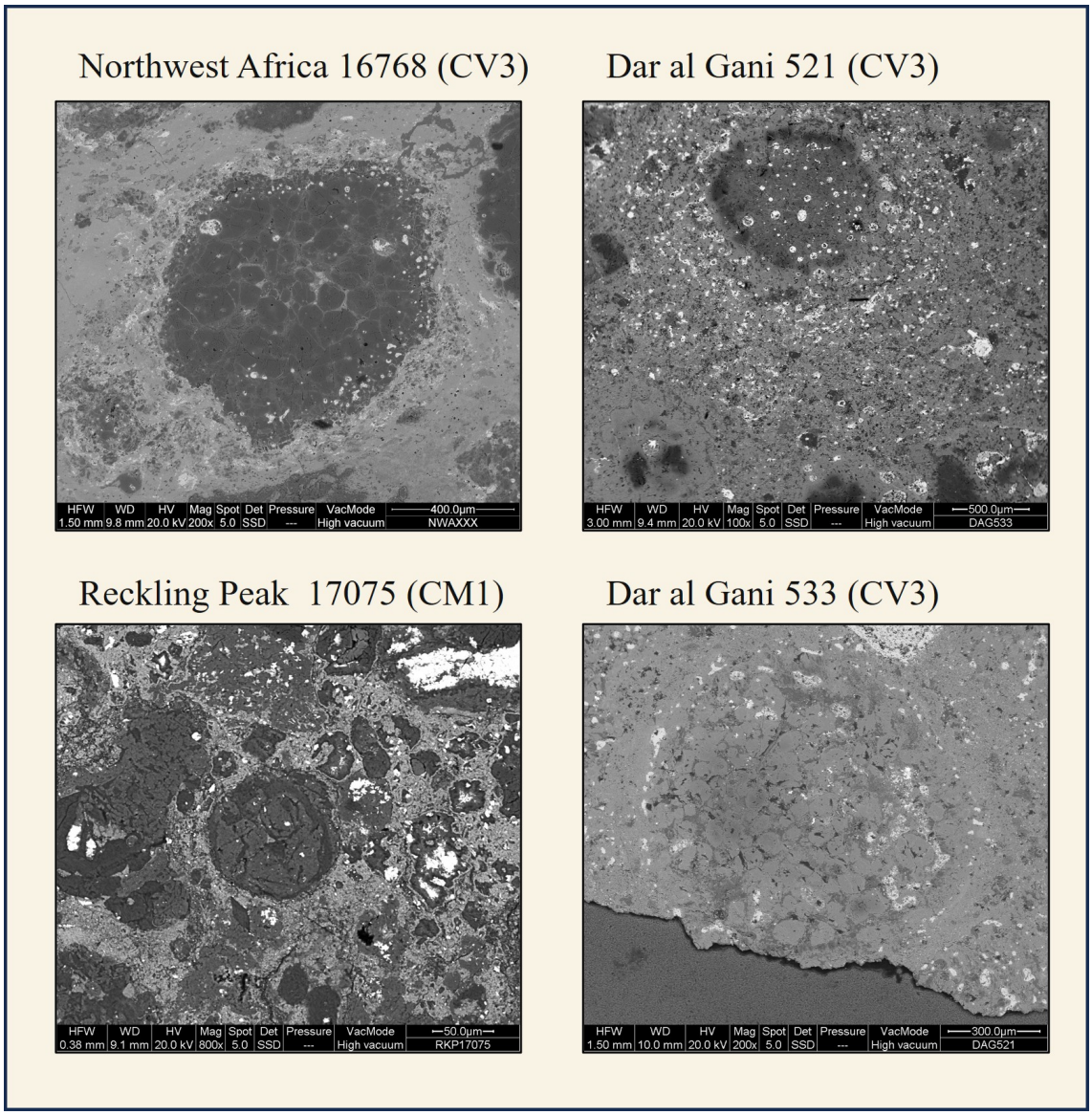

Figure 4.5: Backscattered electron (BSE) image of a meteoritic sample, detailing the textural context. The distribution of metallic and sulphide phases is clearly resolved, appearing both within the chondrules and encircling their peripheries. This image further accentuates the complex interface between chondrules and the surrounding matrix, a place of mineralogical heterogeneity which facilitates a range of potential geochemical interactions relevant to aqueous alteration and organic-inorganic reactions.

dihydrogen phosphate (99.5%) and calcium chloride (granular, 92%) were purchased from Carlo Erba. PolyDHN was synthesized enzymatically following an established procedure. Briefly, 200 mg of DHN was dissolved in methanol and suspended in 125 mL of 0.1 M phosphate buffer (pH 7). HRP (11.5 mg) and 150 μL of H_2O_2 were added under vigorous stirring and the reaction was allowed to proceed for 24 h. The mixture was acidified to pH 3, centrifuged (7000 rpm, 10 min, 4°C), washed, and lyophilized, yielding 136 mg of polyDHN.

Wet–Dry cycling experiments

Wet–dry experiments were performed by mixing 10 mL of 0.1 M glycine solution with 10 mg of catalyst (polyDHN + montmorillonite K-10 or polyDHN + powdered meteorite). Control experiments without catalyst were conducted under identical conditions. Samples were heated until complete evaporation of water, stored at room temperature for 10 min, and subsequently rehydrated with 10 mL of water. This cycle was repeated for a predefined number of iterations. After the final cycle, 4 mL of 0.1 M $CaCl_2$ solution was added to promote oligopeptide release [26]. Samples were sonicated, stirred for 2 h, and centrifuged. The supernatant was analyzed by ion-pairing high-performance liquid chromatography (IP-HPLC), while the solid residue was characterized by mass spectrometry.

Mechanochemical experiments

Mechanochemical reactions were conducted using a Fritsch Pulverisette 23 vibratory mill. Glycine (37.5 mg) was mixed with 5 mg of meteorite powder and processed for 7 h at the maximum oscillation frequency (50 Hz). Experiments were carried out for selected meteorite samples. After milling, residues were cooled to room temperature and treated with 2 mL of 0.1 M $CaCl_2$. Following sonication and stirring for 2 h, samples were centrifuged and analyzed by IP-HPLC and MALDI-MS.

Analytical techniques

IP-HPLC analyses were performed using Agilent 1100 and Shimadzu SPD 10AV systems (Figure 4.6) equipped with UV–Vis detectors and a Phenomenex Sphereclone ODS column (250 × 4.6 mm, 5 μm). Calibration was achieved using authentic standards (glycine, DKP, Gly_2, Gly_3).MALDI-MS analyses were conducted on a Sciex 4800 MALDI ToF/ToF instrument using 2,5-dihydroxybenzoic acid as matrix. Spectra were acquired in positive reflectron mode over the m/z 100–4000 range (laser frequency: 4500 Hz), accumulating 1000 laser shots per spectrum. UV–Vis and ATR–FTIR spectra were recorded using Jasco V-730 spectrophotometer and Nicolet 5700 spectrometer (in transmission mode, scanning the 400–4000 cm^{-1} range at a resolution of 4 cm^{-1}), respectively.

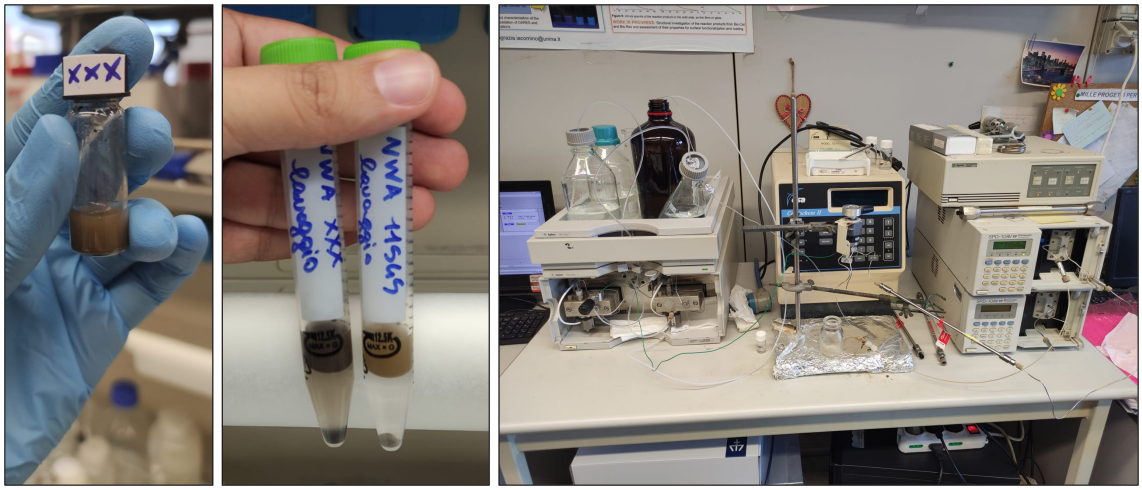

Figure 4.6: The IP-HPLC apparatus (Agilent 1100 and/or Shimadzu SPD 10AV) employed for the separation and quantification of glycine, DKP, and oligopeptides.

4.1.3 Results

The catalytic activity of carbonaceous chondrites in glycine oligomerization was investigated under two distinct prebiotically plausible conditions: wet-dry cycling and mechanochemistry. As shown in Fig. 4.7, during wet-dry cycling, a progressive

darkening of the glycine-meteorite solution was observed over successive wet-dry cycles, with the colour changing from brown to dark brown.

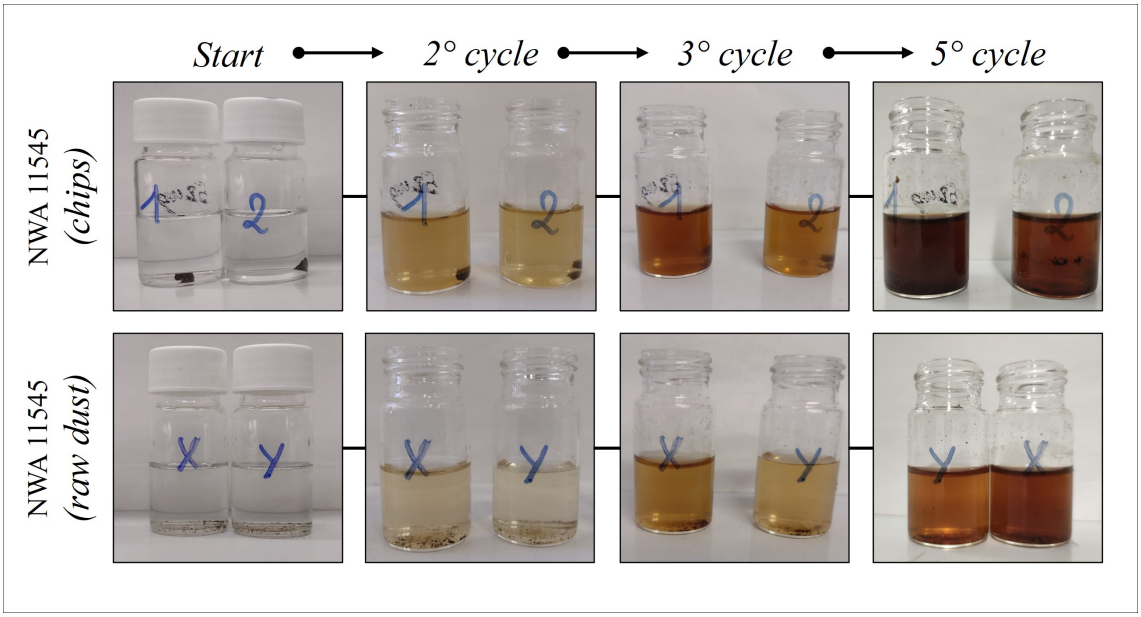

Figure 4.7: Photographic sequence of wet-dry cycling experiments performed on sample NWA 11545. Panels show the physical evolution of the sample (prepared as millimeter-sized chips and unground powder) during successive hydration (left) and desiccation (right) phases.

Initial control experiments established the baseline for glycine oligomerization under wet-dry cycling conditions (150 °C, 14 cycles, 24 hours). As shown in Table 4.3, glycine alone yielded 69 ± 8% unreacted starting material, with diketopiperazine (DKP) as the primary oligomerization product (0.56 ± 0.08%). The addition of montmorillonite or polyDHN as reference catalysts resulted in complete consumption of glycine and significantly increased DKP yields to 3.22 ± 0.01% and 2.89 ± 0.41%, respectively. Analysis of solid residues by MALDI-MS showed that the longest oligomers, up to GLY11, formed with polyDHN, while montmorillonite and glycine alone produced oligomers up to GLY7 and GLY5, respectively.

Under identical wet-dry cycling conditions, all five meteorite samples tested

catalyzed glycine oligomerization (Table 4.4). The CV3 chondrites NWA11545, NWA16768, and DAG533 exhibited the most efficient glycine consumption, with residual glycine concentrations of 9.39 ± 0.69%, 12.11 ± 0.81%, and 17.2 ± 0.5%, respectively. In contrast, the CM1 and CO3 chondrites RKP17075 and FRO99040 showed higher residual glycine levels of 64 ± 3% and 65 ± 2%. The CV3 chondrites also produced the highest yields of GLY3, particularly NWA16768 (1.42 ± 0.11%) and DAG533 (0.90 ± 0.09%). MALDI-MS analysis detected oligomers up to GLY12 in the solid residue from NWA11545, while the other meteorites produced oligomers up to GLY9-GLY10.

Table 4.3: Control experiments: Analysis of glycine oligomers formed under wet-dry cycling.

IP-HPLC Analysis (Supernatant)			(%, mol/mol)[a]
	Glycine	**Glycine + montmorillonite**	**Glycine + polyDHN**
GLY	69 ± 8	n.d.	n.d.
DKP	0.56 ± 0.08	3.22 ± 0.01	2.89 ± 0.41
GLY2	0.05 ± 0.01	0.17 ± 0.02	0.21 ± 0.05
GLY3	0.70 ± 0.02	0.90 ± 0.04	1.14 ± 0.11
MALDI-MS Analysis (Solid Residue)			(% w/w)[b]
Solid yield	32.3 ± 0.9	22.8 ± 0.8	23.5 ± 0.8
Max. oligomer	GLY5	GLY7	GLY11

[a]Yields expressed as molar percent (mol of product per 100 mol of initial glycine). n.d. = not detected.
[b]Yields expressed as weight percent (mass of solid residue per 100 g of initial material).
Experimental conditions: 150 °C, 14 cycles, 24 hours. Each experiment was run in triplicate and data are reported as average ± SD.

In mechanochemical experiments (50 oscillations per second, 7 hours), the meteorites demonstrated different catalytic profiles (Table 4.5). NWA11545 dust showed the highest residual glycine level (45.5 ± 3.2%), while the other samples exhibited more substantial glycine consumption, with residual levels between 11.0 ± 0.9% and 15.7 ± 1.6%. DKP yields were generally lower than in wet-dry experiments, ranging

Table 4.4: Meteorite experiments: Analysis of glycine oligomers formed under wet-dry cycling.

IP-HPLC Analysis (Supernatant)					(%, mol/mol)[a]
	NWA11545 (CV3)	**NWA16768 (CV3)**	**DAG533 (CV3)**	**RKP17075 (CM1)**	**FRO99040 (CO3)**
GLY	9.39 ± 0.69	12.11 ± 0.81	17.2 ± 0.5	64 ± 3	65 ± 2
DKP	0.78 ± 0.05	0.43 ± 0.01	0.50 ± 0.01	0.42 ± 0.03	0.49 ± 0.03
GLY2	0.32 ± 0.04	0.34 ± 0.05	0.50 ± 0.02	0.36 ± 0.01	0.42 ± 0.02
GLY3	0.67 ± 0.07	1.42 ± 0.11	0.90 ± 0.09	0.92 ± 0.07	1.01 ± 0.08
MALDI-MS Analysis (Solid Residue)					(% w/w)[b]
Solid yield	26.6 ± 2.7	26.2 ± 1.9	29.6 ± 3.1	23.6 ± 2.8	24.6 ± 2.4
Max. oligomer	GLY12	GLY10	GLY9	GLY9	GLY9

[a]Yields expressed as molar percent (mol of product per 100 mol of initial glycine).
[b]Yields expressed as weight percent (mass of solid residue per 100 g of initial material).
Experimental conditions: 150 °C, 14 cycles, 24 hours. Each experiment was run in triplicate and data are reported as average ± SD.

from 0.04 ± 0.01% to 0.24 ± 0.03%. Analysis of the solid residues from DAG533, RKP17075, and FRO99040 revealed oligomer formation up to GLY11, GLY9, and GLY9, respectively, with corresponding solid yields of 11.1 ± 2.5%, 6.82 ± 2.7%, and 9.88 ± 3.4%.

4.1.4 Discussion

This study tests the hypothesis that phyllosilicate minerals, abundant in many carbonaceous chondrites, act as primary drivers of prebiotic organic polymerization. Contrary to this expectation, the results reveal the opposite: the most effective catalysts for glycine oligomerization are meteorites characterized by low phyllosilicate content. For instance, the CV3 chondrites (NWA 11545, NWA 16768, DAG 533) demonstrate superior catalytic performance under wet-dry cycling conditions (Table 4.4), consuming 83–91% of initial glycine and producing oligomers up to GLY12.

Table 4.5: Mechanochemistry experiments: Analysis of glycine oligomers formed under ball milling conditions.

IP-HPLC Analysis (Supernatant)					(%, mol/mol)[a]
	NWA11545 (CV3)	**NWA16768 (CV3)**	**DAG533 (CV3)**	**RKP17075 (CM1)**	**FRO99040 (CO3)**
GLY	45.5 ± 3.2	15.7 ± 1.6	13.1 ± 1.1	11.0 ± 0.9	12.9 ± 0.7
DKP	0.24 ± 0.03	0.04 ± 0.01	0.12 ± 0.02	0.05 ± 0.01	0.11 ± 0.02
GLY2	0.23 ± 0.03	0.17 ± 0.01	0.13 ± 0.02	0.07 ± 0.01	0.10 ± 0.02
GLY3	0.14 ± 0.03	0.13 ± 0.01	0.20 ± 0.03	0.10 ± 0.02	0.17 ± 0.01
MALDI-MS Analysis (Solid Residue)					(% w/w)[b]
Solid yield			11.1 ± 2.5	6.82 ± 2.7	9.88 ± 3.4
Max. oligomer			GLY11	GLY9	GLY9

[a]Yields expressed as molar percent (mol of product per 100 mol of initial glycine).
[b]Yields expressed as weight percent (mass of solid residue per 100 g of initial material).
Experimental conditions: 50 oscillations per second, 7 hours. Each experiment was run in triplicate and data are reported as average ± SD. n.d. = not determined.

In contrast, the phyllosilicate-rich CM1 chondrite (RKP 17075) shows significantly lower reactivity, leaving 64% of glycine unconsumed and producing oligomers only up to GLY9.

A progressive darkening of the glycine–meteorite solution was observed during wet–dry cycling, evolving from light brown to dark brown over successive cycles. In atmospheric chemistry, similar browning is attributed to the formation of light-absorbing "humic-like" and "fulvic-like" oligomers, commonly referred to as brown carbon (BrC). This process involves the condensation and oxidation of simple organic precursors, a transformation frequently catalysed by mineral dust surfaces, particularly those containing redox-active metals such as Fe, Ni, or Mn [27–30]. It is therefore proposed that glycine undergoes surface-mediated polymerisation, forming complex macromolecules with extended conjugated chromophores that absorb strongly in the visible range. An analogous mechanism is highly plausible in the

present experiments. The meteorite dust provides reactive mineral surfaces that can catalyse the oligomerisation of glycine, leading to the formation of brown carbon-type products. Although the meteoritic material contains reduced metals and sulfides, and wet–dry cycling could promote the formation of iron oxidation products (e.g., Fe_2O_3, FeOOH), their contribution to colour could be likely minor compared to that of the organic chromophores. Consequently, the most probable origin of the darkening is the heterogeneous catalytic formation of organic oligomers, analogous to atmospheric brown carbon. This optically derived hypothesis is tested and supported by the chemical analyses presented in the following section.

The comparative analysis between montmorillonite and carbonaceous chondrites reveals distinct catalytic profiles. Montmorillonite demonstrates exceptional efficiency in glycine consumption, achieving complete conversion (Table 4.3) and significantly outperforming all chondrites, which leave substantial residual glycine (9–65%; Table 4.4). In contrast, for oligomerization capability, the CV3 chondrites NWA 11545 and NWA 16768 surpass montmorillonite, producing longer peptide chains (GLY12 and GLY10, respectively) compared to GLY7 with montmorillonite. This suggests that while montmorillonite excels at initial activation and consumption of glycine, certain chondrites possess superior capability for promoting extended peptide chain growth, indicating complementary rather than uniformly superior catalytic mechanisms.

The CO3 chondrite FRO 99040 retains 65% of unconsumed glycine, a value comparable to the CM1 sample RKP 17075. However, the CO3 chondrite produces slightly higher yields of GLY3 ($1.01 \pm 0.08\%$ versus $0.92 \pm 0.07\%$) than the CM1. The similarly low catalytic efficiency between the phyllosilicate-rich CM1 and the CO3 chondrite is notable and requires explanation. One potential justification is their shared Antarctic provenance, which suggests that post-recovery terrestrial alteration might influence catalytic activity more than intrinsic mineralogical differences.

Although all samples were pyrolyzed before experiments to eliminate native organic matter and terrestrial contamination, other alteration pathways, such as changes in the oxidation state of iron, could affect reactivity.

Notably, the exceptional catalytic activity of the CV3 chondrites strongly coincides with the presence of Fe^{3+} from hematite (α-Fe_2O_3). As suggested by Mazzaro [31], the proposed mechanism involves hematite functioning as a potent Lewis acid catalyst, efficiently activating carbonyl groups and facilitating peptide bond formation through condensation reactions. This mechanism provides a more robust explanation for the observations than phyllosilicate-mediated catalysis alone, particularly given the enhanced formation of longer oligomers (up to GLY12) in the presence of these Fe^{3+}-rich phases, as evidenced by MALDI-MS analysis (Table 4.4). This could explain the higher efficacy of CV3 compared to CM1 chondrites. Therefore, attributing the catalytic differences solely to the total available iron content may be insufficient. A more nuanced factor than mere abundance is likely at play. The initial iron oxidation state is also an unlikely sole explanation, as all iron phases (metal, Fe_3O_4 (magnetite), or Fe_2O_3 (hematite)) were likely fully oxidized during the wet-dry experiments. Instead, the reactivity and accessibility of the iron from specific host minerals may be the critical factor. To verify this, detailed mineralogical microanalysis of the post-reaction solid residues is essential.

Mechanochemistry experiments (Table 4.5) reveal substantial glycine consumption across all meteorites, with residual glycine levels ranging from 11.0% to 45.5%. Notably, NWA 11545 shows the highest residual glycine (45.5 ± 3.2%) despite being among the most effective catalysts in wet-dry cycling, suggesting different catalytic mechanisms operate under mechanical activation. DAG 533 produces the longest oligomers (GLY11) and shows the highest solid yield (11.1 ± 2.5%) among samples with measured solid residues in mechanochemistry. NWA 16768 achieves the

most efficient glycine consumption (15.7 ± 1.6% residual) among CV3 samples. In contrast, the CM1 and CO3 chondrites (RKP 17075 and FRO 99040) show limited oligomerization capacity in mechanochemistry, producing only up to GLY9 with solid yields of 6.82 ± 2.7% and 9.88 ± 3.4%, respectively.

The maximum oligomer length in mechanochemistry reaches only GLY11 compared to GLY12 in wet-dry cycling. Moreover, soluble oligomer yields in mechanochemistry are substantially lower than in wet-dry experiments, with DKP yields of 0.04–0.24% versus 0.42–0.78% in wet-dry experiments. These differences suggest that while mechanical energy efficiently promotes glycine consumption, it favors different reaction pathways, possibly due to the absence of solvent-mediated reorganization and thermal cycling which may limit progression to longer peptide chains. Accordingly, the lower solid yields in mechanochemistry (6.82–11.1%) versus wet-dry cycling (23.6–29.6%) further support weaker polymerization efficiency in the mechanical method. This reduction could stem from material loss on the steel milling support or from fundamentally less efficient polymerization under dry conditions. Despite these differences, mechanical activation significantly enhances glycine consumption for CM1 and CO3 chondrites and maintains the catalytic efficiency hierarchy observed in wet-dry experiments: CV3 > CO3 > CM1. This consistency across different reaction conditions strengthens the hypothesis that intrinsic mineral properties, rather than the specific activation method, determine catalytic performance.

The persistence of CV3 superiority across both experimental approaches reinforces the conclusion that phyllosilicate content alone cannot explain catalytic efficiency. The unique mineral assemblage of CV3 chondrites provides exceptional catalytic properties for prebiotic peptide synthesis under various environmental conditions.

Limitations of this study should be acknowledged. The sample set, while diverse, represents only a fraction of carbonaceous chondrite varieties. Furthermore, the

complex interplay between different mineral phases within chondrites matrix makes definitive assignment of catalytic activity to specific components challenging. Future work should address these constraints through multiple approaches: (1) correlated, post wt-dry cycles, SEM-FIB-TEM analyses to precisely characterize mineral-organic interfaces in experimentally altered materials, particularly focusing on spatial relationships between iron or iron-oxides and oligomer products; (2) experiments conducted under reducing (or inert) atmosphere or vacuum; and (3) systematic variation of the water-to-mineral mass ratio to optimize the hydration-dehydration cycles that drive condensation reactions.

4.1.5 Conclusion

Our findings show the prebiotic catalytic potential of carbonaceous chondrites for the oligomerization of simple life's building block. Experimental investigation under both wet-dry cycling and mechanochemical conditions reveals that CV3 chondrites (NWA 11545, NWA 16768, DAG 533) consistently exhibit superior performance, consuming 83–91% of initial glycine and facilitating oligomer formation up to GLY12. In contrast, CM1 and CO3 chondrites show significantly lower reactivity. This finding presents an apparent paradox: the most catalytically active chondrites in these experiments are those with lower phyllosilicate content, whereas the most extensively aqueously altered, phyllosilicate-rich CI chondrites in the literature contain the most complex soluble organic matter.

We suggest that the pristine mineral assemblage of less-altered chondrites—containing phases susceptible to aqueous alteration such as fayalite and metal blebs—acts as a potent source of Lewis acidic catalysts (e.g., Fe^{3+}) during the initial alteration stages. This would make parent bodies represented by CV3 chondrites active sites for the synthesis of complex organic molecules. Conversely, extensively altered CI chondrites,

while organically rich, may represent the end product of this process, having largely exhausted their reactive mineral reservoirs and thus their catalytic potential for further synthesis. Furthermore, the mechanochemical experiments demonstrate that energetic processing, analogous to impact events during accretion, serves as a viable alternative pathway for oligomerization.

While consistent with our data, the model has limitations. Our sample set doesn't cover all chondrite varieties, the CO3 chondrite's catalytic role is unclear. Future work employing correlated micro-analytical techniques (e.g., FIB-TEM) on post-experiment residues is necessary to directly characterize the mineral-organic interfaces and test the hypothesized mechanisms.

In summary, carbonaceous chondrites emerge as highly effective catalysts for prebiotic peptide synthesis, outperforming standard phyllosilicate catalysts like montmorillonite in promoting extended chain growth. Their catalytic potential appears intrinsically linked to a dynamic petrological history, where accretion, aqueous alteration, and associated geochemical evolution create a transient, reactive environment uniquely conducive to organic synthesis in the early Solar System.

References for Section 4

[1] S. L. Miller and H. C. Urey (1959). Organic Compound Synthesis on the Primitive Earth. *Science* vol. **130**, 245–251. https://doi.org/10.1126/science.130.3370.245.

[2] P. Ehrenfreund, S. Rasmussen, J. Cleaves, and L. Chen (2006). Experimentally tracing the key steps in the origin of life: The aromatic world. *Astrobiology* vol. **6**, 490–520. https://doi.org/10.1089/ast.2006.6.490.

[3] C. S. Cockell *Astrobiology: Understanding Life in the Universe*. 2nd. Wiley Blackwell, 2020.

[4] S. Fox, H. L. Pleyer, and H. Strasdeit (2019). An automated apparatus for the simulation of prebiotic wet–dry cycles under strictly anaerobic conditions. *International Journal of Astrobiology* vol. **18**, 60–72. https://doi.org/10.1017/S1473550417000441.

[5] J. D. Bernal (1949). The Physical Basis of Life. *Proceedings of the Physical Society. Section A* vol. **62**, 537. https://doi.org/10.1088/0370-1298/62/9/301.

[6] F. S. Brigiano, M. Gierada, F. Tielens, and F. Pietrucci (2022). Mechanism and Free-Energy Landscape of Peptide Bond Formation at the Silica–Water Interface. *ACS Catalysis* vol. **12**, 2821–2830. https://doi.org/10.1021/acscatal.1c05635.

[7] K. Marshall-Bowman, S. Ohara, D. A. Sverjensky, R. M. Hazen, and H. J. Cleaves (2010). Catalytic peptide hydrolysis by mineral surfaces. *Geochimica et Cosmochimica Acta* vol. **74**, 5852–5861. https://doi.org/10.1016/j.gca.2010.07.017.

[8] T. D. Campbell, R. Febrian, J. T. McCarthy, H. E. Kleinschmidt, J. G. Forsythe, and P. J. Bracher (2019). Prebiotic condensation through wet–dry cycling regulated by deliquescence. *Nature Communications* vol. **10**, 4508. https://doi.org/10.1038/s41467-019-12515-9.

[9] J. D. Bernal *The physical basis of life*. Routledge and Paul, 1951.

[10] A. Rimola, M. Sodupe, and P. Ugliengo (2007). Aluminosilicate surfaces as promoters for peptide bond formation: an assessment of Bernal's hypothesis by ab initio methods. *Journal of the American Chemical Society* vol. **129**, 8333–8344.

[11] J. Greenwald, M. P. Friedmann, and R. Riek (2016). Amyloid Aggregates Arise from Amino Acid Condensations under Prebiotic Conditions. *Angewandte Chemie International Edition* vol. **55**, 11609–11613. https://doi.org/10.1002/anie.201605321.

[12] M. Rodriguez-Garcia, A. Surman, G. Cooper, et al. (2015). Formation of oligopeptides in high yield under simple programmable conditions. *Nature Communications* vol. **6**, 8385. https://doi.org/10.1038/ncomms9385.

[13] T. Stolar, S. Grubešić, N. Cindro, E. Meštrović, K. Užarević, and J. G. Hernández (2021). Mechanochemical Prebiotic Peptide Bond Formation. *Angewandte Chemie International Edition* vol. **60**, 12727–12731. https://doi.org/10.1002/anie.202102045.

[14] E. R. D. Scott (2007). Chondrites and the Protoplanetary Disk. *Annual Review of Earth and Planetary Sciences* vol. **35**, 577–620. https://doi.org/10.1146/annurev.earth.35.031306.140100.

[15] A. Rimola, P. Ugliengo, and M. Sodupe (2009). Formation versus Hydrolysis of the Peptide Bond from a Quantum-mechanical Viewpoint: The Role of Mineral Surfaces and Implications for the Origin of Life. *International Journal of Molecular Sciences* vol. **10**, 746–760. https://doi.org/10.3390/ijms10020746.

[16] A. Rubin, J. Trigo-Rodríguez, H. Huber, and J. Wasson (2007). Progressive alteration of CM carbonaceous chondrites. *Geochimica et Cosmochimica Acta* vol. **71**, 2361–2382. https://doi.org/10.1016/j.gca.2007.02.008.

[17] M. D. Suttle, A. J. King, P. F. Schofield, H. Bates, and S. S. Russell (2021). The aqueous alteration of CM chondrites, a review. *Geochimica et Cosmochimica Acta* vol. **299**, 219–256. https://doi.org/10.1016/j.gca.2021.02.001.

[18] A. Brearley, R. Jones, and J. Papike (1998). Planetary materials. *Reviews in Mineralogy and Geochemistry* vol. **36**, 3–1.

[19] C. O. Chandler, C. A. Trujillo, and H. H. Hsieh (2021). Recurrent Activity from Active Asteroid (248370) 2005 QN173: A Main-belt Comet. *The Astrophysical Journal Letters* vol. **922**, L8. https://doi.org/10.3847/2041-8213/ac365b.

[20] T. Ota, C. Potiszil, K. Kobayashi, R. Tanaka, H. Kitagawa, T. Kunihiro, C. Sakaguchi, M. Yamanaka, and E. Nakamura (2023). The Formation of a Rubble Pile

Asteroid: Insights from the Asteroid Ryugu. *Universe* vol. **9**. https://doi.org/10.3390/universe9060293.

[21] R. C. Greenwood and I. A. Franchi (2004). Alteration and metamorphism of CO3 chondrites: Evidence from oxygen and carbon isotopes. *Meteoritics & Planetary Science* vol. **39**, 1823–1838. https://doi.org/10.1111/j.1945-5100.2004.tb00078.x.

[22] R. D. Hanna, R. A. Ketcham, M. Zolensky, and W. M. Behr (2015). Impact-induced brittle deformation, porosity loss, and aqueous alteration in the Murchison CM chondrite. *Geochimica et Cosmochimica Acta* vol. **171**, 256–282. https://doi.org/10.1016/j.gca.2015.09.005.

[23] C. Potiszil, M. Yamanaka, C. Sakaguchi, T. Ota, H. Kitagawa, T. Kunihiro, R. Tanaka, K. Kobayashi, and E. Nakamura (2023). Organic Matter in the Asteroid Ryugu: What We Know So Far. *Life* vol. **13**. https://doi.org/10.3390/life13071448.

[24] T. Iizuka, T. Shibuya, T. Hayakawa, T. Yokoyama, I. Gautam, M. K. Haba, K. T. M. Ito, Y. Hibiya, A. Yamaguchi, Y. Abe, J. Aléon, C. M. O. Alexander, S. Amari, Y. Amelin, K.-i. Bajo, M. Bizzarro, A. Bouvier, R. W. Carlson, M. Chaussidon, B.-G. Choi, N. Dauphas, A. M. Davis, T. Di Rocco, W. Fujiya, R. Fukai, H. Hidaka, H. Homma, G. R. Huss, T. R. Ireland, A. Ishikawa, S. Itoh, N. Kawasaki, N. T. Kita, K. Kitajima, T. Kleine, S. Komatani, A. N. Krot, M.-C. Liu, Y. Masuda, K. Motomura, F. Moynier, K. Nagashima, I. Nakai, A. Nguyen, L. Nittler, A. Pack, C. Park, L. Piani, L. Qin, S. Russell, N. Sakamoto, M. Schönbächler, L. Tafla, H. Tang, K. Terada, Y. Terada, T. Usui, S. Wada, M. Wadhwa, R. J. Walker, K. Yamashita, Q.-Z. Yin, S. Yoneda, H. Yui, A.-C. Zhang, T. Nakamura, H. Naraoka, T. Noguchi, R. Okazaki, K. Sakamoto, H. Yabuta, M. Abe, A. Miyazaki, A. Nakato, M. Nishimura, T. Okada, T. Yada, K. Yogata, S. Nakazawa, T. Saiki, S. Tanaka, F. Terui, Y. Tsuda, S.-i. Watanabe, M. Yoshikawa, S. Tachibana, and H. Yurimoto (2025). Late fluid flow in a primitive asteroid revealed by Lu–Hf isotopes in Ryugu. *Nature* vol. **646**, 62–67. https://doi.org/10.1038/s41586-025-09483-0.

[25] R. Saladino, E. Carota, G. Botta, M. Kapralov, G. N. Timoshenko, A. Y. Rozanov, E. Krasavin, and E. D. Mauro (2015). Meteorite-catalyzed syntheses of nucleosides and of other prebiotic compounds from formamide under proton irradiation. *Proceedings of the National Academy of Sciences* vol. **112**, E2746–E2755. https://doi.org/10.1073/pnas.1422225112.

[26] J. Bujdák and B. M. Rode (1999). Silica, Alumina and Clay Catalyzed Peptide Bond Formation: Enhanced Efficiency of Alumina Catalyst. *Origins of Life and Evolution of the Biosphere* vol. **29**, 451–461. https://doi.org/10.1023/A:1006524703513.

[27] B. Nozière, P. Dziedzic, and A. Córdova (2007). Formation of secondary light-absorbing "fulvic-like" oligomers: A common process in aqueous and ionic atmospheric particles? *Geophysical Research Letters* vol. **34**. https://doi.org/https://doi.org/10.1029/2007GL031300.

[28] M. H. Powelson, B. M. Espelien, L. N. Hawkins, M. M. Galloway, and D. O. De Haan (2014). Brown carbon formation by aqueous-phase carbonyl compound reactions with amines and ammonium sulfate. *Environmental Science & Technology* vol. **48**, 985–993. https://doi.org/10.1021/es4038325.

[29] D. O. De Haan, K. Jansen, A. D. Rynaski, W. R. P. Sueme, A. K. Torkelson, E. T. Czer, A. K. Kim, M. A. Rafla, A. C. De Haan, and M. A. Tolbert (2020). Brown Carbon Production by Aqueous-Phase Interactions of Glyoxal and SO_2.

Environmental Science & Technology vol. **54**, 4781–4789. https://doi.org/10.1021/acs.est.9b07852.

[30] U. Pöschl (2003). Aerosol particle analysis: challenges and progress. *Analytical and Bioanalytical Chemistry* vol. **375**, 30–32. https://doi.org/10.1007/s00216-002-1611-5.

[31] V. Mazzaro "Polymeric PAHs as Mediators for Prebiotic Processes on the Early Earth". PhD thesis. University of Naples Federico II, 2023.

4.2 VF-Smelt: Vacuum Furnace for Space Melts

4.2.1 Experimental Apparatus

A new high temperature furnace-vacuum system for space melt (VF-Smelt) was built in-house using a Carbolite Gero tube furnace. A schematic of the overall system is shown in Fig. 4.9. The system is built around a Carbolite Gero TF1 16-60-180 tube furnace, with a 60 mm work tube and silicon carbide heating elements (maximum power output of 2.5 kW). The maximum operating temperature is 1600 °C, with a 100 mm uniform hot zone (±5 °C) located within the 180 mm heated length. The support structure was assembled from Bosch Rexroth aluminium strut profiles (4 x 5 mm, Robert Bosch GmbH, Stuttgart, Germany). A 30 × 10 × 30 cm Al block was machined to form the prechamber and pressure connection. The vacuum system, comprising a Pirani KP370NT gauge with a piezoresistive sensor and a vacuum pump, is connected to the prechamber via a 60 mm in diameter flexible high-vacuum hose. The samples are contained within graphite crucibles (the fabrication of which is illustrated in Fig. 4.8), which are themselves nested inside a platinum crucible (capacity: two samples). This crucible assembly is introduced through the prechamber, lowered into the hot zone, and secured at the "hot stop" position by a platinum wire. The Al flexible hose and the smaller Al_2O_3 tube (60/8 mm ID, respectively) enable more effective and rapid vacuum generation.

A dedicated air inlet line, comprising a precision metering valve and a porous diffusion stone, allows for a safely controlled return to atmospheric pressure following high-temperature vacuum experiments. The Al_2O_3 tube could be vertically adjusted (up to 600 mm) using quick-release screws on the Bosch profile, enabling precise sample positioning at the furnace hot spot. Two vents on the top of the Al_2O_3 tube dissipated heat during high-temperature runs. Thermal ramps were controlled via PC software Eurotherm iTools (Eurotherm, UK) with an EPC3016P1 controller. Temperature

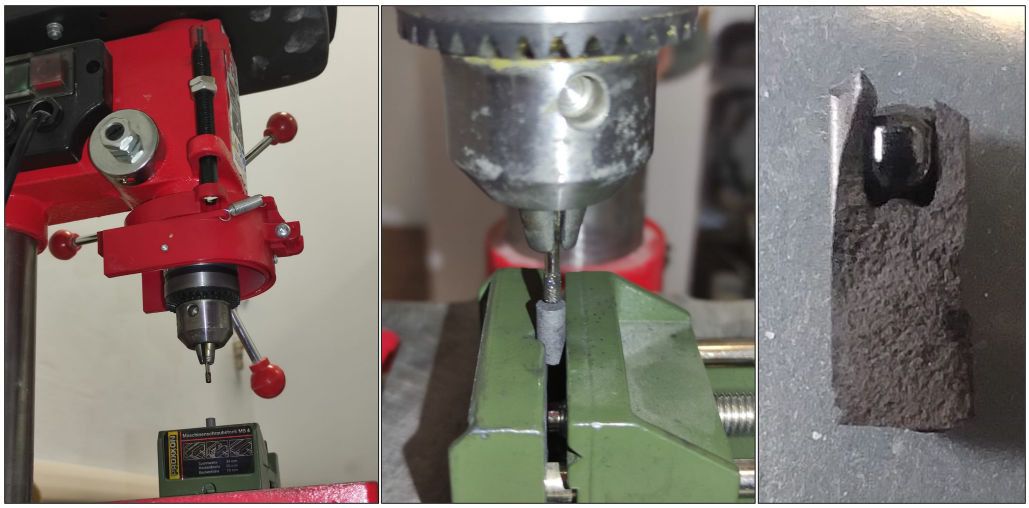

Figure 4.8: This sequence illustrates the in-house production of graphite crucibles using ultra-pure graphite rods drilled with a vertical bench drill. Shown on the right is a cross-section of a crucible containing a glass product synthesized during the experiments.

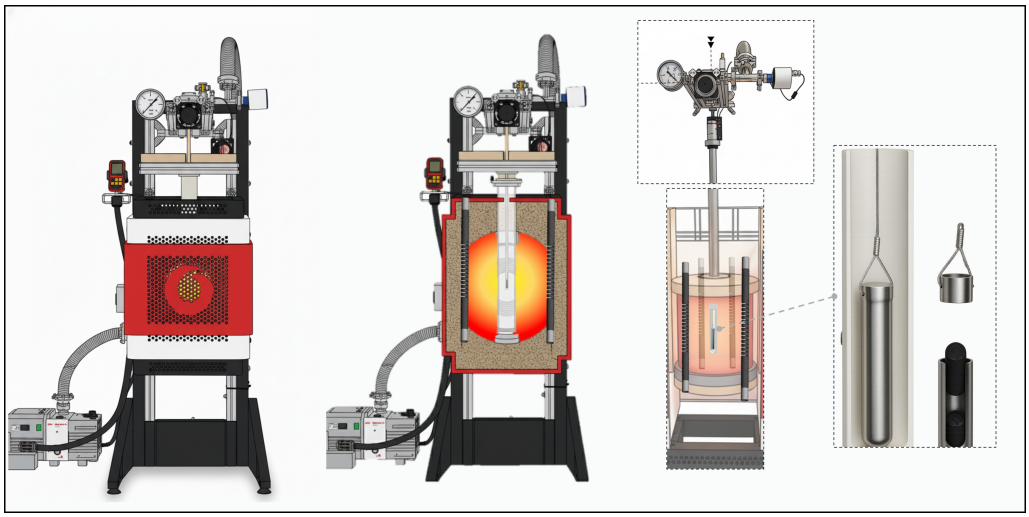

Figure 4.9: Schematic diagram of the VF-Smelt furnace. The illustration shows the Carbolite Gero furnace body, prechamber block, and high-vacuum components (Al_2O_3 vertical tube, Pirani KP370NT gauge, and pump). A cross-sectional detail of the furnace core illustrates the silicon carbide heating elements. A close-up of the prechamber highlights its connection to the alumina tube and the vacuum gauge. Finally a close-up of sample loading.

measurements were performed using a type S thermocouple ($Pt/Pt_{90}Rh_{10}$) positioned at the hot spot. The temperature at the hot spot, measured by the thermocouple, exhibited a deviation of approximately -36 °C from the temperature regulated by the controller. The maximum achievable heating rate, the faster cooling rate (upon power cut-off), and the target 1000 °C/h cooling rate were determined experimentally from thermocouple measurements. The resulting temperature-time profiles are presented in Figure 4.10. The slight non-linear trajectory observed is attributed to the thermal inertia and retained heat within the furnace column.

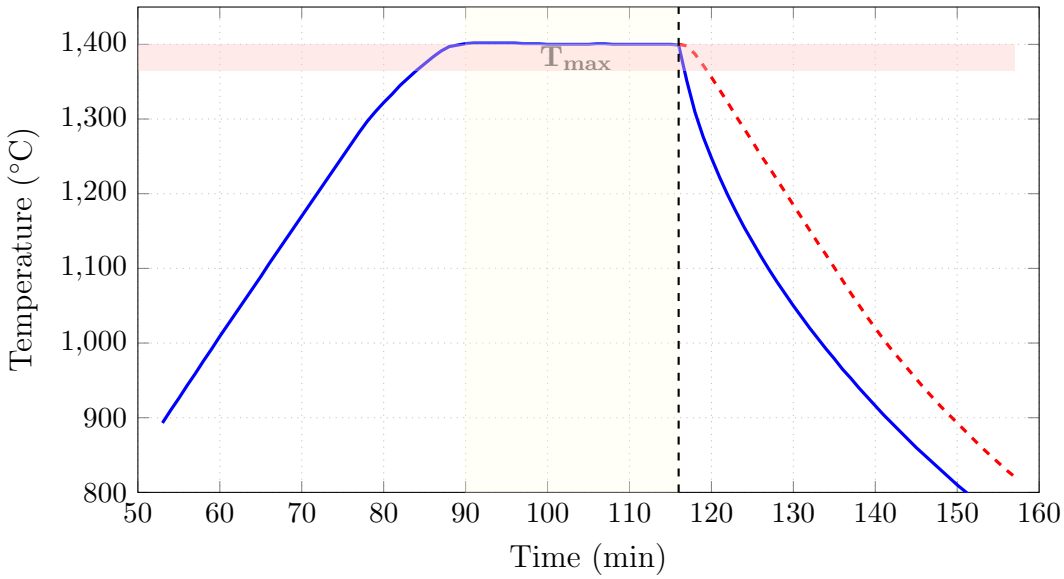

Figure 4.10: Temperature-time profiles for two vacuum experiments showing identical heating (1000 °C/h) and dwell (30 min, 1400 °C) phases. Blue line: furnace quench. Red dashed line: 1000 °C/h cooling. The red shaded band indicates the T_{max} range (1364–1400°C).

4.2.2 The aims of experimental petrology laboratory

The experimental petrology laboratory is dedicated to experimental studies of crystallization in vacuum, conducted on both natural rock samples and laboratory-synthesized glasses. Earth is a planetary forge with an astonishing diversity of

magmas and lavas. However, explorations beyond our planet reveal that other worlds, in their unique way, forge igneous rocks. Many of these worlds lack an atmosphere where lavas cool and crystallize in the vacuum of space (Figure 4.11). Petrological experiments conducted under vacuum or near-vacuum conditions are indispensable to decoding and constraining the igneous processes in airless and low-pressure planetary environments.

(i) Calcium–aluminum-rich inclusions (CAIs) and chondrules formed in the earliest stages of solar system evolution, under extremely low total pressures ($< 10^{-4}$ bar) [1–3]. To constrain their origin, experiments that reproduce the conditions are necessary for quantifying evaporation kinetics, isotopic fractionation, and melt textures under such nebular conditions for modeling these cosmochemical processes [4–9].

(ii) Impact melts originate when a high-velocity impactor strikes a planetary body, generating extreme temperatures that melt and vaporize both the impactor and target rocks. As the resulting vapor plume expands and cools, molten droplets condense and solidify into glassy or crystallized spherules. The size and chemical characteristics of these spherules depend on factors such as impactor size, velocity, target lithology, planetary atmosphere, and vapor plume dynamics [10, 11]. Impact glasses, such as tektites found on Earth, record these factors and can also form on other rocky bodies, as evidenced by glassy spherules on the Moon (e.g., [12, 13]) or Mars (e.g., [14, 15]). Glasses formed in airless conditions, however, are expected to have different chemical signatures from those formed on bodies with atmospheres. This prediction can be tested experimentally and then verified by measuring actual lunar samples or martian samples [14]. Similarly, micrometeorites also experience short-lived melting events during atmospheric entry on planets with atmospheres, recording information about atmosphere composition [16–18]. Vacuum and low-pressure experiments are therefore useful to constrain the oxygen fugacity or elements devolatilization that occur under these specific conditions [19].

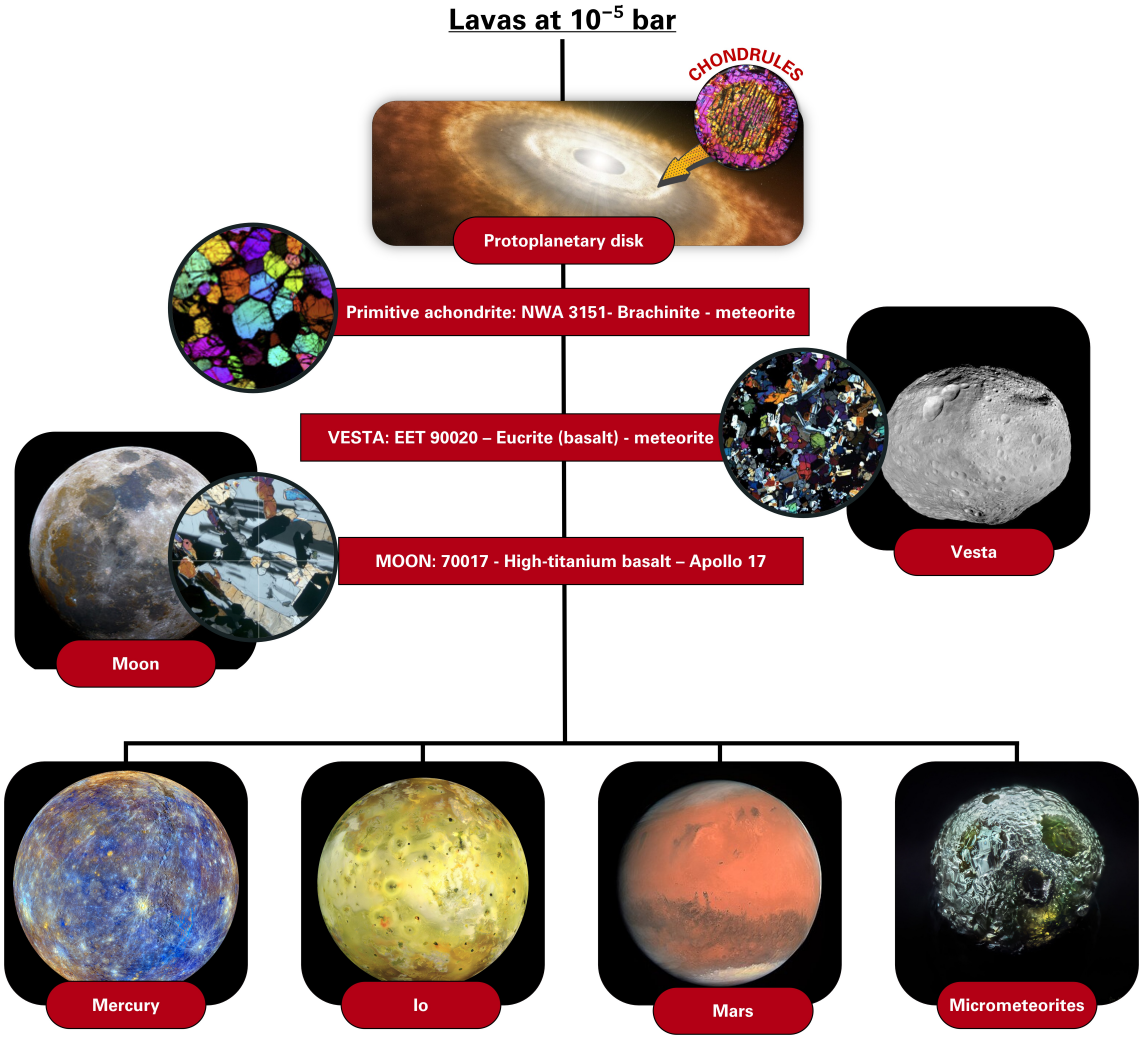

Figure 4.11: Crystallization of lavas in the vacuum of space, a common process on planetary bodies without a significant atmosphere.

(iii) For early planetesimals and planets, such as 4 Vesta, the interaction between a magma ocean and tenuous atmosphere was a key process, governing volatile outgassing, atmospheric formation, and the chemical and isotopic signatures of planetary surfaces [20–23].

(iv) Investigating lava flows on bodies without dense atmospheres, such as the Moon, Mercury, Mars and Io, is useful for interpreting orbital and lander data. In these environments, lava loses heat primarily through radiation rather than convection. This dominant radiative cooling process profoundly affects lava morphology, vesiculation, and eruptive dynamics (e.g., [24]). Furthermore, small volatile concentrations can drive explosive volcanism under vacuum due to the lack of an atmosphere, even minor amounts of volatiles have the potential to cause explosive eruptions in lunar mafic magmas as they approach the surface [25]. The ubiquitous presence of volcanic materials solidified under vacuum across Solar System bodies makes the experimental investigation of magma cooling under such conditions a relevant topic in planetary igneous petrology.

(v) Finally, characterizing silicate melts under vacuum has direct applications for space exploration and technology. In-Situ Resource Utilization (ISRU) is a main topic of space exploration and consist on the practice of leveraging local materials for space missions. Recent designed ISRU techniques include the 3D printing of lunar regolith for construction and the extraction of resources such as water and metals from moon rock [26, 27].

4.2.3 Applications

FIRST: THE JOURNEY OF A BASALT IN VACUUM

The first question I wanted to investigate was to experiment with different cooling rates on chondrule formation. Before investigating typical chondrule compositions,

we began experimenting with the B100 composition of Icelandic basalts, to compare the data obtained in vacuum with previously studied at ambient pressure in previous work [28].

Starting materials.

Natural Iceland basalt (B_{100}) was used as the starting material (the same of [28]). The rock was crushed and then melted in air at 1600 °C for 4 hours in platinum crucibles. The resulting melt was quenched by pouring it onto a cold metal plate to form a glass. To ensure chemical homogeneity, the glass was subsequently crushed and re-melted under identical conditions (1600 °C for 4 hours in air), followed by a second quenching step. The resulting glass was finely ground into a homogeneous powder using a steel ball mill. For sample containment, ultrapure graphite rods were machined into cylindrical crucibles measuring approximately 7 mm in height. A central cavity with a 4 mm inner diameter and 5 mm depth was drilled into each cylinder using a vertical axial drill press. The basaltic glass powder was loaded into these graphite containers and compacted using steel tools. Finally, the graphite capsule assembly was placed within a platinum crucible, preparing the sample for furnace experiments. After vacuum experiments, the recovered run products are typically spheroidal due to the silicate melt's high surface tension and poor wettability on graphite crucibles, as shown in Figure 4.12.

Experimental strategy and techniques.

The experimental strategy was designed to investigate nucleation and crystallization behavior by employing different cooling rate. The experimental strategy investigated nucleation and crystallization by varying the cooling rate under vacuum conditions. A reference experiment (R0) was conducted at atmospheric pressure with a peak temperature of 1600 °C. A series of experiments in vacuum were conducted where B_{100} glass was heated from ambient temperature to a peak temperature of

1400 °C at a rate of 1000 °C/h, held at T_{max} for a specified dwell time, and then cooled to room temperature at various linear cooling rates. All experiments were performed at a constant pressure of approximately 7×10^{-5} bar. **Runs R1 and R2** employed a rapid quench with a 30-minute dwell to assess reproducibility. **Runs R3** quench with dwell times of 10 minutes, to study the effects of dwell time on volatile loss. **Runs R5 and R6** applied slower SSLC rates of 100 and 10 °C/h, respectively, to systematically study crystallization kinetics. Analyses on glass or residual glass in wt% were performed by using a JEOL JXA - iHP200F Hyper Probe at the Institute of Earth System Sciences (IESW), Leibniz University of Hannover (DE).

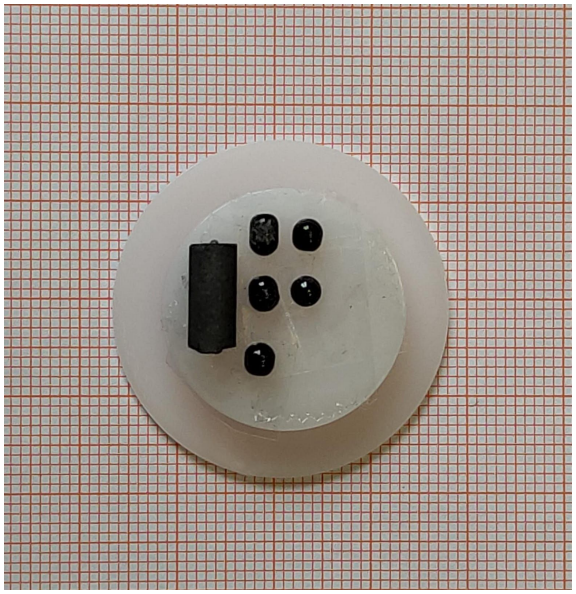

Figure 4.12: Graphite crucible and post run products mounted on the support for resin embedding. Millimeter paper in the background serves as scale.

Preliminary results.

The chemical composition of the glasses produced from the B_{100} is summarised in Table 4.6. Comparison of the Na_2O content in the vacuum runs R1–R4 (1.67 ± 0.17 wt%, 1.82 ± 0.07 wt%, 1.04 ± 0.65 wt%, and 1.49 ± 0.13 wt%, respectively) with that at atmospheric pressure R0 (1.81 ± 0.05 wt%) shows no statistically significant sodium

loss. Additionally, varying the dwell time at the peak temperature from 10 minutes (R3) to 30 minutes (R2) does not yield a significant difference in the final Na_2O content when the analytical uncertainty is considered. The variations in major oxide contents across all experiments are shown in Figure 4.13. General BSE views of the post-run products from all experiments are shown in Figure 4.14

Table 4.6: Chemical composition in wt% of glasses and residual glasses.

Sample	**SiO_2**	**TiO_2**	**Al_2O_3**	**FeO**	**MnO**	**MgO**	**CaO**	**Na_2O**	**K_2O**	**Cr_2O_3**
R0	47.68	0.95	15.63	9.70	0.13	9.51	13.04	1.81	0.06	0.05
	0.40	0.03	0.15	0.11	0.02	0.09	0.08	0.05	0.01	0.02
R1	46.89	0.96	15.23	10.89	0.13	9.89	13.34	1.67	0.06	0.06
	0.44	0.04	0.20	0.36	0.03	0.12	0.14	0.17	0.01	0.02
R2	46.82	0.94	15.24	10.81	0.14	9.82	13.27	1.82	0.05	0.05
	0.33	0.04	0.13	0.28	0.03	0.11	0.08	0.07	0.01	0.02
R3	47.41	0.96	15.46	11.00	0.14	9.86	13.33	1.04	0.07	0.06
	0.71	0.04	0.28	0.27	0.04	0.11	0.10	0.65	0.02	0.02
R4	47.62	0.97	15.47	10.32	0.15	9.84	13.35	1.49	0.05	0.05
	0.66	0.03	0.21	0.43	0.03	0.08	0.16	0.13	0.01	0.02
R5	53.71	1.10	17.74	0.71	0.13	10.98	15.20	0.85	0.04	0.03
	0.66	0.06	0.61	0.64	0.03	0.80	0.46	0.21	0.01	0.02

Note: All compositions in wt% (averages of 20 microprobe points; small font values are 1σ standard errors). R0: starting glass (Pt crucible, air, 1600°C). Runs R1–R5 conducted at 10^{-5} bar and 1400°C: R1 (30 min, quench); R2 (30 min, quench); R3 (10 min, quench); R4 (30 min, 1000 °C/h); R5 (40 min, 100 °C/h).

Experiments cooled at 1000 °C/h show bulk glass FeO contents that are not significantly different (Table 4.6). However, backscattered electron imaging reveals the onset of onset of metallic iron (Fe^0) exsolution (Fig. 4.15), suggesting that the process initiates locally but does not progress sufficiently to measurably change the average composition of the residual glass. A markedly different result is observed for the slowly cooled run R5 (100 °C/h). In this sample, the FeO content of the glass drops dramatically to 0.71 ± 0.64 wt% (Table 4.6). The BSE images for this

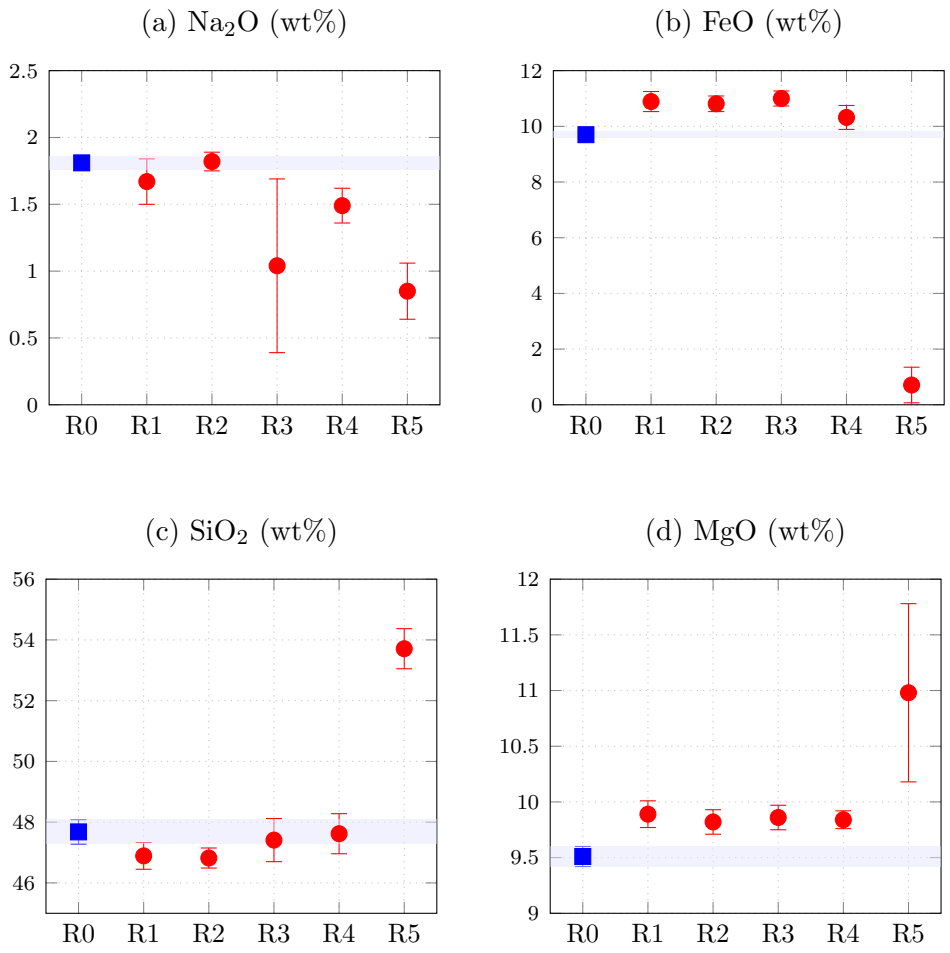

Figure 4.13: Comparison oxide compositions in B_{100} experimental glasses. Square: atmospheric reference glass R0 (1600°C). Circles: vacuum runs (10^{-5} bar, 1400°C). Conditions (dwell time at T_{max}, cooling): R1,R2: 30 min, quench; R3: 10 min, quench; R4: 30 min, 1000 °C/h; R5: 40 min, 100 °C/h. Blue shading: R0 $\pm 1\sigma$ range.

run (Fig. 4.15) confirm a more advanced and widespread iron exsolution texture. Determining whether this efficient iron reduction and loss is primarily driven by the low-pressure environment or the reducing conditions imposed by the graphite capsule requires further experimentation at ambient pressure.

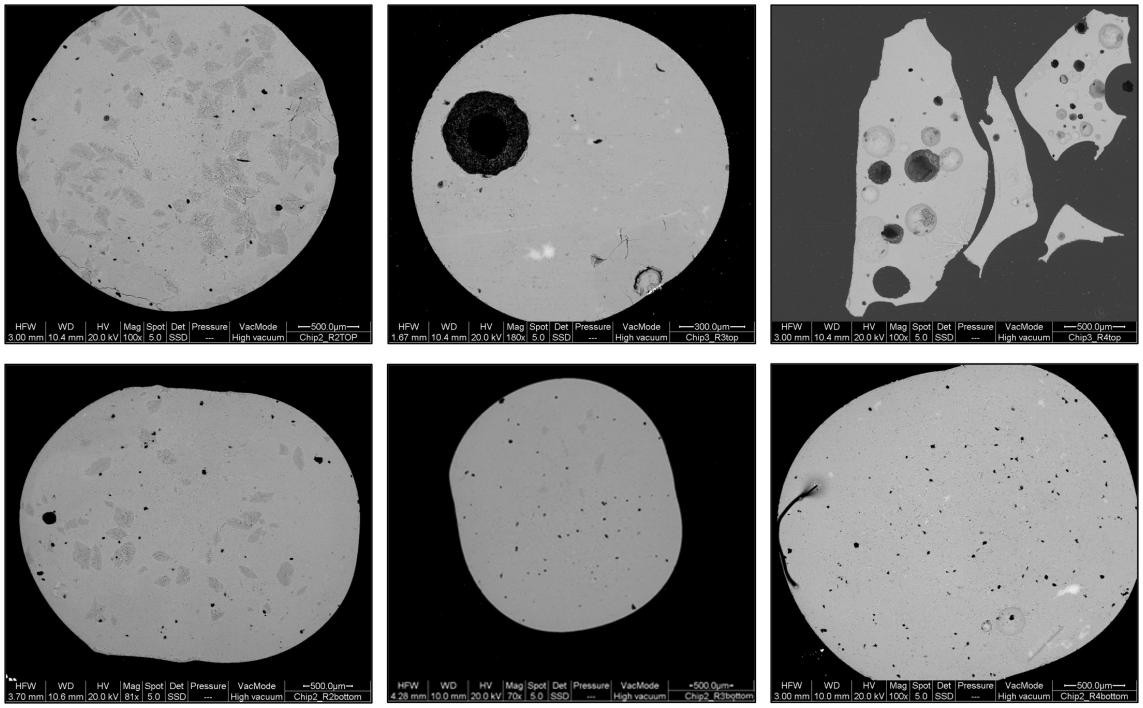

Figure 4.14: Backscattered Electron (BSE) images of post-run products.

Discussion and future perspectives.

Comparison with literature data at air fugacity [28] reveals notable discrepancies due to the reducing conditions in our experiments, which in turn, point to the role of fugacity in modelling silicate crystallisation processes in extraterrestrial environments or in particular Earth System magmatic scenarios. Specifically, increasing oxygen fugacity (fO_2) has been shown to decrease crystallization rates [29], although our data correspond to a system investigated under a shear rate of 0 s^{-1}. Conversely, crystallization of reducing basalt fibers has been reported to initiate at lower temperatures [30], which is consistent with the trends observed in our study.

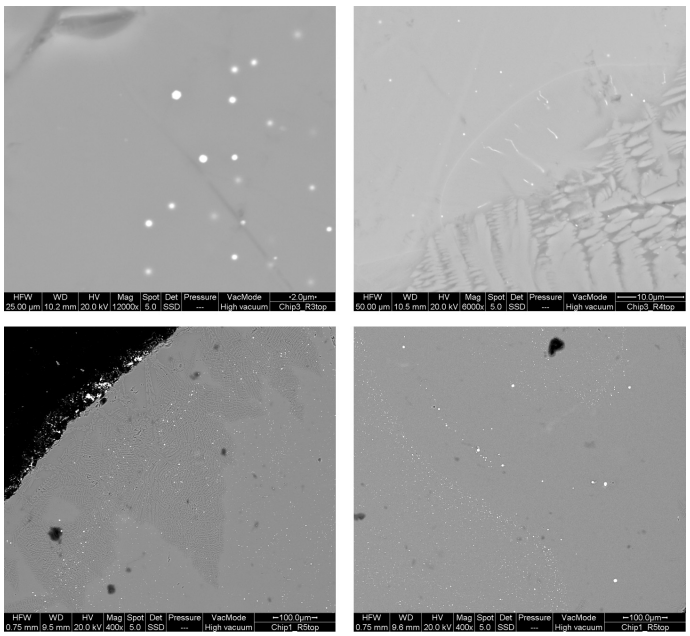

Figure 4.15: Backscattered electron images showing iron exsolution in B_{100} experimental glasses. From top to bottom: R3 (10 min dwell at T_{max}, quench), R4 (30 min dwell at T_{max}, 1000 °C/h cooling), and R5 (40 min dwell at T_{max}, 100 °C/h cooling). All experiments conducted at 10^{-5} bar and 1400°C. The extent of iron exsolution increases with slower cooling rates, with R5 showing the most advanced development of iron-rich phases.

SECOND: CHONDRULES COOLING RATE

Chondrules are signature objects of chondrites. First identified as "rounded globules" by Howard in 1802, they were later described in detail by Sorby (1863), who famously characterized them as "drops of fiery rain" [31]. Today, chondrules are described as sub-millimeter mafic silicate (± metal and sulfide) spherules that formed as free-floating, molten or partially molten droplets in the protoplanetary disk, approximately 1–3 million years after calcium-aluminum-rich inclusions (CAIs) [32, 33].

The textural variety of chondrules arises from differences in their initial composition and thermal history, as illustrated in Fig. 4.16. The main textural classifications are broadly subdivided into porphyritic and non-porphyritic textures. Among porphyritic textures, there are porphyritic olivine chondrules (PO), porphyritic pyroxene chondrules (PP), and the more common porphyritic olivine-pyroxene chondrules (POP). Non-porphyritic chondrules have textures in which olivine and pyroxene grains are elongate, a sign of rapid crystal growth. An iconic and common texture is the barred olivine chondrule (BO), which shows subparallel plates of olivine with a common optical crystal orientation. Among the less common textures are glassy chondrules (GC), cryptocrystalline chondrules (CC), and radial pyroxene chondrules (RP). Despite their significance, the origin of chondrules remains a major unresolved problem in cosmochemistry today. Extensive research involving models, experiments, and constraints from natural samples has led to numerous proposed formation mechanisms, including lightning, magnetic reconnection, energetic phenomena from young Sun, planetesimal collisions, and nebular shocks. By the late 20th and early 21st centuries, consensus shifted toward chondrule formation by transient brief high-temperature events such as shock waves, bow shocks, or planetesimal impacts.

The canonical chondrule formation model postulates that fine-grained dust precur-

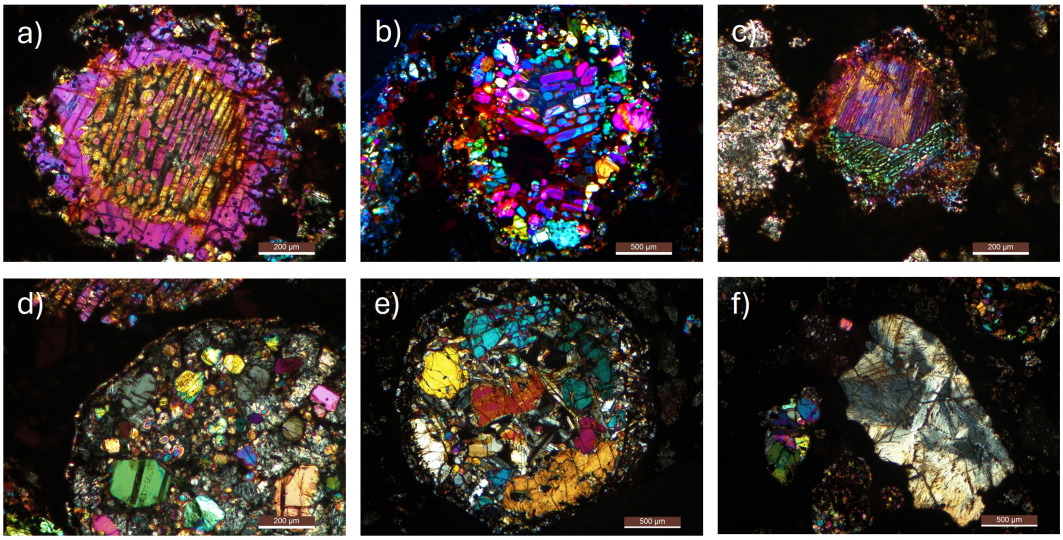

Figure 4.16: Optical micrographs in cross-polarized light showing characteristic chondrule textures from meteoritic samples. **(a-c)** Barred olivine (BO) chondrules displaying variations in bar morphology and crystallographic properties. **(d-e)** Porphyritic olivine-pyroxene (POP) chondrules exhibiting characteristic crystal frameworks. **(f)** Fragment of a radial pyroxene (RP) chondrule showing distinctive spherulitic texture.

sors undergo transient, flash-heating to achieve melting or partial melting, followed by rapid crystallization of the free-floating melt droplets. The presence of multiple generations of recycled chondrules suggest that chondrule formation was a more prolonged process rather than a single event. The debate is ongoing, but there is a consensus that the thermal histories of chondrules—such as the heating rate of the precursor material, the peak temperatures reached, the duration of heating, and the cooling rate—can constrain or test these models and must, therefore, be decoded from chondrule chemistry and textures. To evaluate these different chondrule formation models requires crystallization experiments. Each proposed formation mechanism must be consistent with specific cooling rate profiles. VF-Smelt experiments investigate three principal thermal models [34]: single-stage linear cooling, two-stage cooling (fast-to-slow), two-stage cooling (slow-to-fast), and non-linear cooling.

Here, we present preliminary results from a non-linear cooling experiment,

achieved by rapidly shutting down the furnace power supply to induce its fastest possible cooling rate.

Starting materials.

The starting material had an average composition (in wt%) of 44.54% SiO_2, 13.37% Al_2O_3, 17.82% MgO, 12.68% FeO, 9.63% CaO, 0.55% TiO_2, 0.06% Na_2O, 0.05% K_2O, 0.01% MnO, and 0.01% Cr_2O_3. Analyses on glass or residual glass in wt% were performed by using a JEOL JXA - iHP200F Hyper Probe at the Institute of Earth System Sciences (IESW), Leibniz University of Hannover (DE).

Preliminary Results.

The run-product from the CHR7 vacuum experiment exhibits a distinct spherical shape, as documented by stereomicroscopy images (Fig. 4.17, Fig. 4.18). This spheroidal morphology is attributed to the high surface tension of the silicate melt and its low wetability on the graphite crucible. Stereomicroscopy further reveals the presence of metallic inclusions contained within the translucent silicate portion of the bead. Furthermore, the recovered sample is strongly attracted to a hand magnet, confirming the formation of a significant quantity of Fe metal phase or magnetite during the experiment. Backscattered electron (BSE) imaging showing a large, high-contrast metallic bleb (Fig. 4.19). The chemical compositions of the starting synthetic chondrule glass and the phases crystallised in the CHR7 experiment are reported in Table 4.7. The composition of the post-experiment glass is enriched in SiO_2, increasing from 44.54 wt% in the starting glass to 53.58 wt%. Similarly, Al_2O_3 increases from 13.37 wt% to 19.46 wt%, and CaO increases from 9.63 wt% to 14.19 wt%. The TiO_2 concentration shows a minor increase from 0.55 wt% to 0.77 wt%. In stark contrast, FeO is strongly depleted, decreasing from 12.68 wt% to 0.42 wt%. The MgO content also decreases, from 17.82 wt% to 11.91 wt%.

Discussion and future perspectives.

Table 4.7: Chemical compositions (wt%) of phases in CHR7 experiment and starting material.

Phase/Sample	SiO_2	TiO_2	Al_2O_3	FeO	MnO	MgO	CaO	Na_2O	K_2O	Cr_2O_3	Total
Starting synthetic chondrule glass (atmospheric)											
Starting glass	44.42	0.51	13.26	13.06	0.04	17.89	9.58	0.04	0.06	0.01	98.85
Starting glass	44.60	0.58	13.37	12.56	0.00	17.94	9.65	0.06	0.06	0.02	98.82
Starting glass	44.56	0.54	13.06	12.77	0.02	17.88	9.64	0.06	0.03	0.01	98.57
Starting glass	44.95	0.60	13.56	12.53	0.00	17.78	9.65	0.05	0.06	0.00	99.17
Starting glass	44.32	0.51	13.25	12.78	0.01	17.92	9.46	0.06	0.04	0.00	98.35
Starting glass	44.38	0.58	13.40	12.73	0.01	17.68	9.65	0.07	0.04	0.00	98.54
Starting glass	44.46	0.56	13.41	12.75	0.02	17.88	9.70	0.08	0.08	0.03	98.97
Starting glass	44.45	0.54	13.47	12.52	0.00	17.82	9.69	0.07	0.04	0.02	98.61
Starting glass	44.96	0.54	13.44	12.67	0.01	17.70	9.64	0.07	0.02	0.00	99.05
Starting glass	44.29	0.56	13.48	12.40	0.00	17.64	9.61	0.08	0.07	0.05	98.17
Avg ± 1σ	**44.54**	**0.55**	**13.37**	**12.68**	**0.01**	**17.82**	**9.63**	**0.06**	**0.05**	**0.01**	**98.71**
	0.21	**0.03**	**0.15**	**0.19**	**0.01**	**0.11**	**0.07**	**0.01**	**0.02**	**0.02**	**0.28**
CHR7 olivine											
CHR7 ol	42.61	n.d.	0.20	0.35	0.02	56.77	0.21	n.d.	n.d.	0.02	100.18
CHR7 ol	42.90	n.d.	0.19	0.53	0.00	56.70	0.20	n.d.	n.d.	0.01	100.54
CHR7 ol	43.55	n.d.	0.27	0.32	0.04	56.61	0.24	n.d.	n.d.	0.00	101.03
Avg ± 1σ	**43.02**	**n.d.**	**0.22**	**0.40**	**0.02**	**56.69**	**0.22**	**n.d.**	**n.d.**	**0.01**	**100.58**
	0.47		**0.04**	**0.11**	**0.02**	**0.08**	**0.02**			**0.01**	**0.43**

Table 4.7: Chemical compositions (wt%) of phases in CHR7 experiment and starting material (continued).

Phase/Sample	SiO_2	TiO_2	Al_2O_3	FeO	MnO	MgO	CaO	Na_2O	K_2O	Cr_2O_3	Total
CHR7 clinopyroxene (vacuum)											
CHR7 px	46.38	0.38	8.34	0.57	0.00	39.31	5.09	0.00	0.01	0.01	100.09
CHR7 px	54.05	0.81	20.93	0.41	0.02	8.57	14.67	0.02	0.02	0.00	99.50
CHR7 px	45.55	0.30	6.73	0.63	0.00	43.47	4.19	0.00	0.02	0.01	100.91
CHR7 px	53.92	0.85	20.77	0.46	0.03	7.66	15.46	0.00	0.02	0.00	99.16
CHR7 px	50.17	0.60	15.04	0.54	0.00	23.33	10.39	0.00	0.02	0.01	100.09
CHR7 px	49.56	0.47	13.54	0.63	0.03	28.48	8.22	0.00	0.02	0.02	100.98
CHR7 px	52.36	0.66	17.67	0.46	0.02	17.06	11.64	0.00	0.02	0.02	99.93
CHR7 px	53.80	0.71	20.57	0.51	0.00	9.89	14.13	0.02	0.00	0.01	99.64
CHR7 px	54.64	0.88	21.74	0.08	0.02	5.96	15.50	0.00	0.02	0.00	98.84
CHR7 px	51.99	0.70	18.79	0.12	0.01	13.70	12.91	0.00	0.03	0.01	98.26
Avg ± 1σ	**51.24**	**0.64**	**16.41**	**0.44**	**0.01**	**19.84**	**11.22**	**0.00**	**0.02**	**0.01**	**99.74**
	3.43	**0.19**	**5.32**	**0.20**	**0.01**	**12.96**	**4.23**	**0.01**	**0.01**	**0.01**	**0.74**
CHR7 glass (vacuum)											
CHR7 glass	53.72	0.93	19.54	0.47	0.02	10.26	14.78	0.02	0.05	0.00	99.80
CHR7 glass	54.08	0.74	19.73	0.37	0.06	11.01	14.55	0.01	0.03	0.03	100.61
CHR7 glass	52.03	0.69	17.85	0.61	0.00	14.75	13.29	0.00	0.03	0.06	99.32
CHR7 glass	52.55	0.73	18.43	0.52	0.04	13.72	13.94	0.05	0.03	0.00	100.01
CHR7 glass	53.41	0.78	19.03	0.41	0.02	12.43	14.34	0.00	0.06	0.00	100.46
CHR7 glass	54.26	0.78	21.07	0.40	0.00	9.10	14.62	0.03	0.01	0.03	100.30
CHR7 glass	54.11	0.82	20.25	0.37	0.01	10.46	14.45	0.01	0.02	0.00	100.50
CHR7 glass	54.11	0.83	20.42	0.62	0.00	9.89	14.76	0.00	0.02	0.03	100.69
CHR7 glass	53.54	0.78	18.45	0.22	0.00	14.16	13.69	0.02	0.02	0.00	100.87
CHR7 glass	53.03	0.65	19.80	0.20	0.07	13.22	13.52	0.00	0.00	0.04	100.52
Avg ± 1σ	**53.58**	**0.77**	**19.46**	**0.42**	**0.02**	**11.91**	**14.19**	**0.01**	**0.03**	**0.02**	**100.41**
	0.75	**0.08**	**1.03**	**0.14**	**0.02**	**1.92**	**0.50**	**0.02**	**0.02**	**0.02**	**0.54**

Note: n.d. = not detected. Starting glass: atmospheric reference. CHR7 phases formed under vacuum (10^{-5} bar, 100°C/h cooling). Olivine: forsteritic ($Fo_{99.3}$). Clinopyroxene: bimodal (diopside: high-Mg; augite: high-Al). Glass: shows extreme Fe depletion (12.68% $\rightarrow$ 0.42%) and enrichment in SiO_2, Al_2O_3, CaO.

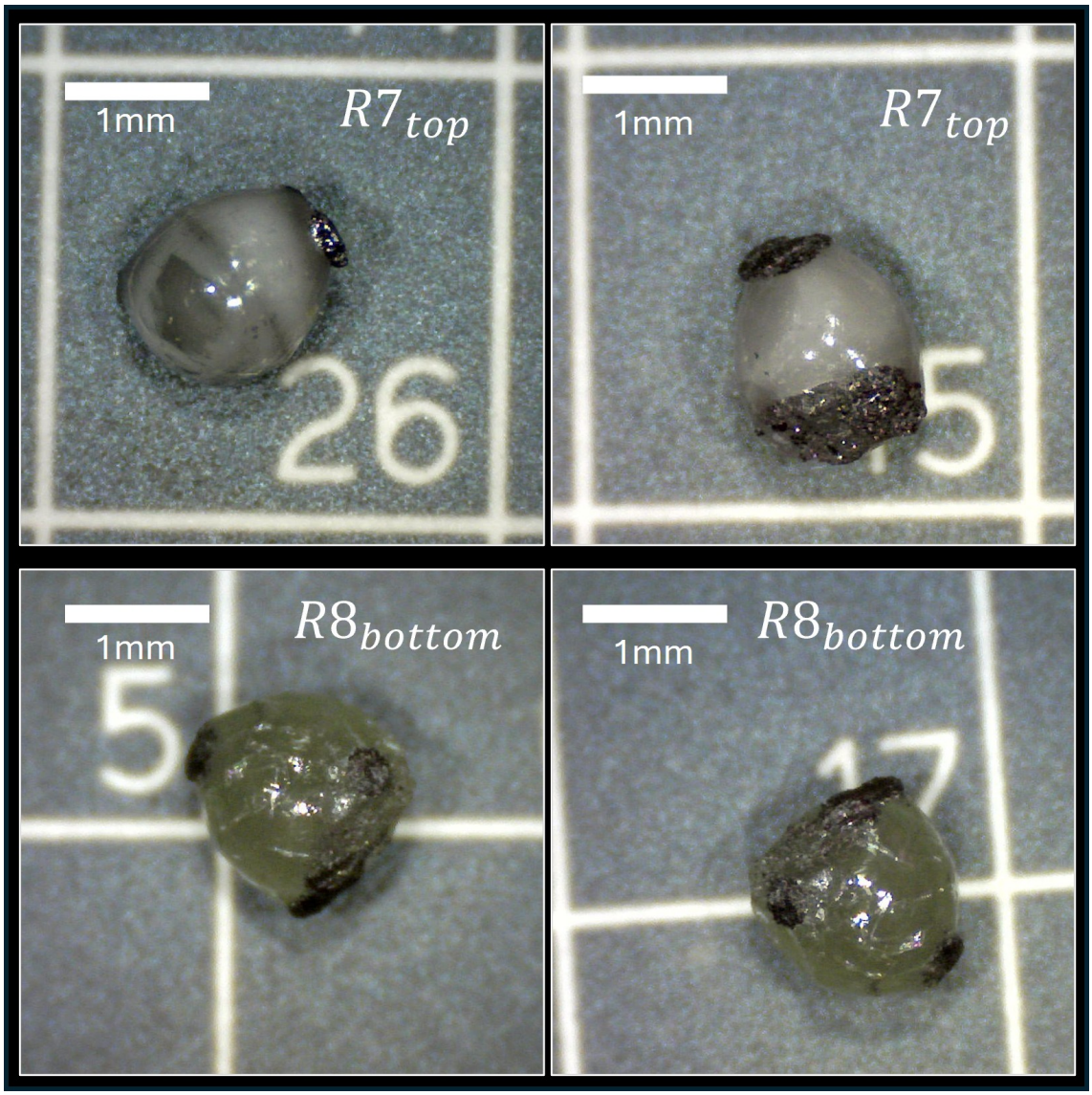

Figure 4.17: Stereoscopic micrograph of experimental spherules.

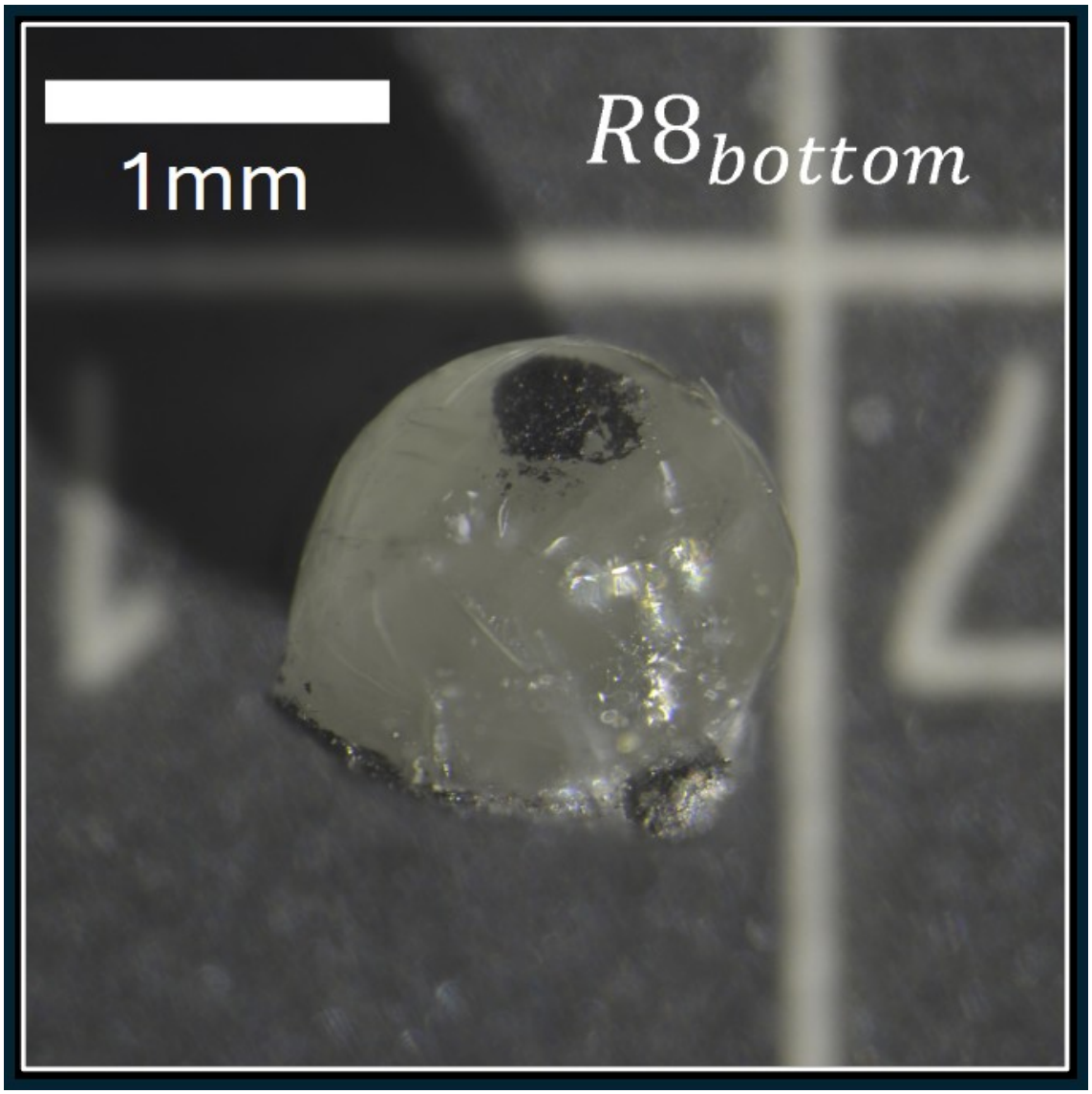

Figure 4.18: Higth quality stereoscopic micrograph of R8.

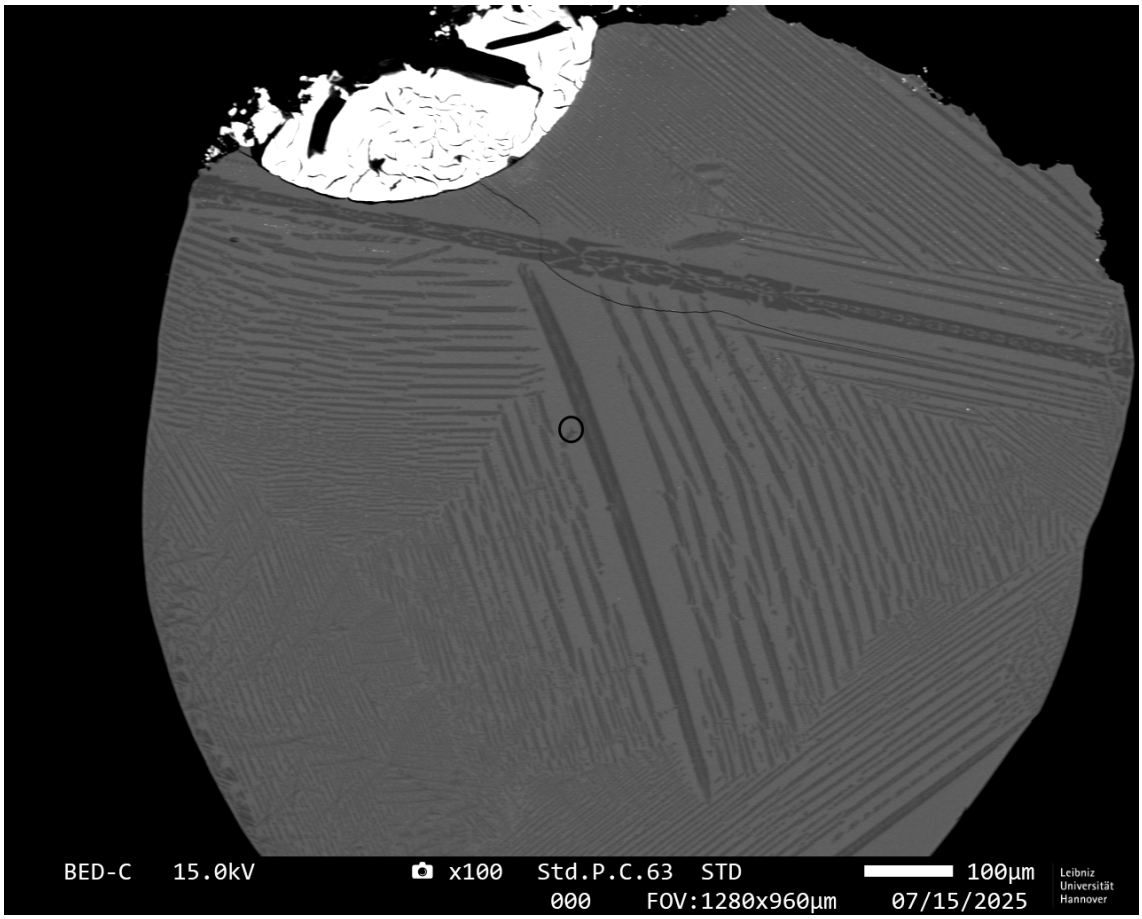

Figure 4.19: BSE image of R7.

We successfully produced a large metal bleb and skeletal olivine crystals with oriented growth patterns similar to barred olivines (BO) found in natural chondrules. The severe depletion of FeO in the residual glass (from 12.68 to 0.42 wt.%) is diagnostic of *in-situ* reduction and metal segregation driven by the reducing conditions imposed by the graphite crucible, which buffered the oxygen fugacity near the IW. The olivine is highly forsteritic ($Fo_{99.3}$, ∼0.4 wt.% FeO), and the clinopyroxene contains very low Fe (<0.6 wt.% FeO). Therefore, the extreme FeO depletion observed in the residual glass cannot be explained by the crystallization of the observed silicates. The skeletal, dendritic morphology of the olivine is a classic indicator of rapid growth under high degrees of undercooling, consistent with the applied rapid cooling rate (∼3000–1000 °C/h). Skeletal forsterite crystals are oriented in a pattern that closely mimics the parallel-barred texture characteristic of many barred olivine (BO) chondrules. Furthermore, the metal occurs as a single, large isolated bleb, analogous to those found in some chondrules and armored chondrule rims. The composition of the residual glass closely matches the typical mesostasis composition find in natural barred olivine chondrules.

Our experiment thus likely captures the initial stage of chondrule formation—rapid crystallization under highly reducing conditions.

References for Section 4

[1] C. Alexander (2004). Chemical equilibrium and kinetic constraints for chondrule and CAI formation conditions. *Geochimica et Cosmochimica Acta* vol. **68**, 3943–3969. https://doi.org/10.1016/j.gca.2004.03.030.

[2] C. M. O. Alexander, J. N. Grossman, D. S. Ebel, and F. J. Ciesla (2008). The Formation Conditions of Chondrules and Chondrites. *Science* vol. **320**, 1617–1619. https://doi.org/10.1126/science.1156561.

[3] L. Grossman (1972). Condensation in the primitive solar nebula. *Geochimica et Cosmochimica Acta* vol. **36**, 597–619. https://doi.org/10.1016/0016-7037(72)90078-6.

[4] E. A. King (1982). Refractory residues, condensates and chondrules from solar furnace experiments. *Journal of Geophysical Research: Solid Earth* vol. **87**, A429–A434. https://doi.org/https://doi.org/10.1029/JB087iS01p0A429.

[5] L. Grossman (1988). Condensation in the primitive solar nebula. *Geochimica et Cosmochimica Acta* vol. **52**, 1719–1744.

[6] A. Davis and A. Hashimoto (1990). Evaporation of forsterite and implications for the origin of CAIs. *Geochimica et Cosmochimica Acta* vol. **54**, 3209–3219.

[7] R. A. Mendybaev, M. Kamibayashi, F.-Z. Teng, P. S. Savage, R. B. Georg, F. M. Richter, and S. Tachibana (2021). Experiments quantifying elemental and isotopic fractionations during evaporation of CAI-like melts in low-pressure hydrogen and in vacuum: Constraints on thermal processing of CAIs in the protoplanetary disk. *Geochimica et Cosmochimica Acta* vol. **292**, 557–576. https://doi.org/https://doi.org/10.1016/j.gca.2020.09.005.

[8] J. Badro, P. A. Sossi, Z. Deng, S. Borensztajn, N. Wehr, and F. J. Ryerson (2021). Experimental investigation of elemental and isotopic evaporation processes by laser heating in an aerodynamic levitation furnace. *Comptes Rendus. Géoscience* vol. **353**, 101–114. https://doi.org/10.5802/crgeos.56.

[9] S. J. Desch, M. A. Morris, H. C. Connolly, and A. P. Boss (2012). The importance of experiments: Constraints on chondrule formation models. *Meteoritics & Planetary Science* vol. **47**, 1139–1156. https://doi.org/10.1111/j.1945-5100.2012.01357.x.

[10] H. Melosh and A. Vickery (1991). Melt droplet formation in energetic impact events. *Nature* vol. **350**, 494–497. https://doi.org/10.1038/350494a0.

[11] B. C. Johnson and H. Melosh (2012). Formation of spherules in impact produced vapor plumes. *Icarus* vol. **217**, 416–430. https://doi.org/10.1016/j.icarus.2011.11.020.

[12] C. Koeberl, W. Kiesl, F. Kluger, and H. Weinke (1984). A comparison between terrestrial impact glasses and lunar volcanic glasses: The case of fluorine. *Journal of Non-Crystalline Solids* vol. **67**, 637–648. https://doi.org/https://doi.org/10.1016/0022-3093(84)90180-7.

[13] R. Pang, J. Yang, R. Li, S. Liu, Q. Li, D. Zhu, W. Du, and Y. Liu (2024). Redox condition changes caused by impacts: Insights from Chang'e-5 lunar glass beads. *Science bulletin* vol. https://doi.org/10.1016/j.scib.2024.03.004.

[14] K. M. Cannon and J. F. Mustard (2015). Preserved glass-rich impactites on Mars. *Geology* vol. **43**, 635–638.

[15] A. Tomkins, M. Genge, A. Tait, S. L. Alkemade, A. Langendam, P. P. Perry, and S. Wilson (2019). High Survivability of Micrometeorites on Mars: Sites With Enhanced Availability of Limiting Nutrients. *Journal of Geophysical Research: Planets* vol. **124**, 1802–1818. https://doi.org/10.1029/2019je006005.

[16] L. Folco and C. Cordier "Micrometeorites". In: *Planetary Mineralogy*. European Mineralogical Union, 2015. https://doi.org/10.1180/EMU-notes.15.9. https://doi.org/10.1180/EMU-notes.15.9.

[17] A. G. Tomkins, L. Bowlt, M. Genge, S. Wilson, H. E. A. Brand, and J. L. Wykes (2016). Ancient micrometeorites suggestive of an oxygen-rich Archaean upper atmosphere. *Nature* vol. **533**, 235–238. https://doi.org/10.1038/nature17678.

[18] M. Suttle, F. Campanale, L. Folco, L. Tavazzani, M. Meier, C. Miller, G. Hughes, M. Genge, T. Salge, J. Spratt, and M. Anand (2023). Fossil micrometeorites from Monte dei Corvi: Searching for dust from the Veritas asteroid family and the utility of micrometeorites as a palaeoclimate proxy. *Geochimica et Cosmochimica Acta* vol. **355**, 75–88. https://doi.org/https://doi.org/10.1016/j.gca.2023.06.027.

[19] A. Toppani, G. Libourel, C. Engrand, and M. Maurette (2001). Experimental simulation of atmospheric entry of micrometeorites. *Meteoritics & Planetary Science* vol. **36**. https://doi.org/10.1111/j.1945-5100.2001.tb01831.x.

[20] Z. Zhang and P. E. Driscoll (2025). Inefficient Loss of Moderately Volatile Elements From Exposed Planetesimal Magma Oceans. *Journal of Geophysical Research: Planets* vol. **130**, e2024JE008671. https://doi.org/https://doi.org/10.1029/2024JE008671.

[21] J. K. Dhaliwal, J. M. Day, and F. Moynier (2018). Volatile element loss during planetary magma ocean phases. *Icarus* vol. **300**, 249–260. https://doi.org/https://doi.org/10.1016/j.icarus.2017.09.002.

[22] H. Tang and E. Young (2020). Evaporation from the lunar magma ocean was not the mechanism for fractionation of the Moon's moderately volatile elements. *The Planetary Science Journal* vol. **1**, 49.

[23] L. Elkins-Tanton (2012). Magma oceans in the inner Solar System. *Annual Review of Earth and Planetary Sciences* vol. **40**, 113–139.

[24] L. Wilson and J. W. Head (2024). Lunar Mare Lava Flow Dynamics and Emplacement: Predictions of Non-Newtonian Flow Dynamics, Syn- and Post-emplacement Cooling and Volatile Release Patterns, and Vertical and Lateral Flow Structure Development. *The Planetary Science Journal* vol. **5**. https://doi.org/10.3847/psj/ad0e12.

[25] L. Wilson and J. W. Head III (1981). Ascent and eruption of basaltic magma on the Earth and Moon. *Journal of Geophysical Research: Solid Earth* vol. **86**, 2971–3001. https://doi.org/https://doi.org/10.1029/JB086iB04p02971.

[26] M. Anand (2012). A brief review of chemical and mineralogical resources on the Moon and likely resource utilization scenarios. *Planetary and Space Science* vol. **74**, 42–48.

[27] M. G. Shaw, G. A. Brooks, M. A. Rhamdhani, A. R. Duffy, and M. I. Pownceby (2021). Thermodynamic modelling of ultra-high vacuum thermal decomposition for lunar resource processing. *Planetary and Space Science* vol. **204**, 105272. https://doi.org/https://doi.org/10.1016/j.pss.2021.105272.

[28] F. Vetere, G. Iezzi, H. Behrens, F. Holtz, G. Ventura, V. Misiti, A. Cavallo, S. Mollo, and M. Dietrich (2015). Glass forming ability and crystallisation behaviour of sub-alkaline silicate melts. *Earth-Science Reviews* vol. **150**, 25–44. https://doi.org/https://doi.org/10.1016/j.earscirev.2015.07.001.

[29] S. Kolzenburg, D. Di Genova, D. Giordano, K. Hess, and D. Dingwell (2018). The effect of oxygen fugacity on the rheological evolution of crystallizing basaltic melts. *Earth and Planetary Science Letters* vol. **487**, 21–32. https://doi.org/https://doi.org/10.1016/j.epsl.2018.01.023.

[30] S. Gutnikov, M. Manylov, Y. Lipatov, B. Lazoryak, and K. Pokholok (2013). Effect of the reduction treatment on the basalt continuous fiber crystallization properties.

Journal of Non-Crystalline Solids vol. **368**, 45–50. https://doi.org/https://doi.org/10.1016/j.jnoncrysol.2013.03.007.

[31] G. J. H. McCall (2006). Chondrules and calcium-aluminium-rich inclusions (CAIs). *Geological Society, London, Special Publications* vol. **256**, 345–361. https://doi.org/10.1144/gsl.sp.2006.256.01.17.

[32] N. T. KITA and T. USHIKUBO (2012). Evolution of protoplanetary disk inferred from 26Al chronology of individual chondrules. *Meteoritics & Planetary Science* vol. **47**, 1108–1119. https://doi.org/https://doi.org/10.1111/j.1945-5100.2011.01264.x.

[33] E. R. D. Scott (2007). Chondrites and the Protoplanetary Disk. *Annual Review of Earth and Planetary Sciences* vol. **35**, 577–620. https://doi.org/10.1146/annurev.earth.35.031306.140100.

[34] A. Smith and R. H. Jones (2024). Experimental constraints on formation of silica-rich igneous rims around chondrules in CR chondrites. *Geochimica et Cosmochimica Acta* vol. **374**, 106–120. https://doi.org/https://doi.org/10.1016/j.gca.2024.04.016.

4.3 Brillouin spectroscopy of natural and chemically complex volcanic glasses: The role of divalent cations

This collaboration enabled me to further strengthen my expertise in high-temperature techniques for glass preparation. This aspect of experimental work is particularly significant, as virtually all petrological experiments conducted under high-pressure and high-temperature conditions rely on glasses as starting materials. Equally critical is the ability to homogenize silicate systems, thereby eliminating compositional heterogeneities that could influence nucleation behaviour or bias the crystallization pathways of the starting material. In particular, achieving complete melting and controlled quenching is essential to ensure chemical homogeneity while minimizing the incorporation of bubbles or microcrystals that might act as unintended nucleation sites. Thus, a critical cooling rate must be applied in order to obtain homogeneous glass starting material. These procedures were complemented by systematic analytical characterization—using techniques such as electron microprobe analysis to verify the homogeneity and structural integrity of the produced glasses. This rigorous approach not only improved the reproducibility of subsequent high/low-pressure experiments at high/low temperature but also contributed to a more reliable interpretation of phase equilibria and crystal-melt interactions within complex silicate systems.

Abstract This work investigates using Brillouin light scattering (BLS) spectroscopy the relationship between chemistry and longitudinal (or pressure) sound-wave propagation on a large dataset of alkaline to sub-alkaline silicate glasses. Results show that the frequency f_B of the Brillouin peak decreases with the silica content and the Silica vs. Calcia - Ferrous oxide - Magnesia (SCFM) parameter, while it increases with the degree of polymerization expressed by the ratio of nonbridging oxygens to

tetrahedral cations (NBO/T). It is possible to infer that the values of both f_B and the real part of the longitudinal elastic modulus M' are tightly related to the content of divalent cations (M^{2+}) participating in the silicate network. Our findings suggest that alkaline earth metals and Fe^{2+} linearly speed up the longitudinal acoustic waves in silicate glasses. This might open a new window on the possibility of using the BLS technique for rapid and accurate determinations of physical and chemical properties of natural glasses present on Earth and other planetary bodies.

This page intentionally left blank.

Appendix

Chemical Geology 681 (2025) 122719

Contents lists available at ScienceDirect

Chemical Geology

journal homepage: www.elsevier.com/locate/chemgeo

Brillouin spectroscopy of natural and chemically complex volcanic glasses: The role of divalent cations

Alessandro Pisello [a,*], Silvia Corezzi [a,*], Michele Cassetta [b,c], Francesco Radica [d,e], Lucia Comez [f], Gianluca Iezzi [d,e,g], Andrea Vitrano [h], Francesco Pasqualino Vetere [h], Diego Perugini [a]

[a] Department of Physics and Geology, University of Perugia, I-06123 Perugia, Italy
[b] Department of Earth Sciences, University of Torino, I-10125 Torino, Italy
[c] Institute of Geosciences and Earth Resources, National Research Council of Italy (CNR-IGG), I-56127 Pisa, Italy
[d] Dipartimento di Ingegneria e Geologia, Università degli studi di Chieti, I-66100 Chieti, Italy
[e] UdA-TechLab, Research Center, University "G. d'Annunzio" of Chieti-Pescara, 66100 Chieti, Italy
[f] CNR - Istituto Officina dei Materiali (IOM) c/o Department of Physics and Geology, University of Perugia, I-06123 Perugia, Italy
[g] Istituto Nazionale di Geofisica e Vulcanologia, Sezione di Roma, via di Vigna Murata 605, 00143 Roma, Italy
[h] Department of Physical Sciences, Earth and Environment, University of Siena, 53100, Italy

ARTICLE INFO

Editor: Dr. Claudia Romano

Keywords:
Silicate glasses
Brillouin spectroscopy
Elastic properties
Chemical composition
NBO/T
SCFM

ABSTRACT

This work investigates using Brillouin light scattering (BLS) spectroscopy the relationship between chemistry and longitudinal (or pressure) sound-wave propagation on a large dataset of alkaline to sub-alkaline silicate glasses. Results show that the frequency f_B of the Brillouin peak decreases with the silica content and the Silica vs. Calcia - Ferrous oxide - Magnesia (SCFM) parameter, while it increases with the degree of polymerization expressed by the ratio of nonbridging oxygens to tetrahedral cations (NBO/T). It is possible to infer that the values of both f_B and the real part of the longitudinal elastic modulus M' are tightly related to the content of divalent cations (M^{2+}) participating in the silicate network. Our findings suggest that alkaline earth metals and Fe^{2+} linearly speed up the longitudinal acoustic waves in silicate glasses. This might open a new window on the possibility of using the BLS technique for rapid and accurate determinations of physical and chemical properties of natural glasses present on Earth and other planetary bodies.

1. Introduction

Magmas are natural silicate melts with high compositional variability which in turn influence petrogenetic, volcanic and viscoelastic rheological properties and processes (Dingwell, 1996; Giordano et al., 2008; Gonnermann and Manga, 2007). Most physical properties of silicate melts reflect their elemental abundance and related molecular arrangement, resulting from an interplay between network-forming elements (four-fold coordinated cations like Si, Al, Ti, ferric Fe and, to a lesser extent, B and P) and network-modifiers, which are mainly Mg, Ca and ferrous Fe (Bansal and Doremus, 2013; Giordano et al., 2008; Mysen and Richet, 2005; Neuville et al., 2022; Radica et al., 2024). Although the liquid and glassy states are different (Webb, 1992), silicate glasses maintain the structure (SRO: short range order) of their supercooled liquid (Zanotto and Mauro, 2017). In this respect, many studies have employed a variety of calorimetric and spectroscopic techniques to investigate the relationship between physical properties and chemical composition of silicate glasses (Behrens and Zhang, 2009; Cassetta et al., 2021; Di Genova et al., 2015; Di Muro et al., 2009; Hess and Dingwell, 1996; Kress and Carmichael, 1991; Le Losq and Neuville, 2013; Le Losq and Sossi, 2023; Vetere et al., 2014).

Brillouin light scattering (BLS) spectroscopy is a rapid and non-destructive technique based on the inelastic scattering of light (photons) by thermally-induced acoustic waves (thermal phonons) that allows one to access the elastic constants of materials in the GHz range of frequencies (Scarponi et al., 2017). BLS has been used to characterize geologically relevant solid materials in both crystalline and glassy states (see Speziale et al., 2014 for a review). For what concerns silicate glasses, most literature focuses on simplified and iron-free compositions (Galeener et al., 1984; Jabraoui et al., 2016; Scannell et al., 2016; Vaills

* Corresponding authors.
E-mail addresses: alessandro.pisello@unipg.it (A. Pisello), silvia.corezzi@unipg.it (S. Corezzi).

https://doi.org/10.1016/j.chemgeo.2025.122719
Received 20 August 2024; Received in revised form 4 February 2025; Accepted 1 March 2025
Available online 7 March 2025

et al., 1993; Weigel et al., 2016; Wu et al., 2017). Therefore, information on crucial properties of magmas (density, compressibility, sound velocities, etc.) and related processes (melt migration in the Earth's mantle and crust) rely on the correlation between vibrational and elastic properties of melts obtained on chemically simple or iron-free multicomponent systems (Hushur et al., 2013; Schilling et al., 2001; Whittington et al., 2012), with few exceptions on SiO_2-poor melts (Malfait et al., 2011; Wu et al., 2017). More recently, studies on peridotitic (Di Genova et al., 2023) and natural (Cassetta et al., 2021) multicomponent glasses have been conducted to gain a more comprehensive understanding of the properties of silicate melts in nature.

Importantly, the viscosity of melts can be estimated from BLS measurements through the ratio of bulk to shear moduli of the parental glasses. Recently, Cassetta et al., 2021, 2023 observed that this parameter correlates linearly with the amount of SiO_2 in very different silicate glasses (both volcanic and technical), suggesting that determining the elastic properties of glasses can provide insights into their chemical composition. Moreover, a BLS study of synthetic aluminosilicates has shown that the structural rearrangement caused by charge-compensating cations substitution results in a substantial change of elastic moduli (Weigel et al., 2016).

In this work, we extend the application of BLS spectroscopy to investigate the most abundant and common glasses with multicomponent chemical compositions by considering different series of natural silicate glasses, either SiO_2-poor and SiO_2-rich, as well as with low and high amounts of alkalis.

2. Methods

2.1. Starting material and preparation

Silicate glasses were produced by melting and mixing end members (one mafic and one felsic) from various volcanic areas having different types of compositional affinity: the first three series were produced and reported in Pisello et al. (2022a, 2022b) and they come from Snake River Plain (SRP; USA see Morgavi et al., 2013), presenting a subalkaline affinity, Etna (Italy, see Corsaro and Métrich, 2016) with a sodium-rich alkaline affinity, and Vulcano (Italy, see De Astis et al., 1997) with a potassium-rich alkaline affinity. Moreover, another sub-alkaline series from Vetere et al. (2013) and Vetere et al. (2015a), obtained by mixing basalt from Iceland and rhyolite from Lipari, was used. In dthis work, we will refer to the sets of glasses produced for each location as follows, respectively: Subalkaline series (SRP), Na-alkaline series (Etna), K-Alkaline series (Vulcano) and Subalkaline -A series, obtained by mixing basalt from Iceland and rhyolite from Lipari (Table 1).

Glasses from the natural samples were produced following the procedure used in Vetere et al. (2013). Each end-member was crushed, melted at superliquidus temperature (1500 °C) in a platinum crucible for four hours, and rapidly quenched by placing the crucible at room temperature. The operation was repeated twice to obtain homogeneous crystal-free glasses. Afterwards, each glassy end-member was ground to powder (grain size <500 μm) and mixed in the desired weight proportions, as listed below, to produce glasses with intermediate compositions. The mixtures were remelted again two times following the same

Table 1
Weight percent of the main oxides measured by EMPA. Results for the series which were produced for this study (Subalkaline, K-alkaline and Ca-alkaline) are reported as the mean value and standard deviation of multiple repetitions. For the other samples, EMPA compositions are taken from their relative studies: [1] Vetere et al., 2015a, 2015b, [2]Iezzi et al., 2011, [3]Iezzi et al., 2011, [4]Tamic et al., 2001.

Series	Sample	SiO2	TiO2	Al2O3	Total Fe as FeO	MnO	MgO	CaO	Na2O	K2O	P2O5
Subalkaline	B	48.32	1.82	16.23	11.70	0.18	7.62	10.81	2.57	0.36	0.34
	St.dev.	0.15	0.05	0.08	0.10	0.03	0.05	0.07	0.05	0.02	0.03
	B8	53.06	1.60	15.52	10.34	0.15	6.14	8.88	2.69	1.22	0.29
	St.dev	0.11	0.04	0.09	0.08	0.05	0.04	0.07	0.07	0.04	0.03
	B6	57.75	1.35	14.94	8.80	0.13	4.68	7.08	2.83	2.08	0.24
	St.dev	0.16	0.04	0.08	0.11	0.03	0.05	0.08	0.06	0.04	0.03
	B4	62.68	1.11	14.26	7.23	0.10	3.19	5.26	2.91	2.97	0.22
	St.dev	0.21	0.04	0.09	0.12	0.02	0.05	0.07	0.07	0.06	0.03
	B2	67.49	0.88	13.71	5.60	0.08	1.70	3.42	3.05	3.84	0.17
	St.dev	0.17	0.03	0.06	0.11	0.02	0.03	0.05	0.06	0.07	0.02
	RB	72.13	0.65	13.20	4.02	0.04	0.25	1.62	3.17	4.75	0.14
	St.dev	0.10	0.03	0.06	0.08	0.03	0.01	0.03	0.05	0.05	0.02
K-alkaline	S	54.23	0.69	16.02	7.94	0.17	4.13	7.68	5.34	3.11	0.49
	St.dev	0.20	0.03	0.11	0.11	0.04	0.05	0.09	0.14	0.04	0.03
	S7	67.57	0.29	14.28	3.89	0.10	1.40	3.09	4.49	4.51	0.17
	St.dev	0.11	0.02	0.09	0.09	0.03	0.03	0.05	0.06	0.05	0.02
	S5	63.83	0.39	14.78	5.06	0.12	2.17	4.44	4.68	4.08	0.27
	St.dev	0.24	0.02	0.09	0.08	0.03	0.03	0.07	0.27	0.07	0.03
	S3	60.38	0.51	15.37	6.12	0.14	2.94	5.71	4.84	3.63	0.29
	St.dev	0.20	0.02	0.08	0.14	0.02	0.04	0.10	0.09	0.05	0.03
	RS	73.25	0.12	13.53	2.11	0.07	0.25	1.12	4.17	5.13	0.05
	St.dev	0.08	0.02	0.08	0.07	0.02	0.02	0.03	0.06	0.05	0.02
Na-alkaline	M	48.50	1.53	14.53	10.90	0.18	7.82	12.13	2.61	1.23	0.45
	St.dev	0.18	0.04	0.08	0.11	0.02	0.07	0.13	0.04	0.03	0.03
	M5	55.36	1.36	15.64	8.23	0.17	4.58	7.62	4.34	2.20	0.37
	St.dev	0.14	0.05	0.12	0.16	0.02	0.05	0.11	0.07	0.02	0.03
	V	63.25	1.20	17.11	5.05	0.17	1.45	3.18	4.92	3.22	0.35
	St.dev	0.25	0.04	0.05	0.08	0.03	0.03	0.05	0.16	0.05	0.04
Subalkaline-A [1]	B100	48.26	0.98	15.67	10.28	0.18	9.47	13.26	1.80	0.04	0.06
	B80	53.50	0.81	15.13	8.62	0.15	7.65	10.89	2.20	1.03	0.02
	B60	58.43	0.66	14.74	7.01	0.13	5.86	8.53	2.61	2.01	0.04
	B40	63.46	0.47	14.21	5.48	0.12	4.06	6.14	2.98	3.06	0.02
	B20	68.80	0.29	13.77	3.74	0.11	2.21	3.68	3.33	4.04	0.02
	R100	73.84	0.12	13.46	2.06	0.08	0.44	1.36	3.74	4.88	0.03
	AMS [2]	57.67	0.40	19.04	4.67	0.10	1.51	4.38	3.85	8.18	0.20
	FRB [2]	56.21	0.61	18.68	6.46	0.10	2.24	5.62	4.46	5.26	0.36
	DPP [3]	58.59	0.59	17.26	6.91	0.18	4.14	7.74	2.46	1.97	0.15
	EDF [4]	76.90	0.11	12.74	0.68	0.07	0.08	0.58	4.06	4.78	

procedure as before at superliquidus temperature (1500 °C) to obtain compositionally homogeneous products (Vetere et al., 2013, 2015a).

The Subalkaline series was produced by mixing the mafic and felsic end-members in the following weight proportions: 100 % basalt, 80 % basalt and 20 % rhyolite, 60 % basalt and 40 % rhyolite, 40 % basalt and 60 % rhyolite, 20 % basalt and 80 % rhyolite, and 100 % rhyolite (referred to as B, B8, B6, B4, B2, RB, respectively; see Table 1). For the K-alkaline series, the following weight proportions were produced: 100 % shoshonite, 70 % shoshonite and 30 % rhyolite, 50 % shoshonite and 50 % rhyolite, 30 % shoshonite and 70 % rhyolite, and 100 % rhyolite (referred to as S, S7, S5, S3, RS, respectively; see Table 1). In the Na-alkaline series the proportions were: 100 % hawaiite, 50 % hawaiite and 50 % benmoreite, and 100 % benmoreite (referred to as M, M5, V, respectively; see Table 1). In total, 14 glasses with different compositions were produced, plus the 6 samples produced in Vetere et al. (2015a).

To further test the results, we also considered additional samples from other studies: four silicate glasses – namely, EDF from Tamic et al. (2001), AMS and FRB from (Iezzi et al., 2008), DPP from (Iezzi et al., 2011) – and pure commercial silica glass (see Table 1 for details on chemical compositions).

2.2. EMPA analyses

Chemical compositions for the Subalkaline, K-alkaline and Na-alkaline series were determined at the Department of Earth- and Environmental Sciences, University of Munich LMU (Germany), with a Cameca SX100 electron microprobe analyzer (EMPA). Samples were embedded in epoxy resin, polished, and then covered with a 13 nm carbon coating. Analyses were performed using an acceleration voltage of 15 kV and an electronic beam current of 20 nA, with a defocused beam of 10 μm on the sample. Standards used for calibration were orthoclase (Al, K), albite (Si, Na), wollastonite (Ca), periclase (Mg), ilmenite (Ti), iron (II) oxide (Fe), and chromium oxide (Cr). The chemical homogeneity of the glasses was tested by performing five chemical analyses for each sample.

2.3. Iron speciation

Ferrous–ferric ratio depends on the glass composition and the *P-T-*fO_2 conditions at which the melting process occurs. In this study, glasses were always prepared at air oxygen fugacity. The iron oxidation state determination was performed using a wet chemical micro-colorimetric method (Schuessler et al., 2008). 7–10 mg of glass chips were dissolved in concentrated HF with the addition of a solution of ammonium vanadate in 5 M sulfuric acid. The released ferrous iron reacts with V^{5+} and forms V^{4+} and ferric iron (for details, see ref. Schuessler et al., 2008 and Vetere et al., 2014). After complete dissolution, boric acid was added to bind fluorine, and the pH value was increased by adding ammonium acetate so that Fe^{2+} was formed again. The concentration of bivalent iron was measured spectrometrically after complexation with bipyridyl, using a 1 cm transmission cell in a UV/VIS spectrometer Shimadzu UV 1800. To calculate the total iron concentration (Fe_{tot}), hydroxylamine hydrochloride was added to the solution to reduce Fe^{3+}.

2.4. Brillouin light scattering measurements

The BLS experiment detects light inelastically scattered by acoustic modes that propagate within the material with wavevector $q = \frac{4\pi n}{\lambda} sin(\theta/2)$, where λ is the wavelength of the incident laser light, θ the scattering angle, and n the refractive index of the material. Measurements were performed on 3–6 mm-sized fragments of glass, not cut nor polished, in air and at ambient temperature, using λ = 532 nm, with the incident and scattered light polarizations selected perpendicular to the scattering plane (VV scattering), in backscattering geometry ($\theta = 180°$). In this configuration, the scattering signal of transverse modes is extinguished, and only the detection of longitudinal modes is allowed. The scattered light was frequency analyzed by a high resolution and high contrast Sandercock-type tandem 3 + 3 pass Fabry–Pérot interferometer at the Department of Physics and Geology of the University of Perugia (Italy) (Scarponi et al., 2017). The interaction of light with longitudinal acoustic modes is responsible for a frequency shift of $\pm f_B$, that gives rise to a couple of peaks (Brillouin doublet) in the spectrum of the scattered light, I(ω), on the left and right of the Rayleigh central line. Multiple scattering contributions do not affect the data analysis (Corezzi et al., 2018). I(ω) was described in a restricted region around the Brillouin peaks with a damped harmonic oscillator function, $I(\omega)=R(\omega) \otimes I_0/\pi\{\omega_B^2\Gamma_B/[(\omega^2-\omega_B^2 + \omega^2\Gamma_B^2\}$, where $R(\omega)$ is the instrumental resolution function, $\otimes$ indicates the convolution operator, $f_B = \omega_B/2\pi$ and Γ_B correspond, respectively, to the frequency position and full-width-at-half-maximum of the Brillouin peaks, and I_0 is an amplitude factor that depends on the scattering cross-section. The Brillouin frequency f_B is related to the velocity v_L of the longitudinal acoustic waves, and then to the real part M' of the longitudinal elastic modulus through the following relationships: of the longitudinal elastic modulus through the following relationships:

$$v_L = \frac{\omega_B}{q} \quad (1)$$

$$M' = \rho\, v_L^2 \quad (2)$$

where ρ is the mass density. Notice that in backscattering geometry, the sound velocity in the material is related to the Brillouin frequency by:

$$v_L = \frac{\lambda f_B}{2n} \quad (3)$$

i.e., the measured f_B scales inversely with the incident laser wavelength λ.

3. Results

The chemical compositions of the analyzed glasses are reported in Table 1 and graphically portrayed on the total alkali-silica (TAS) diagram in Fig. 1 (Le Bas et al., 1986). The two subalkaline series show the most significant variation of SiO_2 content between end-members (48–72 wt% in Subalkaline; 47–74 wt% in Subalkaline-A), covering both K-alkaline (54–73 wt%) and Na-alkaline series (48–63 wt%). Alkaline content ranges from 1.9 wt% (in the SRP basalt B) to 9.3 wt% (in the Vulcano rhyolite RS); the Fe^{2+}/Fe_{tot} ratio varies between 0.59 and 0.72 (Table 2). Concerning the four additional glasses that do not belong to the series mentioned above, we provide their chemical composition and structural descriptors in Tables 1 and 2, respectively. 1) DPP has an andesitic composition which lies within the Subalkaline-A series, while the other samples fall outside the previously considered compositional range; 2) FRB is a trachyandesite with an alkali content higher than the K-alkaline series; 3) AMS is classified as a tephriphonolite, with even higher alkali content (~12 wt%); 4) EDF is a rhyolite whose SiO_2 content (~77 %) is the highest among the investigated glasses.

Fig. 2 shows the Brillouin spectra for the four series of glasses, normalized to the maximum intensity to better visualize the frequency shift of the Brillouin peaks with changes in glass composition. Glass homogeneity was verified by repeating the measurements in at least four different points of each sample. The Brillouin frequency f_B, the refractive index n and the theoretical density ρ of all samples, along with the corresponding values of sound velocity v_L (Eq. 3) and elastic modulus M' (Eq. 2), are reported in Table 3.

The Brillouin frequency of all samples is reported versus SiO_2 and alkaline content in Fig. 3a and b, respectively. The two subalkaline series display the most significant change of f_B (~8 GHz) and a similar and

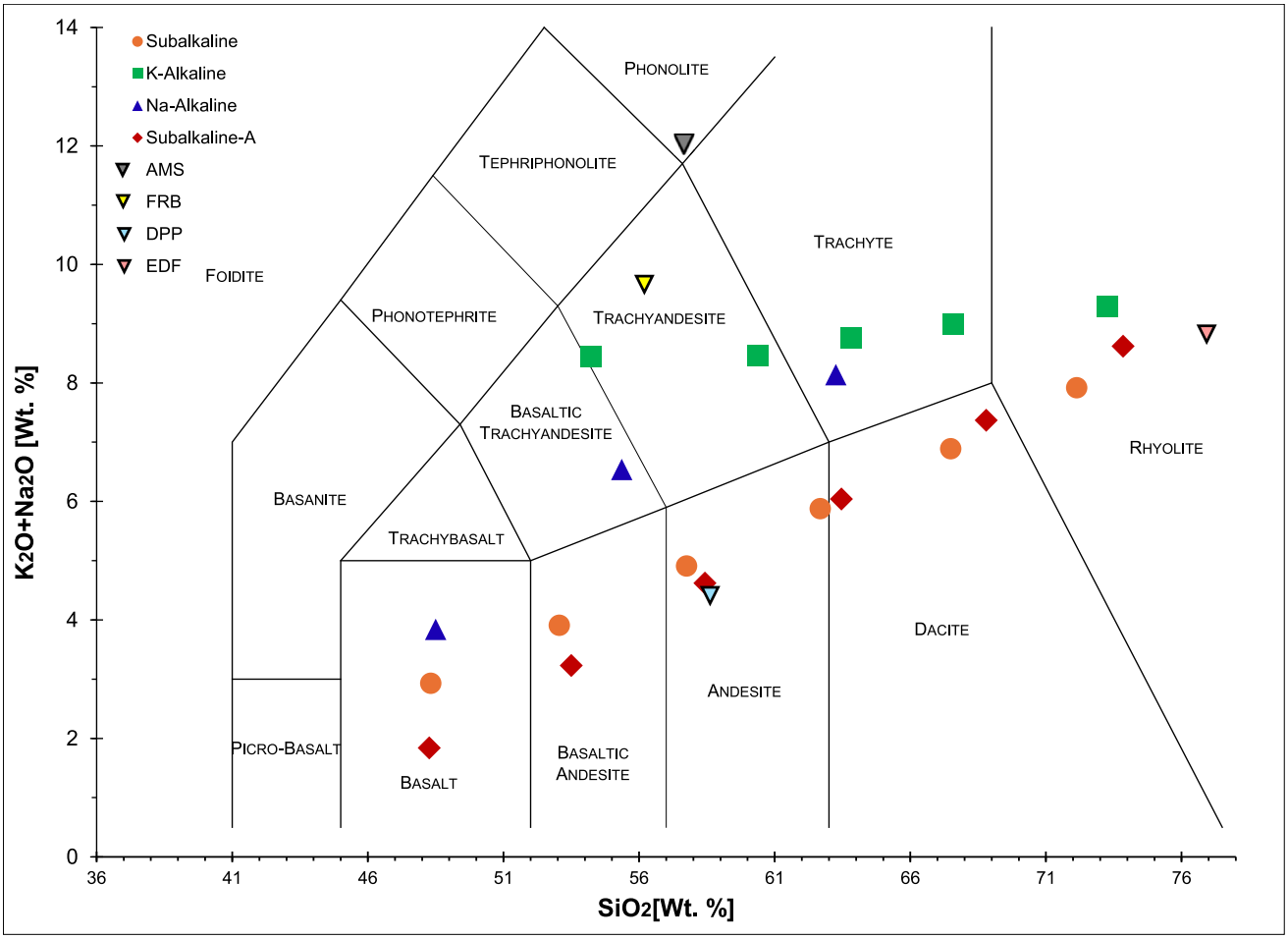

Fig. 1. Compositions of all glasses considered in this study, plotted on a TAS diagram, after Le Bas et al., 1986.

Table 2
Values of iron speciation, NBO/T (Eq. 4), and SCFM (Eq. 5). [1]Calculated as the mean of the values measured in the other members of the same series. [2]Assumed value.

Series	Sample	FeIII/ Fe Tot	NBO/T	SCFM
	B	0.61	2.19	0.68
	B8	0.63	1.68	0.74
	B6	0.70	1.26	0.80
	B4	0.64[1]	0.89	0.85
	B2	0.64[1]	0.57	0.90
Subalkaline	RB	0.59	0.31	0.95
	S	0.69[1]	0.92	0.78
	S3	0.71	0.71	0.85
	S5	0.72	0.53	0.89
	S7	0.71	0.36	0.92
K-alkaline	RS	0.61	0.15	0.97
	M	0.66	2.02	0.67
	M5	0.65	1.16	0.79
Na-alkaline	V	0.61	0.61	0.91
	B100	0.66	2.47	0.64
	B80	0.58	1.80	0.70
	B60	0.59	1.29	0.77
	B40	0.57	0.86	0.84
	B20	0.55	0.49	0.90
Subalkaline-A	R100	0.61	0.20	0.97
	AMS	0.5[2]	0.53	0.88
	FRB	0.5[2]	0.77	0.84
	DPP	0.5[2]	1.27	0.79
	EDF	0.5[2]	0.07	0.99
	Silica	–	0.00	1.00

considerable variation of SiO_2 (~25 wt%) and alkaline content (5–7 wt %). Concerning alkaline glasses, a f_B change of ~5 GHz is associated with a change of ~15 wt% of SiO_2 and ~ 4 wt% of alkalis in the Na-alkaline series; in contrast, in the K-alkaline series a f_B change of only ~3 GHz is associated with a substantial change of SiO_2 (~19 wt%) combined with a minimal change of alkalis (~1 wt%). Within each series, f_B has the highest value in the mafic end-member and decreases linearly with the increase of SiO_2 (Fig. 3a).

n and ρ values are calculated based on glass composition, following (Huggins and Sun, 1943) and (Kloess, 2000) and presented in Table 3. The density (ρ) ranges between 2.35 g/cm^3 (for AMS, the most felsic product) and 2.76 g/cm^3 (for B100, the most mafic product) and, within each series, reasonably decreases with increasing the SiO_2 content. We can compare the results of theoretical ρ with the observed bulk-ρ (Radica et al., 2024; Vetere et al., 2013) for the Subalkaline-A series (see Table 4). For the mafic endmember B100, the model underestimates the observed bulk-ρ of about 1.6 %. Conversely, with increasing silica, the theoretical-ρ values progressively overestimate the observed ones up to 5.6 % for the R100 sample. The mismatch between theoretical and observed densities is likely due to differences in the conceptualization of the atomic packing factor used in the calculations. Specifically, the theoretical density assumes ideal packing, where atoms are spaced according to their ionic radii. However, this idealized packing does not apply to real-case glasses. In glasses, especially the silica-rich ones, larger atomic rings form, and these larger rings are often empty. As a result, the packing efficiency deviates from the expected values derived by averaging the atomic ionic radii.

Table 3 also reports values of *M'*, which range from 118.4 GPa to 78.2 GPa, showing generally lower values for more silicic glasses. *M'* is

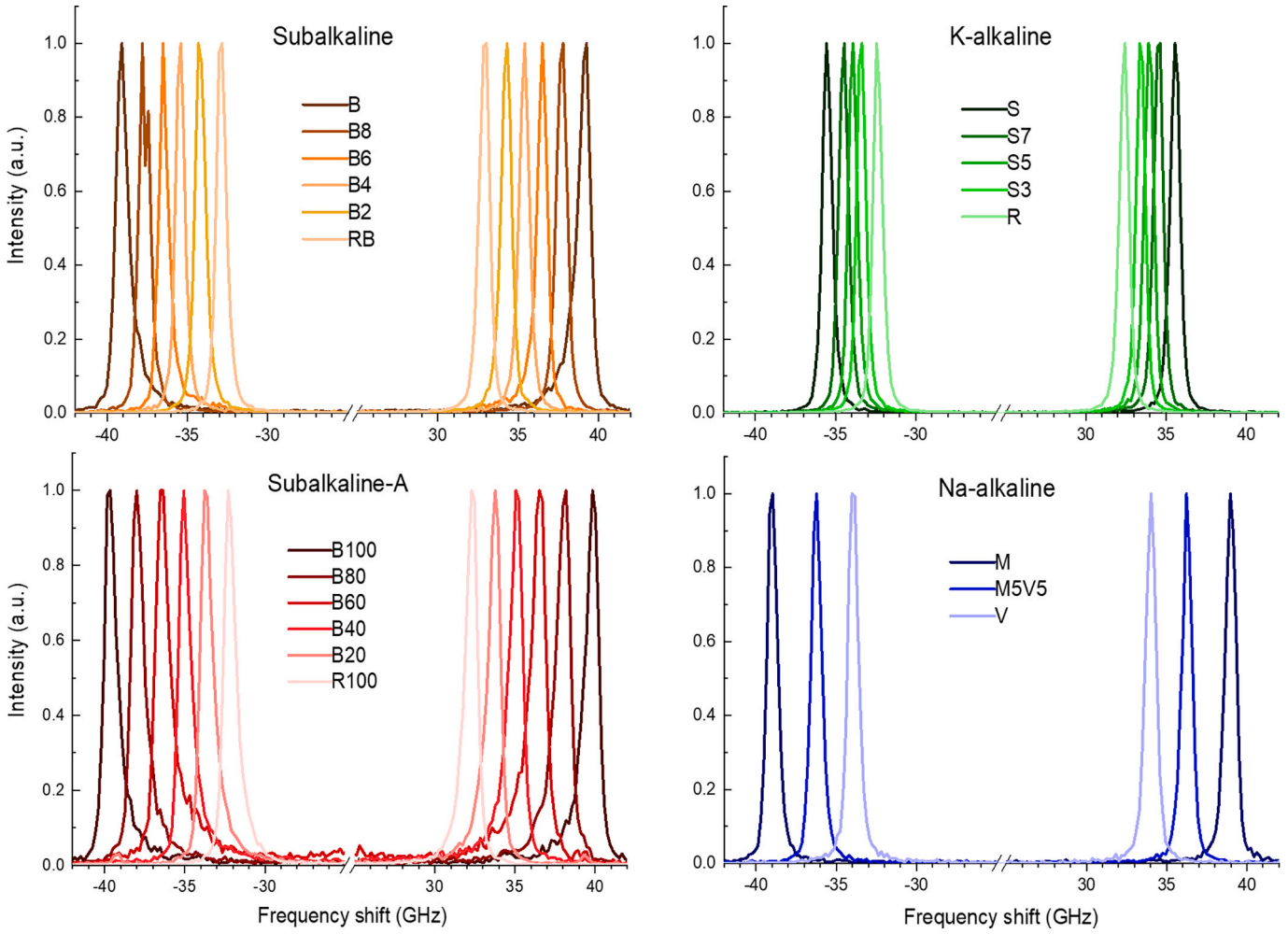

Fig. 2. Brillouin spectra of the four series of glasses investigated, as indicated in the legend.

determined from values of ρ and v_L (Eq. 2), and we can compare values of *M'* determined from calculated densities and from measured densities (Table 4), again resulting dependent on silica content: the discrepancies range from an underestimation of 1.7 % for B100 toward an overestimation of 5.5 % for R100.

Noting that the discrepancies between measured and calculated values are silica-dependent and given that R100 is the most silica-rich of the natural synthetic glasses considered in this study, we graphically present the discrepancy determined for R100 in all figures related to ρ or *M'*.

4. Discussion

On a first basis, the results in Figs. 3a indicate that the Brillouin frequency of silicate glasses depends on their chemical composition, of which SiO_2 is the most abundant component. This observation is in general agreement with previous studies (Malfait et al., 2011). However, the differing slopes observed for the various series of glasses suggest varying sensitivities to silica and, presumably, alkali content across the different series. This is evident for the K-alkaline series, where f_B has the narrowest shift of Brillouin peak (Fig. 2) that results in a lower slope of the behavior, plotted in Fig. 3a. Therefore, silica is not in itself a unique descriptor for the Brillouin frequency of the investigated systems, but other chemical and structural descriptors govern the shift of Brillouin peaks.

However, Vis- and Deep UV-Raman and FTIR spectra of volcanic glasses (in particular the subalkaline ones) suggest that the network connectivity is non-linearly related to the SiO_2 wt% (Cassetta et al., 2024; Radica et al., 2024). Indeed, the analysis of the Qn units suggests that the modification of the macroscopic elastic response of the medium is directly related to the polymerization degree (Benzine et al., 2021). Concerning the relationship between the elastic properties of glasses and their chemical composition, the existing studies on simulant iron-free (Malfait et al., 2011) and natural volcanic glasses (Cassetta et al., 2021a) indicate how introducing network modifier cations within the structure increases elastic moduli like the bulk modulus (K′) or the shear modulus (G'). In our case, Si^{4+} cations are certainly the most crucial network formers; the fact that f_B continually shifts toward lower values with increasing silica content is coherent with a decrease in the longitudinal elastic modulus *M'* (Eq. 2 and Eq. 3) and in agreement with the cited previous studies, being both G' and K′ linked to *M'* by a linear relationship. Nevertheless, since our case study involves glasses with a complex chemical composition, we must consider that other elements could potentially act as network formers under specific conditions: mostly Al^{3+} but also Fe^{3+}, Ti^{4+} and P^{5+} cations might form Ts (Di Genova et al., 2016; Mysen and Richet, 2005; Wu et al., 1999). This happens because alkalis, such as Na and K, act as charge balancers for cations like Fe^{3+} and Al^{3+} that require one electron to be stable in coordination with four oxygen atoms. Therefore, the generally lower Brillouin frequencies observed in our alkaline series (Fig. 3a) could be due to the above-mentioned ability of alkali to increase the number of actual network-forming cations. To provide an approximate description of the glass structure by using only the chemical composition, we correlate f_B with two chemical descriptors: i) NBO/T (Mysen and Richet,

Table 3
Elastic and optical properties of glasses: Density ρ calculated following (Kloess, 2000), refractive index *n* calculated following (Huggins and Sun, 1943), Brillouin frequency f_B, longitudinal acoustic velocity v_L (Eq. 2), and real part of the longitudinal elastic modulus *M'* (Eq. 3).

Series	Sample	ρ (g/cm^3)	*n*	f_B (GHz)	v_L (m/s)	M' (GPa)
Subalkaline	B	2.75	1.62	39.14	6443	114.0
	B8	2.68	1.60	37.64	6272	105.4
	B6	2.61	1.58	36.46	6146	98.6
	B4	2.54	1.55	35.35	6103	94.7
	B2	2.48	1.53	34.21	5976	88.4
	RB	2.41	1.51	32.93	5793	81.0
K-alkaline	S	2.63	1.57	35.51	6068	96.8
	S7	2.55	1.55	34.41	5899	88.7
	S5	2.50	1.54	33.82	5854	85.8
	S3	2.46	1.52	33.35	5830	83.5
	RS	2.39	1.50	32.35	5742	78.6
	M	2.75	1.62	38.81	6382	112.1
	M5	2.63	1.58	36.11	6091	97.5
Na-alkaline	V	2.50	1.53	33.87	5874	86.1
	B100	2.76	1.61	39.75	6554	118.4
	B80	2.67	1.58	38.02	6383	108.9
Subalkaline-A	B60	2.60	1.56	36.49	6209	100.2
	B40	2.53	1.54	35.10	6056	92.6
	B20	2.45	1.52	33.75	5908	85.7
	R100	2.37	1.50	32.33	5746	78.2
	AMS	2.52	1.52	33.69	5882	87.3
	FRB	2.57	1.53	34.59	6002	92.4
	DPP	2.58	1.54	36.01	6231	100.1
	EDF	2.35	1.49	32.76	5866	80.8
	Silica	2.20	1.46	32.91	5993	79.0

2005) describing the *depolymerization* of the tetrahedral network and ii) SCFM which is a phenomenological chemical index proposed by Walter and Salisbury (1989). Both parameters have been used as proxies for the structural configuration and the chemical character of silicate glasses (Cooper et al., 2002; Morlok et al., 2021; Pisello et al., 2019, 2022b, 2023). The NBO/T parameter quantifies the ratio of non-bridging oxygens per tetrahedron, indicating how many oxygens are not shared by two Ts. It conceptually describes the inverse of the development of the mentioned three-dimensional network. Thus, NBO/T values are high in mafic compositions and low in felsic compositions. Assuming that all oxygen atoms are engaged in either non-bridging (T-O) or bridging (T-O-T) bonds, this parameter is given by:

$$\frac{NBO}{T} = \frac{2 \bullet O - 4 \bullet T}{T} \quad (4)$$

Here, NBO is represented by $\sum_{i=1}^{i} nM_i^{n+}$, with M^{n+} representing the moles of network-modifying cations, whilst T represents the total moles of network former cations and O represents the total moles of oxygens. NBO/T parameter is calculated following (Prata et al., 2018), that considers as T the moles of cations of Si^{4+}, Ti^{4+}, and P^{5+}. Moreover, if there is an excess in alkalis for charge balance, also Al^{3+} and Fe^{3+} are assigned the role of T. The NBO/T parameter ranges from 0 in a fully polymerized glass/melt, where all oxygen atoms in each tetrahedral unit TO_4 are linked to adjacent tetrahedra, to 4 in an ideal, fully depolymerized structure.

The SCFM parameter, instead, is defined as:

$$SCFM = \frac{SiO_2}{SiO_2 + FeO + CaO + MgO} \quad (5)$$

where the oxide abundances are expressed in weight per cent. Table 2 reports the measured Fe^{2+}/Fe_{tot} ratio and the calculated NBO/T and SCFM parameters for all the investigated glasses.

Indeed, NBO/T is advantageous because it considers all chemical species but does not account for the coordination states of intermediate elements such as Fe^{3+}or Al^{3+}. On the other hand, SCFM is useful because it includes only a single species that can change its coordination state (Fe^{2+}, which can shift from 6- to 5-fold) but does not consider other chemical and structural components.

Fig. 3b reports the variation of f_B as a function of SCFM. The plot shows that the datapoints of the four investigated series collapse into a master curve described by a linear function (Table 5).

Fig. 3c shows the strong positive correlation between f_B and NBO/T. In this plot, the data from different sample series do not appear scattered like in Fig. 3a but follow the same curve, along which the value for pure silica (star) aligns better if compared to Fig. 3a. The f_B and NBO/T relationship is described by a linear function whose parameters are reported in Table 5.

Since the shift of f_B serves as a proxy for the sound velocity behavior (Eq. 3), the results in Fig. 3 indicate that the propagation of longitudinal sound waves in silicate glasses also correlates with the development of a

Table 4
Comparison between measured and calculated values of density (ρ) for the Subalkaline-A series, and corresponding values of longitudinal elastic modulus (*M'*).

Sample	ρ_{meas} (g/cm^3)	ρ_{calc} (g/cm)^3	Difference (%)	M' (ρ meas)	M' (ρ calc.)	%err
B100	2.804	2.76	-1.6	120.4	118.4	-1.7
B80	2.648	2.67	+0,8	107.9	108.9	+0.9
B60	2.599	2.60	+0,0	100.2	100.2	+0.0
B40	2.460	2.53	+2.8	90.2	92.6	+2.6
B20	2.366	2.45	+3.4	82.6	85.7	+3.6
R100	2.238	2.37	+5.6	73.9	78.2	+5.5

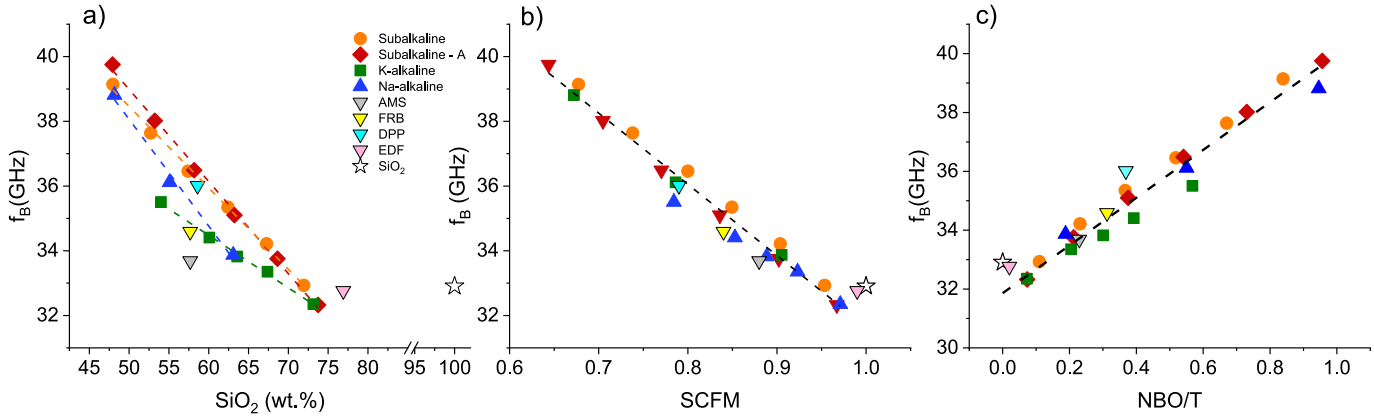

Fig. 3. Brillouin frequency f_B as a function of chemical and structural properties of the glass: a) SiO_2 content expressed as weight percent, b) SCFM calculated according to Eq. 5, c) polymerization degree NBO/T calculated according to Eq. 4. In panels b) and c), the dashed lines represent the linear regression of the data for the four investigated series presented in Fig. 2 (see Table 5 for parameters).

Table 5
Parameters of the linear regression fit of the data for various properties of the investigated glasses (see Figs. 3, 4 and 5).

	f_B (GHz) = a + b * SCFM	f_B (GHz) = a + b * NBO/T
Adj. R-Square	0.97986	0.96469
Intercept (a)	53.79327 ± 0.59793	31.85924 ± 0.17583
Slope (b)	−22.18159 ± 0.71079	8.11168 ± 0.3467
	M' (GPa) = a + b * SCFM	**M' (GPa) = a + b * NBO/T**
Adj. R-Square	0.97369	0.96349
Intercept (a)	190.83174 ± 3.30058	75.99337 ± 0.98313
Slope (b)	−116.23106 ± 3.89777	42.4038 ± 1.89177
	v_L(m/s) = a + b * SCFM	**v_L(m/s) = a + b * NBO/T**
Adj. R-Square	0.94818	0.91774
Intercept (a)	7983.60641 ± 103.41834	5690.79315 ± 29.88761
Slope (b)	−2321.01261 ± 124.29676	839.31517 ± 57.51071
	M' (GPa) = a + b * fB (GHz)	
Adj. R-Square	0.99263	
Intercept (a)	−93.56004 ± 3.2892	
Slope (b)	5.31586 ± 0.09348	

tetrahedral network, that can be described well by both NBO/T (molar ratio) and SCFM (calculated on weight %).

We have already mentioned how, in silicate glasses, introducing network modifiers should increase v_L and M'. In our case, this behavior is shown in Fig. 4a and b, where v_L and M' are calculated from the values of f_B, ρ and n, according to Eqs. 2 and 3 (Table 3). Surprisingly, Fig. 4a and b show that, in the range of variation of the quantities pertaining to silicate glasses of different compositional affinity, the dependence of M' on the parameters NBO/T and SCFM remains qualitatively similar to that of f_B. In fact, for both v_L and M', the data of all the synthetic magmatic series and pure silica are very well interpolated by a linear function vs. NBO/T and SCFM (Table 5). These results quantitatively confirm that the development of a tetrahedral network within the glass changes the elastic properties of the material; the parameters NBO/T and SCFM, even if differently defined, are both effective in describing such behavior. The relationships shown in Figs. 4b and 3c can be useful in retrieving NBO/T when the elastic modulus of natural silicate glasses is available, but a reliable chemical composition is missing. At the same time, the master curve generated by M' as a function of SCFM demonstrates that the elastic modulus is also controlled by the ratio between the main network-former cation (Si^{4+}) and the divalent network-modifiers (Fe^{2+}, Ca^{2+}, Mg^{2+}). This could be explained by the fact that the cations involved have relatively high field strengths, which efficiently reduce the atomic packing density and increase in the elastic moduli (Rouxel, 2007). When complex natural compositions are considered, SCFM captures a simplified scenario by taking into account the contributions of Ca, Mg and ferrous Fe because i) they always act as network modifiers, ii) they have a relative high field strength and iii) together with Si, which is included in SCFM, they represent the 70–80 wt % of the total composition.

It is important to note that the similarity between the behavior of f_B and M' as a function of SCFM in Figs. 3b and 4a and as a function of NBO/T in Figs. 3c and 4b, suggests a linear relationship between M' and f_B, the same for all the investigated glasses, as shown in Fig. 5. Therefore, within the range of variation of the network structure and chemical composition of our silicate glasses the quadratic analytical dependence on f_B, $M' = (\rho\lambda^2/4n^2)f_B^2$, can phenomenologically be replaced by an effective, linear relationship $M' = a + b \cdot f_B$, with a and b common to all glasses. The values of the best-fit coefficients, for λ = 532, are reported in Table 5, which can be readily readapted to different λ values (see Eq. 3). However, we emphasize that the same relationship does not apply to classes of glasses with very different compositions, such as industrial ones. Indeed, the compositions of magmatic rocks are heavily

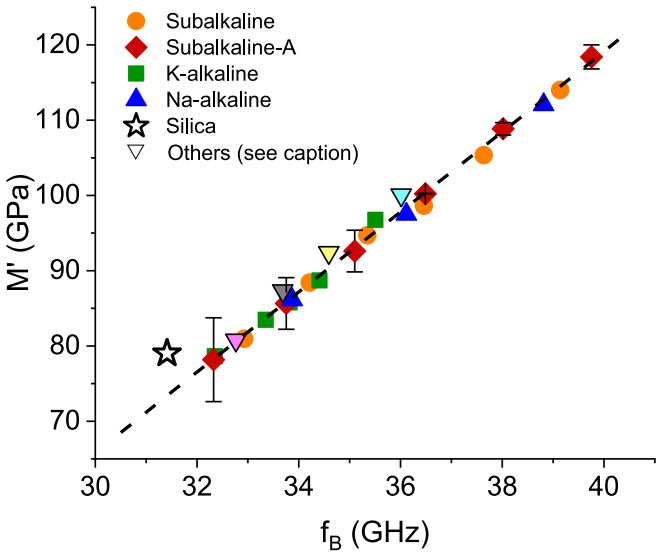

Fig. 5. Real part of the longitudinal elastic modulus M' plotted as a function of the Brillouin frequency f_B. The dashed line is the linear regression fit of the data for the four investigated series presented in Fig. 2 (see Table 5 for parameters).

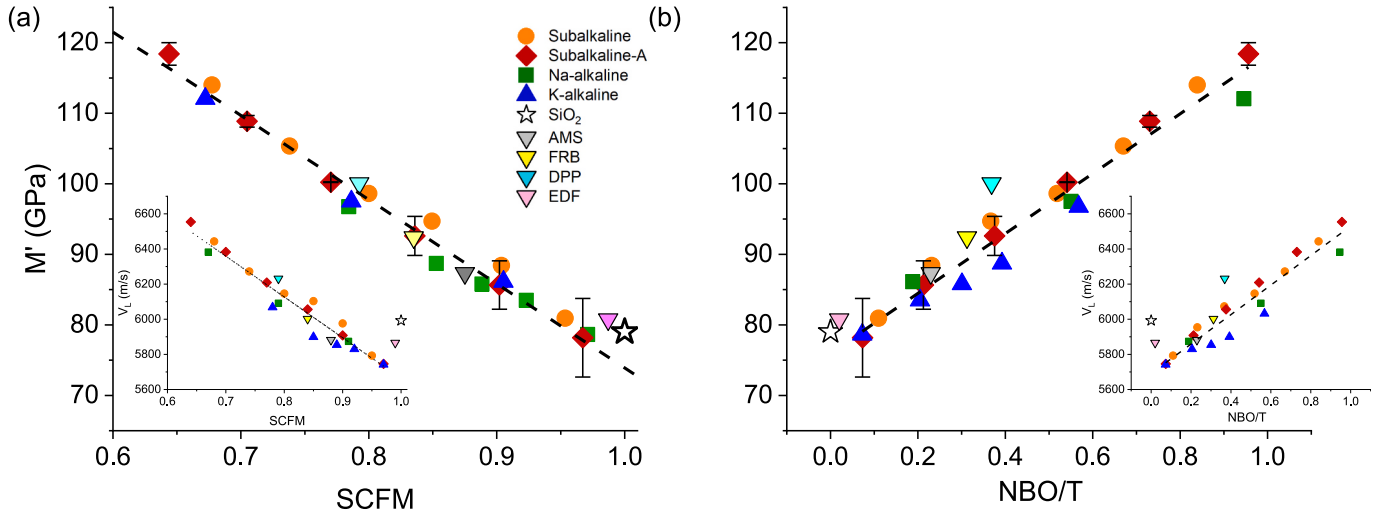

Fig. 4. Real part of the longitudinal elastic modulus M' (main panel) and longitudinal acoustic velocity v_L (inset) plotted as a function of (a) SCFM and (b) NBO/T. Dashed lines represent the linear regression of the data for the four investigated series presented in Fig. 2 (see Table 5 for parameters).

constrained in natural volcanic environments, as chemical parameters do not vary independently of one another (Cox et al., 1979). Generally, as SiO_2 content increases, the levels of FeO + Fe_2O_3, TiO_2, MgO, and CaO tend to decrease, while K_2O and Na_2O typically increase (Whitaker et al., 2005). Therefore, the composition of volcanic rocks can only vary within certain ranges, representing a very specific type of glass.

As a validating test, we have measured f_B for the four natural samples mentioned in the methodology section, namely FRB, DPP, AMS and EDF as well as the industrial SiO_2 glass. As for the four investigated series, these datapoints show a very rough linear relationship between f_B and SiO_2, that collapses into the master curves represented by dashed lines in Fig. 3b and c. In Fig.s 4 and 5, we can observe that these natural samples fit well within the scenario of lab-made silicate glasses, even if we observe a more relatively scattered distribution of external data for v_L.

Thus, we have collected data from other studies in order to observe if these relationships between chemical/structural features and physical properties can be verified and generalised. To do so, we retrieved values of *M'*, using Eq. 3, from various studies which calculated v_L (Cassetta et al., 2021; Hushur et al., 2013; Malfait et al., 2011; Schilling et al., 2001; Whittington et al., 2012) of natural and synthetic silicate glasses that were characterized in those and other studies (Di Genova et al., 2015, 2017, 2020, 2023; Richet and Polian, 1998). To use Eq. 3, we calculated the density of the glasses produced for this study (Kloess, 2000). Results are reported in Fig. 6 where we can observe how v_L and *M'* decrease with increasing SCFM and with decreasing NBO/T.

For what concerns SCFM (Fig. 6a), data from other studies generally follow the same trends as observed in Fig. 4a: v_L and *M'* decrease linearly with increasing SCFM, though a small discrepancy can be observed for peridotitic glasses investigated by Di Genova et al., 2023.

Regarding NBO/T, such discrepancy is even more evident, with the same dataset detaching from the general trend. It must be said that NBO/T values for all these data were calculated with the model proposed by Prata et al., 2018, but, as it is possible to see in Fig. 6b, peridotitic products (Di Genova et al., 2023) present NBO/T values larger than 4, which is conceptually impossible. In Prata et al., 2018, NBO/T is determined by taking into account a complex molar equilibrium of different cations: Si^{4+}, Ti^{4+}, and P^{5+} are always accounted as network formers, whereas Al^{3+} and Fe^{3+} are also accounted as network formers, but only in so far as there are Na^+ and K^+ cations to balance their charge; Fig. 6b shows how, in natural silicate glasses with silicic and mildly mafic compositions, this parameter efficiently represents the complex interplay of different elements and other factors that determine elastic properties of the material. Again, it is not particularly efficient when dealing with peridotitic compositions. Moreover, in simpler compositions showing non-natural compositions, like the ones by Schilling et al., 2001, NBO/T determination is not efficient to exhaustively summarize such complex interplay when important components such as iron or alkalis, which are included in NBO/T calculations, are missing, other factors might arise to be more decisive in determining mechanical properties of the material. Thereby, the NBO/T calculation used in this study is probably not valid for all glasses, but it can only be used as a proxy for the mechanical properties of non-ultramafic natural silicate glasses.

It emerges that alkaline earth ions (M^{2+}) play a crucial role in the propagation of longitudinal waves in silicate glasses. This significant effect can be attributed to their interaction with the tetrahedra present in the structure. Specifically, M^{2+} ions interact twice as much with NBO compared to M^+ ions. These stronger interactions improve the connectivity and stiffness of the silicate framework, enhancing *M'* and resulting in a greater resistance to deformation under compression (de Macedo et al., 2018; Hehlen and Neuville, 2020; Schilling et al., 2001; Weigel et al., 2016). Thus, the sound or mechanical longitudinal waves propagate more efficiently through the material, maintaining their energy and speed. In other words, the concentration of M^{2+} (Ca^{2+}, Mg^{2+} and Fe^{2+}) cations strengthens the structural matrix much better than M^+ (Hehlen and Neuville, 2020), allowing for more efficient transmission of longitudinal waves. This observation is supported by experimental and literature data, which show distinct behavior in materials containing alkaline earths compared to those with only alkali also in terms of the cation size (de Macedo et al., 2018; Weigel et al., 2016). To sum everything up, the scenario emerging from this study shows that the elastic properties of different glasses having complex natural compositions respond to a general rule controlled by the structure (molecular arrangement) of the glass, which is determined by the composition of the glass. However, the development of this structure is not fully captured by the NBO/T parameter. Instead, the relative content of silica and main divalent cation oxides, represented by the SCFM parameter, is empirically more effective in describing the relationship between elastic properties and composition.

5. Conclusions

In this study we have applied Brillouin light scattering spectroscopy on natural silicate glasses and produced a systematic dataset of Brillouin

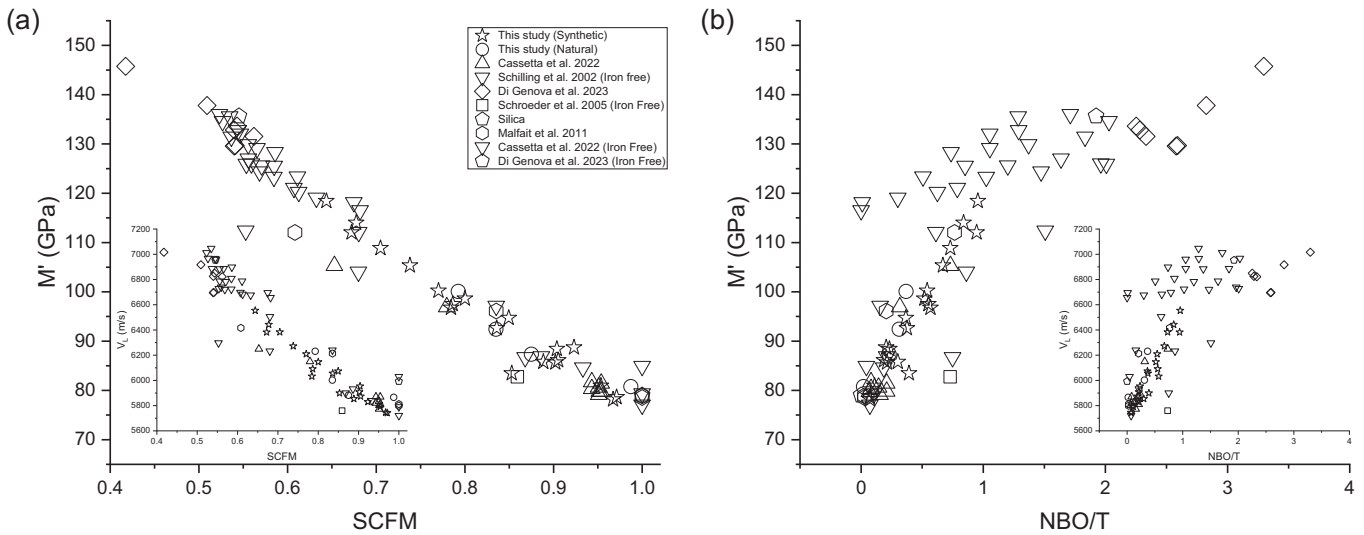

Fig. 6. Real part of the longitudinal elastic modulus *M'* (main panel) and longitudinal acoustic velocity v_L (inset) plotted as a function of (a) SCFM and (b) NBO/T for several glasses, including those investigated in the present work and in other studies (see legend).

spectra, spanning a large range of chemical compositions of igneous rocks cropping out on the planet Earth and other terrestrial analogues. The frequency of Brillouin peaks depends on a complex interplay between network-former and network-modifier cations. However, through parameterization and careful analysis, we have obtained the following results:

- The Brillouin frequency f_B quantitatively correlates with chemical composition, with more felsic glass exhibiting lower frequencies. This correlation is effectively parameterized by NBO/T and SCFM, for which two linear interpolation equations are proposed (Fig. 3c and d, Table 5).
- The relationship between *M'* and NBO/T and SCFM (Fig. 4) is linear, implying that *M'* and f_B are also linearly related (Fig. 5). This linear dependence is highly relevant for analytical petro-geological applications, as it holds for glasses with natural/complex chemical compositions.
- Comparison with data from other studies confirms the linear dependence of *M'* on SCFM in silicate glasses. However, this relationship does not hold for *M'* and NBO/T in ultramafic and iron-free compositions. Overall, we find that technical silicate glasses (i.e., non-natural compositions) do not consistently follow the observed trends.

The shift in f_B observed in alkaline-earth-rich glasses is likely due to the divalent cations, which induce coupled motion in the surrounding structure, whereas vibrations of alkali cations are primarily governed by the cation's own movement. The coupled distribution of cation-network interactions may play a key role in modulating the propagation of longitudinal sound waves, as evidenced by the linear correlation between SCFM and f_B.

These findings have important implications for using Brillouin spectroscopy as a tool for studying Earth and planetary materials, enabling both the chemical characterization of glasses via f_B and, conversely, the estimation of elastic properties from chemical composition, as outlined in Table 5.

Potential applications of this study include the physical characterization of scoriae, lapilli, pumices and ashes, where elasticity assessment is crucial. Due to the small laser spot size on the sample (less than 100 × 100 μm), Brillouin spectroscopy enables micro-mapping of heterogeneous elasticity at a fine scale. It can also be used to analyze stress distribution in heterogenous materials, such as interfaces, profiles, filaments, and phase-separated regions, providing insights into local fragmentation, residual stresses, and elasticity evolution.

Furthermore, expanding the dataset to include additional compositions would provide a solid foundation for comparing potential data collected from planetary surfaces during future space missions equipped with Brillouin systems.

CRediT authorship contribution statement

Alessandro Pisello: Writing – review & editing, Writing – original draft, Visualization, Validation, Supervision, Methodology, Investigation, Formal analysis. **Silvia Corezzi:** Writing – review & editing, Validation, Supervision, Methodology, Investigation, Conceptualization, Funding acquisition, Resources, Project administration. **Michele Cassetta:** Writing – review & editing, Visualization, Validation, Methodology, Investigation, Formal analysis, Data curation. **Francesco Radica:** Writing – review & editing, Methodology, Investigation, Formal analysis, Data curation. **Lucia Comez:** Writing – review & editing, Supervision, Methodology, Formal analysis. **Gianluca Iezzi:** Writing – review & editing, Supervision, Resources, Project administration, Formal analysis, Conceptualization. **Andrea Vitrano:** Writing – review & editing, Visualization, Formal analysis. **Francesco Pasqualino Vetere:** Writing – review & editing, Methodology, Investigation, Funding acquisition, Formal analysis, Data curation, Conceptualization. **Diego Perugini:** Writing – review & editing, Supervision, Resources, Project administration, Methodology, Conceptualization.

Declaration of competing interest

The authors declare that they have no known competing financial interests or personal relationships that could have appeared to influence the work reported in this paper.

Acknowledgments

D. Perugini acknowledges financial support from the European Research Council (Consolidator Grant ERC-2013-COG No. 612776, CHRONOS project); A. Pisello from DAAD-MIUR JMP N. 14103; F. Vetere from *Piano di Sostegno alla Ricerca 2022 per finanziamenti a progetti di ricerca curiosity-driven* (F-CUR CREAMI project); G. Iezzi from the Italian Ministry of University and Research (MUR) under the PRIN project 2009PZ47NA_003 and the National PNRR-MUR project (DM. 1062, 10/08/2021) REACT-EU - PON R&I 2014-2020 (*Azione IV.4 Contratti di Ricerca su tematiche Green*), and from *Fondi Ateneo* of the University G. D'Annunzio of Chieti-Pescara. S. Corezzi and L. Comez acknowledge that this work has been funded by the European Union - NextGenerationEU, Mission 4, Component 2, under the Italian Ministry of University and Research (MUR) National Innovation Ecosystem Grant ECS00000041 - VITALITY - CUP J97G22000170005 and CUP B43C22000470005. Support from the Italian Space Agency (ASI) under the ASI-UniPG agreement 2019-2-HH.0, and from the Italian Ministry of University and Research (MUR) under the *Dipartimenti di Eccellenza 2023-2027* funding program (Department of Physics and Geology, University of Perugia, SUPER-C project) is also acknowledged. The authors thank J. Vasseur (LMU Department of Earth and Environment) for technical support during EPMA analyses and express their gratitude to H. Behrens (Leibniz Universität Hannover) for iron speciation determination, S. Costanzo for inspiring discussions, and T. Witcher and C. Bocconotti for linguistic and technical support.

Appendix A. Supplementary data

A file containing all raw BLS spectra is provided. This file contains the spectral data which, after normalization, are reported in Fig. 2. Supplementary data to this article can be found online at [https://doi.org/10.1016/j.chemgeo.2025.122719].

Data availability

Raw spectral data produced specifically for this study are reported in Appendix A. All the data that were retrieved from calculations are reported in Tables.

References

Bansal, N.P., Doremus, R.H., 2013. Handbook of Glass Properties. Elsevier.
Behrens, H., Zhang, Y., 2009. H2O diffusion in peralkaline to peraluminous rhyolitic melts. Contrib. Mineral. Petrol. 157, 765–780.
Benzine, O., Pan, Z., Calahoo, C., Bockowski, M., Smedskjaer, M.M., Schirmacher, W., Wondraczek, L., 2021. Vibrational disorder and densification-induced homogenization of local elasticity in silicate glasses. Sci. Rep. 11 (1), 1–12. https://doi.org/10.1038/s41598-021-04045-6.
Cassetta, M., Di Genova, D., Zanatta, M., Boffa Ballaran, T., Kurnosov, A., Giarola, M., Mariotto, G., 2021. Estimating the viscosity of volcanic melts from the vibrational properties of their parental glasses. Sci. Rep. 11 (1), 1–14. https://doi.org/10.1038/s41598-021-92407-5.
Cassetta, M., Mariotto, G., Daldosso, N., De Bona, E., Biesuz, M., Sorarù, G.D., Almeev, R., Zanatta, M., Vetere, F., 2023. Viscosity, Boson Peak and Elastic Moduli in the Na_2O-SiO_2 System. Minerals 13, 1166. https://doi.org/10.3390/min13091166.
Cassetta, M., Rossi, B., Mazzocato, S., Vetere, F., Iezzi, G., Pisello, A., Zanatta, M., Daldosso, N., Giarola, M., Mariotto, G., 2024. Deep-UV Raman spectroscopy: a novel heuristic method to characterize volcanologically relevant glasses on Mars. Chem. Geol. 644, 121867. https://doi.org/10.1016/j.chemgeo.2023.121867.

Cooper, B.L., Salisbury, J.W., Killen, R.M., Potter, A.E., 2002. Midinfrared spectral features of rocks and their powders. J. Geophys. Res. Planets 107, 1.
Corezzi, S., Comez, L., Zanatta, M., 2018. A simple analysis of Brillouin spectra from opaque liquids and its application to aqueous suspensions of poly-N-isopropylacrylamide microgel particles. J. Mol. Liq. 266, 460–466.
Corsaro, R.A., Métrich, N., 2016. Chemical heterogeneity of Mt. Etna magmas in the last 15 ka. Inferences on their mantle sources. Lithos 252, 123–134.
Cox, K.G., Bell, J.D., Pankhurst, R.J., 1979. The Interpretation of Igneous Rocks. The Interpretation of Igneous Rocks. https://doi.org/10.1007/978-94-017-3373-1.
De Astis, G., La Volpe, L., Peccerillo, A., Civetta, L., 1997. Volcanological and petrological evolution of Vulcano island (Aeolian Arc, southern Tyrrhenian Sea). J. Geophys. Res. Solid Earth 102, 8021–8050.
de Macedo, G.N.B.M., Sawamura, S., Wondraczek, L., 2018. Lateral hardness and the scratch resistance of glasses in the Na2O-CaO-SiO2 system. J. Non-Cryst. Solids 492, 94–101. https://doi.org/10.1016/J.JNONCRYSOL.2018.04.022.
Di Genova, D., Morgavi, D., Hess, K.-U., Neuville, D.R., Borovkov, N., Perugini, D., Dingwell, D.B., 2015. Approximate chemical analysis of volcanic glasses using Raman spectroscopy. J. Raman Spectrosc. 46, 1235–1244.
Di Genova, D., Hess, K.-U., Chevrel, M.O., Dingwell, D.B., 2016. Models for the estimation of Fe3+/Fetot ratio in terrestrial and extraterrestrial alkali-and iron-rich silicate glasses using Raman spectroscopy. Am. Mineral. 101, 943–952.
Di Genova, D., Kolzenburg, S., Wiesmaier, S., Dallanave, E., Neuville, D.R., Hess, K.U., Dingwell, D.B., 2017. A compositional tipping point governing the mobilization and eruption style of rhyolitic magma. Nature 552, 235–238.
Di Genova, D., Zandona, A., Deubener, J., 2020. Unravelling the effect of nano-heterogeneity on the viscosity of silicate melts: Implications for glass manufacturing and volcanic eruptions. J. Non-Cryst. Solids 545, 120248. https://doi.org/10.1016/J.JNONCRYSOL.2020.120248.
Di Genova, D., Bondar, D., Zandonà, A., Valdivia, P., Al-Mukadam, R., Fei, H., Withers, A. C., Boffa Ballaran, T., Kurnosov, A., McCammon, C., Deubener, J., Katsura, T., 2023. Viscosity of anhydrous and hydrous peridotite melts. Chem. Geol. 625, 121440. https://doi.org/10.1016/J.CHEMGEO.2023.121440.
Di Muro, A., Métrich, N., Mercier, M., Giordano, D., Massare, D., Montagnac, G., 2009. Micro-Raman determination of iron redox state in dry natural glasses: Application to peralkaline rhyolites and basalts. Chem. Geol. 259, 78–88.
Dingwell, D.B., 1996. Volcanic dilemma: Flow or blow? Science 1979 (273), 1054–1055. https://doi.org/10.1126/science.273.5278.1054.
Galeener, F.L., Geissberger, A.E., Weeks, R.A., 1984. On the thermal history of Libyan Desert glass. J. Non-Cryst. Solids 67, 629–636.
Giordano, D., Russell, J.K., Dingwell, D.B., 2008. Viscosity of magmatic liquids: a model. Earth Planet. Sci. Lett. 271, 123–134. https://doi.org/10.1016/j.epsl.2008.03.038.
Gonnermann, H.M., Manga, M., 2007. The fluid mechanics inside a Volcano. Annu. Rev. Fluid Mech. 39, 321–356. https://doi.org/10.1146/annurev.fluid.39.050905.110207.
Hehlen, B., Neuville, D.R., 2020. Non network-former cations in oxide glasses spotted by Raman scattering. Phys. Chem. Chem. Phys. 22, 12724–12731. https://doi.org/10.1039/D0CP00630K.
Hess, K.U., Dingwell, D.B., 1996. Viscosities of hydrous leucogranitic melts: a non-Arrhenian model. Am. Mineral. 81, 1297–1300.
Huggins, M.L., Sun, K.-H., 1943. Calculation of density and optical constants of a glass from its composition in weight percentage. J. Am. Ceram. Soc. 26, 4–11.
Hushur, A., Manghnani, M.H., William, S.Q., Dingwell, D.B., 2013. A high-temperature Brillouin scattering study on four compositions of haplogranitic glasses and melts: High-frequency elastic behavior through the glass transition. Am. Mineral. 98, 367–375. https://doi.org/10.2138/AM.2013.4198/MACHINEREADABLECITATION/RIS.
Iezzi, G., Mollo, S., Ventura, G., Cavallo, A., Romano, C., 2008. Experimental solidification of anhydrous latitic and trachytic melts at different cooling rates: the role of nucleation kinetics. Chem. Geol. 253, 91–101.
Iezzi, G., Mollo, S., Torresi, G., Ventura, G., Cavallo, A., Scarlato, P., 2011. Experimental solidification of an andesitic melt by cooling. Chem. Geol. 283, 261–273.
Jabraoui, H., Vaills, Y., Hasnaoui, A., Badawi, M., Ouaskit, S., 2016. Effect of sodium oxide modifier on structural and elastic properties of silicate glass. J. Phys. Chem. B 120, 13193–13205.
Kloess, G., 2000. Dichtefluktuationen natürlicher Gläser, Habil Thesis. Universität Jena.
Kress, V.C., Carmichael, I.S.E., 1991. The compressibility of silicate liquids containing Fe2O3 and the effect of composition, temperature, oxygen fugacity and pressure on their redox states. Contrib. Mineral. Petrol. 108, 82–92.
Le Bas, M.J., Le Maitre, R.W., Streckeisen, A., Zanettin, B., 1986. A chemical classification of volcanic rocks based on the total alkali silica diagram. J. Petrol. 27, 745–750. https://doi.org/10.1093/petrology/27.3.745.
Le Losq, C., Neuville, D.R., 2013. Effect of the Na/K mixing on the structure and the rheology of tectosilicate silica-rich melts. Chem. Geol. 346, 57–71. https://doi.org/10.1016/J.CHEMGEO.2012.09.009.
Le Losq, C., Sossi, P.A., 2023. Atomic structure and physical properties of peridotite glasses at 1 bar. Front. Earth Sci. (Lausanne) 11, 1040750. https://doi.org/10.3389/FEART.2023.1040750/BIBTEX.
Malfait, W.J., Sanchez-Valle, C., Ardia, P., Médard, E., Lerch, P., 2011. Compositional dependent compressibility of dissolved water in silicate glasses. Am. Mineral. 96, 1402–1409. https://doi.org/10.2138/AM.2011.3718/MACHINEREADABLECITATION/RIS.
Morgavi, D., Perugini, D., De Campos, C.P., Ertl-Ingrisch, W., Lavallée, Y., Morgan, L., Dingwell, D.B., 2013. Interactions between rhyolitic and basaltic melts unraveled by chaotic mixing experiments. Chem. Geol. 346, 199–212. https://doi.org/10.1016/j.chemgeo.2012.10.003.
Morlok, A., Renggli, C., Charlier, B., Reitze, M.P., Klemme, S., Namur, O., Sohn, M., Martin, D., Weber, I., Stojic, A.N., Hiesinger, H., Joy, K.H., Wogelius, R., Tollan, P., Carli, C., Bauch, K.E., Helbert, J., 2021. Mid-infrared reflectance spectroscopy of synthetic glass analogs for Mercury surface studies. Icarus 361, 114363. https://doi.org/10.1016/J.ICARUS.2021.114363.
Mysen, B.O., Richet, P., 2005. Silicate Glasses and Melts: Properties and Structure. Elsevier.
Neuville, D.R., Henderson, G.S., Dingwell, D.B., 2022. Geological melts. Geol. Melts 1–1088. https://doi.org/10.1515/9781501510939/PDF.
Pisello, A., Vetere, P., Bisolfati, M., Maturilli, A., Morgavi, D., Pauselli, C., Iezzi, G., Lustrino, M., Perugini, D., 2019. Retrieving magma composition from TIR spectra: implications for terrestrial planets investigations. Sci. Rep. 9, 1–13.
Pisello, A., De Angelis, S., Ferrari, M., Porreca, M., Vetere, F.P., Behrens, H., De Sanctis, M.C., Perugini, D., 2022a. Visible and near-InfraRed (VNIR) reflectance of silicate glasses: Characterization of a featureless spectrum and implications for planetary geology. Icarus 374, 114801. https://doi.org/10.1016/J.ICARUS.2021.114801.
Pisello, A., Ferrari, M., De Angelis, S., Vetere, F.P., Porreca, M., Stefani, S., Perugini, D., 2022b. Reflectance of silicate glasses in the mid-infrared region (MIR): Implications for planetary research. Icarus 388, 115222. https://doi.org/10.1016/J.ICARUS.2022.115222.
Pisello, A., Bisolfati, M., Poggiali, G., Tolomei, P., Braschi, E., Brucato, J.R., Perugini, D., 2023. Mid-infrared (MIR) spectroscopy of silicate glasses as analogs for mercury's surface: the influence of grain size. Minerals 13, 170. https://doi.org/10.3390/MIN13020170.
Prata, G.S., Ventress, L.J., Carboni, E., Mather, T.A., Grainger, R.G., Pyle, D.M., 2018. A new parameterization of volcanic ash complex refractive index based on NBO/T and SiO2 content. J. Geophys. Res. Atmos. 124, 1779–1797.
Radica, F., Cassetta, M., Iezzi, G., Pisello, A., Vetere, F., Del Vecchio, A., Cestelli Guidi, M., Poe, B.T., 2024. Short-range order and chemical compositions of glasses along the basaltic-rhyolite sub-alkaline join by Raman and FTIR spectroscopies. Chem. Geol. 648, 121938. https://doi.org/10.1016/J.CHEMGEO.2024.121938.
Richet, P., Polian, A., 1998. Water as a dense icelike component in silicate glasses. Science 1979 (281), 396–398. https://doi.org/10.1126/SCIENCE.281.5375.396/ASSET/C5F0EA69-1B68-4218-AD0F-A7B1E68EADE5/ASSETS/GRAPHIC/SE2986680004.JPEG.
Rouxel, T., 2007. Elastic properties and short-to medium-range order in glasses. J. Am. Ceram. Soc. 90, 3019–3039.
Scannell, G., Barra, S., Huang, L., 2016. Structure and properties of Na2O-TiO2-SiO2 glasses: Role of Na and Ti on modifying the silica network. J. Non-Cryst. Solids 448, 52–61.
Scarponi, F., Mattana, S., Corezzi, S., Caponi, S., Comez, L., Sassi, P., Morresi, A., Paolantoni, M., Urbanelli, L., Emiliani, C., others, 2017. High-performance versatile setup for simultaneous Brillouin-Raman microspectroscopy. Phys. Rev. X 7, 31015.
Schilling, F.R., Hauser, M., Sinogeiken, S.V., Bass, J.D., 2001. Compositional dependence of elastic properties and density of glasses in the system anorthite-diopside-forsterite. Contrib. Mineral. Petrol. 141, 297–306. https://doi.org/10.1007/S004100100253/METRICS.
Schuessler, J.A., Botcharnikov, R.E., Behrens, H., Misiti, V., Freda, C., 2008. Amorphous Materials: Properties, structure, and Durability: Oxidation state of iron in hydrous phono-tephritic melts. Am. Mineral. 93, 1493–1504.
Speziale, S., Marquardt, H., Duffy, T.S., 2014. Brillouin Scattering and its Application in Geosciences. Rev. Mineral. Geochem. 78, 543–603. https://doi.org/10.2138/RMG.2014.78.14.
Tamic, N., Behrens, H., Holtz, F., 2001. The solubility of H2O and CO2 in rhyolitic melts in equilibrium with a mixed CO_2–H_2O fluid phase. Chem. Geol. 174, 333–347. https://doi.org/10.1016/S0009-2541(00)00324-7.
Vaills, Y., Luspin, Y., Hauret, G., Coté, B., 1993. Elastic properties of sodium magnesium silica and sodium calcium silica glasses by brillouin scattering. Solid State Commun. 87, 1097–1100.
Vetere, F., Iezzi, G., Behrens, H., Cavallo, A., Misiti, V., Dietrich, M., Knipping, J., Ventura, G., Mollo, S., 2013. Intrinsic solidification behaviour of basaltic to rhyolitic melts: a cooling rate experimental study. Chem. Geol. 354, 233–242. https://doi.org/10.1016/J.CHEMGEO.2013.06.007.
Vetere, F.P., Holtz, F., Behrens, H., Botcharnikov, R.E., Fanara, S., 2014. The effect of alkalis and polymerization on the solubility of H_2O and CO_2 in alkali-rich silicate melts. Contrib. Mineral. Petrol. 167, 1014.
Vetere, F., Iezzi, G., Behrens, H., Holtz, F., Ventura, G., Misiti, V., Cavallo, A., Mollo, S., Dietrich, M., 2015a. Glass forming ability and crystallisation behaviour of sub-alkaline silicate melts. Earth Sci. Rev. 150, 25–44.
Vetere, F., Petrelli, M., Morgavi, D., Perugini, D., 2015b. Dynamics and time evolution of a shallow plumbing system: the 1739 and 1888–90 eruptions, Vulcano Island, Italy. J. Volcanol. Geotherm. Res. 306, 74–82.
Walter, L.S., Salisbury, J.W., 1989. Spectral characterization of igneous rocks in the 8-to 12-μm region. J. Geophys. Res. Solid Earth 94, 9203–9213.
Webb, S.L., 1992. Shear, volume, enthalpy and structural relaxation in silicate melts. Chem. Geol. 96, 449–457. https://doi.org/10.1016/0009-2541(92)90072-D.
Weigel, C., Le Losq, C., Vialla, R., Dupas, C., Clément, S., Neuville, D.R., Rufflé, B., 2016. Elastic moduli of $XAlSiO_4$ aluminosilicate glasses: effects of charge-balancing cations. J. Non-Cryst. Solids 447, 267–272.
Whitaker, M.L., Nekvasil, H., Lindsley, D.H., Whitaker, M.L., Nekvasil, H., Lindsley, D.H., 2005. Potential Magmatic Diversity on Mars. LPI 1440.
Whittington, A.G., Richet, P., Polian, A., 2012. Amorphous materials: Properties, structure, and durability: Water and the compressibility of silicate glasses: a Brillouin spectroscopic study. Am. Mineral. 97, 455–467. https://doi.org/10.2138/AM.2012.3891/MACHINEREADABLECITATION/RIS.

Wu, Z., Romano, C., Marcelli, A., Mottana, A., Cibin, G., Della Ventura, G., Giuli, G., Courtial, P., Dingwell, D.B., 1999. Evidence for Al/Si tetrahedral network in aluminosilicate glasses from Al K-edge X-ray-absorption spectroscopy. Phys. Rev. B 60, 9216.

Wu, L., Yang, D. Bin, Liu, J.X., Hu, B., Xie, H. Sen, Li, F.F., Yu, Y., Xu, W.L., Gao, C.X., 2017. A Brillouin scattering study of hydrous basaltic glasses: the effect of H_2O on their elastic behavior and implications for the densities of basaltic melts. Phys. Chem. Miner. 44, 431–444. https://doi.org/10.1007/S00269-017-0870-9/METRICS.

Zanotto, E.D., Mauro, J.C., 2017. The glassy state of matter: its definition and ultimate fate. J. Non-Cryst. Solids 471, 490–495. https://doi.org/10.1016/J.JNONCRYSOL.2017.05.019.

Acknowledgements

I would like to express my deepest gratitude to my supervisor, **F. Vetere**, for his guidance, mentorship, and for his suggestions, feedback, and encouragement, essential to the completion of this PhD journey. I acknowledge the PhD program in "Scienze e Tecnologie Ambientali, Geologiche e Polari" at the University of Siena and the *"Piano di Sostegno alla Ricerca 2022 per finanziamenti a progetti di ricerca Curiosity-driven (F-CUR CREAMI)"*. I would like to thank the Museo Nazionale dell'Antartide (MNA, Siena) for the loan of the meteorite samples. In particular, I want to thank **Sonia Sandroni** and **Rosaria Palmeri** for their support. I would like to thank **Prof. Giovanna Giorgetti** and **Prof. Cecilia Viti**, *Department of Physical Sciences, Earth and Environment, University of Siena*, for their support. My sincere thanks go to the students and people of the University of Siena, thank you for the stimulating discussions, for sharing your insights, and for creating a supportive and collaborative environment. I am grateful to the administrative staff. I thank **Nicola Corti** from *DFSTA, University of Siena*, and **Domenico Mannetta** from the *Grinding and Thin Section Petrography Laboratory, Department of Earth Sciences, Sapienza Università di Roma*, for their technical assistance in sample preparation.

I sincerely thank **Prof. Paola Manini**, *Department of Chemical Sciences, University of Naples Federico II*, for hosting me in her laboratories and for her support of the astrogeobiology interdisciplinary project, and thanks to all UNINA laboratory scientists who helped me, in particular **Dr. Valeria Mazzini**. I would

also like to thank **Dr. Michele Cassetta** from the *University of Verona, Department of Computer Science*. I thank **Prof. Dr. François Holtz**, **Dr. Renat Almeev**, and **Lea Landgraf** from *Leibniz Universität Hannover, Institut für Mineralogie (Hannover)*, for technical assistance in the electron microscopy facility.

I gratefully acknowledge **M.P. Nuccio**, **F. Foresta Martin**, **S. Rotolo**, **G. Della Ventura**, **F. Lucci**, and **M. Nazzari** for their mentorship and support during the initial study of meteorites as part of my master's thesis.

My deepest and most heartfelt gratitude goes to **my wife, M. Greco**. This journey, with all its challenges and triumphs, was made infinitely brighter because of your love, patience, and unwavering belief in me. Every page of this thesis is a testament to your quiet strength and the beautiful life we are building together. My love for you is as endless as the cosmos I study.

This thesis would not have been possible without the support and contributions of all the people mentioned above. Thank you.

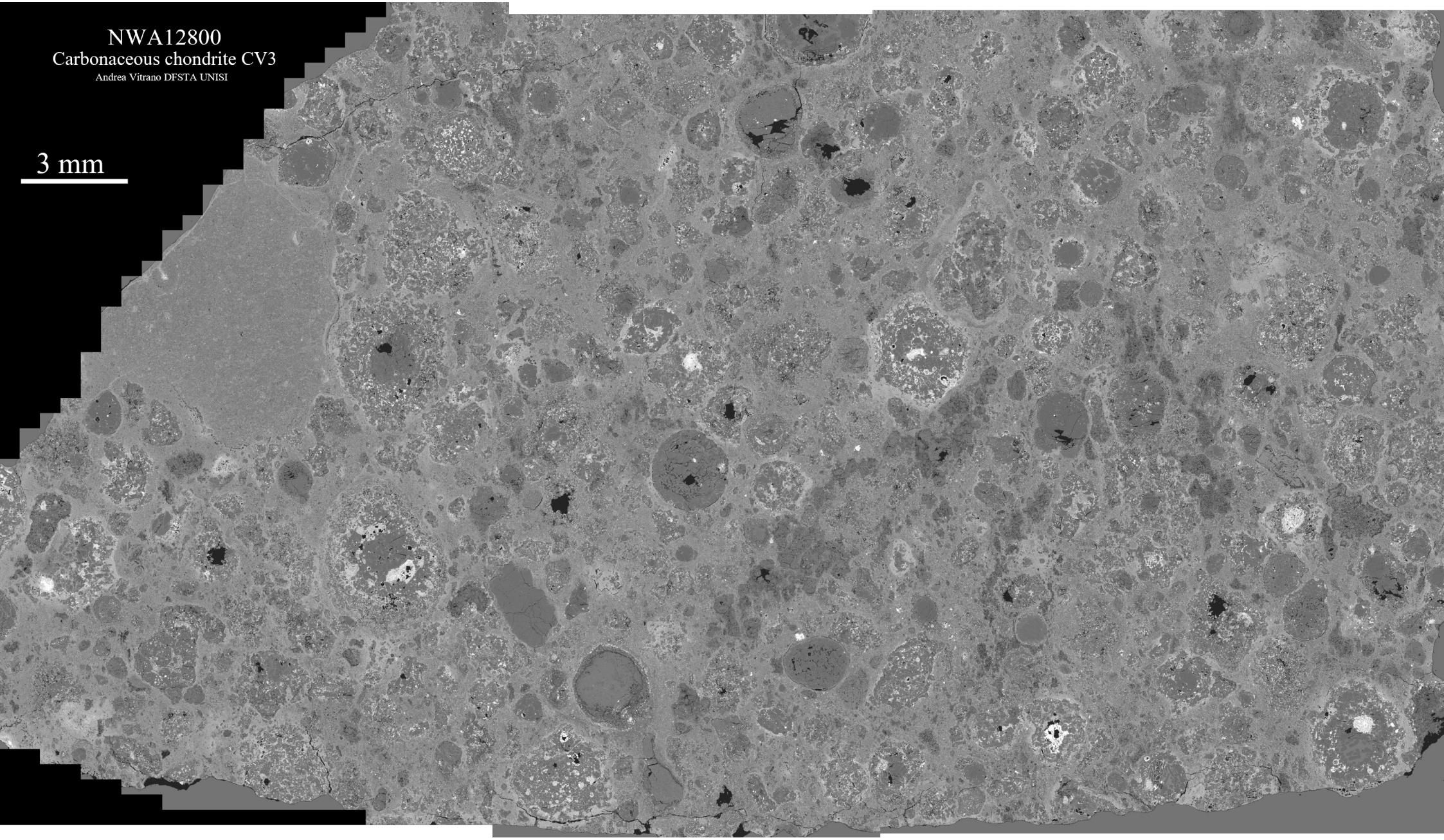
NWA12800
Carbonaceous chondrite CV3
Andrea Vitrano DFSTA UNISI
3 mm


PETROLOGY

This page intentionally left blank.